Continuous Variable Multimode Quantum States at Telecommunication Wavelengths for Quantum Networks

David Fainsin

THÈSE DE DOCTORAT
DE SORBONNE UNIVERSITÉ

Spécialité : Physique

École doctorale n°564: Physique en Île-de-France

réalisée au

Laboratoire Kastler Brossel
Physique quantique et applications

sous la direction de Valentina PARIGI

co-encadrée par Mattia WALSCHAERS

présentée par

David FAINSIN

pour obtenir le grade de :

DOCTEUR DE SORBONNE UNIVERSITÉ

Sujet de la thèse :

Continuous Variable Multimode Quantum States at Telecommunication Wavelengths for Quantum Networks

soutenue le 19 Décembre 2023

devant le jury composé de :

Pr.	Damian MARKHAM	Président du jury
Pr.	Maria V. CHEKHOVA	Rapporteur
Pr.	Peter VAN LOOCK	Rapporteur
Pr.	Valentina PARIGI	Directrice de thèse
Pr.	Sara DUCCI	Membre invitée
Cr.	Mattia WALSCHAERS	Membre invité

Il est pour moi, physicien, absurde de penser que l'univers se soit fait par "hasard".

Alfred Kastler

Contents

Remerciements

Je voudrais commencer par remercier les professeurs *van Loock* et *Chekhova* pour avoir accepté d'évaluer la qualité de ce manuscrit, la période d'écriture fut courte mais très intense. Cette période fut également pleine de doute, de redécouverte, et riche en enseignements tant sur le fond que sur la forme. Les rapports minutieux qu'ils ont établis témoignent de l'intérêt qu'ils ont porté à mon travail et je leurs en suis extrêmement reconnaissant. Je souhaite également remercier *Damian Markham*, directeur de recherche au LIP6, et *Sara Ducci*, professeure à l'Université Paris-Diderot, pour avoir accepté de faire partie de mon jury de soutenance. Le titre de Docteur de Sorbonne Université que vous m'avez délivré m'engage.

Il y a tant de personnes que j'aimerai remercier, il est cruel parfois de ne pas pouvoir dire *merci* à des personnes déjà parties. Je pense en particulier à ma grand-mère maternelle *Louise* et à mon père *Denis* qui m'ont donné, parmi beaucoup d'autres choses, ce goût pour les chiffres et le calcul très jeune. Papa, j'espère que d'où tu es, tes enfants *Laurent, Nicolas, Clément, Émilie* et moi-même te rendons fiers. J'aimerai également remercier ma mère *Véronique* d'avoir toujours pris soin de moi et de m'avoir soutenue dans mes choix d'étude, j'ai encore du mal à imaginer comment tu as accompli tout cela seule, sans jamais flancher. Je continuerai d'être attentif mais, au moment d'écrire ces lignes, je n'ai toujours pas rencontré une Femme aussi forte que toi.

J'aimerai également avoir une attention un peu particulière pour certaines personnes qui ont eu une influence importante sur mon parcours scolaire. Tout d'abord à M. *Dominique Paul*, enseignant au Lycée l'Harteloire Brest, pour avoir poussé un jeune lycéen un peu paumé vers les classes préparatoires. Quelle claque cette période d'éveil scientifique fût pour moi! Merci également aux enseignants que j'ai pu côtoyer pendant ces années, particulièrement M. *Laurent Beau* et M. *Laurent Bernis*, professeurs de MP* au Lycée La Pérouse-Kérichen de Brest. Enfin je voudrais remercier le Pr. *Romain Alléaume* de m'avoir si gentillement accueilli en dernière année à Télécom Paris dans son Master d'ingénierie quantique.

Vous êtes nombreux à m'avoir accompagné pendant ma thèse, vous avez contribué indirectement aux résultats de cette thèse. Merci aux vingt-sept colocataires qui m'ont accompagné pendant ces trois années, pèle-mèle: *Victor, Olivier, Clémence, Aristide, Elisa, Arnoult, Mario, Laure, Ariana, Sara, Mario, Mathilde, Emma, Laura, Sébastien, Romain, Elliot, Emile, Camille, Lucie, Wendy, Johan, Elia, Kay, Frédéric, Yann, Clément.* Merci à mes amis pour leur soutien sans faille, pour toutes ces soirées sur Paris qui m'ont permis de décompresser, les aventures dans la neige à Vaujany, l'Alpe d'Huez et Val Thorens sans oublier nos voyages en Grèce et au Portugal souvent précurseurs d'avancées majeures pour ce manuscrit. Pèle-mèle: *Alexandre, Audrey, Valentin, Camille, Chloé,*

Corentin, Emile, Lucien, Etienne, Gauthier, Gildas, Camille, Julien, Pauline, Mayeul, Quentin, Simon, Thomas, Margot[1]. J'ajouterai une mention particulière à *Cassandre* qui partage une place importante dans ma vie aujourd'hui. Merci également à tous les doctorants et post-doctorants du Laboratoire Kastler Brossel pour m'avoir accompagné et soutenu pendant ces trois années, j'espère avoir pu également contribuer un petit peu à votre enfer quotidien. J'ajouterai tout de même un remerciement particulier à: *Francesca, Clémentine, Adrien, Beate, Hadriel, Tiphaine, Niels, Johan, Carlos, Ilya, Antonin, David, Giacomo, Mathieu, Matthieu, Leonardo, Srinivasan Alex, Iris, Peter, Pierre-Edouard* et *Louis*.

Il me reste à remercier les personnes qui ont contribué directement à la réussite de cette thèse. Un grand merci, à *Victor* et à *Guilherme* qui m'ont chacun accompagnés 1 an et demi sur l'expérience et aux côtés desquels j'ai beaucoup appris. Toutes ces journées entières passées à monter l'expérience de zéro, aligner le guide d'onde et espérer mesurer du squeezing ont fini par payer. Merci également à *Thibault* pour son aide sur le design et l'alignement du Pulse Shaper. Un remerciement particulier à *Ganael* pour toute l'aide qu'il m'a apporté, tant sur les nombreuses ressources (SPOPO manager) que sur le temps passé à répondre à mes questions avec une grande rigueur intellectuelle. Enfin, un grand merci à *Valentina, Nicolas* et *Mattia* de m'avoir donné la chance de vivre cette aventure il y a trois ans. Bien entendu, tout particulièrement à *Valentina* et *Mattia* pour m'avoir encadré, d'avoir subit sans broncher mes apparitions intempestives dans votre bureau pour poser "juste une" question.

[1] J'espère n'oublier personne

Introduction

The history of optics is a captivating saga of discoveries, inventions, and intellectual revolutions that have shaped our understanding of light, vision, and optical phenomena. From the earliest experiments with lenses in antiquity to the complex theories of electromagnetism formulated by James Clerk Maxwell, the field of optics has traversed an extraordinary path. This historical journey has allowed us to transcend the limits of human perception, explore the infinitesimally small, and probe the mysteries of the universe.

The narrative of optics begins worldwide with the first lenses made by ancient Egyptians, Romans, and Greeks, carving crystals and observing the light changing direction. Around the 3rd century BCE, Euclid gave a first geometrical description of such phenomena [Darrigol, 2012], and at the same period in China, Mo Zi reports on the formation of shadows, light propagation, and reflection. Over the centuries, the theory of vision was further explored, especially by Alhazen in the Middle Ages. His studies on reflection, refraction, and the nature of images formed by light rays enabled fundamental advances in understanding geometrical optics. It led to the formulation of Snell-Descartes' laws in the 17th century by Willebrord Snellius and René Descartes. These laws established the foundation for lenses and paved the way for revolutionary inventions such as the microscope, opening an entirely new world of small particles, and the telescope. Galileo's observation of the solar system with his telescope in 1610 revealed unseen worlds to the naked eye, transforming our perception of the universe.

In the early 19th century, the double-slit experiment conducted by Thomas Young [Young, 1804] corroborated the wave-like model of light, confirming the ideas of Huygens and the mathematical description of Augustin Fresnel. This led to crucial discoveries in diffraction and interference, laying the groundwork for wave optics. Then what is known today as classical optics was unified under Maxwell's equations [Maxwell, 1865], and reigned supreme for decades.

In the late 19th-century classical optics began to show its limitations with the so-called "ultraviolet catastrophe" [Ehrenfest, 1911]. The model of classical optics failed to describe accurately the behavior of black-body radiations at short wavelengths, giving rise to a new scientific era that disrupted our understanding of light and matter.

In particular, Max Planck assumed that electromagnetic radiation can be emitted or absorbed only in discrete packets (later denominated "Quanta" by Einstein) in order to solve efficiently the black-body radiation problem [Planck, 1900]. Suddenly, light is not only a wave anymore but is also composed of particles known as photons. The early decades of the 20th century witnessed an extraordinary set of discoveries, marking the first steps of quantum mechanics. This conceptual revolution transformed our view of

the world, replacing classical descriptions with unprecedented rules and laws governing elementary particles and light.

During this period, physics witnessed major breakthroughs. In 1911, Heike Kamerlingh Onnes discovered superconductivity, an enigmatic phenomenon where certain materials lose all electrical resistance at very low temperatures [Onnes, 1991]. This discovery opened the door to significant advances in industry and research, ranging from magnetic levitation trains to future energy storage applications.

In the 1910s, the first description of Hydrogen atoms by Bohr led a few years later to the emergence of synthetic polymers that revolutionized chemistry and the materials industry. Researchers like Hermann Staudinger laid the foundation for our understanding of macromolecules, thus paving the way for modern plastics and a multitude of applications [Staudinger, 1920].

The study of superfluids, fluids that flow without any viscosity at extremely low temperatures, also provided new insights into the nature of matter. Pyotr Kapitsa's 1937 experiment laid the foundations for this understanding [Kapitza, 1967].

One of the most revolutionary discoveries was high-temperature superconductivity, demonstrated by Karl Müller and Johannes Bednorz in 1986 [Bednorz and Müller, 1988]. This breakthrough opened the door to even broader applications of superconductivity, with implications for energy storage, medicine, transportation, and many other fields.

Finally, and most importantly for this manuscript, in 1960, Theodore Maiman constructed the first LASER (Light Amplification by Stimulated Emission of Radiation)[2] [Maiman, 1960], paving the way for an incredibly wide range of applications, from optical communication to laser surgery and the creation of ultra-fast electronic devices.

These major discoveries laid the groundwork for the technological revolution of the 20th century, shaping the modern world we know today. From optical fibers underpinning the Internet to semiconductor-based electronic chips powering computers, advanced medical devices, and advancements in energy production, these breakthroughs have left an indelible mark on our society and continue to inspire us in the pursuit of new scientific frontiers.

These remarkable advances we've just discussed have greatly benefited from the exceptional efficiency of the mathematical model underpinning quantum mechanics. This theoretical framework, brilliantly formulated in the early 20th century by eminent minds such as Max Planck, Albert Einstein, Niels Bohr, Werner Heisenberg, and Erwin Schrödinger, allowed for a precise description of the behavior of elementary particles and light. However, even within this solid mathematical structure, questions began to arise as early as 1935 with the famous EPR (Einstein-Podolsky-Rosen) paradox [Einstein et al., 1935].

The EPR paradox raised profound questions about the nature of quantum reality, highlighting phenomena such as entanglement, where particles can remain closely correlated regardless of the distance separating them. For decades, these questions primarily remained within the realm of philosophy, sparking heated debates among pioneer quantum physicists.

However, progress in manipulating quantum systems has ultimately shifted these debates from the realm of philosophy to the realm of experimentation. Bell's inequalities, formulated by John Bell in 1964, provided a mathematical framework for testing quantum

[2]Following the invention of MASER by Townes

correlations predicted by quantum mechanics [Bell, 1964]. It followed an experiment proposal by John Clauser, Michael Horne, Abner Shimony, and Richard Holt in 1969s, along with an implementation of the experiment few years later [Clauser et al., 1969, Freedman and Clauser, 1972]. This was followed by the work of Alain Aspect and confirmed that quantum phenomena violated Bell's inequalities, thus establishing the existence of non-local correlations [Aspect et al., 1981, Aspect et al., 1982b, Aspect et al., 1982a]. Such confirmation of the quantum mechanic model was declared loophole free in 2015 [Giustina et al., 2015, Hensen et al., 2015, Aspect, 2015].

The rise of quantum information theory brought a new dimension to our understanding of quantum mechanics. The idea that quantum phenomena could be harnessed to revolutionize information technologies came to light during Richard Feynman's talk on simulating physics with quantum computers in 1982 [Feynman, 1982]. This notion was reinforced by early quantum algorithms, such as the Deutsch-Jozsa algorithm, which demonstrated the potential of quantum computers to solve certain problems exponentially more efficiently than classical computers [Deutsch and Jozsa, 1992]. Another important algorithm is the quantum search algorithm described by Grover, which has the potential to speed-up a large class of algorithm for solving NP-complete problems [Grover, 1996].

The advent of quantum cryptography, with the pioneering work of Charles Bennett, Gilles Brassard [Bennett and Brassard, 1884], and later Artur Ekert [Ekert, 1991], opened new perspectives in communication security by leveraging the properties of quantum entanglement to ensure data confidentiality [Pirandola et al., 2020]. However, enthusiasm surged with the development of Shor's algorithm in 1994 [Shor, 1994], which showed that quantum computers could, in principle, quickly break the encryption codes used in classical information security.

These developments propelled quantum information to the forefront of research and sparked a global enthusiasm for exploring the possibilities offered by quantum mechanics in the fields of communication, cryptography, and computation. The excitement in quantum physics research has given rise to a plethora of specialized areas, ranging from trapped ions [Leibfried et al., 2003] to Rydberg atoms [Browaeys and Lahaye, 2020, Jaksch et al., 2000], superconducting qubits [Wallraff et al., 2004], and Nitrogen Vacancy (NV) color centers in diamonds [Doherty et al., 2013]. Such list is not exhaustive but presents the most promising one. Each of these technologies offers exciting prospects for quantum computation, information security, and the simulation of complex quantum systems.

The field of quantum optics has also undergone significant evolution, where two distinct approaches have emerged, each making its unique contribution to the understanding and utilization of quantum mechanics. Initially, the development of discrete-variable quantum optics was marked by major advancements, including the creation of sources of single photons via quantum dots [Dabbousi et al., 1997, Somaschi et al., 2016], entangled photons via Spontaneous Parametric Down Conversion [Ghosh and Mandel, 1987], and the realization of the very first teleportation protocols [Bouwmeester et al., 1997].

However, another path opened up with continuous-variable quantum optics, which differs from the discrete version by manipulating quantum states where information is encoded on the amplitude and phase of the electromagnetic field, such as coherent and squeezed states. This approach offers unique and complementary advantages compared to its discrete-variable counterpart.

It's important to note that most existing protocols in quantum optics, such as quantum

teleportation [Furusawa et al., 1998], quantum computing [Menicucci et al., 2006], and quantum cryptography (QKD) [Grosshans and Grangier, 2002], have their continuous-variable equivalents. This convergence between the two approaches underscores the versatility and power of quantum optics, where the manipulation of continuous variable states can complement and enhance the applications in quantum information [Andersen et al., 2015].

My personal intuition on these two distinct approaches comes from the starting point of merging the fields of quantum mechanics and information theory. An approach from an information theory point of view with 'bits' leads to the emergence of the discrete variable domain with two-level quantum systems, often seen as some of the most simple quantum systems. On the other hand, the quantum physicist's approach led mostly to the Hamiltonian approach, guiding quantum simulation [Georgescu et al., 2014] and adiabatic quantum computing [Kadowaki and Nishimori, 1998, Albash and Lidar, 2018], describing quantum systems with operators evolving in an infinite-dimensional Hilbert space (Continuous Variables).

The Multimode Quantum Optics group at Laboratoire Kastler Brossel, which I had the pleasure to join in 2020, takes its origin in the pioneer work of Antoine Heidmann, Elisabeth Giacobino, Serge Reynaud, and Claude Fabre on OPOs and quantum noise reduction in the 80s [Heidmann et al., 1987, Lugiato et al., 1988, Fabre et al., 1989], achieving the record limit (at the time) of 8.5dB of squeezing in a type-II OPO [Mertz et al., 1991]. Overall, a very wide range of subjects were explored from cavities with movable mirrors [Fabre et al., 1994] to transverse effects and mode-coupling in OPOs [Schwob et al., 1998, Ducci et al., 2001]. Later on, new paths opened with Nicolas Treps on temporally multimode quantum states and optical imaging [Kolobov and Fabre, 2000, Treps et al., 2002, Treps et al., 2003], as well as on the generation of non-classical states of light [Laurat et al., 2003].

Then, with the development of frequency combs and the Nobel prize attributed to John L. Hall and Theodor W. Hänsch in 2005 for their inventions [Hall, 2006, Hänsch, 1972], the idea came to combine femtosecond lasers with OPO's leading the first feasibility study of a Synchrounsly pumped OPO (SPOPO) for the generation of quantum states in 2008 [de Valcárcel et al., 2006, Chalopin et al., 2009, Patera et al., 2009]. The study came to life in the laboratory [Pinel et al., 2012] and was further improved in the next years taking advantage of the multimode structure of the quantum comb to mold the output into graph states [Roslund et al., 2013, Cai et al., 2017, Dufour, 2018, Arzani et al., 2018].

Following the proven necessity of non-gaussian states for computational advantage in continuous variables quantum computation [Mari and Eisert, 2012] the group successfully demonstrated the mode-selective creation of non-Gaussian states via photon subtraction [Averchenko et al., 2016, Walschaers et al., 2017a, Walschaers et al., 2017b, Ra et al., 2019]. Successfully? To ensure such result the group recently took interest into a new domain with the certification of non-gaussian states [Chabaud et al., 2021].

In the meantime, with the arrival of Valentina Parigi, the group developed many collaborations toward achieving the first use cases with our source. In particular, to overcome several limitations of the SPOPO toward large cluster state [Nokkala et al., 2018], the idea emerged of a single-pass approach to multimode squeezing generation. First with bulk crystals [La Volpe et al., 2018, Volpe et al., 2019, Kouadou et al., 2019] and more recently with waveguides showing the compatibility of the source with temporal multi-

plexing [Kouadou et al., 2023]. It permitted new study on Non-Markovianity [Renault et al., 2023a] and machine learning with reservoir computing [Nokkala et al., 2020].

And what about this work? We explored the generation and manipulation of multimodes spectral states at telecom wavelengths in a single-pass scenario. A first feasibility study was done with Victor R. Rodriguez in close collaboration with Pr. Eleni Diamanti from Sorbonne Université and Pr. Christine Silberhorn's group in Padderborn University [Roman-Rodriguez et al., 2021]. We then characterized and mounted together the source for the first time where I was especially in charge of designing the mode-selective detection setup. Early results were presented in [Román Rodríguez, 2022] after what, the source had to be displaced and entirely mounted back in a new dedicated room. Here the source was extensively characterized and led to results published in [Roman-Rodriguez et al., 2023] where Victor and I are both first author. In parallel, I have run a feasibility study in close partnership with the team of Pr. Radim Filip, Vladislav Usenko and Olena Kovalenko in Olomuc University for the source to implement quantum cryptographic protocols multiplexed in frequency. We demonstrated potential improvement on Quantum Key Distribution key rate from the source characterization data, paving the way toward large multipartite cryptographic protocols with continuous variables. Finally, in a more theoretical work, I pursued the exploration for Quantum Routing in large complex multipartite networks begun in [Sansavini and Parigi, 2019] looking forward to establish construction criteria for large quantum internet with continuous variables.

0.1 Thesis outline

Part 1. The fantastic realm of Gaussian Quantum Optics.
This part has two introductory chapters. The first, *Continuous Variable Quantum Theory of Light*, introduces the modes, states, and tools used in this manuscript. The second, *Quantum Communication Protocols*, covers the essential tools in quantum communication theory, focusing on Quantum Key Distribution and Teleportation with continuous variables.

Part 2. Once upon a very short time.
This central part of the manuscript primarily focuses on the experiment conducted during my Ph.D. The first chapter, *Femtosecond Light Engineering*, describes light pulses and provides essential experimental background. The second chapter, *Single-pass Ultrafast Spontaneous Parametric Down Conversion*, explains the theory behind the core of our experiment for generating multimode squeezed states. The third chapter, *Experimental Characterization of the source*, presents the main results of the experiment.

Part 3. And they communicated safely ever after.
This final part consists of two chapters dedicated to quantum information protocols. The first chapter, *Frequency-multiplexed continuous variable quantum key distribution*, explores the feasibility of a cryptographic protocol using the source described in Part 2, along with a proposal for experimental implementation. The second and last chapter, *Quantum Routing in Multipartite Complex Networks*, is a theoretical study aimed at establishing construction criteria for a large-scale quantum internet.

Part I

The fantastic realm of Gaussian Quantum Optics

Chapter 1

Continuous Variable Quantum Theory of Light

Contents

1.1 A quantum harmonic oscillator

1.1.1 Quantization of the Hamiltonian

One of the first Hamiltonian studied in the early age of quantum mechanics is the quantized version of the harmonic oscillator [Bohr et al., 1924, Dushman, 1935]. It is one of the most known Hamiltonians in classical physics as it appears in a large variety of Physic domains, especially considering that for an arbitrary potential, one can locally study the minimum via a parabolic approximation. By 'quantizing' here we mean to build an operator (Hamiltonian) from the energy E of a classical harmonic oscillator $E = \frac{p^2}{2m} + \frac{1}{2}m\omega^2 x^2$ and substituting now the position x and momentum p of the system with their non-commuting operator version $\hat{X}$ and $\hat{P} = \frac{\hbar}{i}\frac{\partial}{\partial x}$. The position and momentum operators satisfy the commutation relation

$$\left[\hat{X}, \hat{P}\right] = i\hbar \tag{1.1}$$

and their eigenstates satisfy the eigenvalue equations

$$\begin{aligned} \hat{X}|x\rangle &= x|x\rangle, \\ \hat{P}|p\rangle &= p|p\rangle. \end{aligned} \tag{1.2}$$

These eigenstates define a complete,

$$\int \mathrm{d}x|x\rangle\langle x| = \mathbb{1} = \int \mathrm{d}p|p\rangle\langle p| \tag{1.3}$$

orthonormal basis,

$$\begin{aligned} \langle x|x'\rangle &= \delta(x - x'), \\ \langle p|p'\rangle &= \delta(p - p'), \end{aligned} \tag{1.4}$$

where δ is the Dirac function. The quantized Hamiltonian is then written as follows

$$\hat{H} = \frac{\hat{P}^2}{2m} + \frac{1}{2}m\omega^2\hat{X}^2. \tag{1.5}$$

Using now (1.1) one can then rewrite (1.5) as

$$\begin{aligned} \hat{H} &= \hbar\omega\left[\sqrt{\frac{m\omega}{2\hbar}}\left(\hat{X} - i\frac{\hat{P}}{m\omega}\right)\sqrt{\frac{m\omega}{2\hbar}}\left(\hat{X} + i\frac{\hat{P}}{m\omega}\right)\right] + \frac{\hbar\omega}{2}\mathbb{1} \\ &= \hbar\omega\left[\hat{a}^\dagger\hat{a} + \frac{1}{2}\mathbb{1}\right] \end{aligned} \tag{1.6}$$

where we defined the unit-free creation $\hat{a}^\dagger$ and annihilation $\hat{a}$ operators with commutation relation

$$\left[\hat{a}^\dagger, \hat{a}\right] = 1. \tag{1.7}$$

These two operators are then related to $\hat{X}$ and $\hat{P}$ by

$$\begin{aligned} \hat{a} &= \sqrt{\tfrac{m\omega}{2\hbar}}\left(\hat{X} + i\tfrac{\hat{P}}{m\omega}\right) & \hat{X} &= \sqrt{\tfrac{\hbar}{2m\omega}}\left(\hat{a} + \hat{a}^\dagger\right) \\ \hat{a}^\dagger &= \sqrt{\tfrac{m\omega}{2\hbar}}\left(\hat{X} - i\tfrac{\hat{P}}{m\omega}\right) & \hat{P} &= i\sqrt{\tfrac{m\omega\hbar}{2}}\left(\hat{a}^\dagger - \hat{a}\right). \end{aligned} \tag{1.8}$$

	This thesis	van Loock	Theoreticians	Experimentalists
Vac. fluct. std	σ_0	$\frac{1}{2}$	$\frac{1}{\sqrt{2}}$	1

Table 1.1: Sum up on the different usual conventions used among the quantum information community

1.1.2 Heisenberg uncertainty principle and operator normalization

It follows directly from (1.8) that $\hat{X}$ and $\hat{P}$ are Hermitian operators thus following the Heisenberg uncertainty principle [Heisenberg, 1927, Robertson, 1929, Nielsen and Chuang, 2010].

Heisenberg uncertainty principle : Suppose $\hat{A}$ and $\hat{B}$ are two Hermitian operators, they should satisfy the inequality

$$\Delta\hat{A}\Delta\hat{B} \geq \frac{1}{2}\left\|\langle\left[\hat{A},\hat{B}\right]\rangle\right\|. \tag{1.9}$$

For position and momentum operators this leads to

$$\Delta\hat{X}\Delta\hat{P} \geq \frac{\hbar}{2}. \tag{1.10}$$

One sensible comment we can make about this inequality is that it is dependent on the operator definition, thus the right hand side would change according to the definition of $\hat{X}$ and $\hat{P}$. First, it is natural to work with unit free operators, renormalizing the vacuum fluctuation without the factor $\hbar$, then one usually consider the easiest definition for its own purpose. Some researchers would like to go alternatively from $\hat{X},\hat{P}$ operators to $\hat{a},\hat{a}^\dagger$ in a symmetric way with $\hat{X} = \frac{1}{\sqrt{2}}(\hat{a}+\hat{a}^\dagger)$ leading then to $\hat{a} = \frac{1}{\sqrt{2}}(\hat{X}+i\hat{P})$. Such convention is highly adopted by **theoreticians** as now the switching is a basis change. This modifies the right hand side of (1.10) to $\frac{1}{4}$. Another standard convention is to redefine these operators such that the right hand side of the Heisenberg inequality is normalized to 1, this way the standard fluctuation of the vacuum becomes 1. This convention is mostly employed by **experimentalists**, espcially it is the one commonly used in our group. Some others would like the quadrature measurement of a coherent state to correspond exactly to the **phase space** representation of the state[1] leading to $\hat{X} = \frac{1}{2}(\hat{a}+\hat{a}^\dagger)$, changing (1.10) to $\frac{1}{16}$. Such convention is adopted in [Brausntein and van Loock, 2005]. To avoid making any confusion between the different conventions inside the community, we define σ_0^2 and recover :

$$\Delta\hat{X}\Delta\hat{P} \geq \sigma_0^2 \tag{1.11}$$

this way σ_0 represent the standard deviation of the quantum fluctuations of the vacuum. We can then give a brief sum up of these conventions in Table. 1.1 It finally implies that

[1] Indeed $|\alpha\rangle$ is dependant on the definition chosen for $\hat{a}$ and $\hat{a}^\dagger$ as $\alpha = \langle\alpha|\hat{a}|\alpha\rangle$

for this manuscript :

$$\begin{array}{ll} \hat{a} = \frac{1}{2\sigma_0}\left(\hat{X} + i\hat{P}\right) & \hat{X} = \sigma_0\left(\hat{a}^\dagger + a\right) \\ \hat{a}^\dagger = \frac{1}{2\sigma_0}\left(\hat{X} - i\hat{P}\right) & \hat{P} = i\sigma_0\left(\hat{a}^\dagger - a\right) \end{array} \tag{1.12}$$

with

$$\left[\hat{X}, \hat{P}\right] = 2i\sigma_0^2 \tag{1.13}$$

Let's now move progressively to a direct application of these preliminary concepts with light description.

1.2 Modal representation of light

1.2.1 Classical light

We call mode of the electromagnetic field a vector field $\vec{f_i}(\vec{r}, t)$ which is a normalized solution of Maxwell's equations recalled below.

$$\begin{array}{ll} \vec{\nabla} \cdot \vec{D} = \rho & \vec{\nabla} \times \vec{E} = -\frac{\partial \vec{B}}{\partial t} \\ \vec{\nabla} \cdot \vec{B} = 0 & \vec{\nabla} \times \vec{H} = \vec{J} + \frac{\partial \vec{D}}{\partial t} \end{array} \tag{1.14}$$

We can define a volume V such that, at any time t, $\vec{f_i}(\vec{r}, t)$ is contained inside this volume i.e

$$\frac{1}{V}\int_V \mathrm{d}\vec{r} \left\| \vec{f_i}(\vec{r}, t) \right\|^2 = 1 \tag{1.15}$$

Beginning with a specified mode $\vec{f_0}(\vec{r}, t)$, which can have any spatial and temporal configuration as long as it satisfies equations (1.14) and (1.15), it is always possible to construct a set of orthonormal modes $\{\vec{f_m}(\vec{r}, t)\}_m$ that serves as a basis i.e.

$$\frac{1}{V}\int_V \mathrm{d}\vec{r} \vec{f_n^*}(\vec{r}, t)\vec{f_m}(\vec{r}, t) = \delta_{m,n}. \tag{1.16}$$

This basis allows the breakdown of any solution to the Maxwell equations where the field is contained in the volume V. The electric field

$$\vec{E}(\vec{r}, t) = \vec{E}^{(+)}(\vec{r}, t) + \vec{E}^{(-)}(\vec{r}, t) \tag{1.17}$$

and in particular $\vec{E}^{(+)}(\vec{r}, t) = \vec{E}^{(-)}(\vec{r}, t)^*$, the complex electric field[2] can be written in this basis

$$\vec{E}^{(+)}(\vec{r}, t) = \sum_m \mathcal{E}_m \vec{f_m}(\vec{r}, t) \tag{1.18}$$

and thus

$$\begin{aligned} \vec{E}(\vec{r}, t) &= \sum_m \left[\mathcal{E}_m \vec{f_m}(\vec{r}, t) + \mathcal{E}_m^* \vec{f_m^*}(\vec{r}, t)\right] \\ &= 2\mathfrak{Re}\left(\vec{E}^{(+)}(\vec{r}, t)\right). \end{aligned} \tag{1.19}$$

[2] commonly associated to the terms oscillating at positive frequencies in the monochromatic plane wave basis

The complex amplitudes of the modes, denoted as $\mathcal{E}_m$, fully characterize a particular field. It will frequently prove valuable to regard the field quadratures, X_m and P_m, as the real and imaginary parts of the $\mathcal{E}_m$ amplitude[3].

$$\mathcal{E}_m = \frac{1}{2\sigma_0}(X_m + iP_m) \tag{1.20}$$

1.2.2 Modal Hilbert space

The set of orthonormal modes $\{\vec{f}_m(\vec{r},t)\}_m$ span through a Hilbert space of infinite dimension. It follows that the represention of $\vec{E}^{(+)}(\vec{r},t)$ is basis dependent and especially for us, the choice of mode basis will be of high importance for the system representation and detection process. Any basis change is done via unitary transformation ${}^{f}_{g}U$ on the initial modes such that for all n

$$\vec{g}_n = \sum_m {}^{f}_{g}U_{nm}\vec{f}_m. \tag{1.21}$$

$\vec{g}_n$ forms a new orthonormal basis of modes and any field can then be expanded as $\vec{E}^{(+)}(\vec{r},t) = \sum_n \mathcal{G}_n\vec{g}_n(\vec{r},t)$.

1.2.3 Modal characteristics: transverse and longitudinal aspects

We narrow down the set of unitary modal transformations U to those that are broken down into transverse and longitudinal components, while keeping the polarization degree of freedom unchanged. This enables us to employ factorized modes, denoted as $\vec{f}_m$, for our analysis [Fabre and Treps, 2020]. The three factors in Equation (1.22) correspond to three different kinds of multimode effects: polarization effects, spatial effects and temporal effects. For simplicity, we consider a single polarization component $\vec{\varepsilon}$ thus[4]

$$\vec{f}_m(\vec{r},t) = \vec{\varepsilon}\vec{f}^{\perp}_i(\vec{r})\vec{f}^{(t)}_j(t). \tag{1.22}$$

A clear separation of spatial and temporal modes is not always possible [La Volpe, 2019] but is valuable in the case where the temporal properties remains unchanged even when diffraction is present in the transverse mode. In the specific case of an electric field we can write

$$\vec{E}^{(+)}(\vec{r},t) = \vec{\varepsilon}\sum_{i,j}\mathcal{E}_{i,j}\vec{f}^{\perp}_i(\vec{r})\vec{f}^{(t)}_j(t) \tag{1.23}$$

which is still solution of the Maxwell equations and especially to the wave propagation equation

$$\Delta\vec{E}^{(+)}(\vec{r},t) + \frac{1}{c^2}\frac{\partial^2\vec{E}^{(+)}(\vec{r},t)}{\partial t^2} = 0. \tag{1.24}$$

Plugging now (1.23) into (1.24) one can recover the Helmotz equations for all m and explicitly study the transverse and temporal mode independently

$$(\Delta + k_i^2)\vec{f}^{\perp}_i(\vec{r}) = 0 \tag{1.25}$$

[3]The notation close to the position and momentum operator defines in the previous section is fully intended, see 1.2.4. Note that in this case X_m and P_m are not dimensionless

[4]Each factor operates on a different Hilbert space, thus in this manuscript expressions in the form $\vec{f}^{\perp}_i(\vec{r})\vec{f}^{(t)}_j(t)$ are tensor products.

and

$$\left(\frac{\partial^2}{\partial t^2} + k_j^2 c^2\right) \vec{f}_j^{(t)}(t) = 0. \tag{1.26}$$

The simplest set of solutions to (1.25) and (1.26) are the monochromatic plane waves $\{\vec{u}_m(\vec{r},t)\}_m$. It is the most commonly employed basis, which is straightforward to manipulate mathematically as at any moment, the mode $\vec{u}_m(\vec{r},t)$ oscillating at frequency $\omega_m = |\vec{k}_m|c$ is uniform through any plane that is perpendicular to a fixed direction $\vec{k}_m$ in space

$$\vec{u}_m(\vec{r},t) = \vec{\varepsilon}_m e^{-i(\vec{k}_m\cdot\vec{r}-\omega_m t)}. \tag{1.27}$$

Remark that this basis is a continuum through all possible frequencies ω_m, it becomes then sometimes more convenient to write an electric field in this basis as a continuous sum as well

$$\vec{E}^{(+)}_{mpw}(\vec{r},t) = \vec{\varepsilon}\int \mathrm{d}\omega \mathcal{E}(\omega) e^{-i(\vec{k}\cdot\vec{r}-\omega t)} \tag{1.28}$$

Moreover, when in this manuscript the electric field is defined with such continuum, if not stated otherwise the reader can assume that we are working in the monochromatic plane wave basis. Nevertheless, when the physical system is clearly defined by a finite number of monochromatic waves, the discrete sum can be employed for clarity. Such definition is often very convenient but lacks physicality as the volume containing the field is not finite anymore. There exist alternative mode bases that align more effectively with the characteristics of the light source and the optical system being examined. The usual ones are spatial, temporal or frequency Hermite-Gauss modes. Dedicated focus to this issue is given in the description of frequency combs in Chapter 3 as at the classical and quantum level, temporal or frequency modes offer a highly suitable approach for portraying light pulses and their correlations.

1.2.4 Quantization of a multimode light field

The energy of the free electromagnectic field is the integral of the energy density over volume V

$$H_R = \frac{\epsilon_0}{2}\int_V \mathrm{d}\vec{r}\left[\vec{E}^2(\vec{r},t) + c^2\vec{B}^2(\vec{r},t)\right] \tag{1.29}$$

where ϵ_0 is the dielectric permitivity of vacuum. Co-decomposing $\vec{E}$ and $\vec{B}$ into the same mode basis, one can rewrite the radiation energy as the sum of energies associated to each mode without cross-terms [Grynberg et al., 2010]. At a quantum level this Hamiltonian is formally identical to an assembly of decoupled quantum harmonic oscillators

$$\hat{H}_R = \sum_m \hbar\omega_m\left(\hat{a}_m^\dagger\hat{a}_m + \frac{1}{2}\right). \tag{1.30}$$

It permits then to introduce nicely the quantum field, that in the Heisenberg picture[5], is a quantized extension of the classical complex field in the basis of monochromatic plane waves modes $\{\vec{u}_m(\vec{r},t)\}_m$

$$\hat{E}^{(+)}(\vec{r},t) = \textstyle\sum_m \mathcal{E}_m^{(1)}\hat{a}_m\vec{u}_m(\vec{r},t) \quad \text{with} \quad \mathcal{E}_m^{(1)} = \sqrt{\frac{\hbar\omega_m}{2\epsilon_0 V}} \tag{1.31}$$

[5] meaning that the operators are time dependent

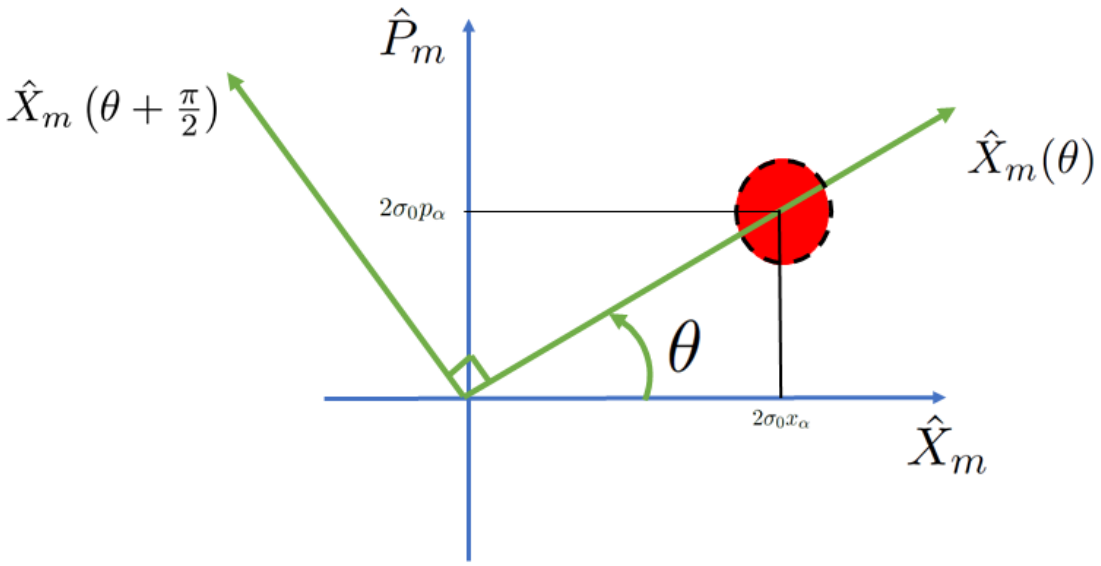

Fig. 1.1 ***Phase space representation.*** *Common representation of a quantum state via its quadratures. In green, the rotated phase space axis.*

Given equation (1.12) and (1.20), the field operator can be expressed using Hermitian quadrature operators $\hat{X}_m$ and $\hat{P}_m$ associated with the distinct modes $\vec{u}_m$, as follows:

$$\hat{X}_m = \sigma_0\left(\hat{a}_m^\dagger + \hat{a}_m\right) \quad \hat{P}_m = i\sigma_0\left(\hat{a}_m^\dagger - \hat{a}_m\right) \tag{1.32}$$

with

$$\left[\hat{X}_m, \hat{P}_{m'}\right] = 2i\sigma_0^2\delta_{m,m'} \tag{1.33}$$

$\hat{X}_m$ and $\hat{P}_m$ being hermitians once again, they are observables. In order to distinctly understand the actual physical nature to which these operators correspond, let's utilize them to rephrase the operator for the real electric field

$$\begin{aligned}\hat{E}(\vec{r},t) &= \sum_m \mathcal{E}_m^{(1)}\vec{\varepsilon}_m\left(\hat{a}_m e^{i(\vec{k}_m\cdot\vec{r}-\omega_m t)} + \hat{a}_m^\dagger e^{-i(\vec{k}_m\cdot\vec{r}-\omega_m t)}\right)\\ &= \sum_m \frac{\mathcal{E}_m^{(1)}\vec{\varepsilon}_m}{\sigma_0}\left(\hat{X}_m\cos\left(\vec{k}_m\cdot\vec{r}-\omega_m t\right) + \hat{P}_m\sin\left(\vec{k}_m\cdot\vec{r}-\omega_m t\right)\right).\end{aligned} \tag{1.34}$$

With this expression we see that the quadrature operators, sometimes referred to as, amplitude and phase, are just the amplitude of the cosine and sine components of the electric field modes. We will also from time to time use quadrature operators in a rotated phase space $\hat{X}_m\left(\theta+\frac{\pi}{2}\right) = \hat{X}_m\cos\theta + \hat{P}_m\sin\theta$, represented in Fig. 1.1

$$\hat{E}(\vec{r},t) = \sum_m \frac{\mathcal{E}_m^{(1)}\vec{\varepsilon}_m}{\sigma_0}\hat{X}_m\left(\vec{k}_m\cdot\vec{r}-\omega_m t\right). \tag{1.35}$$

1.3 Representation of a quantum state

In the earlier part, we provided a concise introduction to a quantum description of light that encompasses multiple modes. Our primary focus was on deriving the specific measurable physical operators, denoted as $\hat{X}_m$ and $\hat{P}_m$. In this section, our attention shifts to the Hilbert space of quantum states. Here, we will introduce various state representations, each of which contains all the information regarding the state. This implies that these representations are equivalent in the sense that they capture the same information. The state of an isolated physical system at time t is represented by a state vector $|\psi\rangle$ belonging to a Hilbert space $\mathcal{H}$ called the state space. Such assertion is known as the first postulate of quantum mechanics. Moreover, any pure quantum system defined on $\mathcal{H}$ can also be defined by a density operator

$$\hat{\rho}_{\text{pure}} = |\psi\rangle\langle\psi|. \tag{1.36}$$

1.3.1 Mixed quantum states

Up to this point, our discussions have centered on what are known as pure systems. However, this description falls short when the quantum state encounters classical noise or is no longer isolated. In such cases, the depiction provided is inadequate. It becomes crucial to account for statistical superpositions of states, which are referred to as mixed states. These mixed states are characterized using the density operator, a concept originally introduced by John von Neumann [Neumann, 1932]:

$$\hat{\rho} = \sum_i p_i |\psi\rangle_i \langle\psi|_i. \tag{1.37}$$

Here, the p_i values represent the statistical weights attributed to the individual pure states thus $\sum_i p_i = 1$. The density matrix obey the following properties

$$\text{Tr}(\hat{\rho}) = 1 \quad \text{and} \quad \text{Tr}\left(\hat{\rho}^2\right) \leq 1 \tag{1.38}$$

with equality $\text{Tr}\left(\hat{\rho}^2\right) = 1$ if and only if $\hat{\rho}$ is pure. This later quantity is denoted in this manuscript $\gamma = \text{Tr}\left(\hat{\rho}^2\right)$ as the degree of purity of the quantum state under study. A significant outcome of the quantum mechanics framework asserts that any mixed state can be represented as a pure state within a larger Hilbert space. Let's outline this outcome more formally. For instance, consider the density matrix $\hat{\rho}_A$ of a non pure state described in the Hilbert space $\mathcal{H}_A$. Let $|\psi\rangle$ denote a pure state within the Hilbert space $\mathcal{H}_A \bigotimes \mathcal{H}_B$. We say that $|\psi\rangle$ is a purification of $\hat{\rho}_A$ if

$$\hat{\rho}_A = \text{Tr}_B\left(|\psi\rangle\langle\psi|\right). \tag{1.39}$$

The density operator is a Hermitian operator that is positive semi-definite. When expressed in a particular basis of the state space, it takes the form of a matrix called the density matrix. This term is frequently used interchangeably with density operator. Furthermore, for any Hermitian operator $\hat{A}$ its mean value when acting on the state described by $\hat{\rho}$ can be calculated as follows

$$\langle\hat{A}\rangle = \text{Tr}\,\hat{\rho}\hat{A}. \tag{1.40}$$

The density operator representation encompasses all the details of the quantum system, as every measurement conducted on the system can be expressed through the concept of expectation value.

1.3.2 Wigner representation of a quantum state

Wigner functions offer a potent visual and analytical framework for exploring the quantum aspects of particles and waves in quantum optics. Such functions were named after being introduced by the physicist Eugene Wigner in the early age of quantum mechanics [Wigner, 1932]. By integrating position and momentum, they provide a comprehensive perspective on the quantum behavior of these systems. Considering a quantum state $|\psi\rangle$ with wavefunction $\psi(x)$ we write

$$W_{|\psi\rangle}(x,p) = \left(\frac{1}{2\pi\sigma_0}\right) \int_{\mathrm{R}} \mathrm{d}y \psi\left(x+\frac{y}{2}\right)^* \psi\left(x-\frac{y}{2}\right) e^{ipy/\sigma_0^2}. \tag{1.41}$$

Additionally, integrating the Wigner function over either the momentum space or the position space retrieves the corresponding marginal probability distributions.

$$\begin{aligned} |\psi(x)|^2 &= \int_{\mathrm{R}} \mathrm{d}p W(x,p) \\ |\psi(p)|^2 &= \int_{\mathrm{R}} \mathrm{d}x W(x,p). \end{aligned} \tag{1.42}$$

The Wigner function has interesting properties. For example, it can take negative values, reflecting the non-classical nature of quantum systems, yet this specific case won't be adressed. In this manuscript we will stick to beautiful, positive Wigner functions only. It also nicely extends to multimode quantum state scenario

$$W_{|\psi\rangle}(x,p) = \left(\frac{1}{2\pi\sigma_0}\right)^N \int_{\mathrm{R}^N} \mathrm{d}^N y \ \psi\left(x+\frac{y}{2}\right)^* \psi\left(x-\frac{y}{2}\right) e^{ipy/\sigma_0^2}. \tag{1.43}$$

Other phase-space representations exist [Husimi, 1940, Glauber, 1963, Sudarshan, 1963]. Finally, Wigner distributions can also describe mixed states as follows

$$W_{\hat{\rho}}(x,p) = \frac{1}{2\pi\sigma_0^2} \int_{\mathrm{R}} \mathrm{d}y \langle x-y|\hat{\rho}|q+y\rangle e^{ipy/\sigma_0^2} \tag{1.44}$$

expression (1.44) being valid for any operator, we can also rewrite (1.40)

$$\mathrm{Tr}\, \hat{\rho}\hat{A} = \int_{\mathrm{R}^2} \mathrm{d}x\mathrm{d}p W_{\hat{\rho}}(x,p) W_{\hat{A}}(x,p) \tag{1.45}$$

1.3.3 Schmidt decomposition

Density operators and partial trace represent just the initial steps within a diverse toolkit crucial for exploring composite quantum systems, which form the core of quantum computation and quantum information endeavors. Let's focus one very powerful one [Schmidt, 1907, Nielsen and Chuang, 2010].

Schmidt decomposition: Suppose $|\psi\rangle$ is a pure state within the Hilbert space $\mathcal{H}_A \bigotimes \mathcal{H}_B$. Then there exist orthonormal states $|u_i\rangle$ for system A, and orthonormal states $|v_i\rangle$ of system B such that

$$|\psi\rangle = \sum_i \sqrt{\lambda_i}|u_i\rangle|v_i\rangle \tag{1.46}$$

where $\{\lambda_i\}$ are the so-called Schmidt coefficients. They are non-negative real numbers satisfying[6] $\sum_i \lambda_i = 1$

The Schmidt decomposition is unique and thus very practical to study any pure bipartite quantum state since the relative amount of entanglement, (pair-wise quantum correlations) can be derived from the schmidt coefficient. One last important number to consider is the Schmidt number

$$K = \frac{1}{\sum_i \lambda_i^2}. \tag{1.47}$$

Since the space of modes is also a Hilbert space, we can also apply the Schmidt decomposition there, and then K represents the number of modes in the system [Brecht, 2014] as we shall see in Chapter 4.

1.3.4 Covariance matrix

Let's consider the column vector containing all quadrature operators of a given mode basis: $\vec{\hat{Q}} = \left(\hat{X}_1, \hat{X}_2, ..., \hat{X}_n, \hat{P}_1, \hat{P}_2, ..., \hat{P}_n\right)^T$, we then define the quantum covariance matrix $\mathbf{\Sigma}_Q$ as the $2n \times 2n$ matrix:

$$\mathbf{\Sigma}_Q = \frac{1}{2}\left\langle \vec{\hat{Q}}\vec{\hat{Q}}^T + \left(\vec{\hat{Q}}\vec{\hat{Q}}^T\right)^T \right\rangle \tag{1.48}$$

Equation (1.48) contains all second moments of the quadrature operators, this is why $\mathbf{\Sigma}_Q$ is often written in blocs

$$\mathbf{\Sigma}_Q = \begin{pmatrix} \mathbf{\Sigma}_{xx} & \mathbf{\Sigma}_{xp} \\ \mathbf{\Sigma}_{px} & \mathbf{\Sigma}_{pp} \end{pmatrix} \tag{1.49}$$

where

$$\mathbf{\Sigma}_{xx} = \left(\langle \hat{X}_i \hat{X}_j \rangle\right)_{i,j}. \tag{1.50}$$

It follows a multimode generalization of the Heinsenberg uncertainty principle [Walschaers, 2021]

$$\mathbf{\Sigma}_Q - i\Omega > 0 \tag{1.51}$$

where

$$\Omega = \begin{pmatrix} 0 & \mathbb{1} \\ -\mathbb{1} & 0 \end{pmatrix}. \tag{1.52}$$

1.4 Gaussian states

Gaussian states hold significance within the realm of continuous-variable quantum optics as they exhibit potential as foundational components for applications in quantum information serving as nonclassical states. These states possess practical value as they can be entirely described by the initial and second-order moments of the quadratures. They are thus named Gaussian states after the Wigner distribution being a Gaussian parametrized

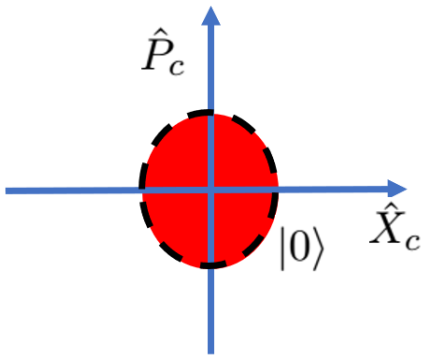

Fig. 1.2 ***Vacuum state in phase space.***

by these two moments. Considering again the column vector containing all 2n quadrature operators $\vec{\hat{Q}}$ associated to a gaussian state, it follows

$$W\left(\vec{Q}\right) = \frac{1}{(2\pi)^n \sqrt{\det \mathbf{\Sigma}_Q}} e^{-\frac{1}{2}\left(\vec{Q}-\langle\vec{\hat{Q}}\rangle\right)\mathbf{\Sigma}_Q^{-1}\left(\vec{Q}-\langle\vec{\hat{Q}}\rangle\right)}. \tag{1.53}$$

The most simple Gaussian state to consider is then the vacuum state $|0\rangle$, when the mean value of the quadratures is zero $\langle\hat{Q}\rangle = 0$ and there is a general saturation of the Heisenberg inequality $\mathbf{\Sigma}_Q = \sigma_0^2 \mathbb{1}$, the Wigner function of the vacuum is then reduced to

$$W_{|0\rangle}(\vec{Q}) = \left(\frac{1}{2\pi\sigma_0^2}\right)^n e^{-\frac{1}{2\sigma_0^2}\|\vec{Q}\|^2} \tag{1.54}$$

meaning the phase space representation of the vacuum is centered on the origin (0,0) and follows a gaussian distribution of standard deviation σ_0 see Fig. 1.2. The purity γ of a Gaussian state is simply related to the covariance matrix by the relation

$$\gamma = \frac{1}{\det \mathbf{\Sigma}_Q} \tag{1.55}$$

1.4.1 Common states in quantum optics

The goal of this section is not to present a complete review on all possible quantum states, we would rather like to introduce only the states that we are going to manipulate in this manuscript, which are mostly gaussian. For a more complete review see [Ferraro et al., 2005, Weedbrook et al., 2012]. If not precise otherwise, we will stick to a single mode scenario in this section.

a) Fock states, an important non-Gaussian state

Fock states, labeled as $|n\rangle$ where n is a natural number, are established as the eigenstates of the number operator $\hat{N} = \hat{a}^\dagger\hat{a}$. These states are linked to the count of particles within

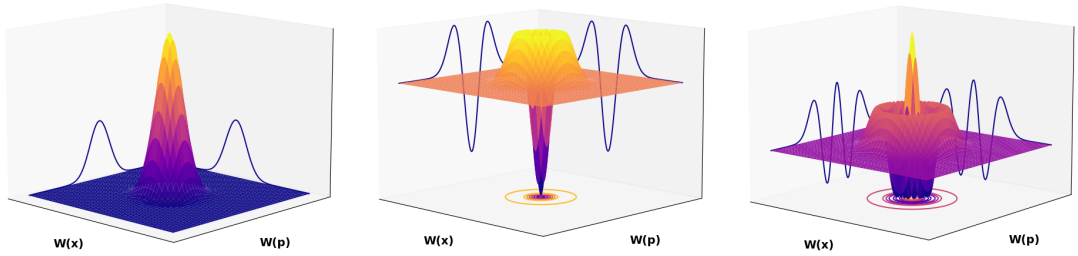

Fig. 1.3 ***Wigner representation of Fock states, from left to right,*** $|0\rangle$**,** $|1\rangle$ ***and*** $|2\rangle$.

a given state, or in the context of quantum optics, the count of photons. This relationship is derived from the properties of annihilation and creation operators

$$\hat{a}|n\rangle = \sqrt{n}|n-1\rangle, \quad \hat{a}^\dagger|n\rangle = \sqrt{n+1}|n+1\rangle \tag{1.56}$$

leading to: $\hat{N}|n\rangle = n|n\rangle$. Its first and second moment are (for $n > 0$)

$$\left\langle \hat{N} \right\rangle = n \tag{1.57}$$

meaning that the mean value of the number operator leads to the number of photons inside the state and

$$\left\langle \Delta\hat{N}^2 \right\rangle = 0, \quad \mathbf{\Sigma}_Q = (2n+1)\sigma_0^2 \mathbb{1} \tag{1.58}$$

The Wigner function of the first Fock states are represented in the figure 1.3 can be described mathematically as follow

$$W_{|n\rangle}(x,p) = \frac{(-1)^n}{2\pi\sigma_0^2} L_n\left(\frac{x^2+p^2}{\sigma_0^2}\right) e^{-\frac{1}{2\sigma_0^2}(x^2+p^2)} \tag{1.59}$$

where $L_n(x) = \frac{e^x}{n!}\frac{\mathrm{d}^n}{\mathrm{d}x^n}\left(e^{-x}x^n\right)$ are Laguerre Polynomials.

b) Thermal states

Thermal state ρ_{th} is the quantum state of the black body radiation which is often associated with thermal noise. Such a state is a statistical mixture of Fock states

$$\rho_{th} = \sum_{n=0}^{+\infty} \frac{\bar{n}_{th}^n}{(1+\bar{n}_{th})^{n+1}} |n\rangle\langle n| \tag{1.60}$$

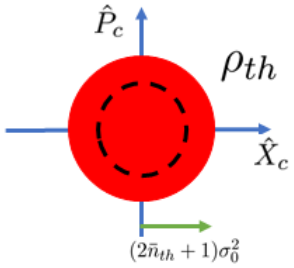

Fig. 1.4 ***Phase space representation of a thermal state.***

where $\bar{n}_{th} = \mathrm{Tr}(\hat{N}\rho_{th})$ is the mean photon number of the state. The mean photon number for a mode with frequency ω, at a given temperature T is determined by the Bose-Einstein distribution

$$\bar{n}_{th} = \frac{1}{\exp\left(\frac{\hbar\omega}{k_B T}\right) - 1} \tag{1.61}$$

where k_B is the Boltzmann constant. Thermal states describe the noise background in noisy gaussian channels. In this context, T is assumed to be the channel temperature[7]. Thermal states are Gaussian states with mean vector (0, 0) and covariance matrix $\Sigma_{th} = (2\bar{n}_{th}+1)\sigma_0^2\mathbb{1}_2$. A phase space representation of a thermal state is given in Fig. 1.4.

c) Coherent states

From a purely theoretical point of view, coherent states $|\alpha\rangle$ are eigenstates of the annihilation operators i.e :

$$\hat{a}|\alpha\rangle = \alpha|\alpha\rangle \tag{1.62}$$

where $\alpha = 2\sigma_0(x_\alpha + ip_\alpha)$ is a complex number associated to the phase space position of the mean quadrature:

$$\left\langle \hat{X} \right\rangle = 2\sigma_0 x_\alpha, \quad \left\langle \hat{P} \right\rangle = 2\sigma_0 p_\alpha. \tag{1.63}$$

Just like vacuum states they saturate the Heisenberg inequality : $\Delta^2\hat{X}\Delta^2\hat{P} = \sigma_0^2$. They can be described by the following Wigner function (represented in Fig. 1.5) :

$$W_{|\alpha\rangle}(x,p) = \frac{1}{2\pi\sigma_0^2} e^{-\frac{1}{2\sigma_0^2}\left[\left(x-\langle\hat{X}\rangle\right)^2+\left(p-\langle\hat{P}\rangle\right)^2\right]} \tag{1.64}$$

It is worth noticing that this state looks like a vacuum state displaced in the phase space, another common approach to coherent states consists in the introduction of the displacement operator $\hat{\mathcal{D}}(\alpha)$ acting on vacuum as illustrated in Fig. 1.5

$$|\alpha\rangle = \hat{\mathcal{D}}(\alpha)|0\rangle \quad \text{with} \quad \hat{\mathcal{D}}(\alpha) = e^{\alpha\hat{a}^\dagger - \alpha^*\hat{a}} \tag{1.65}$$

[7] We use these states in the next chapter where T refers to the channel transmissivity

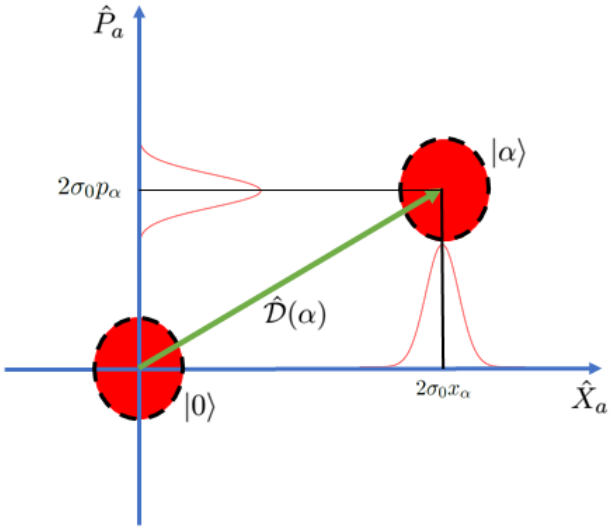

Fig. 1.5 ***Displacement operator***. *The coherent state can be understood as vacuum displaced in phase space.*

d) Squeezed vacuum states

Squeezed states are at the heart of this manuscript, we will see in chapter 4 how we can produce them experimentally. First let's introduce some important theoretical background, starting with the squeezing operator $\mathcal{S}_{\hat{a}}$ [Loudon, 1983a]:

$$\begin{aligned} |\Psi\rangle &= \mathcal{S}_{\hat{a}}(\mathcal{C})|0\rangle \\ &= \exp\left(\frac{\mathcal{C}}{2}\hat{a}^{\dagger 2} + \frac{\mathcal{C}^*}{2}\hat{a}^2\right)|0\rangle \end{aligned} \tag{1.66}$$

where $\mathcal{C} = re^{i\theta}$ is a complex number of amplitude r and phase θ. It is straigforward to show that this operator is unitary $\mathcal{S}^\dagger_{\hat{a}}(\mathcal{C})\mathcal{S}_{\hat{a}}(\mathcal{C}) = \mathbb{1}$. From the exponential series expansion, we can also see that the squeezed vacuum state results in a superposition of number states with only an even number of photons:

$$|\Psi\rangle = \frac{1}{\sqrt{\cosh(r)}}\sum_{n=0}^{\infty}\frac{\sqrt{(2n)!}}{n!}\left(-\frac{1}{2}e^{i\theta}\tanh(r)\right)^n|2n\rangle. \tag{1.67}$$

Using Baker-Campbell-Haussdorff formula we can derive

$$\mathcal{S}^\dagger_{\hat{a}}(\mathcal{C})\hat{a}\mathcal{S}_{\hat{a}}(\mathcal{C}) = \hat{a}\cosh(r) - \hat{a}^\dagger e^{i\theta}\sinh(r) \tag{1.68}$$

thus the mean photon number of a squeezed vacuum state is directly linked to r by:

$$\begin{aligned} \langle N\rangle &= \langle\Psi|\hat{a}^\dagger\hat{a}|\Psi\rangle \\ &= \langle 0|\mathcal{S}^\dagger_{\hat{a}}(\mathcal{C})\hat{a}\mathcal{S}_{\hat{a}}(\mathcal{C})\mathcal{S}^\dagger_{\hat{a}}(\mathcal{C})\hat{a}^\dagger\mathcal{S}_{\hat{a}}(\mathcal{C})|0\rangle \\ &= \sinh^2(r) \end{aligned} \tag{1.69}$$

Let's now have a look at how these operators act on the quadratures, and especially their variances. From (1.68) and its conjugate version we can directly determine that the expectation values of the quadrature operator is 0 :

$$\begin{aligned}\left\langle \hat{X} \right\rangle &= \langle \Psi | \hat{X} | \Psi \rangle \\ &= \sigma_0 \langle 0 | \mathcal{S}_{\hat{a}}^{\dagger}(\mathcal{C})(\hat{a} + \hat{a}^{\dagger}) \mathcal{S}_{\hat{a}}(\mathcal{C}) | 0 \rangle \\ &= 0\end{aligned} \tag{1.70}$$

Then following a similar approach on

$$\begin{aligned}\hat{X}^2 &= \sigma_0^2 \left(\hat{a}^{\dagger 2} + 2\hat{a}^{\dagger}\hat{a} + \hat{a}^2 + \mathbb{1} \right) \\ \hat{P}^2 &= \sigma_0^2 \left(-\hat{a}^{\dagger 2} + 2\hat{a}^{\dagger}\hat{a} - \hat{a}^2 + \mathbb{1} \right)\end{aligned} \tag{1.71}$$

we can then compute the variances of the quadrature

$$\begin{aligned}\Delta^2 \hat{X} &= \sigma_0^2 \left(e^{2r} \sin^2\left(\tfrac{\theta}{2}\right) + e^{-2r} \cos^2\left(\tfrac{\theta}{2}\right) \right) \\ \Delta^2 \hat{P} &= \sigma_0^2 \left(e^{2r} \cos^2\left(\tfrac{\theta}{2}\right) + e^{-2r} \sin^2\left(\tfrac{\theta}{2}\right) \right).\end{aligned} \tag{1.72}$$

Let's choose $\theta = 0$ for simplicity. First, this state still saturates the Heisenberg inequality $\Delta\hat{X}\Delta\hat{P} = \sigma_0^2$. The equality is preserved, but not the variance of the operators. In our case $\Delta\hat{X}$ is squeezed below the standard deviation of vacuum with squeezing factor $s = e^{-2r}$ and thus the complementary quadrature is antisqueezed with value $1/s$. The Wigner function of a squeezed state is represented in Fig. 1.6 and is written

$$W_{|\Psi\rangle}(x, p) = \frac{1}{2\pi\sigma_0^2} e^{-\frac{1}{2\sigma_0^2}\left(sx^2 + p^2/s\right)} \tag{1.73}$$

e) Two-modes squeezed vacua

To give a bit of motivation for the next section, let's first have a look at a specific case of two mode gaussian states. We consider similarly to the squeezing operator a two-mode squeezing operator acting on a quantum state as follow

$$\begin{aligned}|\Psi\rangle_{\text{TMSV}} &= \mathcal{S}^2(\mathcal{C}) |0, 0\rangle \\ &= \exp\left(\frac{\mathcal{C}}{2} \hat{a}^{\dagger}\hat{b}^{\dagger} + \frac{\mathcal{C}^*}{2} \hat{a}\hat{b} \right) |0, 0\rangle \\ &= \frac{1}{\sqrt{\cosh(r)}} \sum_{n=0}^{\infty} \left(\frac{1}{2} e^{i\theta} \tanh(r) \right)^n |n, n\rangle.\end{aligned} \tag{1.74}$$

First, in the limit of $r \to +\infty$ we observe that $|\Psi\rangle_{\text{TMSV}}$ tends to a uniform superposition of Fock states, approximating a maximally entangled state. It follows that $|\Psi\rangle_{\text{TMSV}}$ is the zero eigenvector of $\hat{X}_a - \hat{X}_b$ and $\hat{P}_a + \hat{P}_b$ [Serafini, 2017]. Then the physical interpretation becomes interesting, the measurement of one local quadrature fixes the value of the other one. We say that the quadratures $\hat{X}_a$ and $\hat{X}_b$ are correlated and conversely $\hat{P}_a$ and $\hat{P}_b$ are anti-correlated. This state is probably one of the most famous states of quantum

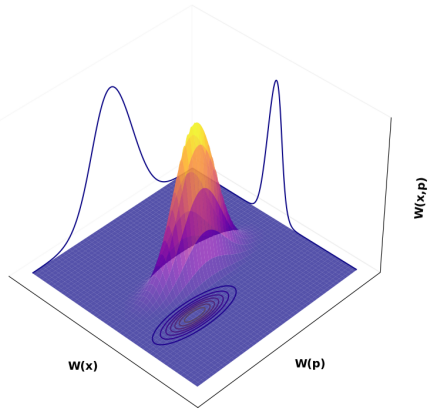

Fig. 1.6 ***Wigner representation of a squeezed state.***

mechanics often called EPR state after Eistein Podolski and Rosen gedanken experiment [Einstein et al., 1935] and is well approximated by two-mode squeezed state. Moreover we can derive for this operator a similar expression as (1.68)

$$\mathcal{S}^2(\mathcal{C})^\dagger \hat{a} \mathcal{S}^2(\mathcal{C}) = \hat{a}\cosh(r) - \hat{b}^\dagger e^{i\theta}\sinh(r) \tag{1.75}$$

With these relations it is easy to check once again that the mean quadrature values of $|\Psi\rangle_{\text{TMSV}}$ is zero:

$$\left\langle \hat{X}_a \right\rangle = \left\langle \hat{X}_b \right\rangle = \left\langle \hat{P}_a \right\rangle = \left\langle \hat{P}_b \right\rangle = 0 \tag{1.76}$$

and the quadratures variances, are given by

$$\Delta^2 \hat{X}_a = \Delta^2 \hat{X}_b = \Delta^2 \hat{P}_a = \Delta^2 \hat{P}_b = \sigma_0^2(\cosh^2(r) + \sinh^2(r)) \tag{1.77}$$

The variances observed in this context consistently surpass the quantum limit σ_0^2. Because of the symmetrical nature of the variances as outlined in Eq.(1.77), the state, when considered in terms of the quadratures for each separate partition $\hat{a}$ and $\hat{b}$, can be referred to as a thermal state. One last, and very important, comment to be made now concerns the behaviour of such state under beamsplitter transformation. Let's introduce a new mode basis $\{\hat{c}, \hat{d}\}$ define after balanced beamsplitter unitary transformation on modes $\{\hat{a}, \hat{b}\}$

$$\hat{c} = \tfrac{1}{\sqrt{2}}\left(\hat{a} + \hat{b}\right) \quad \hat{d} = \tfrac{1}{\sqrt{2}}\left(\hat{b} - \hat{a}\right) \tag{1.78}$$

The first order moment remains 0 for all quadratures of the new mode basis, yet their respective variances now become

$$\begin{aligned} \Delta^2 \hat{X}_c = \Delta^2 \hat{P}_d &= \sigma_0^2 \left(e^{2r} \sin^2\left(\frac{\theta}{2}\right) + e^{-2r} \cos^2\left(\frac{\theta}{2}\right) \right) \\ \Delta^2 \hat{X}_d = \Delta^2 \hat{P}_c &= \sigma_0^2 \left(e^{2r} \cos^2\left(\frac{\theta}{2}\right) + e^{-2r} \sin^2\left(\frac{\theta}{2}\right) \right) \end{aligned} \tag{1.79}$$

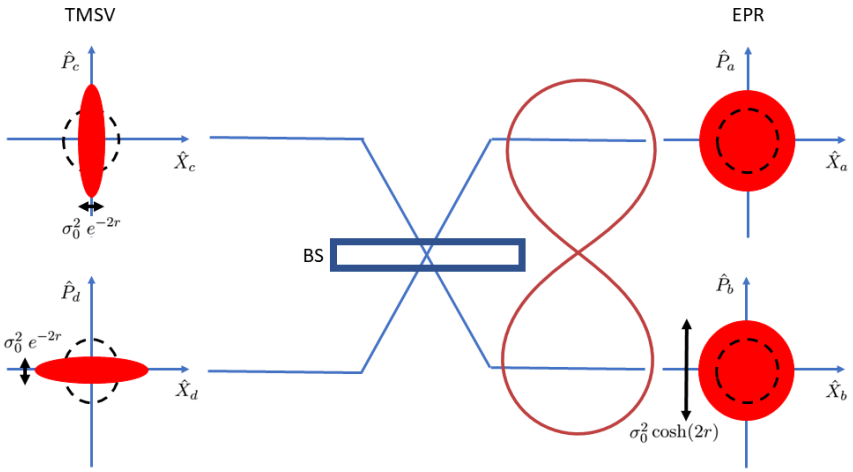

Fig. 1.7 ***Equivalence between squeezing and entanglement.***

Hence the denotation of such state as two-mode squeezed state. The beamsplitter transformation, acting as a change of basis, takes two squeezed states with a constant phase difference[8] and transforms them into an EPR state showcasing quantum correlations in their quadratures. Thus in a gaussian scenario, both squeezing and entanglement are distinctive non-classical attributes that can be exchanged through suitable changes of basis, see Fig. 1.7. The purpose of the next section is to introduce the mathematical tools for generalization of this concept.

1.4.2 Manipulation of gaussian states

a) Symplectic and Unitary transformations

Let's begin by noticing that all operators introduced in the previous part preserved the gaussian statistics of the state i.e. they mapped the gaussian marginal distributions of the Wigner function of vacuum to new gaussian distributions. In general we refer to them as gaussian transformations, this is a very useful large set of transformations to study multimode Gaussian states. They are characterized by the evolution, in the Heisenberg picture, of the $2n$ canonical operators $\hat{\vec{Q}}$ under the dynamics of a, at most, quadratic Hamiltonian $\hat{H}$ i.e. Hamiltonian which are second order polynomials in $\hat{\vec{Q}}$.

$$\hat{H} = \frac{1}{2}\hat{\vec{Q}}^T H \hat{\vec{Q}} + \vec{q}\hat{\vec{Q}}^T \tag{1.80}$$

with $\vec{q} \in \mathbb{R}^{2n}$ and H a symmetric matrix [Serafini, 2017]. From now on, we will take interest only in the purely quadratic term $\frac{1}{2}\hat{\vec{Q}}^T H \hat{\vec{Q}}$. Note that as the second term in

[8] Same optical path and same frequency.

(1.80) is linear in $\vec{\hat{Q}}$, upto a well-chosen displacement operator, the dynamics governed by such Hamiltonian can always be understood considering only the quadratic term. It then follows directly from the Heisenberg evolution

$$\frac{\mathrm{d}}{dt}\vec{\hat{Q}} = \frac{i}{2}\left[\hat{H}, \vec{\hat{Q}}\right] = \Omega H \vec{\hat{Q}} \tag{1.81}$$

The solution to (1.81) is then straightforward $\vec{\hat{Q}}(t) = e^{\Omega H t}\vec{\hat{Q}}(0)$ and since it represents the action of a unitary operation, it must preserve the canonical commutation relation

$$i\Omega = \left[\vec{\hat{Q}}(t), \vec{\hat{Q}}(t)^T\right] = ie^{\Omega H t}\Omega\left(e^{\Omega H t}\right)^T \tag{1.82}$$

Hence, denoting $S_H = e^{\Omega H t}$, equation (1.82) is reduced to $S_H \Omega S_H^T = \Omega$ and we identify the action of quadratic Hamiltonians on canonical operators as symplectic transformation.

$$e^{i\hat{H}t}\vec{\hat{Q}}e^{-i\hat{H}t} = S_H\vec{\hat{Q}} \tag{1.83}$$

This is a very important conclusion as most optics and light field transformations can be described by a quadratic hamiltonian[9] thus assessing the prominent role of the symplectic group in the quantum optic field. Equivalently for linear optics transformations, the dynamics of annihilation operators $\vec{\hat{a}} = (\hat{a}_1, \hat{a}_2, ..., \hat{a}_n)^T$, are well described by unitary transformations $U = X + iY$, matrices such that

$$\begin{aligned} UU^\dagger = U^\dagger U = \mathbb{1} \Leftrightarrow \quad & X^TX + Y^TY = XX^T + YY^T = \mathbb{1} \\ & \text{and} \\ & X^TY = Y^TX, \quad XY^T = YX^T \end{aligned} \tag{1.84}$$

As the unitary group $U(n)$ can be seen as a maximal compact subgroup within the real symplectic group $S_p(2n)$ [Arvind et al., 1995]. Considering a unitary U acting on $\vec{\hat{a}}$, $\vec{\hat{a}} \mapsto U\vec{\hat{a}}$, the corresponding symplectic matrix S acting on $\vec{\hat{Q}}$ is then

$$S = \begin{pmatrix} X & -Y \\ Y & X \end{pmatrix} \tag{1.85}$$

Moments evolution under quadratic Hamiltonian: Considering the symplectic transformation S of a generalized quadratic Hamiltonian acting on the canonical operators, the first and second order moments evolve as

$$\begin{aligned} \left\langle \vec{\hat{Q}} \right\rangle &\mapsto S\left\langle \vec{\hat{Q}} \right\rangle + \vec{q} \\ \mathbf{\Sigma}_Q &\mapsto S\mathbf{\Sigma}_Q S^T \end{aligned} \tag{1.86}$$

[9] if a higher order term might exist, it is often negligible

b) Gaussian state decomposition

One advantageous aspect of Gaussian transformations is their capacity to be broken down into a series of subtransformations, also Gaussian in nature. These subtransformations are simpler to comprehend from a physical standpoint and more feasible to construct in experimental settings. In the case of a unitary transformation, physically a lossless transformation, this breakdown corresponds to the Bloch-Messiah (BM) reduction [Bloch and Messiah, 1962, Horoshko et al., 2019]. However, in situations involving lossy transformations, which are non-unitary, the BM decomposition is not applicable. The presence of losses will lead to classical noise within the quantum state. However, through the utilization of the Williamson decomposition [Williamson, 1936], it becomes possible to represent any Gaussian state as an initial state composed of independent modes, each carrying the classical noise that subsequently evolves under a unitary Gaussian transformation. By combining these two types of decomposition, a comprehensive method for characterizing lossy Gaussian operations can be established.

Bloch-Messiah (or Euler) decomposition: For every symplectic matrix S, there exists orthogonal symplectic matrices O_1 and O_2, and diagonal matrix Z, such that

$$S = O_1 Z O_2 \tag{1.87}$$

where $Z = diag(e^{-r_1}, ..., e^{-r_n}, e^{r_1}, ..., e^{r_n})$.

Hence, the Bloch-Messiah decomposition permits the breakdown of any dynamic symplectic transformation into two passive gaussian transformations encapsulating a series of one-mode squeezers. From a more physical point of view passive gaussian transformations can be considered as within the realm of linear optics, whereas the matrix Z can be considered as a set of n squeezers with parameters $(r_1, ..., r_n)$. Moreover, we introduced in section 1.3.3 the Schmidt decomposition which decompose a state in a bipartite set of entangled modes. Combined with the results of section 1.4.1d) those two decompositions are in-fact equivalent up to a beam splitter transformation. This equivalence will be very useful to efficiently switch from non-degenerate to degenerate scenario of Spontaneous Parametric Down Conversion in Chapter 4.

Williamson decomposition: For every positive definite real matrix V there exists a symplectic matrix S and diagonal matrix D such that

$$V = SDS^T \tag{1.88}$$

where $D = diag(\nu_1, ..., \nu_n, \nu_1, ..., \nu_n)$ and $\{\nu_i\}$ are called symplectic eigenvalues of V.

The Williamson decomposition permits the breaking down of any Gaussian covariance matrix into a symplectic transformation that operates on the state defined by the diagonal matrix D. The diagonal matrix D is associated with a system where each mode exists in a thermal state, characterized by heightened fluctuations in both position and momentum compared to the vacuum state. By combining the Williamson and Bloch-Messiah

decompositions, it can be inferred that any Gaussian state (excluding phase-space displacements) can be generated from independent thermal modes with a change in basis (or a passive interferometer), independent single-mode squeezers, and a final transformation of the mode basis (or another interferometer). This implies the existence of two mode bases in which the "classical" (thermal) fluctuations and the "quantum" fluctuations (squeezing) are decoupled.

$$\mathbf{\Sigma}_Q = O_1 \underbrace{Z O_2 D O_2^T Z}_{\mathbf{\Sigma}_{sup}} O_1^T \tag{1.89}$$

Finally we call *Supermode basis*, the basis in which the covariance matrix of our quantum state is diagonal $\mathbf{\Sigma}_{sup}$, i.e. where all modes are decoupled.

1.5 Graph states

Now that we have built a concrete framework for gaussian state manipulation, we will conclude this introductory chapter by taking interest into a very specific set of multimode quantum states called *cluster states*, a specific sub-class of graph states.

Graph states, were originally introduced in the discrete variable framework by [Raussendorf and Briegel, 2001, Raussendorf et al., 2003] with the concept of 'one-way quantum computation'. They serve as universal resources for quantum computing through measurements [den Nest et al., 2006], enabling deterministic universal computation without the need for controlled two-qubit quantum gates, though with a probabilistic aspect introduced by the measurements of the photonic qubit.

Graph states in quantum physics refer to quantum states that represent a system composed of multiple components, each associated with a specific node of a graph. This graph can be thought of as a pattern of interactions: when two uncorrelated nodes interact through a C_Z gate[10], an edge is formed in the graph connecting the corresponding vertices. This edge shows that the two subsystems are now entangled. Consequently, in a continuous variable scenario [Menicucci et al., 2006, Menicucci et al., 2011, Menicucci, 2014], a simple graph's adjacency matrix, which is a symmetric $n \times n$ matrix for a system comprising n modes, fully describes any given graph state. This perspective allows us to view the graph as a summary of the modes interaction history.

In quantum-gate-based computation, graph states play a significant role as codewords for quantum error correction. They enable reliable storage and processing of quantum information even in the presence of errors by encoding quantum information within quantum states of a larger number of quantum systems. This application of graph states in quantum error correction, known as graph codes [Schlingemann and Werner, 2001], emerged as a secondary use of the concept and is intricately tied to the underlying graph structure.

Finally, the concept of a "theoretical laboratory" [Hein et al., 2006] using graph states facilitates the exploration of challenging aspects of multi-particle entanglement [Nokkala et al., 2018] with direct application to Open Quantum Systems and Non-Markovianity [Renault et al., 2023a], quantum purification an decoherence [Dür et al., 2003] and, as we shall see in the last chapter of this manuscript, quantum communications.

[10] defined in 1.5.1

1.5.1 Theoretical framework for graph states with continuous variables

From the introduction, we model graph states by a pair $G = \{V, E\}$, where V is a nonempty finite set of elements called vertices, and E is a finite set of unordered pairs of distinct vertices, called edges. Another useful tool for describing graphs $G = \{V, E\}$, where $|V| = n$, is the so-called *adjacency matrix* $A_G \in \mathcal{M}_n(\mathbb{R})$. If $V = (v_1, v_2, ..., v_n)$ then the elements $a_{i,j}$ of A_G are defined such that: $a_{i,j} = 1$ if (v_i, v_j) is an element of E and $a_{i,j} = 0$ otherwise. From this definition it appears clear that we chose to restrict our study to unweighted and undirected graphs thus assuming equal interaction strength between all modes and making A_G symmetric.

We can then define the notion of perfect cluster states when we are able to build perfect correlations between modes. We have seen in section(TMSV) that building perfect correlation between our modes requires infinite squeezing, such state are thus non physical (infinite energy). Still let's consider a set of n of these vacuum infinitely squeezed states along the p direction $|0\rangle_p^{\otimes n} = (|0\rangle_{p_1}, |0\rangle_{p_2}, ..., |0\rangle_{p_n})$. We then build correlations between two modes i and j out of operator $\hat{C}_Z = e^{i\hat{x}_i\hat{x}_j}$. It results that a generic n-mode cluster state $|G\rangle$ described by the unweighted graph G can be expressed as

$$|G\rangle = \hat{C}_Z(A_G)|0\rangle_p^{\otimes n} \tag{1.90}$$

where

$$\hat{C}_Z(A_G) = \prod_{1\leq i<j\leq n} e^{ia_{i,j}\hat{x}_i\hat{x}_j} \tag{1.91}$$

Alternatively in the Heisenberg picture, acting on the input quadratures $\vec{\hat{Q}}$ with the $\hat{C}_Z(A_G)$ gate to obtain a graph with the adjacency matrix A_G, we get the following interaction

$$\vec{\hat{Q}}_G = \hat{C}_Z(A_G)^\dagger \vec{\hat{Q}} \hat{C}_Z(A_G) = \begin{pmatrix} \mathbb{1} & 0 \\ -A_G & \mathbb{1} \end{pmatrix} \vec{\hat{Q}} \tag{1.92}$$

where $\vec{\hat{Q}}_G$ represents the quadratures of the cluster state.

1.5.2 Optical cluster states

Since we don't have a physical access to eigenstates of momentum operator, we have to rely on vacuum squeezed states in the momentum quadrature to obtain an approximation of a cluster state $|\tilde{G}\rangle$

$$|\tilde{G}\rangle = \hat{C}_Z(A_G)\left(\mathcal{S}(r)|0\rangle\right)^{\otimes n} \tag{1.93}$$

where $\mathcal{S}(r)$ is the squeezing operator introduced in section... The implementation of the $\hat{C}_Z(A_G)$ is difficult and costly experimentally, requiring online squeezing. Still, noticing that the operator resulting from the product $\hat{U} = \hat{C}_Z(A_G)\mathcal{S}(r)^{\otimes n}$ is a product of symplectic transformation thus symplectic one can apply the Bloch-Messiah decomposition to this operator

$$\hat{U} = \hat{O}_1 \left[\bigotimes_{k=1}^{n} \mathcal{S}(r_k)\right] \hat{O}_2 \tag{1.94}$$

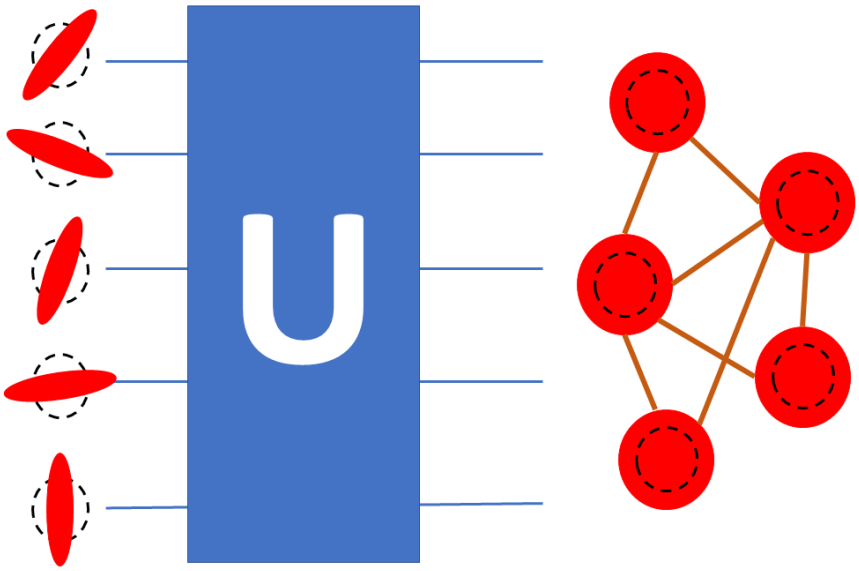

Fig. 1.8 ***Optical cluster state generation from squeezed states and linear optics.***

then combining (1.93) and (1.94) finally leads to

$$|\tilde{G}\rangle = \hat{O}_{A_G}\left[\bigotimes_{k=1}^{n}\mathcal{S}(r_k)\right]|0\rangle^{\otimes n} \tag{1.95}$$

Equation (1.95) is quite illuminating, it affirms we can build experimentally any cluster state out of a set of n squeezers acting on vacuum and a unitary transformation function of the adjacency matrix of the graph $\hat{O}_{A_G}$, as shown in Fig. 1.8. Moreover, [Ferrini et al., 2015] gives an analytical formula to build cluster states in a scenario where the squeezing is fixed by the experiment. The orthogonal matrix should be built as follow

$$\hat{O}_{A_G} = \begin{pmatrix} X & -Y \\ Y & X \end{pmatrix} \tag{1.96}$$

with

$$\begin{aligned} X &= \left(\mathbb{1} + A_G^2\right)^{-1/2} O \\ Y &= A_G\left(\mathbb{1} + A_G^2\right)^{-1/2} O \end{aligned} \tag{1.97}$$

O being in principle any orthogonal matrix but it can be adjusted to optimize the quality of the cluster state. Overall these operations can be performed in a quantum optics lab !!! As we shall see in the next part of this manuscript.

1.5.3 Certification of cluster states

One last concept to introduce concerns the certification of the quality of our cluster state, we need to define an observable (hermitian operator) for this specific purpose. Going back to equations (1.90) and (1.92), breaking $\vec{\hat{Q}}$ in $\left(\vec{\hat{X}}, \vec{\hat{P}}\right)$, we can identify $\left(\vec{\hat{P}} - A_G\vec{\hat{X}}\right)|G\rangle = 0$. We then define the so-called nullifier operators

$$\hat{\delta}_i = \hat{P}_i - \sum_j a_{i,j}\hat{X}_j \tag{1.98}$$

as they all satisfy the relation $\hat{\delta}_i|G\rangle = 0$. Thus, nullifiers provide a multipartite entanglement generalization of the entanglement relations of the ideal EPR state and they give an efficient (but not fully complete) description of the graph. For a full characterization, one should use the Furusawa-van Loock criteria [van Loock and Furusawa, 2003]. It is worth noticing that a direct consequence of this is that perfect cluster states present nullifiers with null variances

$$\Delta^2\hat{\delta}_i = 0 \tag{1.99}$$

for all i. In the case of physical cluster states introduced in the previous section this condition won't be satisfied and we would rather expect their variances to be squeezed below the shot noise limit, formally.

$$\Delta^2\hat{\delta}_i < \sigma_0^2 \tag{1.100}$$

Hence, the lower $\Delta^2\hat{\delta}_i$, the higher the quality of our cluster state is. Finally, if there exist one j_0 such that $\Delta^2\hat{\delta}_{j_0} > \sigma_0^2$ then the state can't be considered as an approximation of a cluster state anymore.

Chapter 2

Quantum Communication protocols

Contents

The purpose of this chapter is to introduce the reader to elementary quantum information protocols within the framework of Continuous Variables only. Such knowledge is essential to understand Chapters 6 and 7. We first define how we model the quantum state interaction with its environment when it is transmitted through a channel. Then we

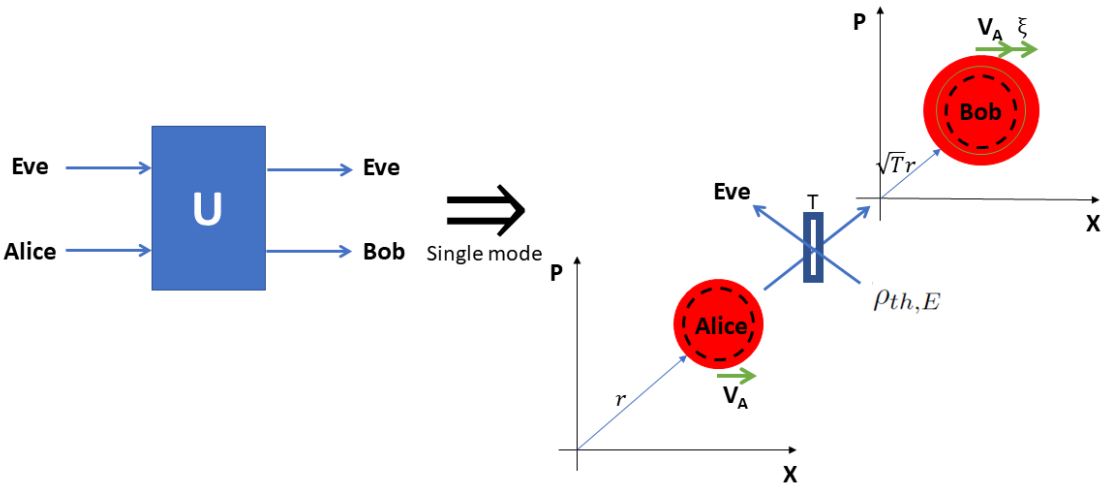

Fig. 2.1 ***A noisy and lossy gaussian channel.***

focus in the quantity of information the input state can carry and how much of it can be recovered. Finally we give two examples of quantum information protocols: quantum key distribution and quantum teleportation. Usually such protocols are presented as a game between at least 2 protagonists. Alice wants to send a classical message to Bob using a quantum state, and Bob does his best to measure the state and recover the message. Another common antagonist is Eve, the eavesdropper.

2.1 Gaussian channel

Gaussian channels play a crucial role as they are used in the standard noise model in various quantum communication protocols. They describe communication processes where the interaction between the mode (which carries the information) and the external environment causing decoherence follows linear and/or bilinear Hamiltonian dynamics i.e. it transforms a Gaussian state into a Gaussian state. Such dynamics are indeed the conditions we work with since Chapter 1. In the simplest scenario, Gaussian channels are memoryless, meaning that different quantum modes are affected independently and in the same way. This memoryless property allows us to initially study the case of a one-mode Gaussian state transmitted. The multimode generalization then follows, as all channels are treated identically and independently.

2.1.1 Single-mode channel

Consider that Alice prepares a single-mode state $\hat{\rho}_A$ and she wants to transmit it to Bob, as shown in Fig. 2.1. Initially, a comprehensive description of the process requires studying the state coupled to the environment $\hat{\rho}_{\text{tot}} = \hat{\rho}_A \otimes \hat{\rho}_E$. Note that the environment should be taken as pure gaussian in our scenario. Without loss of generality, we can consider the environment to be in a multimode vacuum state $\hat{\rho}_E = |0\rangle\langle 0|_E$ [Paulsen, 2003]. The second element to consider is that during transmission, the interaction between the quantum

state and its environment is described by a Completely Positive Trace preserving map (CPT) [Nielsen and Chuang, 2010]. Thus a Gaussian channel can be represented by a unitary interaction U applied to the composite system of the input state $\hat{\rho}_A$ and a pure state $\hat{\rho}_E$ associated with the environment. The state at the channel output is obtained by tracing out the environment

$$\hat{\rho}_B = \mathrm{Tr}_E \left[U \left(\hat{\rho}_A \otimes |0\rangle\langle 0|_E \right) U^\dagger \right]. \tag{2.1}$$

Providing an analytical expression for the evolution equation (2.1) is not trivial, especially when the state is no longer Gaussian. A detailed description of how such model acts on the Wigner function of the state can be found in [Walschaers, 2021]. Yet, as we stick to a gaussian scenario, we can fully represent the state evolution under the unitary transformation U by its covariance matrix evolution. In the case of a single-mode quantum state at Alice, represented by its covariance matrix, the unitary interaction is modeled by a beamsplitter B_T

$$B_T = \begin{pmatrix} \sqrt{T} & -\sqrt{1-T} \\ \sqrt{1-T} & \sqrt{T} \end{pmatrix} \tag{2.2}$$

where T represents the transmissivity of the beamsplitter. Denoting V_A the variance of Alice quadrature[1] under consideration, assuming that the environment is in the vacuum then Bob recovers

$$\begin{aligned} V_B &= \mathrm{Tr}_E \left[B_T \begin{pmatrix} V_A & 0 \\ 0 & \sigma_0^2 \end{pmatrix} B_T^T \right] \\ &= TV_A + (1-T)\sigma_0^2 \end{aligned} \tag{2.3}$$

The question now is how much of Alice initial information and encoded in the state can be recovered by Bob in the best scenario. To answer such question we must do at first, a little 'detour' to classical information theory and channel capacity.

2.1.2 Losses in quantum information - the beamsplitter model

In the previous paragraph, we used a beam splitter to model losses $\eta = 1 - T$ through a Gaussian channel. This framework actually generalizes to many other loss descriptions in quantum optics. Throughout this manuscript, we often use this model to account for all losses and imperfections occurring in our experiment, such as imperfect mode-matching, imperfect photodetectors, optical losses, etc. [Leonhardt and Beck, 1998]. If we consider three different loss sources η_1, η_2, and η_3, we can model them by three different successive beam splitters, which turns out to be completely equivalent to one beam splitter of efficiency $\eta = \eta_1\eta_2\eta_3$, as shown in Fig. 2.2.

2.1.3 Noise in quantum information

Losses in a Gaussian channel involve a decrease in signal power during transmission, while noise refers to random fluctuations introduced into the signal during its transmission (see Fig. 2.1). Essentially, the variance at the channel output increases due to uncertainties

[1] which can be taken as the $\hat{X}$ or $\hat{P}$ quadrature without loss of generality as the transformation is identical on both quadratures

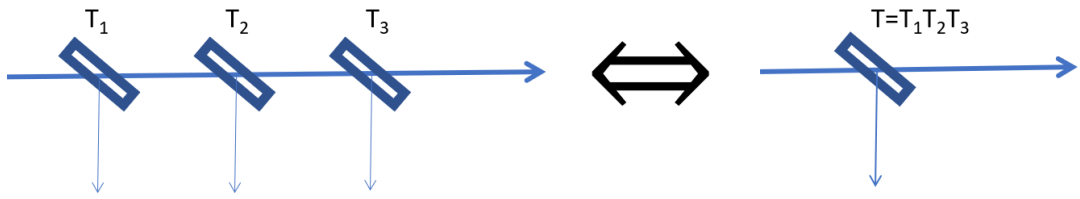

Fig. 2.2 ***Counting losses with beam splitters.***

added by different noise sources. Both phenomena can affect communication quality, particularly in the context of continuous-variable quantum communication, where managing noise and loss is crucial to ensure the reliability of quantum information transmission. Noise is commonly modeled by considering that the environment is in a thermal state. The fluctuations are then represented by a number of thermal photons inserted into the channel, commonly referred to as *excess noise* ξ. The excess noise is defined as the noise that goes beyond the loss-induced noise. This parameter is especially important as it represents a quantity that we cannot control in our experiment. More precisely, it is often associated with the intervention of the eavesdropper on the communication channel. As a result, Bob's variance after tracing out the environment is now

$$V_B = TV_A + (1-T)V_{th,E}. \tag{2.4}$$

with $V_{th,E} = (2\bar{n}_{th,E} + 1)\sigma_0^2$, $\bar{n}_{th,E}$ being the number of thermal photons in the environment. Thus, the excess noise can be expressed as

$$\xi = 2\bar{n}_{th,E}(1-T)\sigma_0^2 \tag{2.5}$$

and the variance of Bob's state at the output of the channel is

$$V_B = TV_A + (1-T)\sigma_0^2 + \xi \tag{2.6}$$

Overall the excess noise is the sum of the variances of all possible noise sources (assuming all noise sources to independant from one another) as defined in [Laudenbach et al., 2018]

$$\xi = \xi_{\text{phase}} + \xi_{\text{RIN}} + \xi_{\text{CMRR}} + ... \tag{2.7}$$

Sometimes distinguishing between loss and noise is essentially about identifying what you aim to trust. Here is an example that aims to illustrate such a difference. Consider a noisy detector; we often describe two terms. The first one is detection losses, accounted for as the imperfect conversion of the signal to a photocurrent. This is modeled by a beamsplitter with efficiency denoted as η_{det}. The second one is the electronic noise, denoted as ν_{el}, which, assuming the detector to be untrusted (often referred to as a paranoid scenario), should be considered as controlled by an eavesdropper and accounted for as excess noise. Nevertheless, in the specific case of homodyne detection, we usually have a more practical approach, considering such noise to be trusted. Thus, electronic losses are modeled via a beamsplitter (see Section 5.3.3). Now that we have completed the description of Gaussian channels, we should take an interest in how much information can be sent through this channel. The answer lies in the notion of channel capacity.

2.2 Channel capacity

The notion of Channel capacity was first introduced classically by Claude Shannon [Shannon, 1948]. It is commonly defined as the ultimate limits on data transmission rates achievable over a classical communication channel. In this section we investigate the quantum generalization of this term, introducing the notion of maximally accessible information.

2.2.1 Classical information theory

Through this paragraph we recall some basic knowledge of classical information theory. We will focus on classical information theory using gaussian random variables, i.e. random variables following normal distributions $\mathcal{N}(\mu, \sigma^2)$. We recall that the probability density of a gaussian random variable X is

$$\mathrm{P}_X(x) = \frac{1}{\sqrt{2\pi}\sigma} e^{-\frac{1}{2}\left(\frac{x-\mu}{\sigma}\right)^2}. \tag{2.8}$$

We then define the level of the quantity of information as the entropy[2] for the associated probability density of the state [Barnett, 2009].

Entropy of a random variable X :

$$H(X) = -\int_{-\infty}^{+\infty} \mathrm{P}_X(x) \log_2 \left(\mathrm{P}_X(x)\right) \mathrm{d}x. \tag{2.9}$$

For a gaussian random variable, $H(X) = \frac{1}{2}\log_2(2\pi e\sigma^2)$. An important quantity is the mutual information between two random variables A and B, it measures the common information shared by A and B, usually expressed in bits.

Mutual Information : Consider two random variables A and B, the mutual information between these two probability distribution is defined as

$$I(A, B) = H(A) + H(B) - H(A, B) \tag{2.10}$$

where $H(A, B)$ stands for the joint entropy

$$H(A, B) = -\int_a \int_b \mathrm{P}(a, b) \log_2 \left(\mathrm{P}(a, b)\right) \mathrm{d}a\mathrm{d}b \tag{2.11}$$

The mutual information between two normal distributions modeled by the covariance matrix Σ_{AB} is

$$I(A, B) = \frac{1}{2} \log_2 \left(\frac{\sigma_A^2 \sigma_B^2}{\det \Sigma_{AB}} \right) \tag{2.12}$$

[2] To be more precise the entropy is linked to information as it represents the level of misinformation in the system.

where

$$\Sigma_{AB} = \begin{pmatrix} \sigma_A^2 & \langle AB \rangle \\ \langle AB \rangle & \sigma_B^2 \end{pmatrix} \tag{2.13}$$

Finally we define the classical capacity of a channel C as the maximum information that a sender, Alice, can send to a receiver, Bob.

Channel coding theorem: Given a noisy channel with capacity, C, and given $0 < \epsilon < 1$, there is a coding scheme that allows Alice to transmit information through the channel at a rate arbitrarily close to channel capacity to Bob with a probability of error lower than ϵ and :

$$C = \max_{\{\mathrm{P}_A(a)\}} I_{AB}. \tag{2.14}$$

In essence, Shannon's channel coding theorem asserts that there exists a certain distribution of A that permits Alice to transmit an average of C bits per symbol to Bob without encountering errors. Conversely, if Alice attempts to transmit more than C bits per symbol, errors will inevitably be introduced during the transmission.

2.2.2 Von Neumann Entropy

Von Neumann Entropy: Consider a quantum state $\hat{\rho} = \sum_i \lambda_i |\phi_i\rangle\langle\phi_i|$. We define the Von Neumann Entropy as a quantum generalization of the entropy $S(\hat{\rho})$

$$S(\rho) = -\operatorname{Tr} \hat{\rho} \log_2(\hat{\rho}) = -\sum_i \lambda_i \log_2 \lambda_i. \tag{2.15}$$

In particular when $\hat{\rho}$ is a n-mode gaussian state, the Von Neumann Entropy can be computed from the symplectic eigenvalues [Demarie, 2012, Weedbrook et al., 2012]

$$S(\hat{\rho}) = \sum_i G\left(\frac{\lambda_i - 1}{2}\right) \tag{2.16}$$

where the symplectic eigenvalues results from the Williamson's decomposition introduced in 1.4.2 and

$$G(x) = (x+1)\log_2(x+1) - x\log_2(x). \tag{2.17}$$

This quantity defines the average information that can be obtained from a quantum state measurement [Neumann, 1932]. It is invariant under unitary transformation $S(\hat{\rho}) = S(U\hat{\rho}U^\dagger)$. It follows a natural definition of the classical mutual information for a quantum system composed of two subsystems A and B.

$$I(A,B) = S(A) + S(B) - S(A,B) \tag{2.18}$$

The Von Neumann Entropy is at the heart of the next section, and plays an important role in quantum key distribution.

2.2.3 Accessible information and Holevo Bound

Analogously to the classical information capacity we define the accessible information of a quantum state as the maximum quantity of bits that can be sent through the quantum channel. While there is no analytic formula for such quantity we can still derive an upper bound [Holevo, 1973].

Holevo's bound: Suppose that Alice hold a set of quantum states $(\hat{\rho}_1, \hat{\rho}_2, ..., \hat{\rho}_n)$ associated to probabilities $(\mathrm{P}_1, \mathrm{P}_2, ..., \mathrm{P}_n)$. She prepares a quantum state $\hat{\rho}_A = \sum_{i=1}^{n} \mathrm{P}_i \hat{\rho}_i$ from this set and sends it to Bob through a gaussian, memoryless channel. By performing a measurement on the quantum state Bob's accessible information is upper bounded by

$$I(A,B)^{\mathrm{acc}} \leq \chi(\hat{\rho}) = S(\hat{\rho}) - \sum_{i=1}^{n} \mathrm{P}_i S(\hat{\rho}_i) \tag{2.19}$$

In practice, this quantity allows to give an upper bound on the quantity of information that the environment, represented by Eve, has on the initial quantum state. Such result is not trivial and paves the way toward the concept of information theoretic security [Shannon, 1949, Diffie and Hellman, 1976].

2.3 Quantum Key Distribution with continuous variables

2.3.1 Modern cryptography in a nutshell

Contemporary cryptography relies on cryptographic keys, typically consisting of a concise string of characters, to encode and decode messages, along with cryptographic algorithms. Cryptography falls into two main types: symmetric [Daor et al., 1999] and asymmetric [Rivest et al., 1978, Koblitz, 1987] key cryptography, depending on the type of keys employed. Both symmetric and asymmetric key cryptography serve the purpose of ensuring data confidentiality. Asymmetric key encryption is occasionally referred to as public key encryption. Public key cryptography gives rise to digital signatures [Miller, 1986], which in turn facilitate the verification of authenticity, integrity, and non-repudiation[3]. Although cryptography plays a pivotal role in enhancing security, there exist endeavors to evade and undermine its application. Given that the majority of cryptographic algorithms are publicly accessible, the security of data largely depends on the safeguarding of cryptographic keys. Consequently, safeguarding cryptographic keys becomes of paramount importance, especially since [Shor, 1994] has shown that computational security of a cryptographic key is not guaranted anymore with a sufficiently powerful quantum computer. This threat leads to the necessity of designing new cryptographic protocols, either with computational security against quantum computers or, with information theoretic securityand this is the purpose of quantum key distribution. This latter concept was first introduced by [Bennett and Brassard, 1884, Ekert, 1991] in the framework of

[3]Non-repudiation is a situation where a statement's author cannot successfully dispute its authorship or the validity of an associated contract.

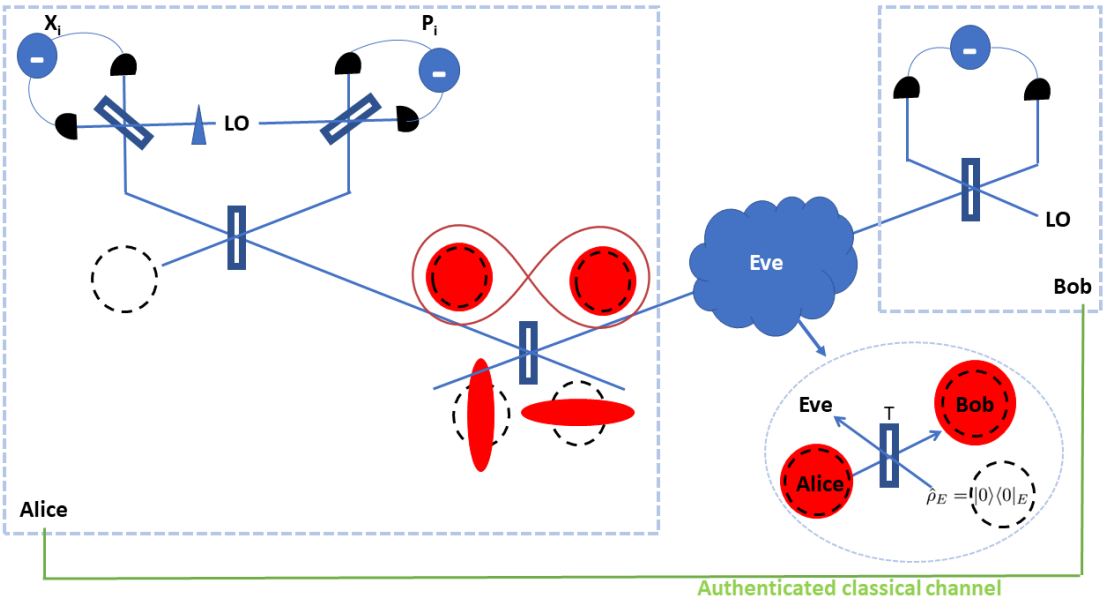

Fig. 2.3 ***Illustration of the GG02 protocol.***

discrete variables, later extended to the continuous variable framework with [Grosshans and Grangier, 2002]. Today the field of quantum key distribution is rich and vast. For a complete review of the domain see [Pirandola et al., 2020]

2.3.2 Overview of the GG02 protocol

a) Prepare and Measure versus Entanglement based protocol

In a prepare and measure scenario, Alice prepares n coherent states $|\alpha_i\rangle_{\{i=1...n\}}$ and sends them to Bob through a memoryless Gaussian channel. Bob uses homodyne detection (see Chapter 5.1) to measure one of the quadrature operators of each quantum state. A complete analog protocol, entanglement based, involves Alice preparing a TMSV state, sending one mode to Bob and measuring the two quadratures of her mode via double-homodyne detection[4]. A detailed proof on this equivalence is given in [Laudenbach et al., 2018].

b) Classical post-processing

We present a concise overview of the specific stages involved in classical data post-processing, as outlined in [Scarani et al., 2009]. These stages are responsible for converting Alice's modulation data and Bob's measurement outcomes into a universally composable secure key [Leverrier and Grangier, 2009, Leverrier, 2015].

- **Parameter estimation.** Once Alice and Bob have transmitted a sequence of states, they will disclose and cross-reference a random portion of the transmitted

[4]Often cited in the literature as heterodyne detection

data along with the corresponding measurements. This process enables them to gauge the overall transmission quality and the presence of extra noise in the channel. Using this information, they can calculate their shared mutual information $I(A, B)$, and constrain Eve's knowledge, represented by χ. If it turns out that χ exceeds $\beta I(A, B)$, the protocol terminates at this stage. The prefactor β represents the imperfect reconciliation between Alice and Bob and is typically taken equal to 0.95 [Denys et al., 2021].

- **Information reconciliation.** Otherwise, if $\beta I(A, B) > \chi$, Alice and Bob will begin the information reconciliation, a type of error correction. There are two ways to perform one-way information reconciliation, where one party shares information about their key with the other: either Bob corrects his bits based on Alice's data (direct reconciliation), or Alice corrects her bits based on Bob's data (reverse reconciliation) [Grosshans et al., 2003]. In the case of forward reconciliation, when the total transmittance η is less than 0.5 (approximately -3 dB), Eve may possess more information about what Alice sent than Bob does. Consequently, it becomes impossible to establish a secret key, assuming Eve can exploit the entire loss for her advantage. This 3 dB loss limit can be overcome by using reverse reconciliation, where Bob sends correction information to Alice, who then adjusts her bit string according to Bob's data. In this setup, Bob's data takes precedence, and because Alice's knowledge of Bob's measurement results always surpasses Eve's, the mutual information $I(A, B)$ can remain greater than χ for any total transmission η. For continuous-variable quantum key distribution (CV-QKD) using Gaussian states, various reconciliation approaches have been proposed, mostly using low-density parity-check (LDPC) codes [Van Assche et al., 2004, Leverrier et al., 2008, Richardson and Urbanke, 2008, Jouguet et al., 2011].

- **Confirmation.** Following the information reconciliation process, Alice and Bob proceed with a confirmation step using a collection of (almost) universal hash functions [Carter and Wegman, 1979]. This step is designed to establish an upper limit on the likelihood of error correction failure. Here's how it works: Alice or Bob, with equal likelihood, select one specific hash function from the family and share this choice with their counterpart. Both Alice and Bob then apply this chosen hash function to their respective keys, resulting in hash values. Afterwards, they exchange and compare these hash values. If the hash values differ, it indicates that the keys are not the same, and they terminate the process. However, if the hash values match, they continue and understand that they have established an upper boundary for the probability that their keys are not identical. This error probability depends on the length of the hash values and the type of hashing functions employed.

- **Privacy amplification.** Following a successful confirmation, Alice and Bob will have, with very high likelihood, the same bit string. Nevertheless, Eve still possesses some level of information about this key. To minimize Eve's chances of accurately guessing (a portion of) the key to an acceptable level, Alice and Bob will execute a

privacy amplification process. This involves utilizing a seeded randomness extractor algorithm on their bit strings. Typically, a family of universal hash functions [Pacher et al., 2015] is employed for this purpose.

- **(Authentication).** In order to prevent a potential man-in-the-middle attack [Weedbrook et al., 2012] by Eve, Alice and Bob must verify the authenticity of their classical communication. They achieve this by employing a family of highly effective universal hash functions but this step is beyond the scope of this manuscript.

2.3.3 Finite size-effect and asymptotic regime

To effectively calculate the secure key rate, it is advantageous to assume that Alice and Bob operate in a scenario where they exchange an infinite number of quantum states, often referred to as the asymptotic regime. This assumption offers two key advantages [Aymeric, 2022]:

- It allows us to disregard the quantum states that are discarded during the parameter estimation process.
- It enables the assumption that we can compute highly accurate estimators of the channel transmissivity and excess noise because we have an infinite amount of samples to work with.

However, it's crucial to note that this idealized scenario diverges from reality, where the number of quantum states sent over the communication channel is finite. This finite quantity has the effect of decreasing the key rate in comparison to the asymptotic scenario.

2.3.4 Information theoretic security in QKD

As mentioned at the begining of the chapter, quantum communication protocols are often represented as a game between several protagonists. In the case of quantum key distribution it usually involves Alice, Bob and Eve already presented. Yet as any game, the rules must be defined clearly. In our assumptions, we generally permit Eve to have complete access to the quantum channel, and she has the freedom to manipulate and control it. She can observe the public channel but is unable to interfere in the communication between Alice and Bob, which necessitates the use of an authenticated channel. For her eavesdropping attempts, Eve is given the liberty to prepare various ancillary states that she can interact with the transmitted quantum signal states. Subsequently, she conducts measurements on these states. Importantly, she may possess a quantum memory that allows her to store these states and carry out measurements at a later time based on the information she acquires during the classical post-processing. The actual level of information-theoretic security offered by a particular quantum key distribution (QKD) protocol strongly depends on the technological capabilities assumed for a potential eavesdropper. Based on her abilities, we classify three distinct types of eavesdropping attacks (i.e., efforts to gain information about the secret key) that are typically considered in security proofs [Scarani et al., 2009]

- **Individual attack.** Eve conducts an attack in which she treats all signals independently and identically (i.i.d.). In this attack, she prepares separate ancillary states, each of which interacts individually with a single signal pulse in the quantum channel. These states are retained in a quantum memory until the sifting procedure is completed (but before the post-processing step), and then they are measured independently, one at a time.

- **Collective attack.** Eve conducts an independent and identically distributed (i.i.d.) attack using separable ancillary states. She stores her state in a quantum memory and, at a later point in time (including after the post-processing stage), carries out an optimal collective measurement on all quantum states simultaneously.

- **Coherent attack.** This represents the most comprehensive form of attack, where no assumptions of independence and identical distribution (i.i.d.) are imposed. Specifically, Eve can create an optimal global ancillary state, whose modes, which may have interdependencies, interact with the signal pulses within the channel. Subsequently, these modes are stored and subjected to collective measurement after the classical post-processing stage.

2.3.5 Key rate derivation

a) The game rules

In the GG02 protocol, Gaussian attacks are optimal for Eve [Leverrier and Grangier, 2010] thus we place ourselves in a prepare a measure scenario where Alice sends a coherent state $|\alpha_i\rangle$ to Bob through a gaussian channel of transmissivity T. We assume that Eve has full control over the environment thus recovers all signal lost on the channel. We also assume that the noise inherent to Bob's laboratory is inaccessible to Eve. We call such quantity the excess noise ξ. We show in this work how Eve can perform a coherent attack within the assumption of asymptotic regime. More sophisticated security proofs in the finite-size regime can be found in [Leverrier et al., 2010].

b) Entangling cloner attack

Denoting $\hat{X}_i$ and $\hat{P}_i$ the quadratures of $|\alpha_i\rangle$ we define the normalized variance of the state with respect to the vacuum fluctuation in an attempt to simplify the computation of this part

$$\begin{aligned} V &= \frac{\Delta^2 \hat{X}_i}{\sigma_0^2} = \frac{\Delta^2 \hat{P}_i}{\sigma_0^2} \\ &= \cosh(2r) \end{aligned} \tag{2.20}$$

where r is the squeezing parameter associated to Alice TMSV, see Fig 2.3. From Chapter 1, we can easily derive the covariance matrix of the TMSV states that Alice prepares:

$$\Sigma_{AB} = \sigma_0^2 \begin{pmatrix} V\mathbb{1}_2 & \sqrt{V^2-1}\sigma_z \\ \sqrt{V^2-1}\sigma_z & V\mathbb{1}_2 \end{pmatrix} \tag{2.21}$$

where $\sigma_z = \begin{pmatrix} 1 & 0 \\ 0 & -1 \end{pmatrix}$ and $V = \cosh(2r)$. She keeps one mode to perform heterodyne detection on it (which is equivalent to preparing a coherent state) and sends the other one to Bob through a Gaussian channel of transmissivity T. Eve generates a TMSVS herself with variance V_E and covariance matrix

$$\Sigma_E = \sigma_0^2 \begin{pmatrix} V_E \mathbb{1}_2 & \sqrt{V_E^2 - 1}\sigma_z \\ \sqrt{V_E^2 - 1}\sigma_z & V_E \mathbb{1}_2 \end{pmatrix}. \tag{2.22}$$

Eve will take advantage of the gaussian channel to entangle her state to the one sent by Alice to Bob. Thus the total covariance matrix after the quantum channel is :

$$\begin{aligned} \Sigma_{\text{tot}} &= S_T \begin{pmatrix} \Sigma_{AB} & 0 \\ 0 & \Sigma_E \end{pmatrix} S_T^\dagger \\ &= \sigma_0^2 \begin{pmatrix} V\mathbb{1}_2 & \sqrt{T(V^2-1)}\sigma_z & -\sqrt{(1-T)(V^2-1)}\sigma_z & 0_2 \\ \sqrt{T(V^2-1)}\sigma_z & [TV + (1-T)V_E]\,\mathbb{1}_2 & \sqrt{T(1-T)}(V_E - V)\mathbb{1}_2 & \sqrt{(1-T)(V_E^2-1)}\sigma_z \\ -\sqrt{(1-T)(V^2-1)}\sigma_z & \sqrt{T(1-T)}(V_E - V)\mathbb{1}_2 & [(1-T)V + TV_E]\,\mathbb{1}_2 & \sqrt{T(V_E^2-1)}\sigma_z \\ 0_2 & \sqrt{(1-T)(V_E^2-1)}\sigma_z & \sqrt{T(V_E^2-1)}\sigma_z & V_E\mathbb{1}_2 \end{pmatrix} \end{aligned} \tag{2.23}$$

with S_T being the symplectic transformation of a beamsplitter between Bob's mode and Eve's first mode. Moreover each inital mode of Eve is a thermal state which fits with the description of a noisy lossy gaussian channel. In practice for Eve to mimic perfectly such channel she must choose

$$V_E = \frac{\xi}{1-T} + 1 \tag{2.24}$$

hence the impact of the environment on the state is modeled by the total excess noise and the transmissivity of the channel.

c) Mutual information and Signal-to-Noise ratio

To evaluate the mutual information between Alice and Bob, we can have a look at the state they share by tracing out the environment, the result is

$$\Sigma_{AB} = \sigma_0^2 \begin{pmatrix} V\mathbb{1}_2 & \sqrt{T(V^2-1)}\sigma_z \\ \sqrt{T(V^2-1)}\sigma_z & [T(V-1) + 1 + \xi]\,\mathbb{1}_2 \end{pmatrix} \tag{2.25}$$

Hence Alice and Bob mutual information, is the classical mutual information between two gaussian distributions

$$I(A,B) = \frac{1}{2}\log_2\left(1 + \frac{T(V-1)}{1+\xi}\right) \tag{2.26}$$

where the factor $\frac{T(V-1)}{1+\xi}$ compare the variances of the signal state transmited and the variances of the Noise added by Eve which is the definition of the Signal-to-Noise Ratio (SNR). Finally

$$I(A,B) = \frac{1}{2}\log_2(1 + \text{SNR}) \tag{2.27}$$

d) Unveiling the Holevo bound in the asymptotic regime

We now evaluate the maximum information Eve can have on Bob's state (reverse reconciliation) via the Holevo Bound

$$\chi(E,B) = S_E - S_{E|B} \tag{2.28}$$

S_E is the Von Neumann entropy associated to the symplectic eigenvalues of

$$\Sigma_E = \sigma_0^2 \begin{pmatrix} [TV_E + (1-T)V]\,\mathbb{1}_2 & \sqrt{T(V_E^2-1)}\sigma_z \\ \sqrt{T(V_E^2-1)}\sigma_z & V_E\mathbb{1}_2 \end{pmatrix} \tag{2.29}$$

and $S_{E|B}$ is the Von Neumann entropy associated to Eve substate conditionned on Bob's homodyne measurement. Considering the state shared by Eve and Bob

$$\begin{aligned}\Sigma_{EB} &= \sigma_0^2 \begin{pmatrix} [TV + (1-T)V_E]\,\mathbb{1}_2 & \sqrt{T(1-T)}(V_E - V)\mathbb{1}_2 & \sqrt{(1-T)(V_E^2-1)}\sigma_z \\ \sqrt{T(1-T)}(V_E - V)\mathbb{1}_2 & [(1-T)V + TV_E]\,\mathbb{1}_2 & \sqrt{T(V_E^2-1)}\sigma_z \\ \sqrt{(1-T)(V_E^2-1)}\sigma_z & \sqrt{T(V_E^2-1)}\sigma_z & V_E\mathbb{1}_2 \end{pmatrix} \\ &= \sigma_0^2 \begin{pmatrix} \Sigma_B & \Sigma_C^T \\ \Sigma_C & \Sigma_{E'} \end{pmatrix}\end{aligned} \tag{2.30}$$

Where $\Sigma_C^T = \begin{pmatrix} \sqrt{T(1-T)}(V_E - V)\mathbb{1}_2 & \sqrt{(1-T)(V_E^2-1)}\sigma_z \end{pmatrix}$, $\Sigma_B = [TV + (1-T)V_E]\,\mathbb{1}_2$, and $\Sigma_{E'} = V_E\mathbb{1}_2$. A homodyne measurement on Bob's mode will destroy the mode and transform Eve's covariance matrix depending on the quadrature that is measured. This is usually described with projectors $\Pi_X = diag(1,0), \Pi_P = diag(0,1)$ acting on the quadratures. In case of homodyne detection of $\hat{X}$ or $\hat{P}$, a partial measurement of B transforms Σ_E to $\Sigma_{E|B}$ as follows:

$$\Sigma_{E|B} = \Sigma_E - \Sigma_C \left(\Pi_{X,P}\Sigma_B\Pi_{X,P}\right)^{-1} \Sigma_C^T \tag{2.31}$$

where here the $^{-1}$ is the Moore-Penrose pseudoinverse. Equation (2.31) can also be rewritten

$$\Sigma_{E|B} = \Sigma_E - \frac{1}{\Delta^2(\hat{X},\hat{P})}\Sigma_C\Pi_{X,P}\Sigma_C^T \tag{2.32}$$

Note that a more universal analysis, putting no assumption on Eve behaviour toward Alice's input state, Eve can hold a purification of $\hat{\rho}_{AB}$. This way Eve information becomes

$$\chi(E,B) = S_{AB} - S_{A|B} \tag{2.33}$$

and $\chi(E,B)$ can be computed the same way but this time with the symplectic eigenvalues of Σ_{AB} and $\Sigma_{A|B}$ Finally we can compute the key rate K in bits/channel use with the Devetak-Winter formula [Devetak and Winter, 2005]

$$K = \beta I(A,B) - \chi(E,B) \tag{2.34}$$

or alternatively the key rate in bits/s multiplying (2.34) by the symbole rate, commonly taken to be the repetition rate of the laser source f_{rep}.

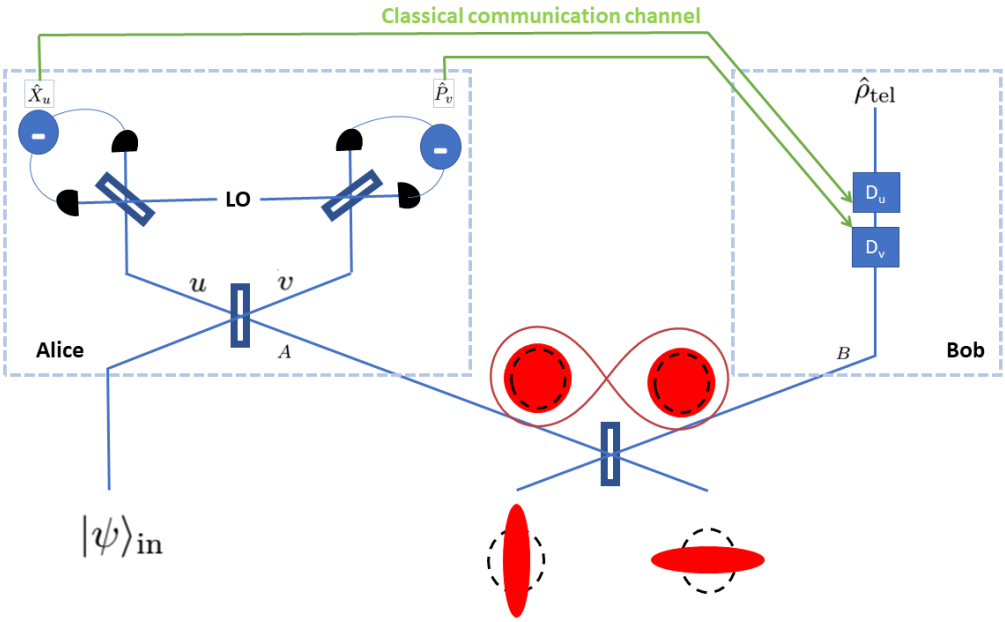

Fig. 2.4 ***Illustration of the teleportation protocol.***

e) The PLOB bound

It is intriguing to explore whether there exists a fundamental restriction on the maximum secret key rate achievable through quantum key distribution. This specific value is referred to as the two-way secret key capacity, denoted as $C(T)$, and it depends on T, representing the channel transmittance. This inquiry was addressed in reference [Pirandola et al., 2015] and the fundamental bound is now named after the authors of this paper i.e. the PLOB bound. The authors determined $C(T)$ without regard to the specific QKD protocol under consideration, expressed as

$$C(T) = -\log_2(1-T) \tag{2.35}$$

2.4 Teleportation with continuous variables

2.4.1 The protocol

Consider Alice and Bob share an EPR pair, Fig. 2.4, such that

$$\begin{aligned} \langle(\hat{X}_A - \hat{X}_B)^2\rangle &= \sigma_0^2 e^{-2r} \\ \langle(\hat{P}_A + \hat{P}_B)^2\rangle &= \sigma_0^2 e^{-2r} \end{aligned} \tag{2.36}$$

Alice now mix her part of the EPR pair with the state to be teleported $|\psi\rangle_{\text{in}}$. It's important to note that technically it is not the physical state itself that is teleported through such protocol but the information encoded on the state. This information is characterized by its quadratures $(\hat{X}_{\text{in}}, \hat{P}_{\text{in}})$ in the Heisenberg picture [Brausntein and van Loock, 2005]. We assume that Alice uses a perfectly balanced beamsplitter and that she

has no knowledge about the input state information to be teleported. Otherwise, she could cheat and transfer this information to Bob, using classical communication channel. The result is then

$$\begin{array}{ll} \hat{X}_u = \frac{1}{\sqrt{2}}\left(\hat{X}_{\text{in}} - \hat{X}_A\right) & \hat{P}_u = \frac{1}{\sqrt{2}}\left(\hat{P}_{\text{in}} - \hat{P}_A\right) \\ \hat{X}_v = \frac{1}{\sqrt{2}}\left(\hat{X}_{\text{in}} + \hat{X}_A\right) & \hat{P}_v = \frac{1}{\sqrt{2}}\left(\hat{P}_{\text{in}} + \hat{P}_A\right) \end{array} \tag{2.37}$$

and thus using equation (2.36) and (2.37) we can rewrite Bob's quadratures as

$$\begin{aligned} \hat{X}_B &= \hat{X}_{\text{in}} - (\hat{X}_A - \hat{X}_B) - \sqrt{2}\hat{X}_u \\ &= \hat{X}_{\text{in}} - \sigma_0 e^{-r}\hat{X}^{\text{vac}} - \sqrt{2}\hat{X}_u \\ \hat{P}_B &= \hat{P}_{\text{in}} + (\hat{P}_A + \hat{P}_B) - \sqrt{2}\hat{P}_v \\ &= \hat{P}_{\text{in}} + \sigma_0 e^{-r}\hat{P}^{\text{vac}} - \sqrt{2}\hat{P}_v \end{aligned} \tag{2.38}$$

If now Alice measures the quadratures $\hat{X}_u$ and $\hat{P}_v$ and send the results to Bob, the latter can effectively displace his state to recover

$$\begin{aligned} \hat{X}_B &= \hat{X}_{\text{in}} - (\hat{X}_A - \hat{X}_B) \\ &= \hat{X}_{\text{in}} - \sigma_0 e^{-r}\hat{X}^{\text{vac}} \\ \hat{P}_B &= \hat{P}_{\text{in}} + (\hat{P}_A + \hat{P}_B) \\ &= \hat{P}_{\text{in}} + \sigma_0 e^{-r}\hat{P}^{\text{vac}} \end{aligned} \tag{2.39}$$

and thus in the limit of infinite squeezing Bob's state is now exactly $|\psi\rangle_{\text{in}}$

$$\begin{aligned} \hat{X}_B &= \hat{X}_{\text{in}} \\ \hat{P}_B &= \hat{P}_{\text{in}} \end{aligned} \tag{2.40}$$

2.4.2 Fidelity

In the previous section, we explained how it was possible to transfer information from Alice to Bob via the so-called teleportation protocol. However, achieving perfect information transfer required several assumptions: infinite squeezing, a perfectly balanced beamsplitter, perfect measurement of Alice's quadratures, and a perfect displacement at Bob's stage. To evaluate how close the transfered state $\hat{\rho}_{\text{tel}}$ is to the initial state $|\psi\rangle_{\text{in}}$ we often use the Fidelity

$$\mathcal{F} = \langle\psi|_{\text{in}}\hat{\rho}_{\text{tel}}|\psi\rangle_{\text{in}} \tag{2.41}$$

as a metric (even though it is not technically a distance).

Part II

Once upon a very short time

Chapter 3

Femtosecond light engineering

Contents

The purpose of this chapter is to give an extensive description of light pulses in the femtosecond regime, how they propagate in space and how we manipulate them in the laboratory via dispersion compensation and pulse shaping. Additionally, this chapter explores classical nonlinear effects, such as Second Harmonic Generation, using short pulses.

3.1 Introduction to femtosecond pulses

As introduced in Chapter. 1, the complex electric field can be written in a basis of solution of Maxwell equations, 1.2.1.

$$\vec{E}^{(+)}(\vec{r},t) = \sum_m \mathcal{E}_m \vec{f}_m(\vec{r},t) \tag{3.1}$$

When considering a breaking of the modes into transverse and longitunal modes as in 1.2.3, they must solve the Helmholtz equation (1.25) and the propagation equation (1.26). Thus

$$\vec{E}^{(+)}(\vec{r},t) = \vec{\varepsilon}\sum_{i,j} \mathcal{E}_{i,j} \vec{f}_i^{\perp}(\vec{r}) \vec{f}_j^{(t)}(t) \tag{3.2}$$

with

$$(\Delta + k_i^2)\vec{f}_i^{\perp}(\vec{r}) = 0 \tag{3.3}$$

and

$$\left(\frac{\partial^2}{\partial t^2} + k_j^2 c^2\right) \vec{f}_j^{(t)}(t) = 0. \tag{3.4}$$

Pulses of light are often modeled as a wavepacket (propagating along axis z) formed by combining frequency modes with wavevectors near an average value of $\vec{k}_0$ (paraxial approxiamtion) and frequencies close to a central frequency $\omega_0 = c|\vec{k}_0|$ (narrowband approximation) [Grynberg et al., 2010]. We thus define the group velocity of the pulse as $v_g = \frac{\mathrm{d}\omega}{\mathrm{d}k}$. The paraxial approximation $\vec{f}_i^{\perp}(\vec{r}) = \vec{g}_i^{\perp}(\vec{r})e^{ik_0 z}$, leads to the paraxial Helmholtz equation

$$\Delta_{\perp}\vec{g}_i^{\perp}(\vec{r}) + 2ik_0\frac{\partial \vec{g}_i^{\perp}(\vec{r})}{\partial z} = 0. \tag{3.5}$$

In a similar way, the narrowband approximation permits to rewrite the temporal mode as $\vec{f}_j^{(t)}(t) = \vec{g}_j^{(t)}(t)e^{-i\omega_0 t}$. A basis of solutions to equation (3.5) are the Hermite-Gauss functions, extensively discussed in section 3.1.2, for now without any assumption made on the transverse and temporal mode, we can rewrite the complex electric field as

$$\begin{aligned}\vec{E}^{(+)}(\vec{r},t) &= \vec{\varepsilon}\left[\sum_{i,j}\mathcal{E}_{i,j}\vec{g}_i^{\perp}(\vec{r})\vec{g}_j^{(t)}(t)\right]e^{-i(\omega_0 t - k_0 z)} \\ &= \vec{\varepsilon}\mathcal{E}(\vec{r},t)e^{-i(\omega_0 t - k_0 z)}\end{aligned} \tag{3.6}$$

$\mathcal{E}(\vec{r},t)$ carries the information about the spatial mode and the envelope of the pulse defined by the inverse Fourier transform of the pulse spectrum centered at frequency ω_0. Such pulses find extensive use in research laboratories as temporal probes, enabling unparalleled resolutions. Additionally, they play a crucial role in information technologies for transmitting information through optical fibers [Hache, 2016]. Another pivotal feature, central to this manuscript, is the high peak power that leads to efficient nonlinear processes.

3.1.1 Propagation equation

To study the propagation of light pulses we neglect the vectorial aspect of the electric field and consider only the electric field as its temporal mode travelling along the z axis

$$E(z,t) = \mathcal{E}(z,t)e^{i(k_0 z - \omega_0 t)} + c.c = E^{(+)}(z,t) + E^{(-)}(z,t) \tag{3.7}$$

$\mathcal{E}(z,t)$ being the envelope of the pulse centered at frequency ω_0 with spectral bandwidth $\Delta\omega \ll \omega_0$. This pulse is one solution of the standard propagation equation (3.8) derived from Maxwell Equations (1.14)

$$\frac{\partial^2 E(z,t)}{\partial z^2} - \mu_0 \frac{\partial^2 D(z,t)}{\partial t^2} = 0. \tag{3.8}$$

We can then derive the standard propagation equation in the frequency domain by Fourier transform of (3.8), here keeping only the terms oscillating at positives frequencies

$$\frac{\partial^2 E^{(+)}(z,\omega)}{\partial z^2} + k^2(\omega)E^{(+)}(z,\omega) = 0 \tag{3.9}$$

where

$$E^{(+)}(z,\omega) = \int_{-\infty}^{+\infty} E^{(+)}(z,t)e^{-i\omega t}\mathrm{d}t = \int_{-\infty}^{+\infty} \mathcal{E}(z,t)e^{i(k_0 z - \omega_0 t)}e^{-i\omega t}\mathrm{d}t = \mathcal{E}(z,\omega-\omega_0)e^{ik_0 z} \tag{3.10}$$

and $k(\omega) = n(\omega)\frac{\omega}{c}$. Inserting (3.10) into (3.9) we obtain

$$\frac{\partial^2 \mathcal{E}}{\partial z^2}(z,\omega-\omega_0) + 2ik_0\frac{\partial \mathcal{E}}{\partial z}(z,\omega-\omega_0) + (k^2(\omega) - k_0^2)\mathcal{E}(z,\omega-\omega_0) = 0 \tag{3.11}$$

A Taylor expansion of the wavevector $k(\omega) = k(\omega_0) + (\omega-\omega_0)k'(\omega_0) + \frac{(\omega-\omega_0)^2}{2}k''(\omega_0)$, after a few line of computation in the slowly varying envelope approximation[1] [Hache, 2016] finally gives us the standard propagation equation for a short pulse in a linear media.

$$\frac{\partial \mathcal{E}}{\partial z}(z,\omega-\omega_0) - i\frac{k_0''}{2}(\omega-\omega_0)^2\mathcal{E}(z,\omega-\omega_0) = 0 \tag{3.12}$$

From (3.12), we find that the envelope shape will change depending on $k_0'' = \frac{\partial}{\partial\omega}\left(\frac{1}{v_g}\right)$ i.e. due to the group velocity being itself frequency dependant. We thus usually call this term **Group Velocity Dispersion (GVD)** expressed usually in $\mathrm{fs}^2/\mathrm{cm}$. The solution of equation 3.12 is

$$\mathcal{E}(z,\omega) = \mathcal{E}(0,\omega-\omega_0)e^{i\frac{k_0''}{2}(\omega-\omega_0)^2 z} \tag{3.13}$$

showing that through propagation the spectrum of the pulse does not change but the spectral phase does. This results in a temporal dispersion of our pulse. More on this effect and how to compensate the dispersion is mentioned in section. 3.2.

[1] which assumes that the variation, in the amplitude, of the envelope $\mathcal{E}$ as it propagates over a wavelength is very small. Mathematically we can neglect $\frac{\partial^2\mathcal{E}}{\partial z^2}$ and $k_0'\frac{\partial^2\mathcal{E}}{\partial z\partial\omega}$ with respect to $k_0\frac{\partial\mathcal{E}}{\partial z}$

3.1.2 Transverse propagation equation

Up to this point, we have represented the complex electric field as a pulse traveling along the z-axis without making any assumptions about its transverse profile. The spatial extent of a beam is finite, and the distribution of light in a transverse plane is non-uniform. In this context, the propagation equation in a vacuum (3.8) involves the gradients of the electric field in the transverse directions, denoted as $\Delta_\perp$, which are responsible for the phenomena of light diffraction:

$$\Delta_\perp \mathcal{E}(\vec{r}) + 2ik\frac{\partial \mathcal{E}(\vec{r})}{\partial z} = 0 \tag{3.14}$$

It has been demonstrated that the set of Hermite-Gauss functions constitutes a comprehensive basis of solutions for the paraxial Helmholtz equation [Delsart, 2008]. This implies that every solution of Equation (3.14), and consequently, every paraxial wave, can be expressed as a linear combination of various Hermite-Gauss functions, as illustrated in Fig. 3.1. These functions collectively define a variety of spatial patterns within the electromagnetic field. They can be explicitly expressed as:

$$\mathcal{E}(\vec{r})_{l,n} = \mathcal{E}(0)_{l,n} H_l\left(\frac{\sqrt{2}x}{w(z)}\right) H_n\left(\frac{\sqrt{2}y}{w(z)}\right) e^{-i\left(k\frac{x^2+y^2}{2R(z)} - (l+n+1)\phi(z)\right)} \tag{3.15}$$

with

$$\mathcal{E}(0)_{l,n} = \sqrt{\frac{2}{\pi}\frac{1}{l!n!2^{l+n}}}\frac{w_0}{w(z)} \tag{3.16}$$

and H_l being the l^{th} order Hermite polynomial

$$H_l(x) = (-1)^l e^{x^2}\frac{\partial^l}{\partial x^l}\left(e^{-x^2}\right) \tag{3.17}$$

The position $z = 0$ corresponds to the minimum size of the beam, the waist w_0. In this position, the wavefront is a plane. As the electromagnetic wave propagates away from the waist, the beam size changes as:

$$w(z) = w_0\sqrt{1 + \left(\frac{z}{z_R}\right)^2} \tag{3.18}$$

Meanwhile, the wavefront curves, gradually approaching a spherical wave in the far field induced by the presence of the term $R(z)$ called radius of curvature.

$$R(z) = z\left(1 + \left(\frac{z_R}{z}\right)^2\right) \tag{3.19}$$

The characteristic focal size of the beam is determined by the Rayleigh length, denoted as z_R. This length represents the propagation distance required to double the beam's cross-sectional area:

$$z_R = \frac{\pi w_0^2}{\lambda} \tag{3.20}$$

Finally $\phi(z) = \arctan\left(\frac{z}{z_R}\right)$ is called the Gouy Phase.

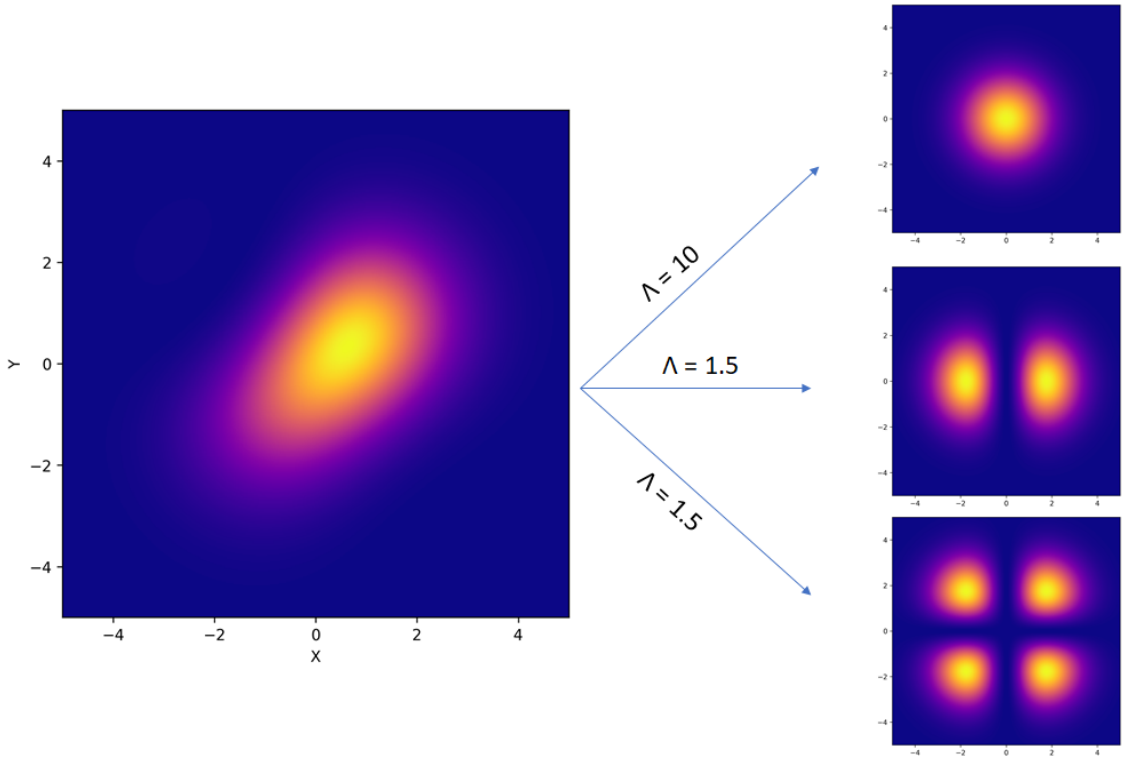

Fig. 3.1 ***Transverse Mode.*** *Representation of an arbitrary spatial profile with its decomposition in the spatial Hermite Gauss basis. The factor Λ represent the weight of each spatial mode in the decomposition.*

3.1.3 Optical Frequency combs

The term 'optical frequency comb' refers to a specific category of pulsed lasers in which a significant number of spectral modes within the laser cavity are coherently stimulated through a technique known as mode-locking. This broadband excitation range, combined with a high level of coherence, enables the generation of extremely short pulses, reaching durations in the femtosecond and even attosecond regime. Initially developed as instruments for measuring the cycles of atomic optical clocks, frequency combs exhibit remarkable phase stability among the discrete 'teeth' of the comb, allowing for unparalleled precision in time and frequency measurements. Subsequently, they have found diverse applications and have been extensively employed in fundamental research across various domains, including metrology, spectroscopy, and investigations of optical, atomic, molecular, and solid-state systems [Udem et al., 2002, Fortier and Baumann, 2019, Cladé et al., 2019].

Very recently[2], Anne L'Huillier, Pierre Agostini, and Ferenc Krausz were awarded the Nobel Prize 'for experimental methods that generate attosecond pulses of light for the

[2] As of the time of writing this manuscript

study of electron dynamics in matter' [Antoine et al., 1996, Krausz, 2016, Agostini and DiMauro, 2004].

In the following, we will give a mathematical description for the output of a mode-locked laser. The output field can be depicted, in the temporal domain, by an optical wave with carrier frequency ω_0 and envelope $\mathcal{E}(t)$

$$E(t) = \mathcal{E}(t)e^{-i\omega_0 t} + c.c. \tag{3.21}$$

Since the train of pulses is periodic in time $\mathcal{E}(t) = \mathcal{E}(t - T_{\text{rep}})$, one can decompose it on a discrete Fourier basis

$$E(t) = \sum_m \mathcal{E}_m e^{-i(\omega_0 + m\omega_{\text{rep}})t} + c.c \tag{3.22}$$

where $\mathcal{E}_m$ are the Fourier components of $\mathcal{E}(t)$ and $\omega_{\text{rep}} = \frac{2\pi}{T_{\text{rep}}}$. The spectrum of the output of a mode-locked field is, therefore, represented by a comb of equally separated frequencies around ω_0

$$\omega_m = \omega_0 + m\omega_{\text{rep}} \tag{3.23}$$

Please note that this result have been obtained under the assumption of identical pulses. Generally, for any pulse shape, there exists a carrier-envelope phase ϕ_{CE} that corresponds to the phase shift between the peak of the envelope and a given wavefront of the carrier wave. In presence of dispersive material, the difference between group and phase velocities is at the origin of ϕ_{CE}. After a round-trip, the phase accumulated between the envelope and the carrier is

$$\phi_{CE} = \left(\frac{1}{v_g} - \frac{1}{v_\phi}\right) L\omega_0 \tag{3.24}$$

where v_g and v_ϕ are, respectively, the group and phase velocities and L is the length of the laser cavity. The consequence is that the phase carrier-envelope induces a rigid shift of the frequencies of the comb by an amount ω_{CE} that is linked to ω_0 through the relation

$$\omega_{CE} = \omega_0 \frac{\phi_{CE}}{2\pi} \tag{3.25}$$

There exist different mechanisms for locking the phases of lasing longitudinal modes based on active or passive phase modulators. In our specific case, the mode-locking is done in an all polarization-maintaining fiber laser architecture with a recently developped technique known as Additive Pulse Mode-Locking [Hänsel et al., 2017].

3.1.4 Electric field of a Gaussian pulse

a) Elementary knowledge about Gaussian in experiments

Let's begin this short review by recalling that a normal distribution $\mathcal{N}(x_0, \sigma)$ is characterized by the following probability density, reprensented on Figure X

$$H(x) = \frac{1}{\sqrt{2\pi}\sigma} e^{-\frac{1}{2}\left(\frac{x-x_0}{\sigma}\right)^2} \tag{3.26}$$

Experimentally σ is not often employed to characterize the gaussian, we would rather use the Full Width Half Maximum value (FWHM), denoted Δx, defined by the difference

between the two values x_1, x_2 at which the distribution is equal to half of its maximum value.

$$H(x) = \sqrt{\frac{\ln 2}{\pi}} \frac{2}{\Delta x} e^{-4\ln 2\left(\frac{x-x_0}{\Delta x}\right)^2} \tag{3.27}$$

Alternatively, the gaussian is sometimes characterized by its value at $1/e^2$, called the waist[3] w_0 of the gaussian. It results that we can rewrite

$$H(x) = \sqrt{\frac{2}{\pi}} \frac{1}{w_0} e^{-2\left(\frac{x-x_0}{w_0}\right)^2} \tag{3.28}$$

This means that when we measure effectively these quantities (waist and FWHM) we have to be careful. Almost all the time what we measure directly is the field intensity. We can thus define the field expression with the measured values, considering a gaussian temporal pulse with spectrum in FWHM $\Delta\omega$ and tranverse profile TEM00 characterized by the waists w_x and w_y we find

$$I(\vec{r}, \omega) = I_0 e^{-2\left(\frac{x^2}{w_x^2} + \frac{y^2}{w_y^2}\right)} e^{-4\ln 2\left(\frac{\omega-\omega_0}{\Delta\omega_{\text{int}}}\right)^2} \tag{3.29}$$

Alternatively by Fourier Transform we could consider the pulse intensity by its pulse duration in FWHM

$$I(\vec{r}, t) = I_0 e^{-2\left(\frac{x^2}{w_x^2} + \frac{y^2}{w_y^2}\right)} e^{-4\ln 2\left(\frac{t}{\Delta t_{\text{int}}}\right)^2} \tag{3.30}$$

with the following relation between Δt_{int} and $\Delta\omega_{\text{int}}$

$$\begin{aligned} \Delta t_{\text{int}} \Delta\omega_{\text{int}} &= 4\ln 2 \\ &\approx 2\pi \times 0.441 \end{aligned} \tag{3.31}$$

This definition then leads to the following expression for the electric field defined with the quantities accessible experimentally

$$\begin{aligned} \vec{E}(\vec{r}, t) &= \vec{E}_0 e^{-\left(\frac{x^2}{w_x^2} + \frac{y^2}{w_y^2}\right)} e^{-2\ln 2\left(\frac{t}{\Delta t_{\text{int}}}\right)^2} e^{i(\omega_0 t - k_0 z)} \\ &= \vec{E}_0 e^{-\left(\frac{x^2}{w_x^2} + \frac{y^2}{w_y^2}\right)} e^{-4\ln 2\left(\frac{t}{\Delta t_{\text{amp}}}\right)^2} e^{i(\omega_0 t - k_0 z)} \end{aligned} \tag{3.32}$$

Elementary relations for Gaussians in experiment.

$$\begin{aligned} \text{FWHM} &= 2\sqrt{2\ln 2}\sigma \\ \sigma_{\text{amp}} &= \sqrt{2}\sigma_{\text{int}} \\ w &= 2\sigma_{\text{int}} \end{aligned} \tag{3.33}$$

[3] More precisely, the waist is the radius at which the field amplitudes fall to $1/e$ of their axial values (i.e., where the intensity values fall to $1/e^2$ of their axial values)

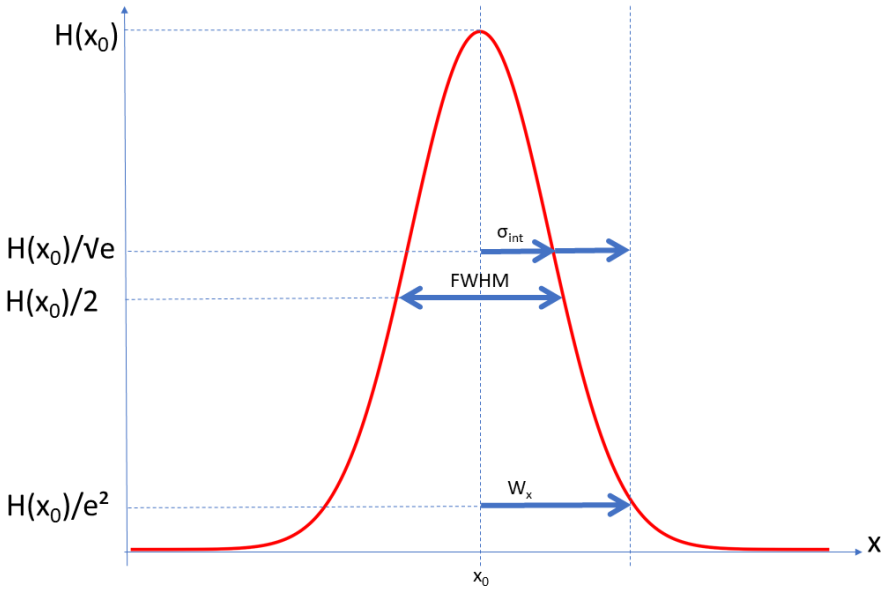

Fig. 3.2 ***Sum up on elementary relations for Gaussians.***

b) Energy and Peak power

To define the solution of Maxwell's equation we considered the field to be contained in a volume $V = S \times L$ where S is the surface covered by the transversal mode. We define then the power $\mathcal{P}$ of the field by integrating the intensity over transverse coordinates i.e.

$$\mathcal{P}(z,t) = \int_S I(\vec{r},t)\mathrm{d}^2S \tag{3.34}$$

as well as the energy of the field $\mathcal{W}$ by integrating the power in time

$$\mathcal{W} = \int_T \mathcal{P}(z,t)\mathrm{d}t \tag{3.35}$$

T is typically the integration time of the detector, much larger than the time duration of the pulse. Because of the dependency between the t and z variables, the integral over t cancels the longitudinal component of these quantities. Yet, when measuring in the laboratory the power with a powermeter, these instruments measure power through heating, and are therefore incapable of resolving the power in a single pulse. The result of such a measurement is the power averaged over a second $\mathcal{P}_{\text{avg}}$ (in W). By assuming a train of continuously repeated, periodical, square pulses with repetition rate f_r, pulse duration Δt and average power $\mathcal{P}_{\text{avg}}$, the pulse peak power $\mathcal{P}_{\text{peak}}$ calculations is trivial, with pulse energy provided by the ratio between average power and repetition rate and peak power provided by the ratio between energy and pulse duration:

$$\mathcal{P}_{\text{peak}} = \frac{T_{\text{rep}}}{\Delta t}\mathcal{P}_{\text{avg}} \tag{3.36}$$

where $T_{\text{rep}} = 1/f_{\text{rep}}$ is linked to the repetition rate of our laser.

c) The time-bandwidth product

Let's now highlight an important characteristic of short pulses that will play a crucial role later: a short pulse, i.e., narrow in the time domain, will have a broad spectrum in the frequency domain. This property is a direct consequence of the Fourier transform (FT), as the time-frequency spaces are conjugate through this transformation. If we denote Δt as the pulse duration, defined as the full width at half maximum (FWHM) of the intensity curve $I(t)$, and $\Delta\nu = 2\pi\Delta\omega$ as the width of the spectrum of this pulse, then $\Delta\nu\Delta t \geq \Lambda$, where Λ is a constant that depends on the pulse shape. Table. 3.1 provides the value of Λ for different classical pulse shapes. It is important to note that this is an inequality. When $\Delta\nu\Delta t = \Lambda$, it is referred to as a Fourier-transform-limited pulse, representing the shortest possible pulse duration T_0 for a given spectral width. However, as we will see later, the pulse duration can be much larger than this minimum duration. In practice, short pulses effects become noticeable when the associated spectral width becomes significant compared to the pulse's central frequency; this occurs in the femtosecond domain.

Table 3.1: Usual short pulses in the temporal and spectral domain

	$\mathcal{E}(t)$	$\lvert\mathcal{E}(\nu)\rvert^2$	Λ
Gaussian	$e^{-(t/T)^2}$	$e^{-\nu^2T^2/2}$	0.441
Sech^2	$\mathrm{sech}^2(t/T)$	$\mathrm{sech}^2(\pi\nu T/2)$	0.315
Lorentzian	$\left[1+(t/T)^2\right]^{-1}$	$T^2\,\mathrm{e}^{-T\nu}$	0.142

3.1.5 Laser characterization

A detailed characterization of our laser source was done in [Roman-Rodriguez et al., 2021], here we recall briefly the main working principle of the laser and essential characteristics. The MenloSystems laser is a relatively high power (500 mW per output) laser with low Relative Intensity Noise (RIN) making it powerful and stable enough for high precision experiments [Raabe et al., 2017,Hänsel et al., 2017]. The laser system consists of two main parts: a mode locking system and an optical amplification system. In the mode-locking setup, a loop is formed using a single-mode fiber, resembling a Fabry-Perot cavity. Within the fiber, a laser medium and partially transparent dielectric induce phase shifts in light due to self-modulation, creating an artificial saturable absorber beyond a given intensity limit. This influences cavity losses, establishing phase relations among resonator modes, resulting in consistent ultra-short pulse generation. The fiber loop length controls pulse repetition. This technique, known as additive-pulse mode locking, drives this process, and this laser section is called the "oscillator." After leaving the oscillator, pulses move through an Erbium-doped fiber amplifier in a loop mirror, serving as a low-noise optical amplifier. Amplification occurs via a nonlinear interference effect. The laser's output is then a train of ultrashort pulses at $\lambda = 1560$ nm with linear vertical polarization and a repetition rate of 100 MHz. The laser unit also delivers a synchronized electrical signal that can be used for pulse synchronization in experiments.

From the autocorrelation presented in Fig. 3.4b, we could measure the pulse duration

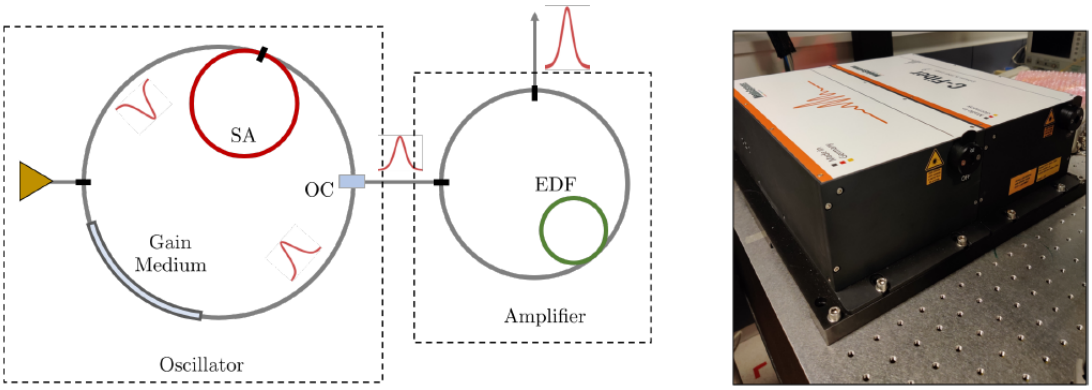

Fig. 3.3 ***Laser presentation.*** *Left: Simplified scheme of the laser system. Right: the Laser in our laboratory.*

Δt to be about 64 fs. The spectral width $\Delta\lambda$ is not easy to define given the shape of the spectrum in Fig. 3.4a. We estimate it to be approximately 56 nm from the autocorrelation signal, considering a Fourier limited gaussian pulse at the output.

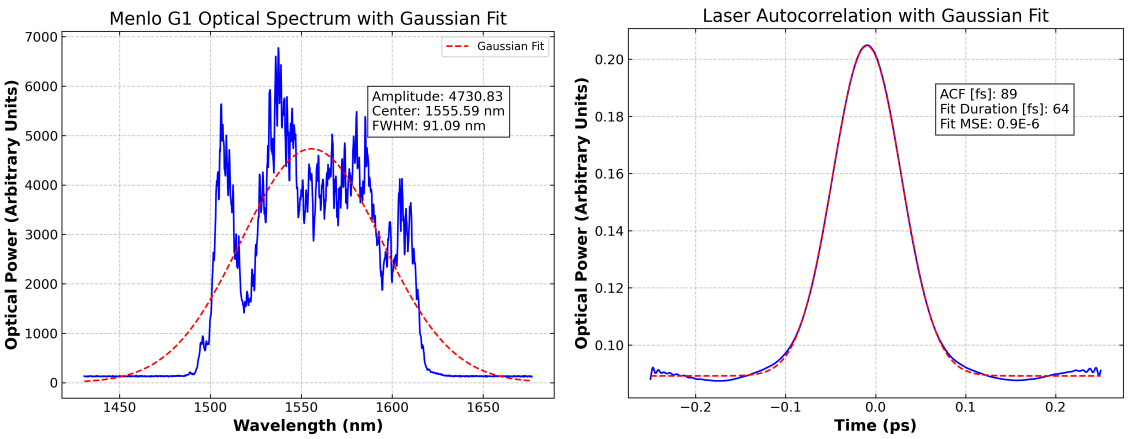

(a) (b)

Fig. 3.4 *(a)* ***Laser spectrum****. Acquired with spectrometer Avesta ASP-IR. The red dotted line is a gaussian fit. (b)* ***Laser autocorrelation signal****. Acquired with autocorrelator APE mini-TPA. The red dotted line is a gaussian fit.*

3.2 Dispersion

3.2.1 Theoretical framework for pulse dispersion

From the solution of the linear propagation equation of a pulse (3.12) we can directly derive the pulse duration as a function of the propagation length :

$$\Delta t^2(z) = \int_{-\infty}^{+\infty} \tau^2 |\mathcal{E}(z,\tau)|^2 d\tau \tag{3.37}$$

Applying Parseval Plancherel formula to (3.37) along with (3.13) leads to

$$\Delta t^2(z) = \int_{-\infty}^{+\infty} \left| \frac{\partial \mathcal{E}(z,\omega)}{\partial \omega} \right|^2 d\omega = \int_{-\infty}^{+\infty} \left| \frac{\partial \mathcal{E}(0,\omega)}{\partial \omega} + i k_0'' \omega^2 z \mathcal{E}(0,\omega) \right|^2 d\omega. \tag{3.38}$$

$\Delta t^2(z)$ is a second order polynomial of z with general form [Hache, 2016]

$$\Delta t^2(z) = \Delta t_0^2 + k_0''^2 \Delta\omega^2 z^2 \tag{3.39}$$

where Δt_0^2 is the minimum pulse duration and the term $\Delta\omega$ is the spectral width of the pulse. This has a simple physical interpretation: the pulse broadens because the different spectral components do not have the same group velocity. The period of the electric field oscillations changes within the envelope, and this phenomenon is referred to as *chirp*. In the case of a constant time-bandwidth product, as introduced in 3.1.4, $\Lambda = \Delta t_0 \Delta\nu$, we can rewrite (3.39) as

$$\Delta t(z) = \Delta t_0 \sqrt{1 + \left(\frac{(4\ln 2) k_0'' z}{\Delta t_0^2} \right)^2}. \tag{3.40}$$

We see from Eq. (3.40) that the temporal broadening will be even more significant when the initial duration of the pulse is short. When working with femtosecond pulses it is essential to control the influence of dispersion in the full experimental setup. Two specific examples :

- To have a good temporal mode matching in homodyne detection we should have a good temporal overlap between the signal and local oscillator pulses.
- Chirp should be avoided in the pump of the SPDC process to prevent unwanted modification of the quantum process.

Assuming now our pulse is traveling through a crystal of length L, we define the Group Delay Dispersion (GDD) as $GDD = k_0'' L$, isolating this term in (3.40) leads to :

$$GDD = \frac{1}{4\ln 2} \sqrt{\left(\frac{T(L)\Lambda}{\Delta\nu} \right)^2 - \left(\frac{\Lambda}{\Delta\nu} \right)^4}. \tag{3.41}$$

Equation (3.41) permits to experimentally infer the pulse duration at the output of the crystal $T(L)$ via autocorrelation technique and $\Delta\nu = c\frac{\Delta\lambda}{\lambda_0^2}$ via a spectrometer to recover the GDD. Another more theoretical approach consist via Sellmeier's equation to directly compute $k_0'' = \frac{\lambda^3}{2\pi c^2} \frac{d^2 n}{d\lambda^2}$. In practice, we measured the GDD experimentally, ensuring the value had the right order of magnitude according to Sellmeier's equations.

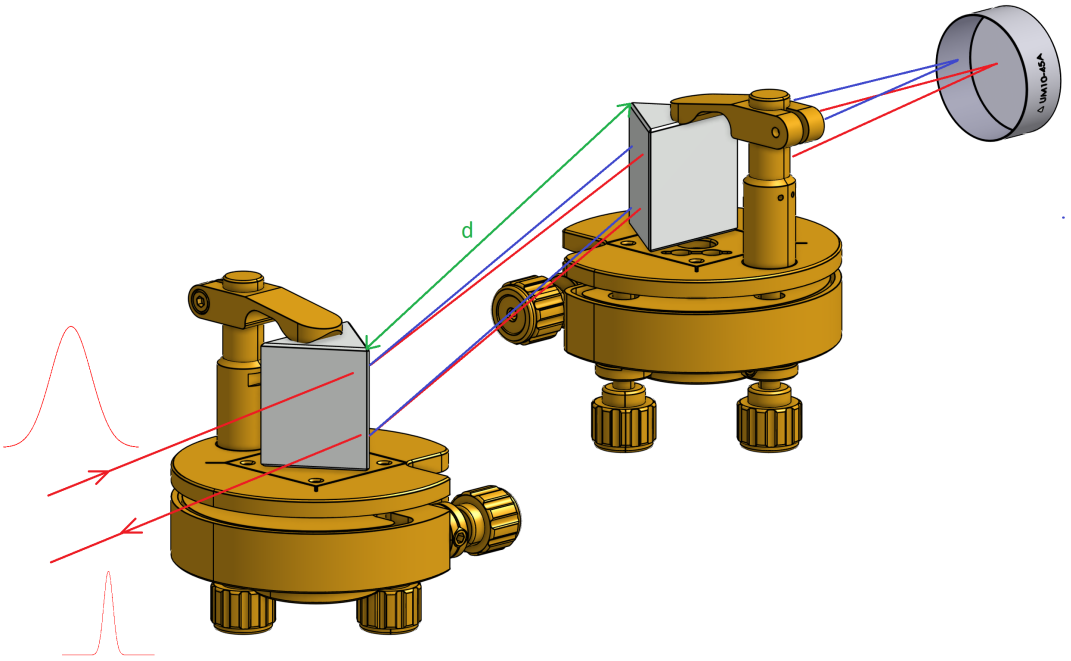

Fig. 3.5 ***Pulse Compressor.*** *A compact optical setup used in our experiment to prevent chirp.*

3.2.2 Pulse compression

Now that we know how to evaluate the dispersion in our pulse, let's have a look at a standard technique called prism compression to compensate for this phenomena. The overall idea, as some wavelength are travelling faster than other (creating dispersion) is to create a frequency dependant path to compensate [Akturk et al., 2006]. It involves two head-to-toes prisms separated by a distance d and a mirror as shown in Fig. 3.5. Each prism has an apex angle equal to the Brewster angle for a specific wavelength, and the prisms are arranged in a manner that allows the beam to enter and exit each prism at the Brewster angle. Usually this arrangement minimizes the reflection losses at a specific polarization (horizontal is our case). The first prism disperses the beam, while the second prism collimates the dispersed beam. A 0° low GDD mirror then send the beam backward into the two prisms to recombine all frequency components, ensuring that the beams entering and exiting the compressor are spatially identical. The wavelength-dependent path length, $P(\lambda)$, caused by dispersion can be expressed as

$$P(\lambda) = 2d\cos\beta \tag{3.42}$$

β is the angle of the dispersed beam after the first prism. The GDD introduced by this setup is

$$GDD_{pc} = \frac{\lambda^3}{2\pi c^2}\frac{d^2P(\lambda)}{d\lambda^2} \approx \frac{\lambda^3}{2\pi c^2} 8\left[D_{1/e^2}\frac{d^2n}{d\lambda^2} - d\left(\frac{dn}{d\lambda}\right)^2\right] \tag{3.43}$$

The first term on the right side of equation (3.43) stands for the dispersion induced inside the prisms material (of the sign of $\frac{d^2n}{d\lambda^2}$) [SCHOTT, 2017][4] while the second depends on the prism separation and introduces a negative dispersion contribution. From an experimental point of view, we adjusted the distance between the prisms in order to minimize the pulse duration.

3.3 Pulse shaping

3.3.1 Concept

A very important tool for our experiment is the pulse shaper, placed on the Local Oscillator path, it is at the core of our mode-selective homodyne detection. By changing the temporal shape of LO and taking avantage of the projective character of the homodyning, one can select the spectral-temporal mode to measure [Fabre and Treps, 2020]. If $E_{in}(t)$ is the field at the input of the pulser shaper and analogously $E_{out}(t)$ at the output, then passives shaping technique consist in making the field interact with a material. We call then $R(t)$ the temporal response function of the system excited by the impusion.

$$E_{out}(t) = \int_{-\infty}^{t} R(t'-t)E_{in}(t')dt' = R(t) \otimes E_{in}(t) \tag{3.44}$$

The temporal response function is the sum of all the contribution of the field who interacted with the material at all anterior times t'. In practice femtosecond pulses are too short, direct temporal shaping is not practically doable. We then usually take advantage of the large frequency spectrum to adress all frequency components. The fourier transform of (3.44) leads to :

$$E_{out}(\omega) = R(\omega)E_{in}(\omega) \tag{3.45}$$

Then shaping amplitude and phase of the different frequency components leads naturally to the corresponding temporal shaping.

3.3.2 Fourier Optical Processing

One standard technique to shape temporally a femtosecond pulse is by Fourier Optical Processing [Monmayrant et al., 2010]. Such dispositive was initially designed by [Froehly et al., 1983] and results experimentally in a 0-dispersion line composed of a grating, a cylindrical mirror and spatial light modulator (SLM) as described in Figure 3.6. All the frequencies of the pulse are mapped into spatially separated components via a holographic grating and then focused with a cylindrical mirror on the SLM liquid crystal screen which permits the fine tuning of the amplitude and phase of the different frequency components in the Fourier plane. An important point to not overlook is the ability of a pulse shaper to generate complex pulses, meaning that it requires the independant shaping of a large number of spectral components. It is possible to design and implement a customized 4f line for specific spectral ranges and applications by carefully selecting the focal length and the number of grooves per mm of the grating. One way to quantify the shaping capability

[4] This term is always positive in the visible domain, it is not necessary the case at telecom wavelength.

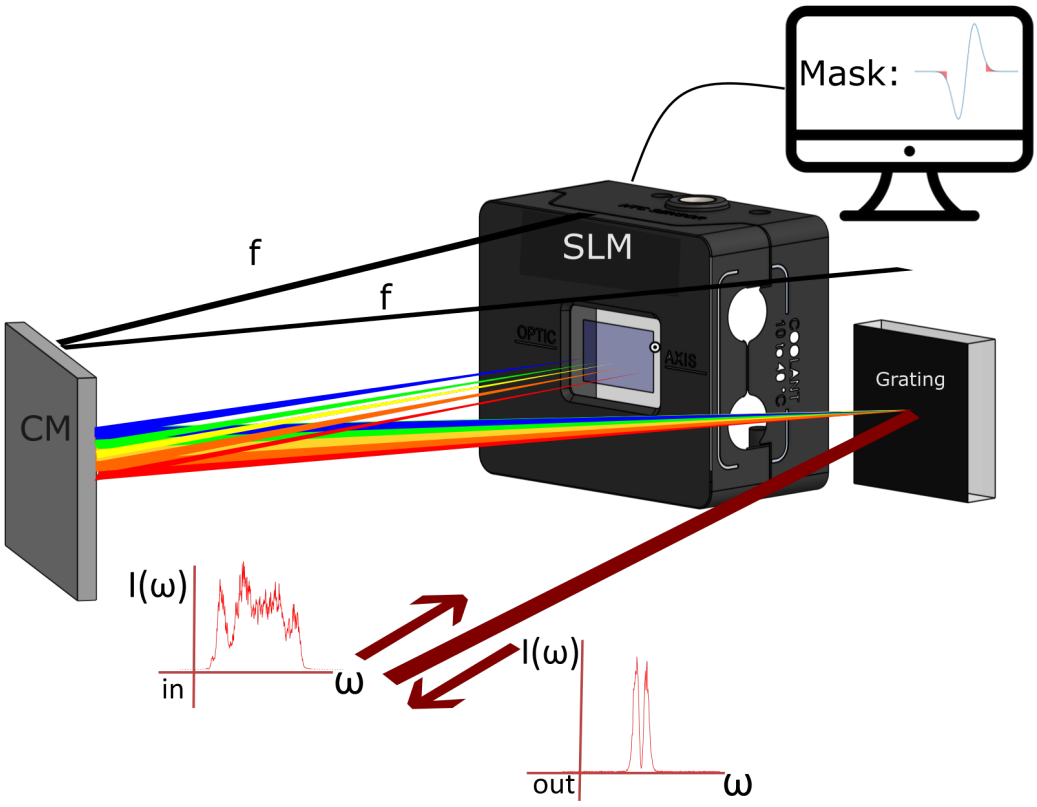

Fig. 3.6 ***Pulse Shaper.*** *A zero dispersion line composed of a grating, a cylindrical mirror focal length f , arranged in a 4f set-up with a Spatial Light Modulator (Hamamatsu LCOS X15213). The output pulse is shaped according to the mask printed on the SLM and the input pulse spectrum. In the Fourier plane, all the spectral components are spatially separated and focused.*

from the optics selected is the optical complexity η_{opt}. The optical complexity is often defined as the ratio between the largest element and the smallest element present in the pulse profile, either in the spectral domain or in the time domain.

$$\eta_{opt} = \frac{\Delta t}{\delta t} = \frac{\Delta \omega}{\delta \omega} \tag{3.46}$$

In a more practical way, it can be seen as the ratio between the size of total spectrum shining on the mask ΔL compared to the size of a spot for an individual frequency components δx_{opt}. Consider a pulse characterized by its waist w_0 and its spectrum $\Delta\lambda$ (in FWHM) centered at λ_0 entering the 4f-line. The grating is characterized by its number of grooves per mm g, it is optimized to diffract in order -1 so the relation between input angle θ_i and diffracted angle θ_d can be established from the fundamental relation of gratings

$$\theta_d(\theta_i, \lambda) = \arcsin\left(-\frac{\lambda}{g} - \sin\theta_i\right) \tag{3.47}$$

and the waist of each frequency components after the grating can be established with the following relation

$$w = \frac{\cos\theta_d^{(0)}}{\cos\theta_i^{(0)}} w_0. \tag{3.48}$$

The cylindrical mirror is characterized by its focal length f. Assuming the spectrum is not too broad and the individual spectral components have the same spatial shape, the typical total spread on the SLM can be derived from the diffraction angle of the grating [Michel, 2021]

$$\theta_d(\lambda) \approx \theta_d^{(0)} - \frac{1}{g\cos\theta_d^{(0)}}(\lambda - \lambda_0). \tag{3.49}$$

Overall the spatial dispersion of the pulse shaper is $\alpha = \frac{f}{g\cos\theta_d^{(0)}}$ and the total spread on the SLM is

$$\Delta L = \alpha\Delta\lambda = \frac{f\Delta\lambda}{g\cos\theta_d^{(0)}}. \tag{3.50}$$

On the other hand, the cylindrical mirror is expected to focus the different frequency components along their horizontal waist such that

$$w_f = \frac{\lambda_0 f}{\pi w} \tag{3.51}$$

so the waist on the SLM screen of each individual component is

$$w_f = \frac{\lambda_0 f}{\pi w_0}\frac{\cos\theta_i^{(0)}}{\cos\theta_d^{(0)}} \tag{3.52}$$

following relations established in 3.1.4 the typical size of each individual component (in FWHM) is

$$\delta x_{opt} = \sqrt{2\ln(2)}\frac{\lambda_0 f}{\pi w_0}\frac{\cos\theta_i^{(0)}}{\cos\theta_d^{(0)}} \tag{3.53}$$

and finally the optical complexity is

$$\eta_{opt} = \frac{\Delta L}{\delta x_{opt}} = \frac{\Delta\lambda\pi w_0}{\sqrt{2\ln(2)}g\lambda_0\cos\theta_i^{(0)}} \tag{3.54}$$

Another constraint that appears when shaping with an SLM is the pixelisation of the mask due to the finite size of screen. The pixel has a definite size δx_{px} to be taken into account. We commonly define then the pixel complexity η_{px} as the ratio between the spatial size of the total spectrum shining on the SLM and the size of a pixel.

$$\eta_{px} = \frac{\Delta L}{\delta x_{px}} = \frac{f\Delta\lambda}{g\cos\theta_d^{(0)}\delta x_{px}} \tag{3.55}$$

In the common case where a pixelated mask is used, the shaped pulse is accompanied by a certain number of temporal replicas [Monmayrant, 2019]. This can be easily understood through Fourier transform considerations: the pixelated mask behaves as a discrete

transfer function in the spectral domain, which corresponds, in the time domain, to a periodic response function. As a result, the shaped pulse is accompanied by an infinity of regularly spaced copies in time. However, these replicas are less problematic than they may seem because they tend to be distorted and attenuated. Still, pixellization should be taken into account when selecting the optics for the shaping.

Ultimately we should design the shaping with $\eta_{opt} \approx \eta_{px}$ so one fequency components has the size of a pixel and minimize the impact of pixellization. If this equality cannot be achieved, we consider that the ultimate limitation on our shaping capabilities is determined by the smaller complexity, making it pointless to increase one while the other remains small. This quantity will then gives a good estimate of the number of orthogonal modes that can be shaped with our setup. In our case we find $\eta_{px} = 933$ and $\eta_{opt} = 200$ meaning that it should be feasible to shape the LO spectrum with more than 100 orthogonal modes, much more than what we would need. Nevertheless, by comparision with previous shaping experiments in the visible domain [Renault, 2022,Kouadou, 2021] we are more limited by the optical complexity due to the central wavelength at the denominator (see Eq. (3.54). It could be compensated by increasing slightly the size of the input waist $\omega_{in} = 2mm$ but not indefinitely due to the SLM screen vertical limitations, or by choosing a grating with more grooves/mm. This later option is not extremely viable as well as the wavelength dispersion is also limited by the horizontal dimension of the SLM or requiring a shorter focal length, decreasing the pixel complexity and making the experimental implementation impractical.

3.3.3 Transfer function

The standard universal mask that we use for pulse shaping consist in applying a sawtooth profile on each column of the SLM as depicted in Fig. 3.7a. The distribution of the intensity in the different orders of diffraction is dictated by the profile $f(x) = hx$ of the sawtooth printed on the SLM [Albero et al., 2012]. The proportion in order k is given by the Fourier coefficient c_k of $f(x)$:

$$c_k = \frac{1}{2\pi} \int_{-\pi}^{\pi} e^{if(x)} e^{-ikx} dx \tag{3.56}$$

For our sawtooth function, the proportion of diffracted light in the first order depends on the sinc of the depth of the sawtooth. For a depth of 0, meaning a flat mask, no light is diffracted, and for a depth of 1, all the light goes into the first order. The supplementary phase component is achieved by translating the pattern along the y axis. If ω_0 is the frequency component on the colomn x_0 of the SLM screen we get the transfer function $G(\omega_0)$:

$$E_{out}(\omega_0) = \underbrace{e^{-i\phi(x_0)} \operatorname{sinc}(1 - A(x_0))}_{G(\omega_0)} E_{in}(\omega_0) \tag{3.57}$$

where $A(x_0)$ and $\phi(x_0)$ corresponds respetively to the amplitude (depth) and global phase of the sawtooth function on column x_0. So knowing the amplitude of the different frequency components in $E_{in}(\omega)$ we can adequately chose the values of $[A(\omega), \phi(\omega)]$ for all ω displayed on the screen, and hence shape the pulse spectrum in amplitude and phase.

It directly implies that by knowing $E_{in}(\omega)$, and especially the amplitudes of its different frequency components, we can choose adequately the values of $[A(\omega), \phi(\omega)]$ for all ω

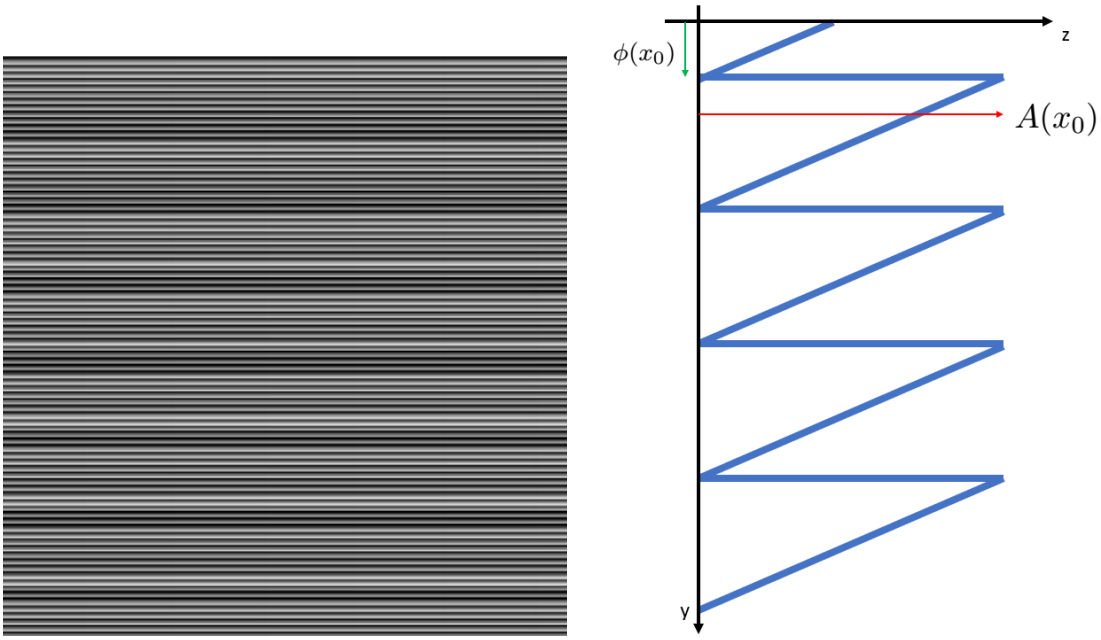

(a) (b)

Fig. 3.7 *(a)**SLM Mask**. An example of a uniform sawtooth function printed on the SLM screen. (b)**Sawtooth Scheme**. Typically printed on every column of the SLM.*

displayed on the screen, to shape the pulse spectrum in amplitude and phase. Finally, experimentally we don't print on the SLM a perfect sawtooth but rather a pixelized version of it. The effects on shaping are not detrimental and were adressed in [Renault, 2022].

3.3.4 Calibration

A carefull calibration of the 0-dispersion line is necessary to ensure an accurate pulse shaping. In short, the distances between the optics should be exactly equal to the focal length, the input beam should travel in a plane parallel to the optical table. Otherwise, [Michel, 2021] described in details what would be the consequences for the shaped beam. In the following we give a brief summary.

Vertical spatial chirp. Precise alignment of the diffraction grating's rulings perpendicular to the optical table is essential to achieve horizontal beam diffraction; misalignment causes reduced resolution due to dispersed single-frequency components, leading to a vertical spatial chirp that requires iterative grating rotation for minimization. This can also be caused by a rotation of the cylindrical mirror in plane transverse to the one parallel to the optical table.

Temporal chirp. The critical distance between the cylindrical mirror and the grating determines if the output beam has temporal chirp; ensuring it equals the focal length compensates for optical path differences and avoids such chirp. Incorrect distances cause temporal chirp due to spectral phase differences and improper recombination of frequency components.

Reduced optical resolution, ellipticity and Horizontal chirp. If your output beam is spatially elliptical then it means the SLM is not placed exactly in the focal plane of the cylindrical mirror. Horizontal chirp will also appear due to imperfect recombination on the output grating. Moreover this means that each frequency component has a bigger spot on the SLM, resulting in a reduced optical complexity. Adjusting carrefully this distance is thus mandatory.

Furthermore, a carreful calibration of the SLM itself is necessary. Knowing the position of each frequency component on the screen permits to design a custom mask to compensate for flatness defects of the liquid crystals (from data interpolation provided by Hamamatsu). The spread should be linear on the screen [Weiner, 2011], and the optimal depth of the sawtooth functions should be adapted to every frequencies following data provided by Hamamatsu. It is also possible to access experimentally the sawtooth depth by increasing progressively the depth and looking at the intensity of the field in the first order. The optimal depth corresponds to the intensity maxima of the sinc^2 profile, expected from (3.57). Finally, a last check consist in shaping the spectrum and comparing it the expected shaping. In Fig. 3.8 we sum up a few comparison between shaped spectra and their expected waveform demonstrating a good agreement between theory and experiment.

3.4 Second Harmonic generation

3.4.1 Nonlinear propagation equation

Let's have a look now at what happens when a pulse propagates through a nonlinear media [Boyd, 2011]. The incident pulse, $E_1(z,t)$, centered on frequency ω_0 is called the fundamental beam, expressed in (3.7), while the one centered[5] at double frequency $2\omega_0$ is called the harmonic. Both electric fields propagate in the z-direction and pass through a crystal of thickness L. It is assumed that there is no harmonic beam sent at the entrance of the crystal. The harmonic beam is expressed as follow

$$E_{\mathrm{SHG}}(z,t) = \mathcal{E}_2(z,t)e^{i(k_2 z - 2\omega_0 t)} + c.c. \tag{3.58}$$

The polarization of the electromagnetic field at time t depends on all the contributions of the field that interacted in the nonlinear media at anterior time. Formally it means that the polarization of the media is not a linear function of the electric field anymore but rather we will consider a Taylor expansion in $E_1(z,t)$ up to order 2. It leads us to rewrite the dielectric displacement as

$$D(z,t) = \epsilon_0 E_1(z,t) + P^L(z,t) + P^{NL}(z,t) = \epsilon_0\epsilon_r E_1(z,t) + P^{NL}(z,t). \tag{3.59}$$

with

$$P^{NL}(z,t) = 2\epsilon_0\chi^{(2)}E_1^2(z,t) \tag{3.60}$$

P^{NL} represent the polarization that oscillates at the frequency $\omega = \omega_1 + \omega_2$, identical to that of the electromagnetic field whose evolution we are seeking. Indeed, only a polarization at ω can interact with a field of frequency ω. On the one hand, there is nothing that

[5] Mentionning this process as second harmonic generation is an abuse of language, the process is a particuliar case of Sum Frequency Generation (SFG).

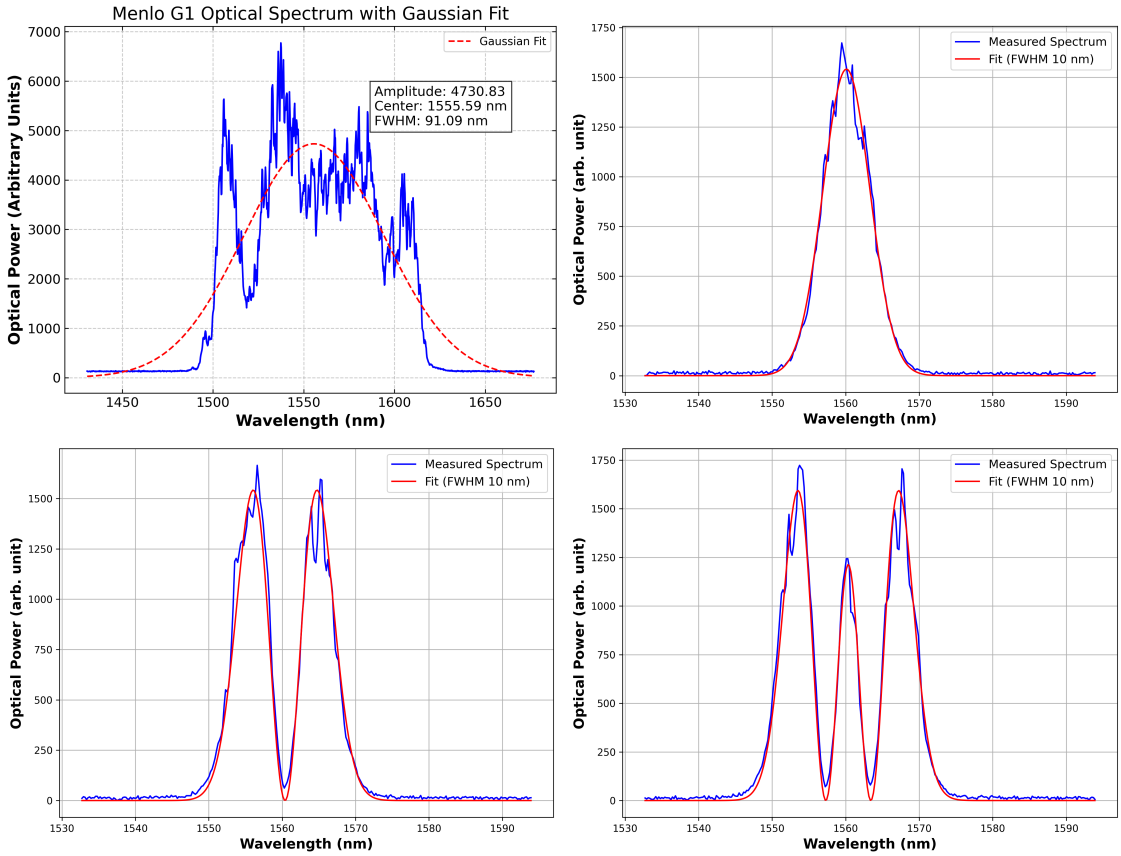

Fig. 3.8 *Demonstration of the shaping capabilities with our the pulse shaper. In the upper left the original spectrum before shaping is represented. All other spectra acquisition are at the PS output with different Hermite-Gauss masks on SLM. Moreover we plotted on top the expected spectra in red.*

fixes the wave vector of the polarization to $k(\omega)$. On the other hand, the wave vector of the polarization is imposed by the nonlinear phenomenon under consideration. For example, in the case of second harmonic generation it derives as:

$$\begin{aligned} P^{NL}(z,t) &= 2\epsilon_0\chi^{(2)} \int\int \frac{\mathrm{d}\omega_1}{2\pi}\frac{\mathrm{d}\omega_2}{2\pi}\mathcal{E}_1(z,\omega_1)\mathcal{E}_1(z,\omega_2)e^{i(k_1(\omega_1)+k_1(\omega_2))z}e^{-i(\omega_1+\omega_2)t} \\ &= 2\epsilon_0\chi^{(2)} \int \frac{\mathrm{d}\omega}{2\pi}e^{-i\omega t}\int \frac{\mathrm{d}\omega_1}{2\pi}\mathcal{E}_1(z,\omega_1)\mathcal{E}_1(\omega-\omega_1)e^{i(k(\omega_1)-k(\omega-\omega_1))z} \\ &= 2\epsilon_0\chi^{(2)} \int \frac{\mathrm{d}\omega}{2\pi}e^{-i\omega t}P^{NL}(z,\omega) \end{aligned} \tag{3.61}$$

This extra term in dielectric displacement leads to a new propagation equation, derived once again from (3.8), called nonlinear propagation equation where we dropped the dispersion term k_0'' to focus on the nonlinear process

$$\frac{\partial\mathcal{E}_2}{\partial z}(z,\omega) = i\frac{\omega_0\chi^{(2)}}{n_0c}\int \frac{\mathrm{d}\omega_1}{2\pi}\mathcal{E}_1(z,\omega_1)\mathcal{E}_1(\omega-\omega_1)e^{i(k_1(\omega_1)-k_1(\omega-\omega_1)-k_2(\omega))z}. \tag{3.62}$$

Now we identify a new term $\Delta k = k_1(\omega_1) - k_1(\omega - \omega_1) - k_2(\omega)$ being the wavevector mismatch in the degenerate case scenario of second harmonic generation. Solving (3.62) we get

$$\mathcal{E}_2(z,\omega) = i\frac{\omega_0\chi^{(2)}}{n_0 c}\int \frac{\mathrm{d}\omega_1}{2\pi}\mathcal{E}_1(\omega_1)\mathcal{E}_1(\omega-\omega_1)\frac{e^{i\Delta k z}-1}{i\Delta k} \tag{3.63}$$

we see that, when the media is not dispersive $\Delta k(\omega) = 0$ for all ω, the second harmonic frequency bandwidth will result from the superposition of all the couples $\omega_1, \omega-\omega_1$ in the initial pulse spectrum i.e. $\mathcal{E}_{2,ND}(z,\omega) = i\frac{\omega_0\chi^{(2)}}{n_0 c}\int \mathcal{E}_1(\omega_1)\mathcal{E}_1(\omega-\omega_1)\frac{d\omega_1}{2\pi}$. In a dispersive media, with the following a Taylor expansion of the wavevector mismatches :

$$\begin{aligned} k_1(\omega) &\approx k_1(\omega_0) + k_1'(\omega_0)(\omega-\omega_0) \\ k_2(\omega) &\approx k_2(2\omega_0) + k_2'(2\omega_0)(\omega-2\omega_0). \end{aligned} \tag{3.64}$$

Now assuming the phasematching to be achieved at the central frequencies of both pulses, i.e. $2k_1(\omega_0) - k_2(2\omega_0) = 0$, we finally find by integration over the cristal length L [Hache, 2016]

$$|\mathcal{E}_2(z,\omega)|^2 = |\mathcal{E}_{2,ND}(z,\omega)|^2 \,\mathrm{sinc}^2\left((\omega-2\omega_0)\frac{\Delta k' L}{2}\right). \tag{3.65}$$

Thus, the harmonic spectrum is convolved with a sinc^2 function, which results in reducing the spectral width as the propagation distance increases. This detail is important as it permits to consider the spectral width as a tunable parameter, that as we will see in the next chapter is useful for the design of the ultrafast parametric down conversion process. It can also be observed that the broadening depends on $\Delta k' = k_1'(\omega_0) - k_2'(2\omega_0)$, which is the difference in group velocities between the fundamental and the harmonic. So during the propagation in the crystal, the two pulses do not travel at the same velocity, leading to elongation of the harmonic pulse.

3.4.2 Experimental implementation

We work in a regime where we focused the input pulse inside a PPLN crystal (from HCPhotonics) as presented in Fig. 3.9. A detailed experimental characterization of this crystal can be found in [Roman-Rodriguez et al., 2021], here we simply here recall the main results and we discuss few improvements. We achieved an overall conversion efficiency above 34% after a careful alignment and adjustment of the $\chi^{(2)}$ crystal temperature. This slight improvement in the conversion efficiency, compared to first characterization done in [Roman-Rodriguez et al., 2021], is also attributed to a better investigation and control of the pulse duration (at the Fourier Limit), and the cleaning of the input beam polarization. The SHG spectrum is about 2-nm wide, with the expected sinc-profile predicted in (3.65), see Fig. 3.10a. Its temporal duration has quite a large uncertainty. The autocorrelation shown in Fig. 3.10b was measured after pulse compression of the filtered output, we adjusted experimentally the distance between the prism to minimize the pulse duration. Still the Δt value measured from the gaussian fit, if assumed to be Fourier limited, would lead to a pulse of 3 nm (FWHM) which is incompatible with the measured spectrum but in the range of uncertainty (expected 450 fs).

Finally, when focusing our pulse inside the PPLN, a bright green light appeared, not represented in Fig. 3.9. We attribute this effect to cascaded frequency conversion (second

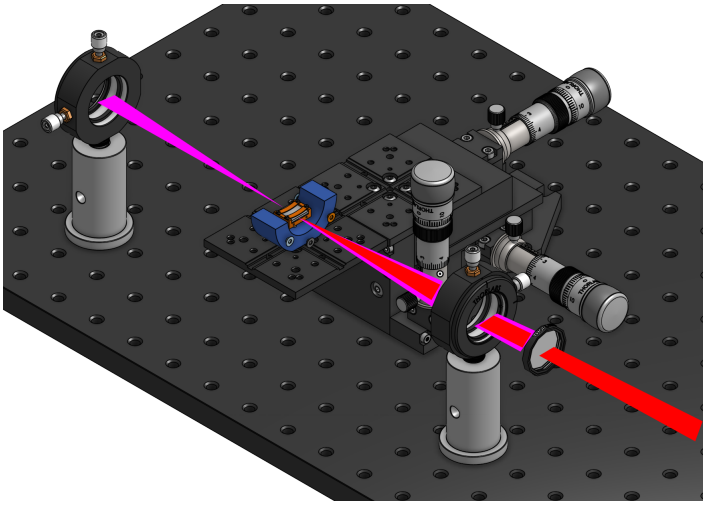

Fig. 3.9 ***Second Harmonic generation.*** *The input beam at telecom wavelength is focused inside a PPLN crystal from HCPhotonics. The phasematching conditions are adjusted with the help of a oven. At the output the telecom beam is filtered out, leaving only a collimated beam at 780 nm.*

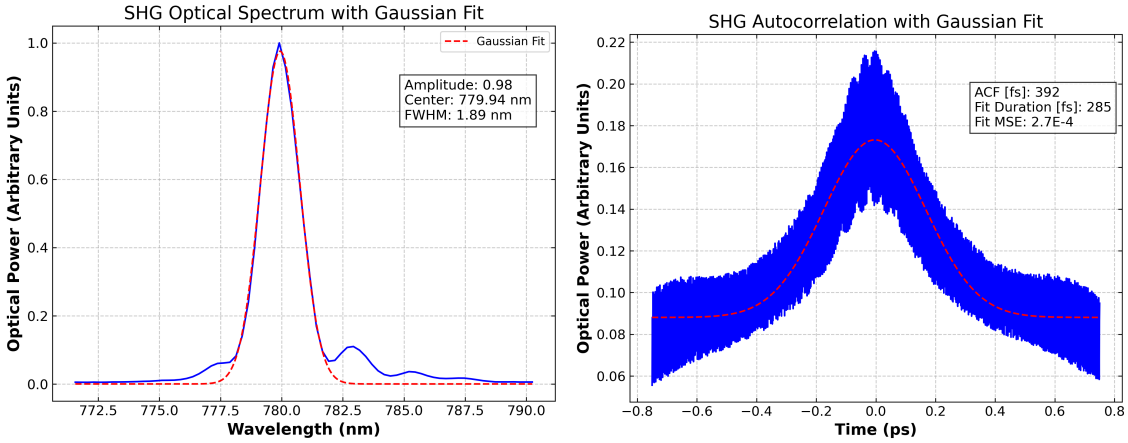

(a) ***SHG spectrum acquisition.*** (b) ***SHG autocorrelation signal.***

order effect) [Rasputnyi et al., 2022]. This can't be a third harmonic generation, because as it is shown in [Hache, 2016], this phenomena is null when pumped with a focused beam, in contrast to what is obtained with a calculation for plane waves. This surprising result is linked to the Gouy phase in a scenario where $L \gg z_R$. Due to this phase, the harmonic and fundamental beams undergo a phase shift during propagation, leading to a similar problem as phase mismatch: destructive interferences cancel out the harmonic intensity.

Chapter 4

Single Pass Ultrafast Spontaneous Parametric Down Conversion

Contents

Spontaneous Parametric Down Conversion (SPDC) is a particular case of Difference Frequency Generation [Kulkarni et al., 2022], a phenomenon that arises from interaction between light and a $\chi^{(2)}$ nonlinear material. It is a second order nonlinear effect, just as second harmonic generation, in which a pump photon at frequency ω_p is down converted to two photons, commonly labeled signal and idler, respectively at frequency ω_s and ω_i. SPDC obeys several conservation laws. Energy conservation dictates that the sum of the energies of the signal and idler photons must equal the energy of the pump photon (4.1). Momentum conservation requires the total momentum of the interacting photons to be conserved (4.2), as we will see this nicely appears when deriving the theoretical model. These two conditions are called *phase-matching conditions*.

$$\omega_p = \omega_s + \omega_i \tag{4.1}$$

$$\vec{k}_p = \vec{k}_s + \vec{k}_i \tag{4.2}$$

A first theoretical model and experimental demonstration of such parametric effect was done in the 60's [Fano, 1961, Glauber, 1963, Harris et al., 1967, Magde and Mahr, 1967, Burnham and Weinberg, 1970]. Since then, this process is at the heart of many quantum

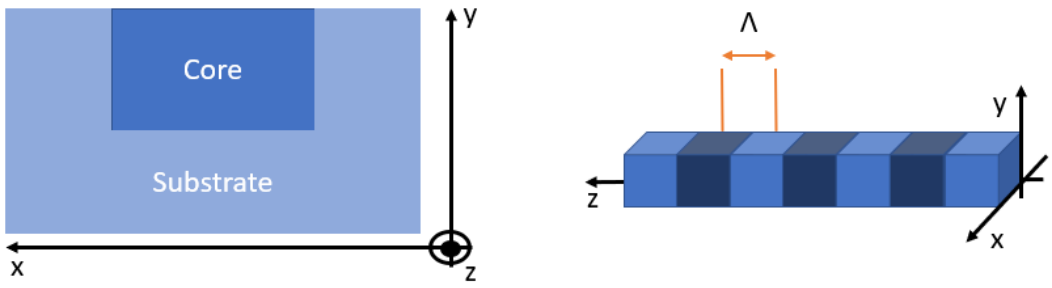

Fig. 4.1 ***Waveguide scheme*** *Left : Representation of a channel waveguide. Right : A periodically poled waveguide with poling period* 2Λ.

optics experiments for applications, e.g., in quantum cryptography [Gisin et al., 2002], quantum computing [O'Brien, 2007] but also simply for testing fundamentals laws of physics in quantum mechanics [Sinha et al., 2010].

4.1 Spontaneous parametric down conversion in waveguide

We aim to produce and study high-dimensional cluster states for telecommunication protocols. A natural approach is to use technologies already employed in classical communications. Commonly, it implies lasers at telecom wavelength, an optical frequency chosen to minimize losses in optical fibers [Dutton, 1998], that is modulated in amplitude and phase (standard QAM16 methods) and a coherent detection to measure the information encoded in the state in phase space. The focus of this chapter is on the production of non-classical states of light within this framework and to do so, we take advantage of Spontaneous Parametric Down Conversion. Moreover, to maximize the interaction strength, we confine the light in a waveguide. Waveguides also leads to a more compact SPDC source, when compared to standard cavity OPO experiment [Pinel et al., 2012], and they are compatible with integrated optics. Through this chapter, we first discuss some elementary features about the waveguide model, then derive the interaction Hamiltonian of the nonlinear process, and finally perform numerical simulations for the expected experimental results.

4.1.1 General consideration on waveguides

The waveguides used in this thesis confine light over the two transversal directions, x and y, and are called Channel Waveguides, see Fig. 4.1. In our case, the waveguide is made in a Potassium Titanyl Phosphate (KTP) crystal and was manufactured by ADVR-inc. It is necessary to apply a poling process to the waveguide region to ensure phase matching for the desired wavelength conversion process, as discussed in more details in 4.1.3. The choice to work with KTP instead of another standard crystal like LN is justified in [Roman-Rodriguez et al., 2021]. It does not rely solely on the criteria of nonlinearity; otherwise, LN would be a better fit. KTP rather offers a better balance between the

expected number of quantum modes, the overall spectral bandwith of the output pulse and the waveguide dimensions. Achieving similar performances with LN would require waveguide with dimensions smaller than 1.5 μm thus switching to a completely different regime. Moreover it appears that LN waveguides suffer from photorefraction at high pump power [Domeneguetti et al., 2023].

4.1.2 Hamiltonian approach to quantum optics

This quantum phenomena is usually easier to understand and study in the Hamiltonian approach. Nevertheless this approach is possible only when assuming no coupling between spatial and temporal modes [Volpe et al., 2020]. We model the energy of the entire system under study {Fields + waveguide} by the following hamiltonian

$$\hat{H}_{sys} = \hat{H}_0 + \hat{H}_{field/crystal} = \frac{1}{2}\int_V \mathrm{d}\vec{r}\left[\vec{\hat{E}}_{tot}(\vec{r},t)^2 + \vec{\hat{B}}_{tot}(\vec{r},t)^2\right] + \int_V \mathrm{d}\vec{r}\hat{P}^{NL}(\vec{r},t)\vec{E}_p(\vec{r},t) \tag{4.3}$$

$\hat{H}_0$ represents the energy of the free propagation of the total field and $\hat{H}_{field/crystal}$ represents the interaction energy between the crystal and the pump field characterized by the nonlinear polarization.

As we aim for a single-pass production of a multimode quantum state in waveguide we will, without loss of generality, consider a propagation of the pump, signal and idler fields in the z direction (just as we did for the SHG). To stay compliant with waveguide physics only the allowed modes will be able to travel inside the crystal. We limit our study to the case of a single spatial mode for all three involved fields. A more general derivation, considering all possible spatial modes, was done in [Román Rodríguez, 2022] and showed that given the waveguide dimensions we consider, there is only one dominant spatial mode propagating for all fieds. Thus, we drop the multimode spatial structure from the beginning. Finally, in order to capture the specific quantum features like the vacuum fluctuations of signal and idler fields, as well as the squeezing generation we have to treat these latter as quantized fields. The pump will be treated as a classical field, i.e a bright coherent field which can be represented by its mean field only. This assumption is justified by the fact that the input power of the pump field (few mW) is large compared to the few photons generated by the process. We define[1]:

$$\begin{aligned} E_p(z,t) &= i\int \mathcal{E}_p(\omega_p)e^{-i(\omega_p t - k_p z)}\mathrm{d}\omega_p + c.c \\ \hat{E}_{s,i}(z) &= i\int \hat{a}_{s,i}(\omega_{i,s})e^{-ik_{s,i}z}\mathrm{d}\omega_{i,s} + h.c \\ \hat{P}^{NL}(z) &= 2\epsilon_0\chi^{(2)}\hat{E}_s(z)\hat{E}_i(z). \end{aligned} \tag{4.4}$$

Injecting this into the expression of $\hat{H}_{field/crystal}$, and keeping only the relevant terms of interest for Parametric Down Conversion (associated to a creation of a couple of signal and idler photons) we get

$$\hat{H}_{PDC} = -i2\epsilon_0\chi^{(2)}\int \mathrm{d}\omega_p\mathrm{d}\omega_s\mathrm{d}\omega_i\mathcal{E}_p(\omega_p)e^{-i\omega_p t}\hat{a}_s^\dagger(\omega_s)\hat{a}_i^\dagger(\omega_i)\int \mathrm{d}z e^{-i\Delta k z} + h.c \tag{4.5}$$

[1]The signal and idler fields are defined without the time dependant term in the Schrödinger picture.

where $\Delta k = k_p - k_s - k_i$ is the wavevector mismatch in its most common form. From now we will consider a quasi-phasematching scenario described in 4.1.3, this is done without loss of generality in the rest of the derivation. Integration over the waveguide length leads to a new important quantity called the phasematching function $\phi(\omega_p, \omega_s, \omega_i)$

$$\hat{H}_{PDC} = -i2\epsilon_0\chi^{(2)} \int \mathrm{d}\omega_p \mathrm{d}\omega_s \mathrm{d}\omega_i \mathcal{E}_p(\omega_p) e^{-i\omega_p t} \phi(\omega_p, \omega_s, \omega_i) \hat{a}_s^\dagger(\omega_s) \hat{a}_i^\dagger(\omega_i) + h.c \tag{4.6}$$

with

$$\phi(\omega_p, \omega_s, \omega_i) = L \,\mathrm{sinc}\left(\frac{L}{2}\Delta k\right). \tag{4.7}$$

From here we finally get the interaction Hamiltonian[2]

$$\hat{H}_{int}(t) = e^{\frac{i\hat{H}_0 t}{\hbar}} \hat{H}_{PDC} e^{\frac{-i\hat{H}_0 t}{\hbar}}. \tag{4.8}$$

Using Baker-Campbell-Haussdorff formula, equation (4.8) derives nicely as:

$$\hat{H}_{int}(t) = -i2\epsilon_0\chi^{(2)} \int \mathrm{d}\omega_p \mathrm{d}\omega_s \mathrm{d}\omega_i \mathcal{E}_p(\omega_p) \phi(\omega_p, \omega_s, \omega_i) \hat{a}_s^\dagger(\omega_s) \hat{a}_i^\dagger(\omega_i) e^{-i(\omega_p - \omega_s - \omega_i)t} + h.c \tag{4.9}$$

ensuring that this interaction happens only under energy conservation $\omega_p = \omega_s + \omega_i$ we can then write the interaction Hamiltonian in its final form :

$$\hat{H}_{int} = -i2\epsilon_0\chi^{(2)} \int \mathrm{d}\omega_s \mathrm{d}\omega_i \mathcal{E}_p(\omega_s + \omega_i) \phi(\omega_s, \omega_i) \hat{a}_s^\dagger(\omega_s) \hat{a}_i^\dagger(\omega_i) + h.c \tag{4.10}$$

Hence, the interaction depends on two main terms, the pump field amplitude $\mathcal{E}_p(\omega_s, \omega_i)$ and the nonlinear crystal phasematching function $\phi(\omega_s, \omega_i)$. We usually call this product the joint spectral amplitude (JSA), as it contains all the information about the parametric interaction combining properties of the waveguide and the pump spectrum

$$\mathcal{J}(\omega_s, \omega_i) = \mathcal{E}_p(\omega_s + \omega_i)\phi(\omega_s, \omega_i). \tag{4.11}$$

4.1.3 Quasi-Phasematching conditions in KTP

Under certain conditions, it's not possible achieve the phase matching conditions $\Delta k = 0$ at the desired central frequency $\omega_{p,0}$. If such condition cannot be achieved then the intensity of the downconverted field will scale as $\sin^2 \frac{\Delta k z}{2}$ i.e. the field intensity will be maximum if the crystal length is $l_c = \frac{2\pi}{\Delta k}$, called *coherence length*. On the other hand, when $\Delta k \to 0$ the down converted field intensity scale as z^2 (assuming the pump is not depleted). Thus achieving the phase-matching conditions is very important for the efficiency of the nonlinear process and an idea emerged, based on coherence length [Hache, 2016]. The idea is simple: since after a coherence length, the generated harmonic starts to interfere destructively, why not change the sign of the second-order nonlinear susceptibility and thereby enforce the harmonic to interfere constructively again. This gave rise to the concept of quasi-phasematching. This inversion of regions is achievable in ferroelectric media, such as LiNbO3 (ppLN) or KTP (ppKTP), where the sign of $\chi^{(2)}$ depends on an

[2]The quantum state will evole following $i\hbar\frac{\mathrm{d}}{\mathrm{d}t}|\psi_I(t)\rangle = \hat{H}_{int}(t)|\psi_I(t)\rangle$ the relation between the state in the interaction picture and the Schrodinger picture is then $|\psi_I(t)\rangle = e^{\frac{i\hat{H}_0 t}{\hbar}}|\psi_S(t)\rangle$

applied electric field. Such devices are now commonly employed, particularly in planar waveguide geometries. We consider a nonlinear medium formed by alternating layers, in which its second-order nonlinear susceptibility is varying along the z-axis, see Fig. 4.1:

$$\chi^{(2)}(z) = \chi^{(2)} \sum_{m=0}^{+\infty} d_m e^{-imk_{\mathrm{QPM}}z}. \tag{4.12}$$

with $k_{\mathrm{QPM}} = \frac{2\pi}{\Lambda}$, Λ being the periodic poling length. This is a Fourier series where the Fourier coefficients are defined by

$$d_m = \frac{1}{\Lambda} \int_0^{\Lambda} \chi^{(2)}(z) e^{imk_{\mathrm{QPM}}z} \mathrm{d}z. \tag{4.13}$$

Injecting equation (4.12) in (4.5) one can recover the quasi-phasematching condition :

$$\Delta k = k_p - k_s - k_i - k_{\mathrm{QPM}} \tag{4.14}$$

Ajusting carrefully the poling period Λ, $\Delta k = 0$ is now achievable.

4.1.4 Kleinman Symmetries in KTP

In the frequency domain, the second-order susceptibility establishes a link between all possible pairs of cartesian components of the electric field, denoted as $E_j(\omega)$ and $E_k(\omega)$, with the orthogonal component of the polarization field, represented by $P_i(\omega)$. Moreover, it is essential to note that the susceptibility coefficients associated with this relation are not constant but vary with frequency. Hence, we express them as $\chi^{(2)}_{ijk} = \chi^{(2)}_{ijk}(\omega)$. In the context of a three-wave mixing process, three frequencies play a role: ω_n, ω_m, and $\omega_3 = \omega_n + \omega_m$. Explicitly, the expression of the polarization given the electric field components is:

$$P_i(\omega_n + \omega_m) = \epsilon_0 \sum_{j,k} \sum_{n,m} \chi^{(2)}_{ijk}(\omega_n + \omega_m; \omega_n; \omega_m) E_j(\omega_n) E_k(\omega_m) \tag{4.15}$$

In non-linear materials, when the external field frequencies are far from any atomic resonance, the second-order susceptibility can be treated as frequency-independent. Additionally, assuming a lossless medium, the third-order tensor $\chi^{(2)}$ exhibits full permutation symmetry. This symmetry condition implies that the frequency arguments of the nonlinear susceptibility can be interchanged freely, as long as the corresponding cartesian indices are also interchanged simultaneously. For example, it can be demonstrated that:

$$\chi^{(2)}_{ijk}(\omega_3 = \omega_1 + \omega_2; \omega_1; \omega_2) = \chi^{(2)}_{jki}(\omega_1 = \omega_3 + \omega_2; \omega_2; \omega_3) = \chi^{(2)}_{kij}(\omega_2 = \omega_3 + \omega_1; \omega_3; \omega_1) \tag{4.16}$$

The aforementioned outcome is commonly referred to as the Kleinman Symmetry condition. This condition enables us to express the susceptibility tensor in a more compact form, which involves using a 3 by 6 matrix d_{il}. The matrix is typically denoted as follows:

$$d_{il} = \frac{1}{2} \chi^{(2)}_{i(jk)} \tag{4.17}$$

jk	11	22	33	23,32	31,13	12,21
l	1	2	3	4	5	6

So we end up rewriting the components of the nonlinear process in the frequency domain, taking into account symmetry conditions

$$\begin{pmatrix} P_x \\ P_y \\ P_z \end{pmatrix} = 2 \begin{pmatrix} d_{11} & d_{12} & d_{13} & d_{14} & d_{15} & d_{16} \\ d_{16} & d_{22} & d_{23} & d_{24} & d_{14} & d_{12} \\ d_{15} & d_{24} & d_{33} & d_{23} & d_{13} & d_{14} \end{pmatrix} \begin{pmatrix} E_x^2 \\ E_y^2 \\ E_z^2 \\ 2E_yE_z \\ 2E_xE_z \\ 2E_xE_y \end{pmatrix} \tag{4.18}$$

This work uses two nonlinear materials: Lithium Niobate (LN) for SHG and Potassium Titanyl Phosphate (KTP) for SPDC. In both cases, the susceptibility tensor experiences can be significantly simplified, for example[3]

$$d_{KTP} = \begin{pmatrix} 0 & 0 & 0 & 0 & d_{15} & 0 \\ 0 & 0 & 0 & d_{24} & 0 & 0 \\ d_{15} & d_{24} & d_{33} & 0 & 0 & 0 \end{pmatrix} \tag{4.19}$$

These tensors play a crucial role in showing the allowed processes within the crystals. For example, if we consider a mixing process involving two input frequencies, where one is polarized along the x-axis and the other along the y-axis, the induced polarization will be oriented along the x-axis. This alignment is due to the fact that only the term d_{15} couples this specific combination. This specific combination corresponds to a type-II Parametric Down-Conversion (PDC) process, wherein a pump photon polarized along the x-axis splits into two photons; one polarized along x and the other along y. Similar conclusions can be derived from other field combinations and nonlinear effects. Furthermore, we emphasize the significance of the crystal-cut, as it establishes a relation between the crystal's propagation axis, the transversal directions and the cartesian axes used when constructing the susceptibility matrix. A different crystal-cut leads to a repositioning of the coefficients in the d matrix. Hence, it becomes crucial to consider the crystal-cut when designing experiments involving nonlinear bulk crystals or waveguides. Looking now in closer details at the values of d_{KTP} [Crystals, 2016] the most significant one, by nearly an order of magnitude, is d_{33} corresponding to a type-0 process, a scenario where the signal and idler photons are degenerate and present the same polarization as the one of the input pump. Thus when studying the interaction hamiltionian in 4.1.5 we will focus our study on a type-0 scenario.

4.1.5 The supermode basis

In section 4.1.2 we derived the Hamiltonian of interaction of the SPDC process, equation (4.10), as a function of the JSA acting on all pairs of creation and annihilation operator $(\hat{a}_s^\dagger(\omega_s), \hat{a}_s^\dagger(\omega_i))$ where $\omega_s + \omega_i = \omega_p$. This expression gives a little bit of intuition on what happens during the physical process will all frequency components of the pump downconverting to couples of new entangled signal and idler frequencies. Yet, we need to study more extensively the behaviour of the JSA to have a full characterization of the physical process. A very intuitive tool we introduced in chapter 1 when dealing with

[3]The matrix d_{KTP} here consider x as the propagation axis.

bipartite systems is the Schmidt decomposition. Applying it to the JSA permits to rewrite it in a unique way where signal and idler fields are a sum of decoupled modes.

$$\mathcal{J}(\omega_s, \omega_i) = \sum_k \sqrt{\lambda_k} h_k(\omega_s) g_k(\omega_i) \tag{4.20}$$

$\{\lambda_k\}_k$ are the Schmidt coefficients. From here we can easily derive a new set of operators $\{A_k, B_k\}$ that are the creation and annihilation operators of a new basis that we call *supermode basis*.

$$\begin{aligned} \hat{A}_k^\dagger &= \int \mathrm{d}\omega_s h_k(\omega_s) \hat{a}_s^\dagger(\omega_s) \\ \hat{B}_k^\dagger &= \int \mathrm{d}\omega_i g_k(\omega_i) \hat{a}_i^\dagger(\omega_i) \end{aligned} \tag{4.21}$$

In the specific case of type-0 SPDC, the two laters output field are made indistinguishable meaning that $\hat{A}_k^\dagger = \hat{B}_k^\dagger$ for all k and therefore the quantum state after the waveguide is :

$$\begin{aligned} |\Psi\rangle &= \exp\left(\frac{1}{i\hbar}\int_{-\infty}^{+\infty} \hat{H}_{int}(t)\mathrm{d}t\right)|0\rangle \\ &= \exp\left(\sum_k \sqrt{\lambda_k}\mathcal{C}\left(\hat{A}_k^\dagger\right)^2 + h.c.\right)|0\rangle \\ &= \prod_k \hat{S}_{\hat{A}_k}\left(\mathcal{C}\sqrt{\lambda_k}\right)|0\rangle \end{aligned} \tag{4.22}$$

with $\mathcal{C} = \frac{-2\epsilon_0\chi^{(2)}}{\hbar}$. Here we clearly identify that SPDC with ultra short pulses of light is able to produce a set of squeezed vacua in the spectral domain. Thus the covariance matrix of our state in the supermode basis $\mathbf{\Sigma}_{sup}$ is diagonal. In the degenerate scenario the Schmidt coefficients $\{\lambda_k\}_k$ characterize the squeezing distribution in the multimode quantum state and give access to the number of squeezed mode of light via the Schmidt number $K = \frac{1}{\sum_k \lambda_k^2}$ [Brecht, 2014].

4.2 Numerical simulation

4.2.1 Joint-Spectral Amplitude

An analytical diagonalization of the JSA in the gaussian approximation was perform in [Patera et al., 2009]. In most of the cases however, we cannot find an analytical solutions for this Hamiltonian, thus numerical simulations were performed in order to predict the properties of the independent squeezed modes at the output of the waveguide. We found an optimal configuration for a waveguide length of 15 mm, cross-section of 3×3 μm and poling period $\Lambda = 13.4$ μm. By optimal, we mean a cross-section allowing at most one spatial mode at telecom wavelength and with a good balance between the number of squeezed modes and the spectral size of such supermodes. Indeed too many modes, would decrease the quantity of squeezing per mode and very large mode would be hard to detect in terms of bandwith accessible to our Local Oscillator [Roman-Rodriguez et al., 2023, Kouadou et al., 2023]. We give more details about it in the chapter 5. Using Sellmeier's equation, we computed the wavevector mismatch Δk and thus the phase-matching function $\phi(\omega_s, \omega_i)$. We then used the experimentally measured FWHM from

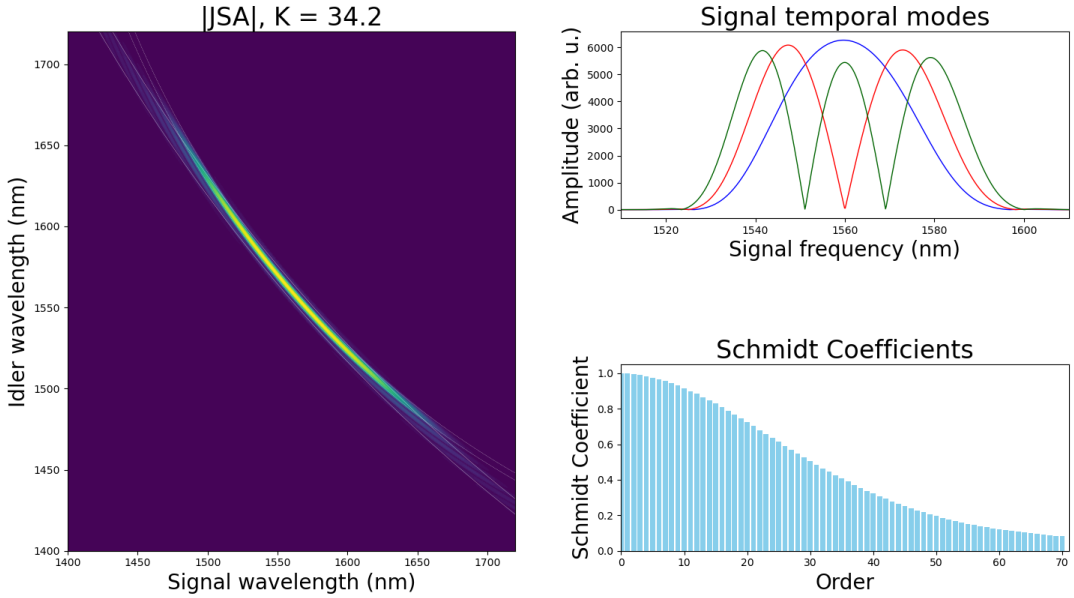

Fig. 4.2 ***Numerical simulation of the independent squeezed states.*** *Left: JSA function, Right: First three frequency modes, resembling Hermite-Gauss and the distribution of the Schmidt coefficients for every supermode.*

the SHG spectrum, see 3.4.2 to compute the JSA. The results are shown in Fig. 4.2. A number of about 34 modes is expected with the Schmidt distribution, $\{\lambda_k\}$, shown in the figure. The first three frequency modes, similar to Hermite-Gauss modes, are also shown [Roman-Rodriguez et al., 2021].

4.2.2 Covariance matrix analysis

The earlier method successfully addressed the issue of determining the supermodes and their corresponding relative squeezing values directly from the Hamiltonian, which characterizes how the system evolves differentially over time. While it yields the same physical outcomes, there are instances where it's more convenient to work with the input-output relationships that pertain to the system's evolution for a finite period or its progression through a finite crystal length. The primary advantage of this approach is its simplicity in deriving the covariance matrix of the output state, which encodes information about its noise characteristics [Arzani et al., 2018]. Let's consider the equations governing the motion of annihilation operators in the Heisenberg picture

$$\frac{\mathrm{d}}{\mathrm{d}t}\vec{\hat{a}} = \frac{i}{\hbar}[\hat{H}_{int}, \vec{\hat{a}}] = \mathcal{C}\mathcal{J}\vec{\hat{a}}^{\dagger} \tag{4.23}$$

where $\mathcal{J}$ is the JSA, thus

$$\frac{\mathrm{d}}{\mathrm{d}t}\begin{pmatrix}\vec{\hat{a}}\\ \vec{\hat{a}}^{\dagger}\end{pmatrix} = \mathcal{C}\tilde{\mathcal{J}}\begin{pmatrix}\vec{\hat{a}}\\ \vec{\hat{a}}^{\dagger}\end{pmatrix} \tag{4.24}$$

where

$$\tilde{\mathcal{J}} = \begin{pmatrix} 0 & \mathcal{J} \\ \mathcal{J}^* & 0 \end{pmatrix} \tag{4.25}$$

Solving for (4.24) then leads to

$$\begin{pmatrix} \vec{\hat{a}}(t) \\ \vec{\hat{a}}^\dagger(t) \end{pmatrix} = \exp(\mathcal{C}\tilde{\mathcal{J}}t) \begin{pmatrix} \vec{\hat{a}}(0) \\ \vec{\hat{a}}^\dagger(0) \end{pmatrix} \tag{4.26}$$

and in the canonical operators point of view to

$$\begin{aligned} \begin{pmatrix} \vec{\hat{X}}(t) \\ \vec{\hat{P}}(t) \end{pmatrix} &= \sigma_0 \begin{pmatrix} \mathbb{1} & i\mathbb{1} \\ \mathbb{1} & -i\mathbb{1} \end{pmatrix}^\dagger \begin{pmatrix} \vec{\hat{a}}(t) \\ \vec{\hat{a}}^\dagger(t) \end{pmatrix} \\ &= \underbrace{\sigma_0 \begin{pmatrix} \mathbb{1} & i\mathbb{1} \\ \mathbb{1} & -i\mathbb{1} \end{pmatrix}^\dagger \exp(\mathcal{C}\tilde{\mathcal{J}}t)\sigma_0 \begin{pmatrix} \mathbb{1} & i\mathbb{1} \\ \mathbb{1} & -i\mathbb{1} \end{pmatrix}}_{S} \begin{pmatrix} \vec{\hat{X}}(0) \\ \vec{\hat{P}}(0) \end{pmatrix} \end{aligned} \tag{4.27}$$

And the final covariance matrix in what we call the *frexel* basis is

$$\mathbf{\Sigma}_\omega = \frac{1}{2} S S^T \tag{4.28}$$

Thus from the JSA computed numerically in Fig. 4.2, we can derive the expected covariance matrix in the frequency domain discretizing with small frequency interval i.e. a high number of frequency bands. This is the case of Fig. 4.3 where we discretized over 64 frequency bands and ploted respectively $\mathbf{\Sigma}_{xx}$ and $\mathbf{\Sigma}_{pp}$. The overall shape of the covariance matrices is interesting to comment. Indeed, it appears as if the correlations inside the down-converted spectrum would be built pairwise with respect to the central frequency. In practice, this is not exactly true and we adress this in the next section using the PPT entanglement criterion. We would like to point out that this covariance matrix can be analyzed using the Bloch-Messiah decomposition, which was introduced in Section 1.4.2. This decomposition ultimately results in the expected supermodes

4.2.3 Peres-Horodecki Criterion

The Peres-Horodecki criterion [Horodecki et al., 2009], is also known as the Positive Partial Transpose (PPT) criterion. It provides a necessary and so practical condition to determine whether a given quantum state shared between two or more systems is separable. In particular we use its extension to the continuous variables regime introduced by [Simon, 2000]. To compute the PPT value, we split the state spectrum into 8 frexels. The PPT value is calculated for each of the 127 potential bipartitions, representing various ways of arranging the 8 frequency bands into two distinct sets, some examples are shown in Fig. 4.4. The test is based on a partial transpose operation on the state's density operator, which transforms its covariance matrix $\mathbf{\Sigma}_\omega$ into $\tilde{\mathbf{\Sigma}}_\omega = \mathcal{P}\mathbf{\Sigma}_\omega\mathcal{P}$ using the operation $\mathcal{P}$. This operation alters the sign of the p coordinate for one of the bipartitions. A necessary requirement for the state to be separable is given by the condition $P = \tilde{\mathbf{\Sigma}}_\omega - i\Omega \geq 0$, where Ω has the symplectic form. It means that if one eigenvalue of P is negative then the state

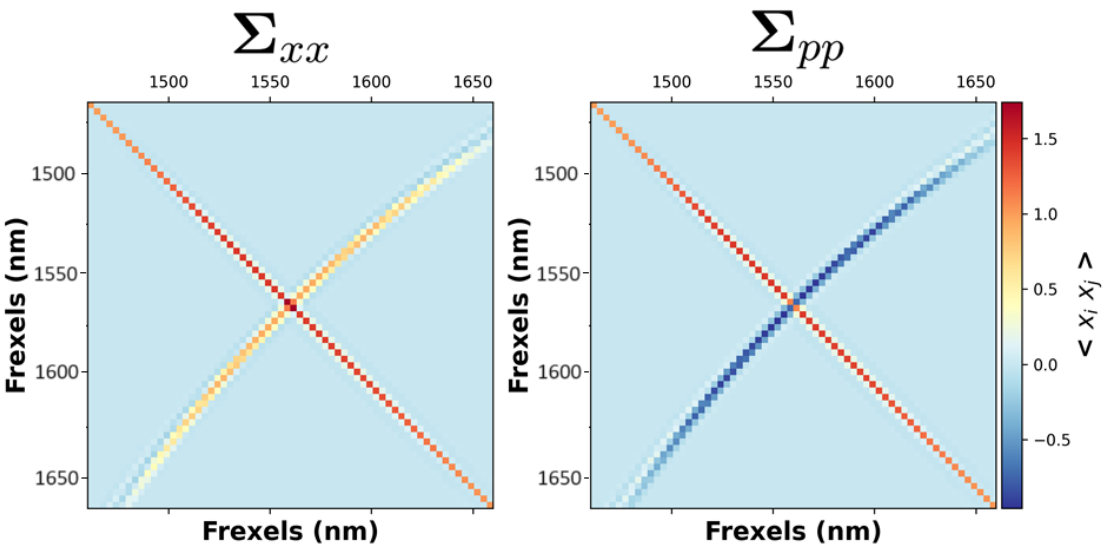

Fig. 4.3 ***Numerical simulation of the covariance matrix.***

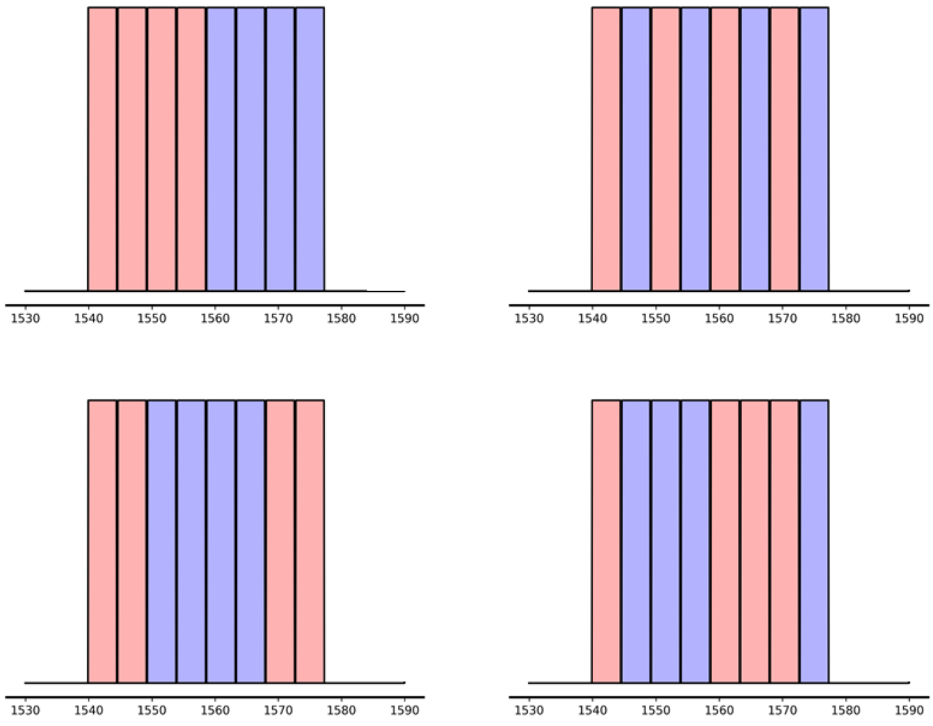

Fig. 4.4 ***Bipartition example.*** *4 of the 127 possible bipartitions of the spectrum are represented, a bipartition does not necessary has the same number of frequency bands on each side.*

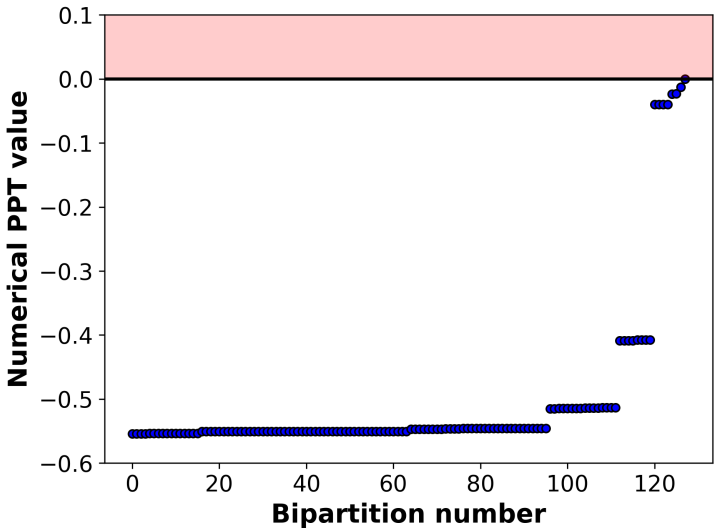

Fig. 4.5 ***PPT criterion applied to all 127 possible bipartitions out of the 8 frexels***. *The values are obtained from the numerical JSA computed.*

is not separable. For each possible bipartition we thus compute the minimum eigenvalue of P which we call the PPT value [Medeiros de Araújo et al., 2014,Kouadou et al., 2023]). The result is shown in Fig. 4.5 where we see that, in a scenario without loss, inseparability holds for all bipartitions. The only point that is non-negative corresponds to the trivial bipartition where the all the frequency bands belong to one party. This conclusion is very appealing for us as we want to use such state for quantum communication protocols. It means that this ressource can be demultiplexed in frequency and we can distribute the entanglement through the different frequency bands. This conclusion will be at the core of Chapter 6.

Chapter 5

Experimental characterization of the source

Contents

Through this chapter we report on the experimental demonstration of a source that generates spectrally multimode squeezed states of light over the infrared C-Band. This is achieved using a single-pass Spontaneous Parametric Down Conversion (SPDC) process in a periodically-poled KTP waveguide that is pumped with the second harmonic of a femtosecond laser. A first version of the experiment was mounted with Victor R. Rodriguez in 2021. Early results were reported in his Ph.D manuscript in 2022 [Román Rodríguez, 2022]. Then, I mounted a second version of the experiment, improving the detection setup by adding a waveguide on the Local Oscillator path for spatial mode-matching and improving the selection and coupling of the pump inside the waveguide. I performed the most recent characterization of the source and the result have given a common publication where both Victor and I are first author [Roman-Rodriguez et al., 2023].

We begin this chapter by introducing the reader to mode selective homodyne measurement. We then give a proper characterization of the waveguide chip as well as a roadmap on how to identify the appropriate waveguides. Our measurements then show significant squeezing in more than 21 frequency modes, with a maximum squeezing value over 2.5 dB[1]. Moreover, we demonstrate multiparty entanglement across 8 individual frequency bands by reconstructing the covariance matrix of their quadratures. Finally, we use the reconfigurable mode-selective homodyne detection to mold the output into cluster states of various shapes.

5.1 Principle of mode selective homodyne measurement

5.1.1 A projective measurement

One standard approach to reconstruct a spectral field is the use of coherent detection. In particular homodyne detection is a standard technique used to efficiently recover the amplitude and phase of a modulated light beam in quantum physics [Grynberg et al., 2010]. The signal to measure is mixed on a balanced beam splitter with a bright local oscillator (LO), then directed to two photodiodes. The homodyne signal result from the subtraction of the two photocurrents, see Fig. 5.1. Let's consider two fields with their operators, $\hat{\vec{E}}_s(\vec{r},t)$ associated to the signal to be measured and $\hat{\vec{E}}_{LO}(\vec{r},t)$ our bright beam named Local Oscillator (LO). More precisely, we can decompose our signal state in a basis made of decoupled transverse and longitunal modes and assume our Local Oscillator to be a bright coherent state i.e. it can be describe by a dominant term in the mean-field basis[2]. To simplify slightly, we assume that the fields have perfect polarization overlap, thus we drop this term.

$$\begin{aligned}\hat{\vec{E}}_s^{(+)}(\vec{r},t) &= \sum_{i,j} \hat{a}_{i,j,s}\vec{g}_{i,s}^{\perp}(\vec{r})\vec{u}_{j,s}(t)\\ \hat{\vec{E}}_{LO}^{(+)}(\vec{r},t) &= \alpha_{LO}\vec{g}_{LO}^{\perp}(\vec{r})\vec{u}_{LO}(t)\end{aligned} \tag{5.1}$$

[1] A proper definition of this quantity is given in 5.1.2

[2] The mean-field basis means that we can effectively write $\hat{\vec{E}}_{LO}^{(+)}(\vec{r},t) = \alpha_{LO}\vec{g}_{LO}^{\perp}(\vec{r})\vec{u}_{LO}(t) + \mathcal{E}_0\sum_n \delta\hat{a}_{n,LO}\vec{g}_{n,LO}^{\perp}(\vec{r})\vec{u}_{n,LO}(t)$ with $\delta\hat{a}_{n,LO} = \hat{a}_{n,LO} - \langle\hat{a}_{n,LO}\rangle \ll \langle\hat{a}_{n,LO}\rangle$ Since the operators $\delta\hat{a}_{n,LO}$ are zero-mean, we can write the LO field keeping only the dominant term

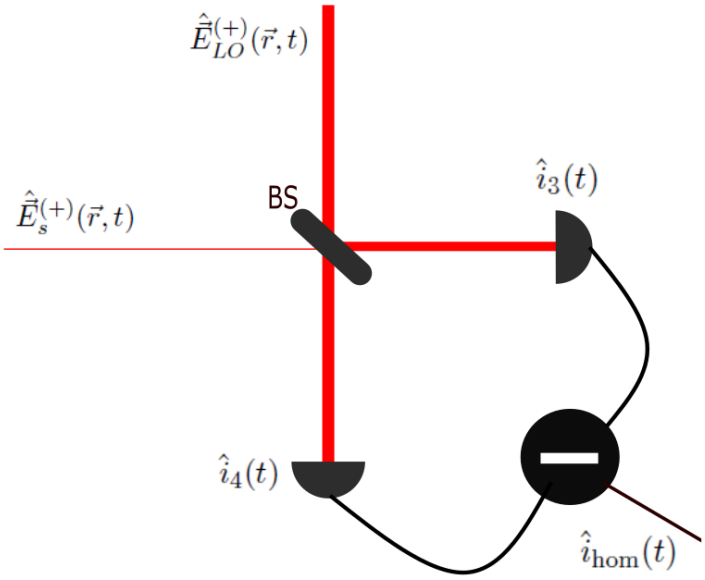

Fig. 5.1 ***Homodyne detection scheme.***

While the local oscillator is traditionally considered as a single mode classical field, we will denote it as a quantum operator only during the derivation, yet dropping the hat notation off the scalar α_{LO} for lisibility. We can then compute the total complex electrical field in the two arms of the homodyne setup after the beamsplitter

$$\hat{\vec{E}}_{\mathrm{tot}}(\vec{r},t) = \frac{1}{\sqrt{2}}\left(\hat{\vec{E}}_s(\vec{r},t) \pm \hat{\vec{E}}_{LO}(\vec{r},t)\right). \tag{5.2}$$

Each arm is then converted to a photocurrent. To do so, we introduce first the quantum intensity operator [Loudon, 1983a]

$$\hat{I}(\vec{r},t) = 2\epsilon_0 c \hat{\vec{E}}^{(-)}(\vec{r},t)\hat{\vec{E}}^{(+)}(\vec{r},t) \tag{5.3}$$

and the photocurrent operator from the photodiode is proportional to the responsivity $\mathcal{R}$ of the detector during the impulsion duration with detector temporal response $r(\tau)$ and over all the photodetector surface S:

$$\hat{i}(t) = \mathcal{R}\int_S \mathrm{d}x\mathrm{d}y \int_T \mathrm{d}\tau r(\tau)\hat{I}(\vec{r},t-\tau) \tag{5.4}$$

Moreover, the temporal response of the photodiode is typically a gate function of much longer duration than the pulse duration (tens of nanoseconds versus tens of femtoseconds in our case) meaning that this quantity can be considered approximately 1 during the process. The homodyne photocurrent is obtained after the two photocurrents from the

photodiodes is subtracted.

$$\begin{aligned}\hat{i}_{\text{hom}}(t) &\propto \hat{i}_3(t) - \hat{i}_4(t)\\ \hat{i}_{\text{hom}}(t) &\propto \int_S \mathrm{d}x\mathrm{d}y \int_T \mathrm{d}\tau \hat{\vec{E}}_s^{(+)}(\vec{r}, t-\tau)\hat{\vec{E}}_{\text{LO}}^{(-)}(\vec{r}, t-\tau) + h.c\end{aligned} \tag{5.5}$$

Now replacing inside (5.5) the field by their expressions in (5.1) we can rewrite the full homodyne signal as :

$$\begin{aligned}\hat{i}_{\text{hom}}(t) &\propto \int_S \mathrm{d}x\mathrm{d}y \int_T \mathrm{d}\tau \sum_{i,j} \hat{a}_{i,j,s}\vec{g}_{i,s}^{\perp}(\vec{r})\vec{u}_{j,s}(t)\alpha_{LO}^*\vec{g}_{LO}^{\perp *}(\vec{r})\vec{u}_{LO}^*(t) + h.c\\ \hat{i}_{\text{hom}}(t) &\propto \alpha_{LO}^* \sum_{i,j} \hat{a}_{i,j,s}\left(\int_S \mathrm{d}x\mathrm{d}y \vec{g}_{i,s}^{\perp}(\vec{r})\vec{g}_{LO}^{\perp *}(\vec{r})\right)\left(\int_T \vec{u}_{j,s}(t)\vec{u}_{LO}^*(t)\right) + h.c\end{aligned} \tag{5.6}$$

and so the homodyne signal is proportional to the overlap integrals, spatially and temporally, between the signal and the LO modes. This overlap integral is also sometimes called coherence Γ of the field. Assuming now a perfect spatial overlap and that we can select the temporal mode of the Local Oscillator to be precisely the k^{th} signal temporal modes, doable via pulse shaping technique presented in Chapter 3, then (5.6) reduces to

$$\hat{i}_{\text{hom}}(t) \propto \alpha_{LO}^*\hat{a}_{k,s} + \alpha_{LO}\hat{a}_{k,s}^\dagger \tag{5.7}$$

with $\alpha_{LO} = \sqrt{N_{LO}}e^{i\theta}$ carrying the information of the mean field amplitude (in terms of photon number N_{LO}) and relative phase between signal and LO θ we can rewrite (5.7) in terms of field quadratures in a rotated phase space

$$\begin{aligned}\hat{i}_{\text{hom}}(t) &\propto \sqrt{N_{LO}}\hat{X}_{k,s}(\theta)\\ \hat{i}_{\text{hom}}(t) &\propto \sqrt{N_{LO}}\left(\hat{X}_{k,s}\cos\theta + \hat{P}_{k,s}\sin\theta\right)\end{aligned} \tag{5.8}$$

The scan of the relative phase θ permits to access the value both quadratures $\hat{X}_{k,s}$ and $\hat{P}_{k,s}$ associated to the k^{th} mode. Homodyne measurement, coupled to a temporally reconfigurable local oscillator, is mode-selective and permits to measure both quadratures of the signal field. Such measurement technique has also the avantage of amplifying the quadratures signal to be measured by the Local Oscillator intensity N_{LO}.

5.1.2 Sideband squeezing measurement

In the previous part we have shown how the photoelectric current produced by homodyne detection is proportional to the quadrature of the signal field. Yet, coming back to squeezing, the main quantity of interest is the variance of the quadrature. Accessing this quantity is done, in this manuscript, with a spectrum analyzer which display the power spectral density (PSD) defined as

$$S(\Omega) = \int \mathrm{d}\tau \langle \Delta i(t)\Delta i(t+\tau)\rangle e^{i\Omega\tau} \tag{5.9}$$

where $\langle \Delta i(t)\Delta i(t+\tau)\rangle = \langle i(t)i(t+\tau)\rangle - \langle i(t)\rangle\langle i(t+\tau)\rangle$ is the photocurrent autocorrelation function. In a stationary regime, [Fabre, 1997] shows how the PSD is linked to the variance of $i(t)$

$$\Delta^2 i = \int_{-\infty}^{+\infty} \|f(\Omega)\|^2 S(\Omega)\frac{\mathrm{d}\Omega}{2\pi} \tag{5.10}$$

where $f(\Omega)$ represent a linear filtering process in the Fourier space, characterizing the finite bandwidth of the detection process. Thus in the specific case of a narrowband pass filter of frequency δf centered around the pulsation Ω_0, (5.10) reduces to

$$\Delta^2 i = 2\delta f S(\Omega_0) \tag{5.11}$$

and thus, combining (5.11) with (5.8) the filtered PSD is proportional to the variance of the quadrature signal. Defining $\mathcal{K}_0$ to be the proportional factor we get

$$S(\Omega_0) = \mathcal{K}_0 \Delta^2 \hat{X}_{k,s}(\theta). \tag{5.12}$$

Note that, in this specific situation $\mathcal{K}_0$ is independent of the signal field measured. Thus, we can experimentally acces $\mathcal{K}_0$ by measuring the signal of the vacuum state (experimentally by simply blocking the signal to be measured, leaving the entry of the beamsplitter to be the vaccum). This quantity is denoted as the 'shot noise'. Finally

$$\Delta^2 \hat{X}_{k,s}(\theta) = \frac{S(\Omega)}{S(\Omega)_{\text{vac}}} \tag{5.13}$$

where

$$S(\Omega)_{\text{vac}} = \mathcal{K}_0 \Delta^2 \hat{X}^{\text{vac}} = \mathcal{K}_0 \tag{5.14}$$

In a spectrum analyzer, such final filter δf that is applied to the input signal is given by the resolution bandwidth (RBW) with a minimum span. Finally, it is common to present such quantity in decibel

$$\Delta^2 \hat{X}_{k,s}(\theta)_{\text{dB}} = 10 \log_{10} \left(\frac{S(\Omega)}{S(\Omega)_{\text{vac}}} \right) \tag{5.15}$$

when $S(\Omega) < S(\Omega)_{\text{vac}}$, we say that the quadrature variance $\Delta^2 \hat{X}_{k,s}(\theta)_{\text{dB}}$ is squeezed below the shot noise limit.

5.2 Waveguide characterization

Through this section we present the central element of our experiment in more details. As in Chapter 4 we call *pump* the pulse at 780 nm that enters into the waveguide for the purpose of squeezing production at 1560 nm. Moreover, for the alignment of the experiment and the characterization of the source we also couple into the same waveguide a small portion of the inital laser at telecom wavelength (introduced in Chapter 3). This pulse is called *seed* in the rest of the manuscript.

5.2.1 Chip features

From the numerical JSA computed in Chapter 4 we also derived the required physical parameters (dimension of the waveguide, length, poling period) [Roman-Rodriguez et al., 2021]. Advr inc. manufactured the waveguide according to these parameters, they supplied us with a chip, shown in Fig. 5.2, 15 mm in length and 1.5 mm in width, containing 30 waveguides organized into 5 groups of 6 waveguides with cross-sections dimension of

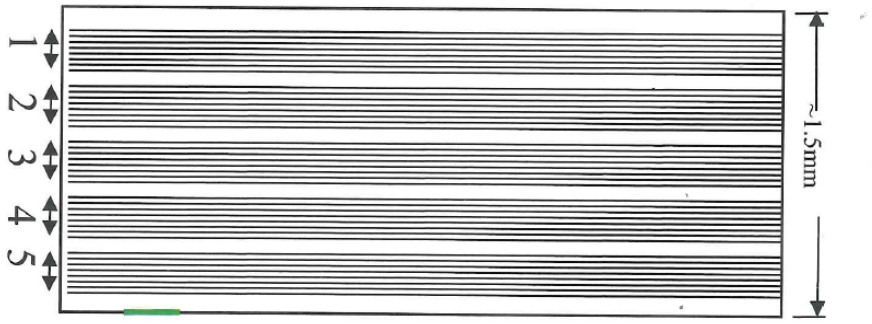

Fig. 5.2 ***Schematic of the waveguide chip provided by AdvR.*** *Each group contains 6 waveguides of cross-section 2 μm, 3 μm and 4 μm.*

2, 3 and 4 μm[3]. Each of these 30 waveguides exhibits unique performance characteristics that require evaluation before proceeding with the experiment. This is due to the fabrication process not being fully deterministic. A full characterization of the chip was done in [Román Rodríguez, 2022]. I will show in the following section what are the important criteria we used to chose the waveguide for the experiment.

5.2.2 Input-output coupling efficiency

A first, quite obvious, parameter of interest is the ability to couple light inside the waveguide. The efficacy of coupling mechanisms directly impacts the overall performance of our setup in terms of nonlinear interaction. A well-designed coupling interface not only optimizes the injection of light into the waveguide but also minimizes losses and distortions. Achieving this balance involves meticulous choice of the input/output components, such as achromatic lenses, tailored to match the modal properties of the waveguides. In Fig. 5.3 we present the results of coupling efficiency for both pump and seed realized independantly. Another important point comes when we now need to couple, at the same time, both seed and pump inside the same waveguide, either for parametric amplification, see 5.2.4, or simply for alignment of the detection setup. We need to take into account the focal shift between the two beams, meaning that the focusing with the same lens won't happen precisely in the same plane due to the wavelength dependancy of the refractive index. From a practical point of view, we prioritize the coupling of the pump into the waveguide as the squeezing is directly proportionnal to it. Moreover we want to have a good control over the nonlinear process that is dependent on the spatial mode coupled into the waveguide. On the seed side a degraded coupling is not that problematic. Too large power is even detrimental as in parametric amplification we should avoid pump depletion. Moreover the waveguide is designed to be monomode spatially for the telecom wavelength and, having a seed that is less powerful than the pump reduce the risks of damaging the coating of the chip.

[3] A group of 6 waveguides is organized in the following order of cross-sections: 2, 3, 4, 2, 3, and 4 μm.

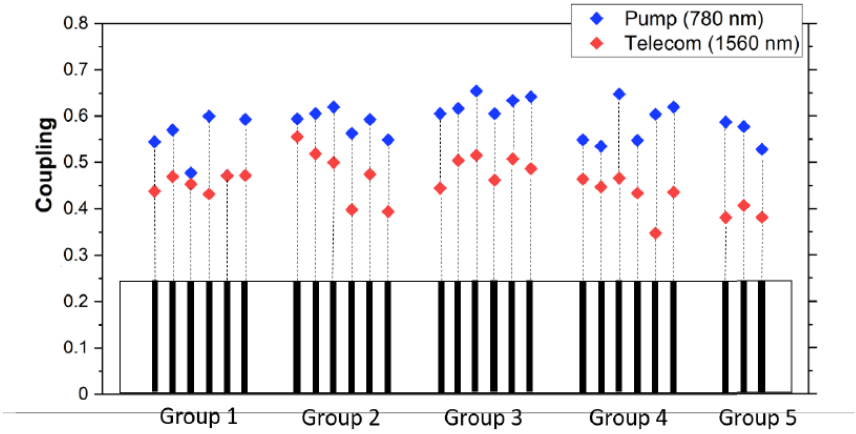

Fig. 5.3 ***Coupling efficiency*** *at pump and seed wavelengths for every waveguide measured along the chip. In all cases the polarization was set to vertical to prevent frequency conversion.*

5.2.3 Second Harmonic characterization

The SHG characterization of our waveguides was performed by coupling them to the C-band wavelength (1560 nm). A measurement of the spectrum of the second harmonic field produced by the C-band input gives an estimate on the homogeneity of the waveguide along the propagation direction. We look for a sinc-like function corresponding to the Fourier transform of a square non-linear profile, that is expected for a homogeneous structure, see Chapter 3.4. We show in Fig. 5.4 the second harmonic field measured from two waveguides, identical in dimension, and in the same group of the chip. The result is quite clear by eye: the SHG profile of waveguide N is much closer to a sinc function than waveguide N+3. Experimentally the waveguide N does not present a better coupling or better nonlinear coefficient, yet the purity of the non-linear process appears to be better. The amount of second harmonic field produced from the telecom input gives an estimate on the order of magnitude of the nonlinear coefficient of the waveguide.

5.2.4 Phase sensitive amplification

Prior to any squeezing measurement, we built a degenerate Optical Parametric Amplifier, or OPA, by pumping the waveguide with both seed and pump. The seed is taken at low power ($\approx 100\ \mu W$) to avoid pump depletion and unwanted cascaded frequency conversion. The phenomenon of parametric amplification can be observed as a modulation of the seed amplitude at the output of the waveguide, depending on the relative phase ϕ between the seed and the pump fields. Indeed, in the scenario of a single-mode OPA, considering the seed as coherent state $|\alpha\rangle$ with $\alpha = |\alpha|e^{i\phi}$, the number of photons inside the seed before the waveguide is

$$N_{in} = |\alpha|^2 \tag{5.16}$$

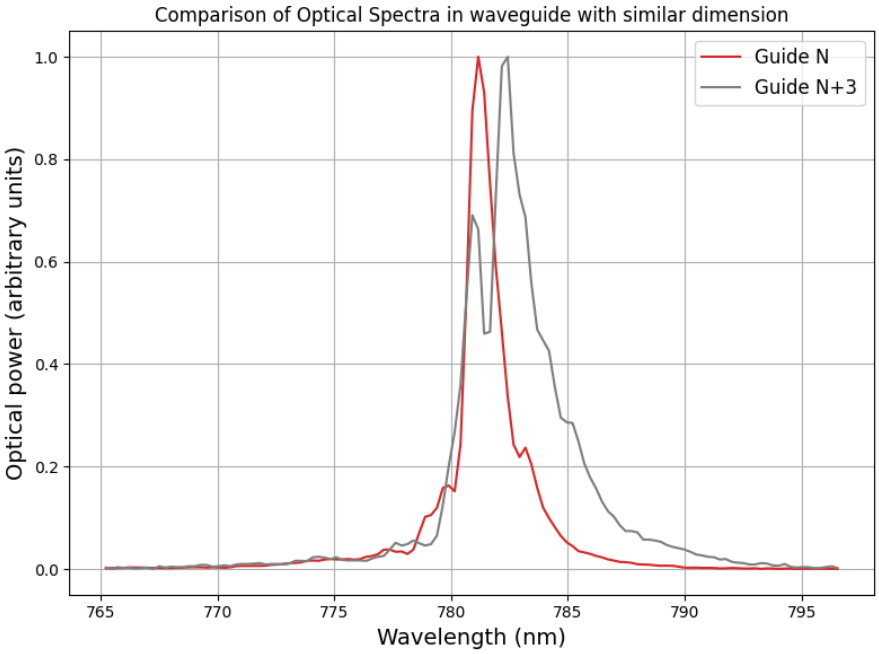

Fig. 5.4 ***Second Harmonic characterization***. *Measured spectra for two different consecutive waveguide identical in dimension.*

whereas after interaction with the down-converted pump inside the waveguide the number of photon is [Gigan, 2004]

$$N_{out} = |\alpha|^2 \left[\cosh(2r) + \sinh(2r)\cos(2\phi)\right] \tag{5.17}$$

where r is the squeezing factor introduced in Chapter 1.4. This measurement shows the existence of parametric gain $G = \frac{N_{out}}{N_{in}}$ in our waveguides. In particular when $\phi = 0$ the gain is e^{2r} (maximum amplification) and when $\phi = \frac{\pi}{2}$ the gain is e^{-2r} (maximum deamplification). Such amplification and deamplification of the seed is a precondition of squeezing generation, even though the levels of multimode squeezing cannot be predicted in this way as we derived the gain in a monomode scenario. The extrema of the parametric gain, $G_{\pm}$, can be approximated, for a single-mode OPA, with the characteristics of our system as [Serkland et al., 1995, Umeki et al., 2011]:

$$G_{\pm} \sim \exp\left(\pm 2\sqrt{\eta_{\mathrm{PSA}} P}\right), \tag{5.18}$$

where P is the pump power and η_{PSA} is the parametric efficiency. Ideally, the minimum deamplification, G_{-}, should be symmetric with respect to G_{+}, although a disparity between the two has been reported when using pulsed lasers, and attributed to a distortion of the spatial or temporal profile inside the nonlinear material [La Porta and Slusher, 1991]. The disparity appears at sufficiently high power density in the material. Fig. 5.5 shows the parametric gain measured as a function of the pump power. The data fits well Eq. (5.18) and gives two values for the parametric efficiency due to their asymmetry. However, a measurement of the second harmonic efficiency in the same nonlinear waveguide

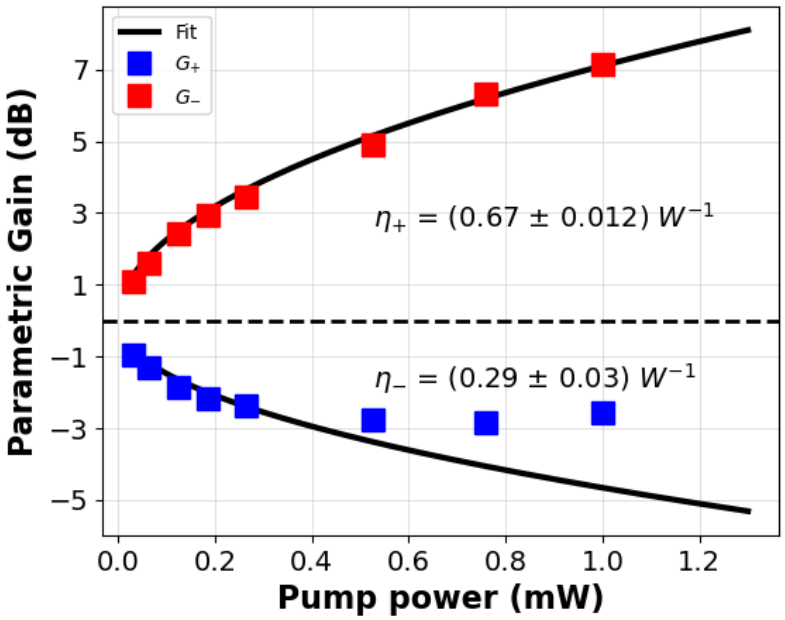

Fig. 5.5 ***Parametric gain vs pump power.*** *Extrema in the modulation of the amplitude for the degenerate OPA, fit to Eq. ((5.18)) gives the parametric efficiency, related to the total squeezing level.*

gives an efficiency of $\eta_{\text{SHG}} = 0.33\ \text{W}^{-1}$, which is in good agreement with the extracted parametric efficiency for the deamplification. Nevertheless this elementary model tells us about the functioning of the source only, and does not take into account the temporal profile of the seed $\vec{u}_{\text{seed}}(t)$ which in the end is the one that either amplified or deamplified. A more sophisticated model would derive a mean gain over the temporal profile of the seed

$$\begin{aligned} \langle G_\pm \rangle &= \int_{-T}^{T} G_\pm(t) u_{seed}(t) \mathrm{d}t \\ &= \int_{-T}^{T} \exp\left(\pm 2\sqrt{\eta_{\text{PSA}} P(t)}\right) u_{seed}(t) \mathrm{d}t \end{aligned} \tag{5.19}$$

Then by shaping in the temporal domain the seed, we could measure the gain associated to different temporal modes that are relevant in our multimode quantum source, as was done in [Huo et al., 2020]. Overall, the conclusion of the phase sensitive experiment is that, at pump powers of few mW, we can expect at least some dB of squeezing in our multimode states.

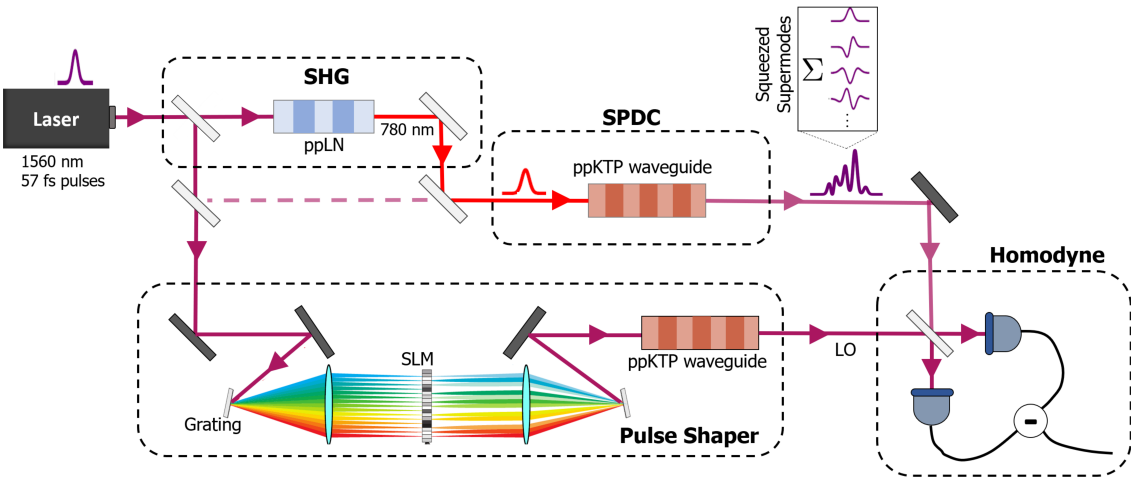

Fig. 5.6 ***Experimental scheme for the generation of the multimode states.*** *A telecom wideband (bandwidth around 55 nm) pulsed laser is up converted to its second harmonic with a ppLN crystal and then coupled to a nonlinear ppKTP waveguide. Type 0 SPDC interaction generates squeezing in a set of independant frequency modes. Each mode is addressed individually with homodyne detection, where the LO is shaped spectrally with the use of a pulse shaper.*

5.3 Experimental realization of a multimode squeezing source

5.3.1 Description of the experiment

The experimental setup for generating multimode squeezed states is illustrated in Fig. 5.6. We start with a broadband femtosecond laser, introduced in Chapter 3 that emits light pulses with the following properties: bandwidth of approximately 55 nm in FWHM, pulse duration about 57 fs, repetition rate of 100 MHz, and power output of around 500 mW. This laser is centered at a wavelength of 1560 nm.

A portion of this laser's is directed towards our periodically poled Lithium Niobate (ppLN) crystal, presented in 3.4, designed for second harmonic generation. After passing through the ppLN crystal, we recall that the light bandwidth is approximately 2 nm, with a central wavelength of 780 nm. This second harmonic field is our pump.

Next, the pump is coupled into a single-mode, rectangular, nonlinear waveguide made from periodically poled Potassium Titanyl Phosphate (ppKTP). This waveguide down-converts the pump field to C-band[4] telecom wavelengths and generates the multimode squeezed states.

On the other side, a big fraction of the original power from the laser is sent to a pulse shaper, described and characterized in 3.3, in order to generate a spectrally configurable LO. The LO is then passed through another ppKTP waveguide (identical in dimensions)

[4]In infrared optical communications, C-band (C for "conventional") refers to the wavelength range 1530–1565 nm, which corresponds to the amplification range of erbium doped fiber amplifiers (EDFAs).

Hermite-Gauss	Sqz	ASqz
0	-1.03	1.39
1	-0.68	1.31
2	-0.62	1.16
3	-0.61	1.27
4	-0.57	1.41
5	-0.58	1.46

	Sqz	ASqz
6	-0.73	1.45
7	-0.74	1.27
8	-0.54	1.16
12	-0.55	1.15
15	-0.60	1.36
20	-0.53	0.85

Flat modes	Sqz	ASqz
0	-2.66	6.99
1	-2.43	6.49
2	-2.32	6.83
3	-2.01	6.47

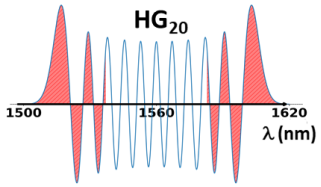

Fig. 5.7 ***Multimode Squeezing Curves.*** *Left : We summarize, for each Hermite-Gauss mode (supermode) the quantity of squeezing and anti-squeezing measured experimentally. The shot noise stands as reference (0 dB). For each mode, the red area represents the part of the spectrum not accessible to our Local Oscillator. Top Right : Measurement in the 'flat' mode basis. Down right: A zoom on the necessary spectral range for mode HG20.*

before mixing it with the quantum signal. This is done to spatially match the LO and the signal, effectively decreasing losses in the detection. The signal field from the waveguide and the LO are mixed and directed to separate photodiodes, whose electrical outputs are subtracted to obtain the homodyne signal.

5.3.2 Multimode squeezing measurement

a) Hermite-Gauss modes characterization

Fig. 5.7 summarizes the squeezing values obtained in each of the measured modes, where the shot noise stands as reference (0 dB). The quadrature noise was measured as a function of the relative phase between the signal and the LO, for different LO spectral shapes, via a spectrum analyzer.

We first performed the experiment by projecting the states into the family of Hermite-Gauss (HG) modes. The particular family we used, derived from the numerical simulation performed in Chapter 4, is defined by a fundamental HG_0 mode with 45 nm of FWHM (in amplitude). A complete description of this family can be found in Appendix A. The squeezing values were obtained by averaging 15 maxima/minima over every single Hermite-Gauss mode, performing homodyne detection with a linear phase shift in time via a piezoelectric mirror. The acquisition is monitored by the ascending signal ramp ($\sim$ 300 mHz) applied to the piezo electric such that it always starts with the same phase reference. This detail is especially important for the covariance matrix reconstruction in the next section. One example of squeezing traces is depicted in Fig. 5.8 for the first mode, full data acquistion can be found in Appendix A. The mean squeezing and anti-

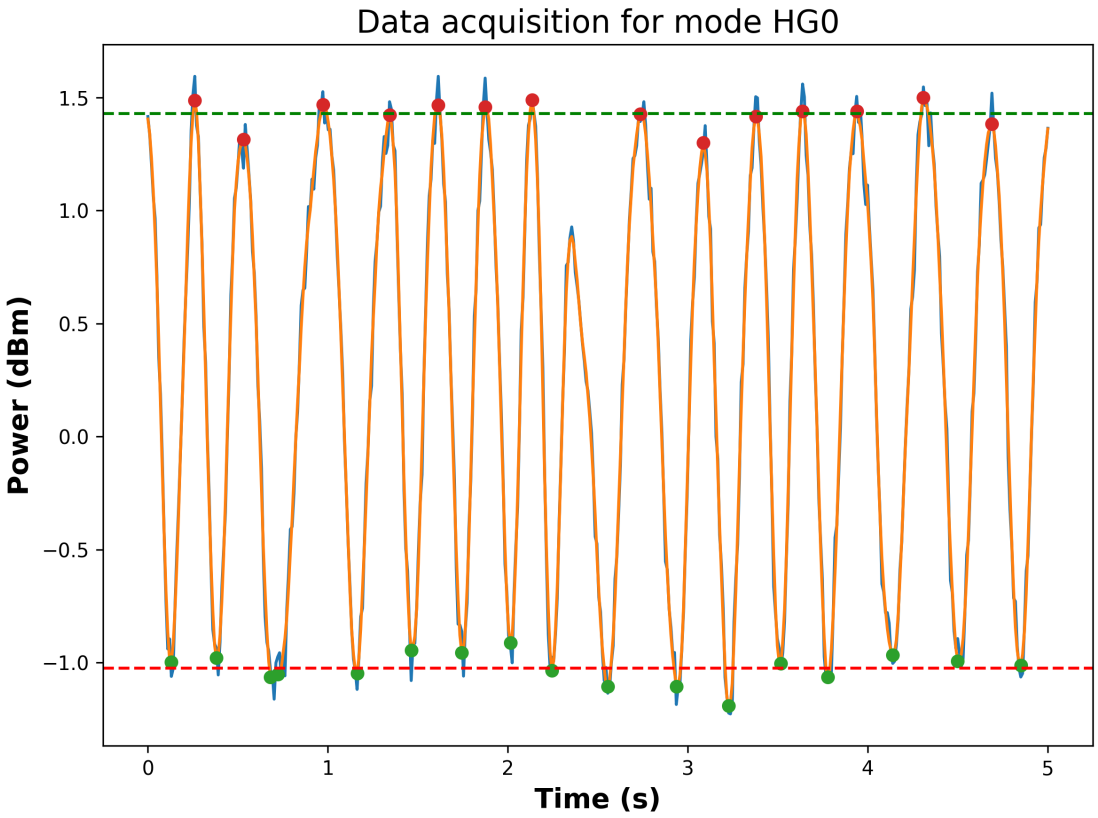

Fig. 5.8 ***Squeezing trace for the projection onto the first Hermite Gauss mode***. *The average squeezing and anti-squeezing values are shown as the dotted red and green horizontal lines. One point is ignored on purpose as the local maxima is due to the piezo electric mirror changing direction.*

squeezing values where computed after applying a Savitsky-Golay filter to smooth the data without distorting the signal and avoiding unwanted local extrema. Typically the local extrema are generated by the piezoelectric mirror when changing direction and so were intentionally ignored. The asymmetry between squeezing and antisqueezing levels (typical values are -1.0 dB for squeezing and 1.4 dB for antisqueezing), is attributed to experimental optical losses. The complete characterization of optical losses is done in the 5.3.3, still we can already highligh that the main loss source is the non-optimal spatial mode-matching between the signal and LO optical modes.

b) The flat-mode basis

Furthermore, we projected the states into a basis of a form of orthogonal and flattened HG modes that we call *flat* modes. For such modes we observed larger squeezing values - with more than 2 dB of squeezing up to the 4th mode - than for the HG modes. The flat modes and their squeezing level are shown in the right side of Fig. 5.7. This result implies that the HG basis shown on the left side of Fig. 5.7 is not the family of supermodes, since those should be the most squeezed modes in the system by definition.

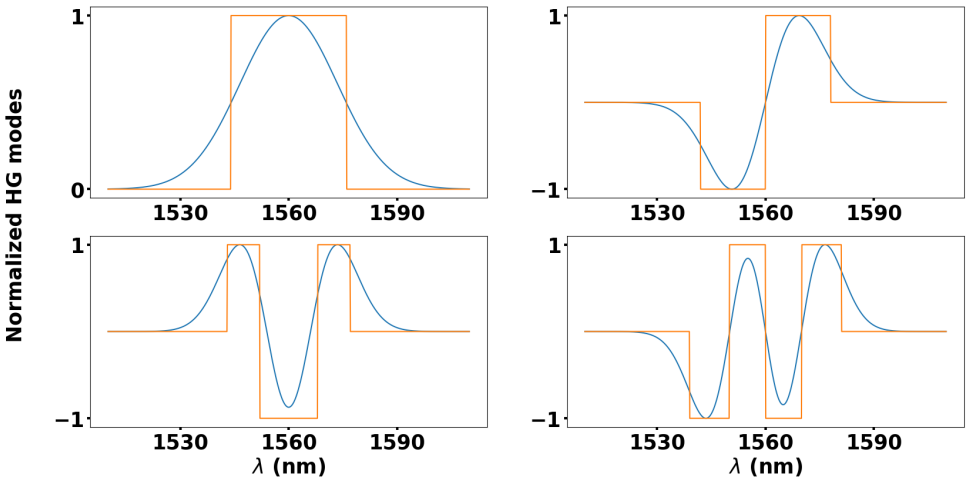

Fig. 5.9 *First 4 Hermite-Gauss modes measured (blue) and the corresponding spectral flat modes (orange).*

The spectral flat mode basis is orthogonal, taking advantage of even and odd symmetries for the subsequent mode functions. It was specifically designed to resemble the first 4 Hermite-Gauss modes, so that the spectral width of each flat mode was obtained by minimizing the l^2 norm distance to the corresponding Hermite-Gauss modes in intensity. Fig. 5.9 shows the 4 flat modes constructed and implemented in the experiment, together with the first 4 Hermite-Gauss modes from the supermode basis.

Further evidence that the tested HG modes are not the family of supermodes is given by the covariance matrix measurements in the next section, showing that the spectral widths of the theoretically predicted HG modes are probably underestimated. We therefore expect that the measured squeezing values in Fig. 5.7 constitute a lower bound for the potential squeezing that can be achieved with larger mode-matching visibilities and without optical clipping. This is also witnessed by the significant asymmetry in the squeezing and antisqueezing values measured in the flat mode basis.

To summarize the above discussion, Fig. 5.7 demonstrates the experimental realization of an optical multimode squeezed state composed of at least 21 frequency modes, with reasonable margin for improvement, and that can be used for quantum information protocols.

c) Optical clipping in the pulse shaper

Fig. 5.7 also shows the spectral shapes set in the LO pulse shaper to measure the corresponding squeezing values. A detrimental effect in our setup is what we call optical clipping, which arises due to the limited size of the cylindrical mirror responsible for focusing the light beam onto the SLM for pulse shaping. Since the beam comes from a refractive element (a grating), some wavelengths at the extremes of the spectrum are therefore cut off. Due to this effect, the LO spectral extremes cannot be used in homodyne detection (the corresponding clipped regions for the different modes are shown in

red in Fig. 5.7).

It means that a perfect spectral overlap between the signal and the LO shaped as one of the supermode is not practically doable at the time of the measurement, but considering the full wavelength range spanned by our laser it should be possible. Moreover this was more evident when considering higher order supermodes, which are known to be broader spectrally.

Due to the optical clipping, the cut HG modes in which we project our state are technically not orthogonal anymore. The dimension of the subspace spanned by the modes shown in Fig. 5.7 is nevertheless close to 21 HG modes. This number depends on the dimensionality of the vector space spanned by the non-orthogonal modes. In order to account for that, we evaluate the rank of the matrix composed by these modes performing a singular value decomposition on the set of 21 vectors. The non-zero singular values count the number of linearly independent modes and hence the dimension of the space we are looking for. The singular values resulting from the decomposition is summarized in Table 5.1. Since this is a numerical computation, we need a somewhat arbitrary criterion

Table 5.1: **Singular values obtained from clipped Hermite-Gauss modes used in the experiment**.

Singular Value	0	1	2	3	4	5	6	7	8	9	10
	1.42	1.40	1.31	1.28	1.21	1.19	1.18	1.12	1.09	1.08	1.02
Singular Value	11	12	13	14	15	16	17	18	19	20	
	0.99	0.97	0.94	0.90	0.84	0.60	0.30	0.08	0.02	0.005	

to give a whole number indicating the dimension of our vector space from this result. In our case, we obtain the dimension of the vector space by accounting for singular values that are at least 10% of the highest one. This criterion gives us 18 linearly independent modes. The value being close to the 21 Hermite-Gauss modes indicates that the optical clipping did not have a large impact in reducing the dimensionality of the modes measured in the experiment.

5.3.3 Practical homodyne measurement

The homodyne measurement was performed with a detector designed and manufactured at C2N[5], including the two photodetectors and the transimpedance circuit outputting the homodyne electrical signal. The total homodyne efficiency, η_{h}, can be calculated following the beam-splitter model developped in Chapter 2.1. It results in the following terms:

$$\eta_{\mathrm{h}} = \eta_{\mathrm{PD}} \cdot \eta_{\mathrm{el}} \cdot \eta_{\mathrm{opt}} \cdot \eta_{\mathrm{mod}}, \tag{5.20}$$

where η_{PD} is the photodetector's efficiency (around 85% in our case), η_{opt} is related to the optical losses in the homodyne circuit ($< 2\%$ in our case), η_{mod} is the mode matching efficiency, *i.e.*, how close are the LO and the signal in terms of polarization, spatial and temporal profile when interfering, and η_{el} is the efficiency associated to the electronic noise. Let's give a bit more detail about the different losses.

[5]Centre for Nanosciences and Nanotechnologies in Paris Saclay.

a) Optical losses on the signal

This stands for all potential losses than can happen before the homodyne detection due to optics imperfections. It is probably the easiest loss to evaluate experimentally, we can take advantage of the seed, more precisely its intensity at the output of the waveguide and compare it with the intensity after all optics before the photodiodes. In our case we limited drastically the optics quantity in that path, thus the near unity result in terms of efficiency mentioned above.

b) Electronic noise

We have seen in 5.1 that an ideal homodyne signal permits, in principle, to measure the quadrature of the signal field $i_{hom}(t) = \alpha(t)\hat{q}_s(t)$ with $\alpha(t)$ being the strong matching mode reference field. We can make a preliminary observation regarding the dependence of the measured quadratures on the mode of the Local Oscillator (LO). In other words, the specific temporal mode that is measured is determined by the mode of the LO. Still this formula stands with the assumption of perfect photodiodes response, free of electronic noise. In practice we model the homodyne signal as :

$$\begin{aligned}\hat{i}_{hom}(t) &= \int_T \hat{I}_e(\tau)\mathrm{d}\tau + \mathcal{R}\int_S \mathrm{d}x\mathrm{d}y \int_T \mathrm{d}\tau r(\tau)\hat{I}(\vec{r}, t-\tau) \\ &= \hat{i}_e + \mathcal{R}\int_S \mathrm{d}x\mathrm{d}y \int_T \mathrm{d}\tau r(\tau)\hat{I}(\vec{r}, t-\tau)\end{aligned} \tag{5.21}$$

where i_e is the electronic noise contribution [6] [Appel et al., 2007]. From Eq.(5.21) we can see the impact of the electronic noise is minimized by raising the power of the local oscillator and the amplifier gain. However, practical possibilities of increasing the gain without proportionally increasing the electronic noise are limited. The Local Oscillator power must also be restricted to avoid saturation of the photodiodes and eliminating the classical noise. The electronic efficiency can be written as [Kumar et al., 2012],

$$\eta_e = 1 - \frac{\langle \hat{i}_e^2 \rangle}{\langle \hat{i}_{hom}^2 \rangle} = 1 - \frac{1}{\mathrm{SNR}} \tag{5.22}$$

with SNR the signal to noise ratio, *i.e.*, the ratio between the shot noise at a certain input intensity and the value in the absence of any input signal (electronic noise). Note that the ability to express the electronic noise as a loss in the setup is a specific property of homodyne detection, in general the electronic noise of a photodetector cannot be expressed in such a simple way. We measured the best Signal-to-Noise Ratio (also called clearance, if one measures it in dB) at a demodulation frequency of 2 MHz, where the clearance C was about 20 dB at 2 mW of input power and is accessed by comparing the electronic spectra in presence and absence of Local Oscillator

$$\mathcal{C} = \frac{S_e(\nu)}{S(\nu)} \tag{5.23}$$

where $S(\nu)$ is defined in 5.1.

[6] Any non-desirable ambient noises, dark current noises from the photodiodes and the intrinsic noise of the amplifiers fall under the umbrella of electronic noise.

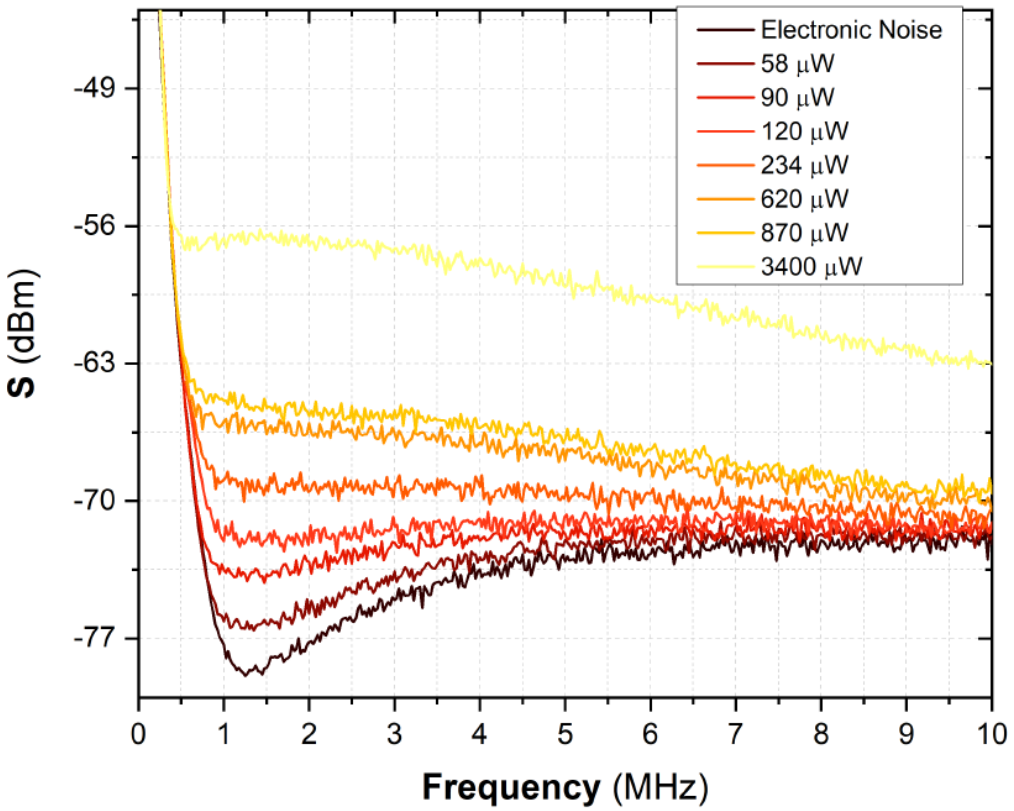

Fig. 5.10 ***Clearance of our homodyne detector***. *Experimental characterization of the homemade balanced homodyne detectors. We progressively increased the LO power until saturation to access the maximum clearance, doublind the power everytime to ensure that the detector response is linear.*

c) Mode-matching efficiency with perfect spectral overlap

The coherence between the signal and Local Oscillator field in such a configuration, which is the one of the measurements in Fig. 5.7, reaches the value of 77%. To evaluate the Coherence we first match our seed with the quantum signal via phase-sensitive amplification technique (described in 5.2.4), maximizing this interaction inside the waveguide sets a reference for the spatial profile, temporal position and polarization. Then we mix the seed and LO (at equal intensity) on the homodyne beam splitter optimizing the horizontal and vertical alignment.

Such value was measured ensuring a perfect overlap between the seed and LO spectra by applying a spectral filter on the seed side (1560 ± 6 nm in FWHM) and a equivalent mask on the pulse shaper. The polarization overlap was compensated using zero-order waveplate on the LO path. The temporal chirp was optimized by applying some chirp on the LO. We thus explain the non-ideal coherence by residual differences between the

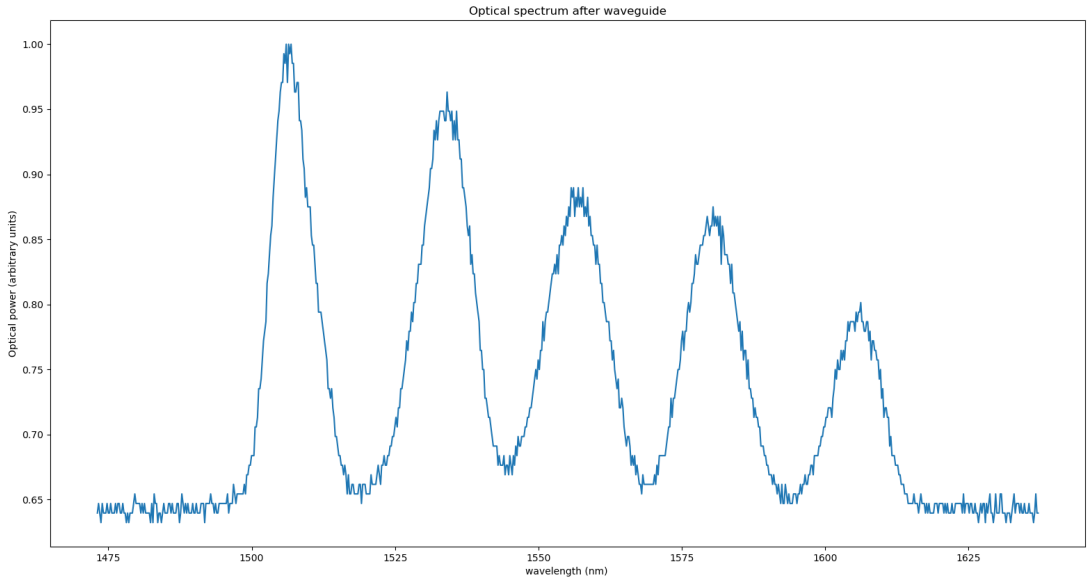

Fig. 5.11 ***Spectral modulation inside the waveguide****. Such effect appears only when the spectral bandwidth of the seed is too large. For example, when we apply a spectral filter of 12 nm on the seed, this modulation is not present anymore.*

spatial modes of the signal and the LO. This can be due to inhomogeneities in the two waveguide structures that are known to appear when the waveguide is long ($\sim$ cm scale) [Brecht, 2014]. In terms of losses, η_{mm} is linked to the coherence Γ by $\eta_{mm} = \Gamma^2$ [Gupta et al., 2020]. By scanning the relative phase between the two coherent pulses we can access the coherence by measuring the maximum and minimum intensity on a photodiode:

$$\Gamma = \frac{I_{max} - I_{min}}{I_{max} + I_{min}} \tag{5.24}$$

We achieved a value above 77%, leading to a mode matching efficiency of $\eta_{mm} \approx 0.6$. It has to be noted that this quantity is in principle mode-dependant, due to the supermode being one another spectrally different, we cannot use this efficiency as a general loss in our setup.

d) Spectral coherence

Without the presence of optical clipping described in 5.3.2 we would then expect larger values for the measured squeezing levels due to a better spectral coherence between the signal and the LO, thus decreasing losses during the measurement process. Another parameter of importance to be solved is what appears to be a modulation of the LO (and seed) spectrum when travelling through the waveguide. An example is given in Fig. 5.11 for the seed who's spectrum before the waveguide was the one of the laser given in Fig. 3.4a. This phenomena still needs to be further investigated. We do not expect

it to be present on the signal side as it appears to be power dependent. One way, for further investigations, could be to use a Spatial Light Modulator on the LO side instead of a waveguide for the spatial mode-matching. Another way could be to confine both the signal and LO inside a fiber to filter the spatial mode, at the expense of substantial losses in the signal path. This later idea is part of the experimental proposition in Chapter 6.

Finally, this modulation makes difficult the investigation on why the flat mode presents a larger squeezing value than the expected HG modes.

5.4 Covariance matrix reconstruction

5.4.1 Reconstruction from homodyne measurement

In this section, we explain the application of homodyne detection (HD) to reconstruct the covariance matrix of a Gaussian quantum state using a specific real mode basis $\{u_k(r,t)\}$ (known as the measurement basis). However, it's important to note that this technique only enables partial recovery of the covariance matrix. In other words, while HD provides valuable information about the quantum state, it does not yield a complete reconstruction of the covariance matrix for the Gaussian state under consideration. Indeed, to use standard homodyne detection for reconstructing the covariance matrix of a Gaussian quantum state, an assumption is necessary, which sets the amplitude-phase (xp) correlation terms of the covariance matrix to zero. Consequently, the off-diagonal blocks of the covariance matrix, which represent correlations between different quadrature components, become effectively zero due to this assumption. Such property was effectively quantified in similar experiment [Cai et al., 2021], making the assumption reasonable.

$$\mathbf{\Sigma}_Q = \begin{pmatrix} \mathbf{\Sigma}_{xx} & \mathbf{\Sigma}_{xp} \\ \mathbf{\Sigma}_{px} & \mathbf{\Sigma}_{pp} \end{pmatrix} = \begin{pmatrix} \mathbf{\Sigma}_{xx} & 0 \\ 0 & \mathbf{\Sigma}_{pp} \end{pmatrix} \tag{5.25}$$

Let's focus on the reconstruction of the xx and pp blocks of the covariance matrix $\mathbf{\Sigma}_Q$ using homodyne measurements. We previously outlined the fundamental principle of homodyne detection in 5.1. When considering a coherent local oscillator (LO) beam in mode $u_k(r,t)$ with an amplitude $\alpha = \sqrt{N_{LO}}e^{i\theta}$, the signal of the subtracted photocurrent can be expressed as follows

$$\hat{i}_{hom}(t) = i_e + \sqrt{N_{LO}}\hat{X}_k(\theta) = i_e + \sqrt{N_{LO}}\left(\hat{X}_k\cos\theta + \hat{P}_k\sin\theta\right) \tag{5.26}$$

The variables $\hat{X}_k$ and $\hat{P}_k$ represent samples obtained from the signal quadratures in mode u_k, while i_e accounts for electronic noise. By conducting a scan of the LO phase with low speed compared to our acquisition speed, we can compute the variance over a rolling window to obtain

$$\Delta^2\hat{X}_k(\theta) = N_{LO}(\cos^2(\theta)\langle\hat{X}_k^2\rangle + \sin^2(\theta)\langle\hat{P}_k^2\rangle + 2\cos(\theta)\sin(\theta)\langle\hat{X}_k\hat{P}_k\rangle) + \langle i_e^2\rangle \tag{5.27}$$

For simplicity of notation and without loss of generality we assume $\langle\hat{X}_k\rangle = \langle\hat{P}_k\rangle = 0$. We can measure the electronic noise (dark noise) and shot noise variance separately by blocking either all inputs or only the signal input to the homodyne detection and using

these measures, calculate the corrected signal variance trace

$$\Delta^2\overline{\hat{X}_k(\theta)} = \frac{\Delta^2\hat{X}_k(\theta) - \langle i_e^2\rangle}{N_{LO}} \tag{5.28}$$

which can be rewritten with the assumption $\langle\hat{X}_k\hat{P}_k\rangle = 0$ in the following form :

$$\Delta^2\overline{\hat{X}_k(\theta)} = \frac{\langle\hat{X}_k^2\rangle + \langle\hat{P}_k^2\rangle}{2} + \cos(2\theta)\frac{\langle\hat{X}_k^2\rangle + \langle\hat{P}_k^2\rangle}{2} \tag{5.29}$$

we easily access the quadratures variances by sum and differences of the amplitude and offset of the homodyne signal directly readable on the spectrum analyzer traces. Repeating the procedure with all the modes $\{u_k(r,t)\}$ we access the diagonal terms of the matrices $\mathbf{\Sigma}_{xx}$ and $\mathbf{\Sigma}_{pp}$.
To reconstruct the non-diagonal terms, we gather homodyne traces where the LO mode is shaped into all possible sums of pairs of modes from the set $\{u_k(r,t)\}$. By shaping the LO mode (using a pulse shaper) into the mode $\frac{u_k+u_{k'}}{2}$, the corrected variance of the signal obtained $\Delta^2\overline{\hat{X}_{k+k'}(\theta)}$. We then directly access the offdiagonal terms of the covariances matrices by :

$$\langle\hat{X}_k\hat{X}_{k'}\rangle = \Delta^2\overline{\hat{X}_{k+k'}} - \frac{\Delta^2\overline{\hat{X}_k} + \Delta^2\overline{\hat{X}_{k'}}}{2} \tag{5.30}$$

with a similar expression for $\langle\hat{P}_k\hat{P}_{k'}\rangle$. Hence using standard homodyne detection it is possible to reconstruct the covariance matrix.

5.4.2 Experimental realization

In order to check the presence of entanglement, *i.e.*, quantum correlations, in our multimode state, we measured the covariance matrix in different basis from the one of the supermodes [Brausntein and van Loock, 2005]. In particular, we used the so-called *frexel* basis, which is composed of a number of equally spaced frequency bands covering the total spectrum of the LO. This is a suitable basis, not only because it is easily accessible via the shaping capability of the LO, but also because the frexel modes can be easily spatially separated via dispersive elements and sent to different locations, which is necessary for multiparty quantum protocols. We therefore measured the covariance matrix that characterizes our gaussian state, in the frexel basis, using 8 equally spaced frequency bands[7].

The covariance matrix is shown in Fig. 5.12. The non-zero off-diagonal elements in the data show the presence of correlations between the frequency bands defining the 8 frexels in our state. This can be associated to the entanglement between the frequency bands that can be tested via the positive partial transpose (PPT) criterion. We obtained violation of the PPT criterion for almost all of the possible bipartitions of our system. Fig. 5.13 shows the PPT value for the different bipartitions of our covariance matrix, showing the violation of the PPT criterion, *i.e.*, negativity in the partial transpose matrix, in 120 bipartitions out of 128 ($\sim 94\%$). More details about the PPT criterion applied to the covariance matrix can be found in chapter 4.

[7] each frexel is about 7nm bandwidth

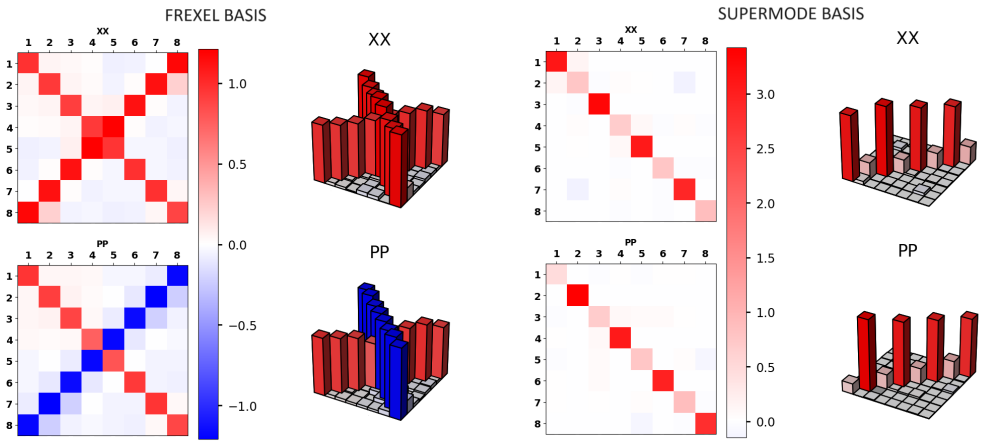

Fig. 5.12 ***Reconstructed covariance matrix.*** *The covariance matrix on the left is obtained by measuring the multimode state in the frexel basis, using 8 frequency bands. On the right, we show a numerical diagonalization of the measured covariance matrix for recovering the squeezed supermodes.*

On the right of Fig. 5.12, we perform a numerical diagonalization of the measured covariance matrix to recover the eigenmode basis, where no entanglement is present. Thus we expect these eigenvectors to resemble discretized versions of the supermodes, with eigenvalues related to a squeezing level value over the frequency band composing the frexel. Overall, the numerical eigenvectors obtained in the diagonalization are in good agreement with the theoretical prediction of approximate Hermite-Gauss modes, except that their spectral widths are larger than the theoretically predicted modes. This is consistent with the measurement of larger squeezing values in the flat modes basis rather than in the theoretically derived HG mode basis, as shown in the previous section.

The numerical diagonalization of the covariance matrix gives back the supermode basis where there are no quantum correlations. We therefore expect the numerical eigenmodes to resemble discretized versions of the quasi-Hermite-Gauss supermodes found in our numerical simulations from theory.

Fig. 5.14 shows the numerical eigenmodes obtained after the diagonalization. In general, the supermode shapes are in very good agreement with the expected theoretical Hermite Gauss modes. The bandwdith of every Hermite-Gauss is systematically higher than the theoretical value, which together with the optical clipping in the pulse shaper and the LO bandwidth could be causing the degradation of the measured squeezed values described in the main text.

On a technical note, the 55 nm bandwidth, in total, of our LO was slightly smaller than the bandwidth of our expected quantum signal. This limits the experimentally accessible modes if the wavelengths outside the LO bandwidth are involved in the spectral features of the supermode. This effect is noticeable for high-order modes, which are the most broadband. In Fig. 5.14, the red area highlights the wavelength range that was not accessible with our LO bandwidth. The necessary bandwidth for a complete evaluation was estimated to around 80nm during the phase sensitive amplification process,

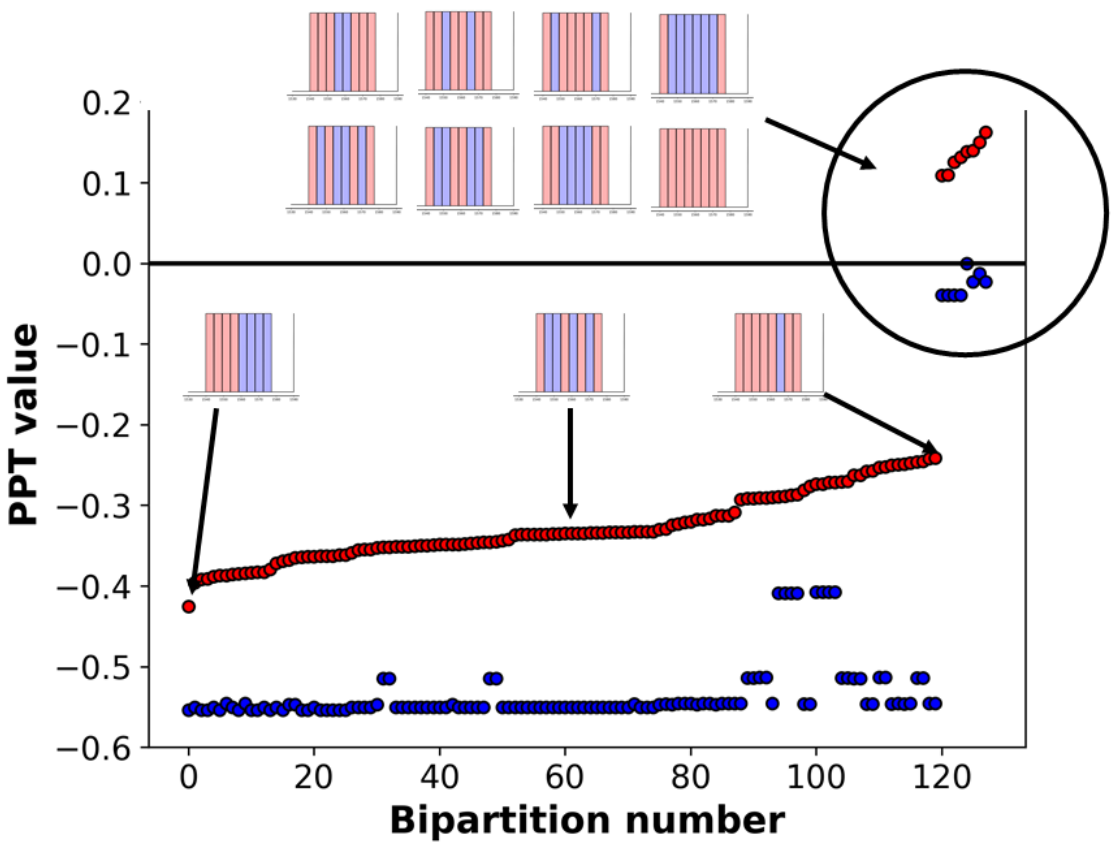

Fig. 5.13 ***PPT values computed for all 127 possible bipartitions.*** *The PPT values from the experimental covariance matrix are in red while the one derived from numerical simulations presented in the last chapter are in blue. The simulated one were reordered to correspond to the experimental one. Overall, it appears that in the presence of losses the curve is shifted up, progressively increasing the number of separable bipartitions.*

see Appendix A.

Note also that the eigenvalues of the covariance matrix are directly related to the expected squeezing levels of each eigenmode. Fig. 5.15 shows the eigenvalues obtained in the diagonalization, which are consistent with those directly measured in the supermode/flatmode basis.

5.5 Cluster state measurement

5.5.1 Measuring cluster states with homodyne detection

In section 5.3.2 we have studied a basis that approximate the supermodes, we denote $\{u_i^{sup}\}_{i=1,2,...}$ this set of modes associated to the corresponding squeezing value $\{\lambda_i\}_{i=1,2...}$. We now want to certify the measurement of cluster state associated to an adjacency matrix A_G. In the introductory chapter we mentioned how the supermodes quadratures

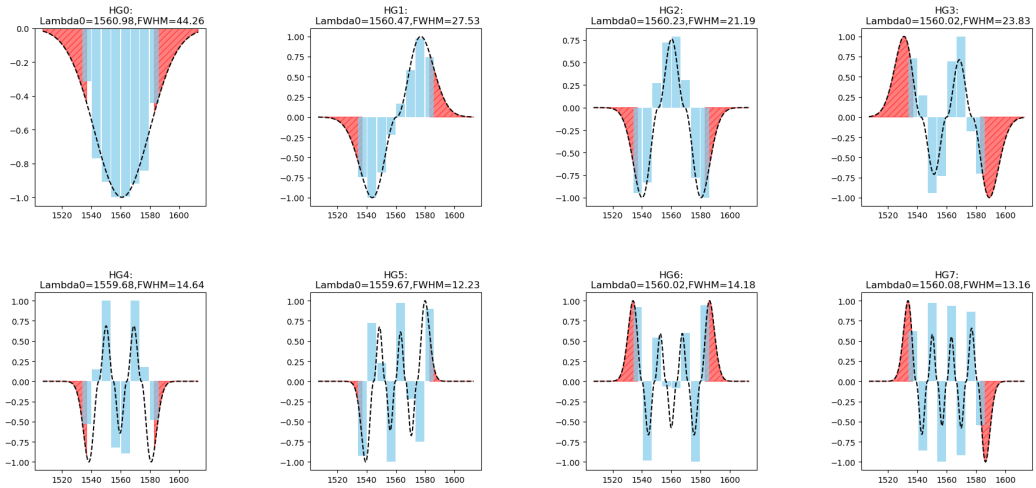

Fig. 5.14 ***Eigenmodes of the covariance matrix*** *The amplitudes of the eight eigenmodes were plotted and fitted with Hermite Gauss functions. The wavelength outside of the Local Oscillator bandwidth was emphasized by marking it with a red hatched area.*

are linked to the quadratures of the cluster state with matrix A_G

$$\vec{\hat{Q}}_G = \begin{pmatrix} X & -Y \\ Y & X \end{pmatrix} \vec{\hat{Q}} \tag{5.31}$$

with

$$\begin{aligned} X &= \left(\mathbb{1} + A_G^2\right)^{-1/2} O \\ Y &= A_G \left(\mathbb{1} + A_G^2\right)^{-1/2} O \end{aligned} \tag{5.32}$$

O being any orthogonal matrix. We also defined the nullifiers $\vec{\hat{\delta}}$ as observables for cluster certification

$$\hat{\delta}_i = \hat{P}_i^G - \sum_j a_{i,j} \hat{X}_j^G \tag{5.33}$$

where $\hat{P}^G$ and $\hat{X}^G$ are denoted this way to highligh that they corresponds to the cluster state quadratures. Combining (5.31) and (5.33) we get

$$\vec{\hat{\delta}} = \begin{pmatrix} -A_G & \mathbb{1} \end{pmatrix} \begin{pmatrix} X & -Y \\ Y & X \end{pmatrix} \vec{\hat{Q}} \tag{5.34}$$

Having a clear relation between the supermode quadratures and the nullifiers permits then to operate the adequate basis change on the supermodes $\{u_i^{sup}\}_{i=1,2,...}$ to build a set of mode $\{w_i^{null}\}_{i=1,2,...}$ to measure directly the different nullifiers. Is is done practically by first computing the cluster modes $\{w_i^c\}_{i=1,2,...}$ using equation (1.95)

$$w^c = (X + iY)\, u^{sup} = (1 - iV)(1 + V^2)^{-1/2} O u^{sup} \tag{5.35}$$

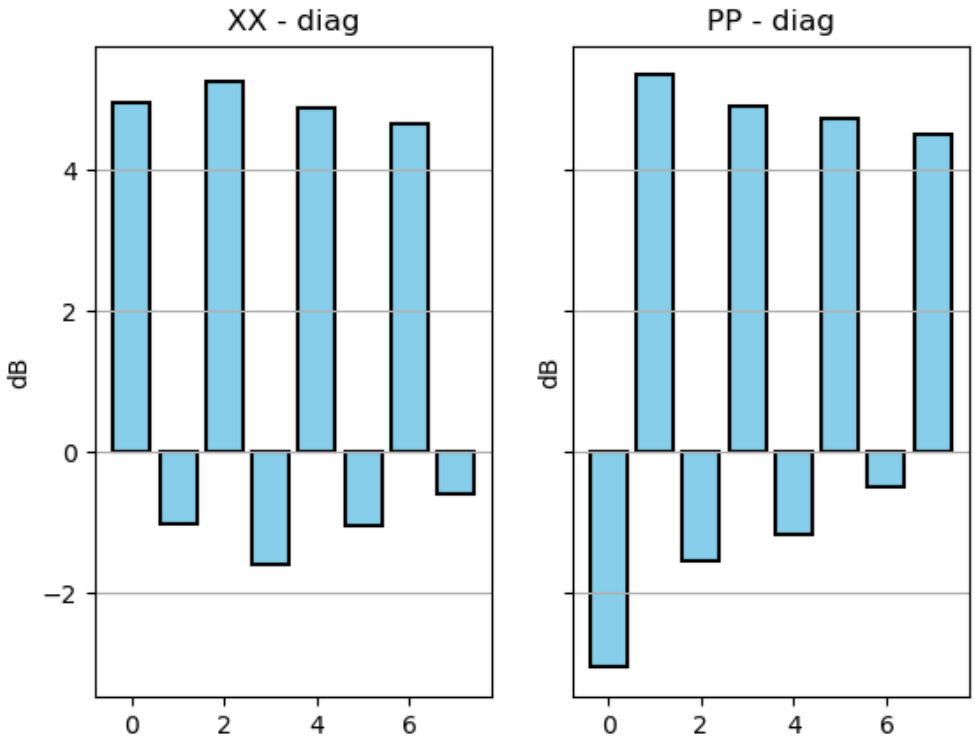

Fig. 5.15 ***Squeezing values obtained from the numerical diagonalization of the covariance matrix in the frequency basis***. *The modes have been arranged in decreasing order of antisqueezed quadratures, and the first eigenmode is squeezed in the $\hat{P}$ quadrature by convention.*

Then we build the nullifiers modes by linear combination on the quadratures of the cluster modes

$$w^{null} = [diag(r_1, r_2, ...)(1 - iV)]^{\dagger}\, w^{c} \tag{5.36}$$

where $r_i = \sqrt{1 + n_i}$ is a normalizing factor linked to the number of nearest neighbout n_i of node i. More details on this can be found in [Dufour, 2018]. Thus from the supermodes, using the reconfigurability of the Local Oscillator via pulse shaping we can directly measure the nullifiers variance.

5.5.2 Experimental results

Finally, we used the experimental setup for the deterministic generation of some few-node cluster states, as a proof of principle on the versatility of the source. We probe the generation of the cluster states by measuring squeezing in the nullifiers that characterize a specific adjacency matrix, *i.e.*, a particular topology defining the graph. Changing from one topology to another can be achieved by appropriately changing the mask on the pulse shaper . Furthermore, the quality of the probed cluster state can be qualitatively

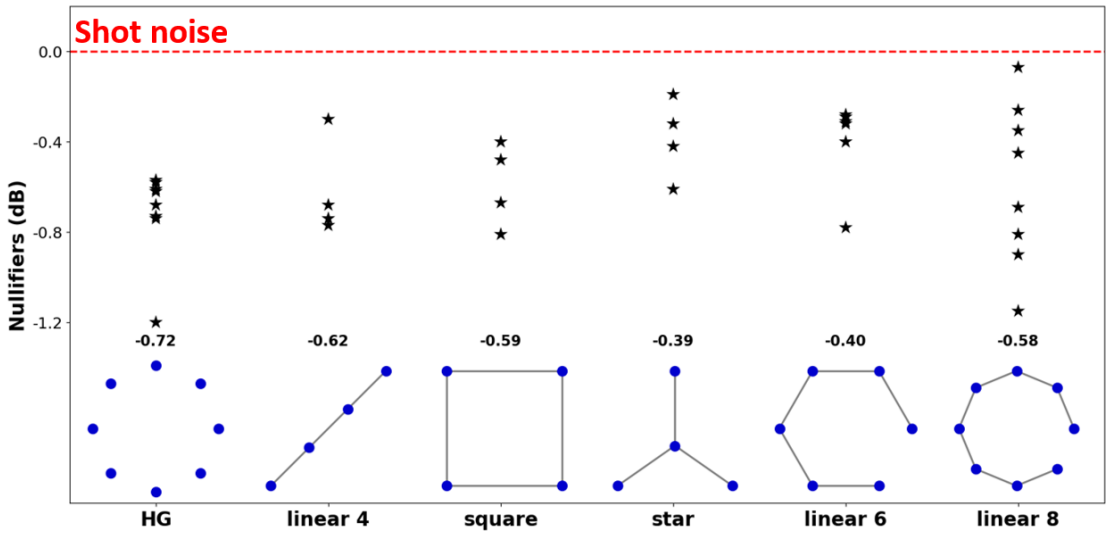

Fig. 5.16 ***Cluster state generation.*** *The maximum squeezing value for the first HG modes and the nullifiers of different cluster state size and topologies. The numerical values indicate the mean nullifiers's squeezing value.*

obtained by the amount of squeezing measured in the nullifiers [Van Loock et al., 2007]. We measured 4-node cluster states with different topologies and whose nullifier's level of squeezing is summarized in Fig. 5.16 for each cluster topology. Additionally, we show that all nullifiers are squeezed below the shot noise up to an 8-mode linear cluster. This test demonstrates the potential for creating cluster states within this setup. To achieve true clusters, access to supermodes would be necessary. This result paves the way for the implementation of continuous variable quantum information protocols at telecommunication wavelengths, with applications in multiparty, entanglement-based quantum communication and computation.

Part III

And they communicated safely ever after

Chapter 6

Frequency-multiplexed continuous variable quantum key distribution

Contents

Continuous Variable Quantum key distribution benefits from cutting-edge technology such as high-speed mode-selective homodyne detection with minimal electronic noise, even under room temperature conditions [Lvovsky and Raymer, 2009]. When combined with the encoding of information into modulated fragile entangled states of light within a continuous-variable framework, it becomes feasible to securely transmit keys across distances of up to 300 kilometers through lossy optical fiber channels [Madsen et al., 2012]. These protocols are more resilient to channel noise and tolerate certain limitations in data processing efficiency compared to protocols using coherent states [Ma et al., 2007]. To further enhance the secret key rate in this setup, one can increase the system clock rates and employ frequency-mode multiplexing of optical transmission channels [Qu and Djordjevic, 2017]. This approach on frequency multiplexing was conducted recently in the discrete variable domain with entangled photons [Appas et al., 2021]. Earlier, it was also demonstrated with continuous variables in a prepare and measure scenario using frequency combs where it is possible to increase the key rate by a factor of 20 with 35 comb lines [Wang et al., 2019]. In Chapter 5, we have implemented an experiment using a source of femtosecond optical pulses entangled in the frequency domain, demonstrating entanglement between eight frequency bands (frexels). Throughout this chapter

we present a protocol for frequency-multiplexed quantum key distribution in continuous variables. Firstly, we study the expected performance of the source via a joint work with Olomouc university based on the results of [Kovalenko et al., 2021]. Then, we propose an experimental setup for the realization of the protocol, specifying the main milestones to achieve. Finally, we propose an extension to a multipartite key distribution protocol.

6.1 Protocol description

We are exploring the use of our spectrally entangled source in a multimode CV QKD experimental setup. This testbed relies on the use of frequency-multiplexed femtosecond light pulses, which include four different frequency bands to begin with. To assess the suitability of this source for QKD purposes, we assume a specific configuration: the lower half of the frequency modes is allocated to Alice, while the upper half is allocated to Bob and sent to him via a multimode lossy Gaussian channel, as shown in Figure 6.1. It is important to emphasize that this division of modes, in the frequency basis, is not implemented yet in the current experimental setup. Spectrally splitting a light beam into two halves can be accomplished using straightforward experimental techniques. For example, it can be done by employing a dispersive element: a grating, a dichroic mirror, or a prism. In Section 6.3, we suggest to use Coarse Wavelength Division Multiplexer (CWDM) [Liu et al., 2016] to achieve the frequency splitting, attempting to show the compatibility of our source with other standard integrated components used in fibered telecommunications. To measure the generated multimode state, we employ once again a mode-selective homodyne detection. We consider a typical scenario in Quantum Key Distribution (QKD). In this scenario:

- We assume that Alice's preparation is trustworthy, meaning it is beyond the control of a potential eavesdropper, Eve. Alice measures her modes locally using a multimode homodyne setup.
- Bob's modes travel directly to his detection setup, where he employs mode-selective homodyne detections, which are also assumed to be trustworthy. This trustworthiness extends the knowledge of parameters as the as detector efficiency and the electronic noise (non-paranoid scenario).

The ability to accurately address individual local modes in homodyne detection is crucial for the multiplexing of channels in Continuous Variable QKD (CV QKD). The multimode structure of entangled states can potentially interfere with protocols if not properly managed [Usenko et al., 2014] as at first it can be used by an eavesdropper as a side-channel. The multimode character of both the sources of entanglement and the homodyne detectors can cause a security breach, even for a perfect channel when trusted parties are unaware of the detection structure

To deliberately investigate the effects of a lossy channel, we introduce attenuation to Bob's measurement results. This emulates an untrusted channel, characterized by its transmittance (T), which is assumed to be under the control of an eavesdropper, Eve, who is capable of carrying out collective attacks. We assume a purely lossy (attenuating) channel for this analysis. This approach is appropriate because in actual optical fiber channels, background noise is already minimal. It allows us to model both fiber-based

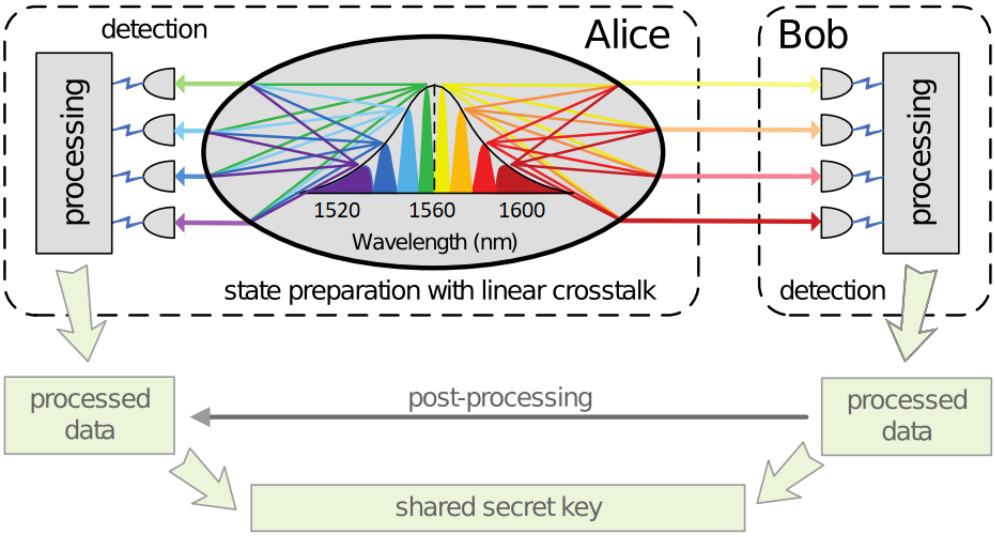

Fig. 6.1 ***Frequency multiplexed QKD scheme***. *The colorful diagram depicts a setup for a Continuous-Variable Quantum Key Distribution (CV QKD) test-bed, focused on examining a multimode entangled source from the perspective of the sender, Alice. In this configuration, there is crosstalk coupling between the frequency modes in both of the two beams originating from the source. The entangled source operates based on eight pairs of modes. Here's how the process unfolds.* ***Mode Distribution:*** *Initially, half of the modes (those below the central frequency) are locally measured by Alice, while the other half (above the central frequency) is transmitted to a remote trusted party, Bob. The trusted devices are represented by dashed blocks in the diagram.* ***Homodyne Detection:*** *Both of the multimode beams, one at Alice's end and the other at Bob's end, are subjected to homodyne detectors. These detectors capture the quantum information contained in the modes.* ***Crosstalk Mitigation:*** *The data from the detectors are processed to optimally eliminate crosstalk between the modes. This processing involves a local physical multimode symplectic transformation, fine-tuned to enhance the secret key rate between the trusted parties.* ***Secure Key Generation:*** *Following successful crosstalk elimination, the trusted parties can employ an authenticated classical channel for post-processing. This post-processing includes error correction and data privacy amplification, which are conducted numerically. The goal is to obtain a quantum-secure key as the final outcome. This part of the protocol, involving post-processing and key generation, is represented in paler colors in the diagram.*

and free-space channels, where fluctuations due to atmospheric turbulence are typically slow compared to the signal repetition rate [Usenko et al., 2012]. While we assume crosstalk happens at the source in line with the experimental test where the multimode source was characterized, the methodology we use, following [Kovalenko et al., 2021], can also address crosstalk within the channel and detectors.

6.2 Expected performances of the source

The security of Continuous Variable Quantum Key Distribution (CV QKD) is assessed by examining the positivity of the lower bound on the key rate, as presented in Chapter 2. Specifically, in scenarios involving collective attacks and reverse reconciliation, this lower bound is expressed by the Devetak-Winter bound:

$$K = \beta I(A,B) - \chi(E,B) \tag{6.1}$$

This approach inherently provides security against general attacks [Renner and Cirac, 2009, Leverrier et al., 2013]. For our analysis of frequency-multiplexed CV QKD, we evaluate the lower bound on the key rate per multimode channel use in the following way. $I(A,B)$ is the classical information between Alice and Bob in $\hat{P}$ quadrature (we chose it because in this experiment it gives larger key than in $\hat{X}$). We then evaluate the classical mutual information between Alice and Bob from the covariance matrix by summing over the classical information channel per channel

$$I(A,B) = \sum_{i=1}^{8} I(A_i, B_i) \tag{6.2}$$

with

$$I(A_i, B_i) = \frac{1}{2}\log_2(1 + \mathrm{SNR}_i) \tag{6.3}$$

The calculation of the Holevo bound is a more complex process and is carried out under the assumption that Eve has the capability to perform a collective measurement on the eight-mode state affected by the attenuating channel. This is akin to the scenario in single-mode Continuous Variable Quantum Key Distribution (CV QKD) where the channel is purely lossy, as presented in Chapter 2. In this context, it is assumed that Eve's vacuum modes, which correspond to the loss experienced in each of the individual modes, are not correlated with each other. This assumption underpins the calculation of the Holevo bound in this scenario. Assuming Eve holds a purification of the state we have

$$\chi(E,B) = S_{AB} - S_{A|B} \tag{6.4}$$

S_{AB} is obtained from the symplectic eigenvalues of the covariance matrix shared between Alice and Bob, Σ_{AB}, using the bosonic entropy function $G(x)$ introduced in Chapter 2. $S_{A|B}$ is conditionned on Bob's measurement and it is also computed as in (2.31). From the covariance matrices acquired in Chapter 5 we can then compute the expected key rate as a function of the channel loss; the results are shown in Figure 6.2a. Another interesting figure of merit is the key rate achievable per channel, as shown in Figure 6.2b, which already exhibits an improvement of the key rate by a factor 3 with 4 frequency bands. The results are presented in bits/symbol, the total rate achievable in bits/s is then given by multiplying this quantity by the repetition rate of our laser, which is 100 MHz.

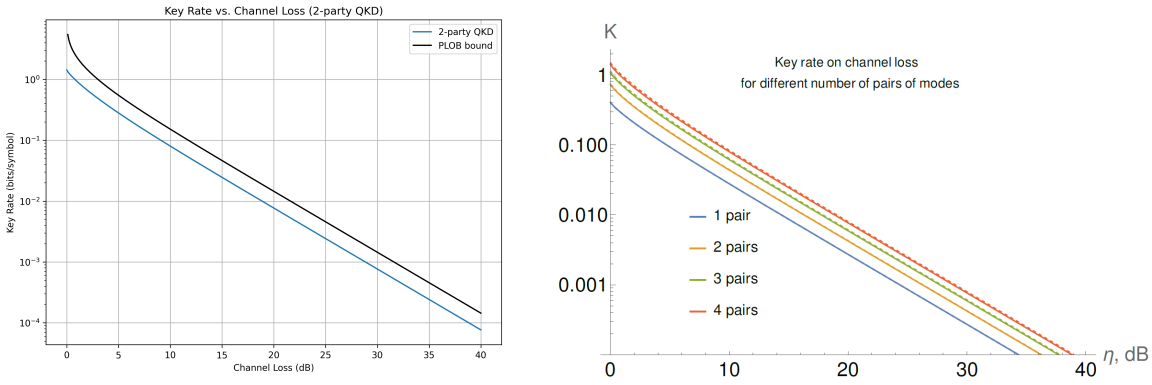

(a) (b)

Fig. 6.2 *(a)* ***Expected total key rate****. The key rate (in blue) is achieved with 4 pairs and compared to the PLOB bound (in black). (b)* ***Scaling of the key rate****. The key rate is presented as a function of the number of channels.*

6.3 Proposal for experimental realization

6.3.1 Overview the experimental setup

The purpose of this section is to move from the model to an actual experimental implementation of the protocol. As presented in Chapter 5, the current experiment is conducted in free-space. To efficiently separate the different users in space to a few kilometers without introducing too much loss, the most natural approach, given that we are working at the telecom wavelengths, is to use fibers. Furthermore the spectral bandwidth of the signal state is centered at 1560 nm, which is compatible with the standard communication bands of Coarse Wavelength Division Multiplexers (CWDMs), typically 1530, 1550, 1570 and 1590 +/- 13 nm. It appears that the splitting using off-the-shelf fibered components is then doable. We propose in Figure 6.3 an experimental implementation of the protocol using fibered components only. For the sake of readability, only one of the frequency band path is shown, but we expect to implement a similar setup on all arms. Each arms of the Local Oscillator side includes the essential components for mode-matchings issues at the homodyne detection. If such fiber-based approach was to fail, because of high insertion loss even without lossy connectors (i.e. via direct splicing of the fiber components), it would be possible to keep a full free-space approach for a first implementation.

6.3.2 Technological barriers

If we go deeper into the experimental implementation, we need to visualize not only the optics on the table but also all equipment surounding us and helping toward the key establishment. For such an experiment to happen on the D-day a few technological barriers will have to be overcome. The list we make here is probably not exhaustive, and further investigation will be carried out depending on the elements chosen in the final implementation.

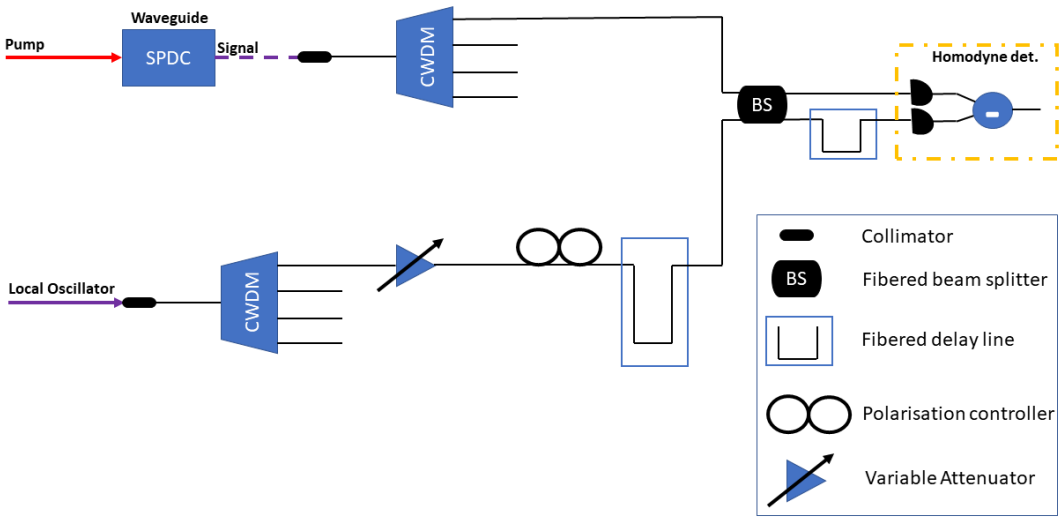

Fig. 6.3 ***Experimental implementation proposal.*** *Scheme of the setup, where both the telecom quantum source and the Local Oscillator for homodyne detection are frequency multiplexed via CWDM. Couple of LO and signal frequency bands will be sent in different locations where homodyne detection will be performed. (Only one of the 4 homodyne setups is shown in the scheme)*

a) Ultrafast homodyne detection

One critical point for the protocol implementation is to transition from measuring sideband squeezing to effectively measuring the quadratures of the field pulse-by-pulse. Overall, the detection system is crucial; in [Laudenbach et al., 2018], the detection noise makes up about 60% of the total excess noise. The pulsed regime is not trivial as it requires the development of a sufficiently fast homodyne detection, meaning able to resolve the quantum signal of a pulse with enough clearance at $f_{\text{rep}} = 100$ MHz and with a good Common Mode Rejection Ratio (CMRR). The CMRR assesses how well the device can filter out the typical noise from the Local Oscillator. This is especially crucial when dealing with pulsed scenarios, as a low CMRR, indicating ineffective noise reduction, can lead to the signal being mixed with the pulse's repetition frequency and its harmonics, causing contamination. In a perfectly balanced homodyne detection, we want the output voltage to be a function of the voltages output by each photodiode

$$V_{hom} = \mathcal{G}(V_+ - V_-). \tag{6.5}$$

In pratice, the electric response of each photodiode (Common mode) is never perfectly identical even when adjusting the photodiode temporal response by acting on their bias. Thus, the real homodyne photocurrent is

$$V_{hom} = \mathcal{G}(V_+ - V_-) + \mathcal{G}_{cm}(V_+ + V_-) \tag{6.6}$$

where $\mathcal{G}_{cm}(V_+ + V_-)$ is a contribution from both photodiode due to imperfect cancelling of the photocurrent. The CMRR is then mathematically defined as the ratio between the homodyne gain when both photodiode are illuminated and the common mode gain (obtained when only one photodiode is illuminated). It is usually expressed in dB as follow

$$\mathrm{CMRR} = 10\log_{10}\left(\frac{\mathcal{G}}{\mathcal{G}_{cm}}\right) \tag{6.7}$$

Such development was undertaken for a similar experiment in [Kouadou, 2021] and resulted in a pulse-by-pulse measurement, as reported in [Kouadou et al., 2023]. A comparable unit was constructed and characterized for our setup, achieving approximately 14 dB of clearance at 100 MHz with a continuous-wave (CW) laser and over 45 dB of Common Mode Rejection Ratio (CMRR)[1] with a pulsed laser. However, unexpected saturation of the electronic circuit occurs in the pulsed regime and still needs to be addressed by adjusting the component selection of the electronic card.

b) Cross-talk mitigation

Multiplexed modes tend to interfere with each other either at the source or elsewhere in the protocol, resulting in crosstalk, which can severely diminish the gain. For example an imperfect spectral splitting of the source can generate cross-talks when the different frequency bands are overlapping. Fortunately, proper data processing techniques of homodyne data offer a solution. This advantage distinguishes CV protocols from those using single-photon detectors, which lack the capability for similar data processing methods. We still have to evaluate such cross-talks for commercial demultiplexers, but the effect was evaluated and corrected in a previous experiment where the splitting was done at a multipixel homodyne detection. This multipixel homodyne detection [Thiel, 2015] is built using a grating and set of microlenses focusing the different frequency bands to different photodiodes. During this process, some crosstalks naturally appeared. However, it is possible to offset some of this cross-talk by applying a comprehensive symplectic transformation that optimizes the mutual information. Unfortunately, in the context of quantum communication, implementing such a global transformation is not possible. Still, we can make significant strides in reducing the cross-talk by having Alice and Bob each carry out independent local operations. Both Alice and Bob have control over some modes within the shared state. They can introduce specific linear, passive operations on their respective sides to minimize cross-talk while ensuring the security of the protocol. To achieve this, we actively seek for two local symplectic transformation matrices that can effectively function as a series of linear optical devices. It is important to note that there is no need to maximize the key rate, as unitary transformations do not affect the Holevo bound (the von Neumann entropy of the states is preserved). Therefore, maximizing the mutual information suffices. The key rate before and after the optimization are visualized in Figure 6.4, with the raw data acquired in Chapter 5. Compared to previous application of this optimization protocol on similar experiments [Cai et al., 2017,Kovalenko et al., 2021], this time the improvement is not significant. This is essentially due to the reconstruction of the covariance matrix in Chapter 5, which was done with a single homodyne detector and with frexels that did not overlap, limiting crosstalks during the acquisition. The

[1] In the pulsed regime, a good CMRR should be in the order of 30 dB.

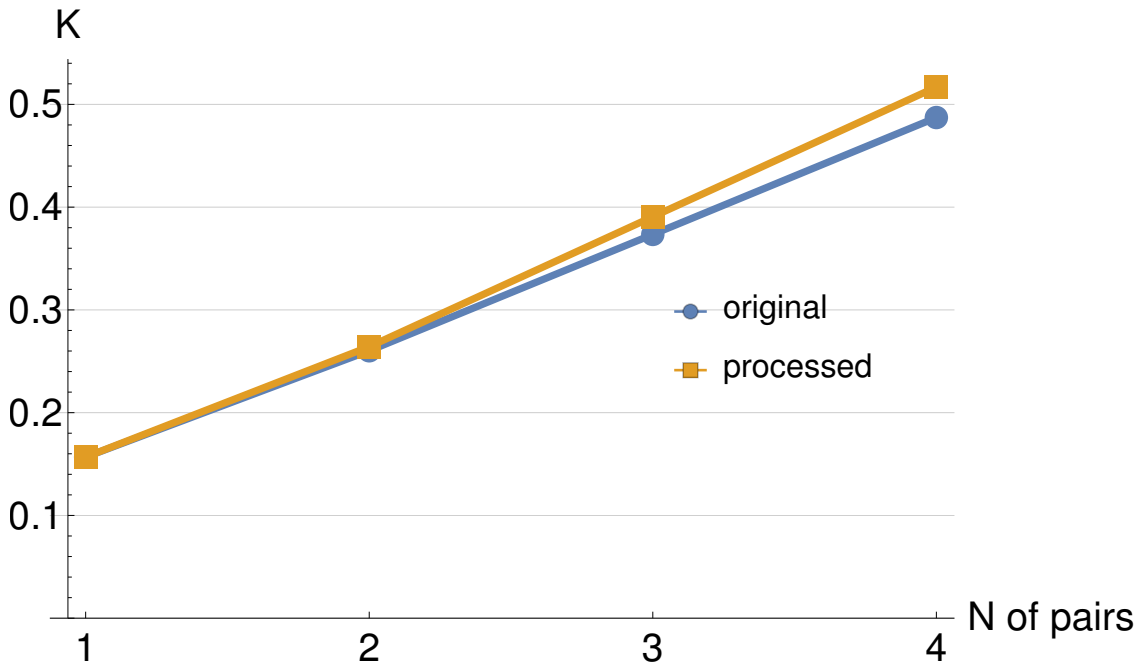

Fig. 6.4 ***Key rate before and after crosstalk processing***. *For this optimization, the limited memory Broyden–Fletcher–Goldfarb–Shannon (l-BGFS) optimization algorithm with bound constraints from the SciPy library was used.*

matrix representing the optimized interaction is determined during the parameter estimation step of the Quantum Key Distribution (QKD) protocol, relying on the estimation of the state shared between the trusted parties in terms of its covariance matrix [Leverrier, 2015]. This optimization can be performed on either the sender or the receiver side and then made public. Importantly, the optimization parameters are unrelated to the raw key data, eliminating the need for further disclosure or discarding of key bits. The knowledge of the optimized interaction by a potential eavesdropper does not affect the security of the protocol because the security proof already assumes that the eavesdropper can perform an optimal collective measurement on the intercepted signal [Grosshans, 2005]. Moreover, the Holevo bound is not influenced by the linear interactions between the signal modes on the trusted sides, as the Von Neuman Entropy is not.

c) Optical phase-locking and Digital Signal Processing

To effectively detect the quantum signal, it is essential to have a precise understanding of the relative phase and frequency of the transmitter signal and the Local Oscillator. Otherwise it has an impact on the quadrature measurement $\hat{X}(\theta)$ that is phase-dependent. Additionally, the transmitter laser introduces some phase noise, denoted as $\delta\theta$. In experiments involving both a SPDC process and a homodyne detection we simultaneously lock the seed with the signal and the Local Oscillator. The signal-seed lock is done using the phase-sensitive amplification signal on the filtered pump at the output of the waveguide.

This might not be sufficient in pratice as when multiplexing the different frequency bands inside the signal will follow different optical paths. Another approach can be the use of a "local" Local oscillator [Qi et al., 2015, Soh et al., 2015, Kleis et al., 2017, Suleiman et al., 2022]. In such case, both this phase-noise and any phase differences between the signal laser and Local Oscillator can be corrected by using a strong reference signal sent by Alice, referred to as the *pilot tone*. This pilot tone maintains a well-known phase, denoted as ωt. Bob employs double homodyne detection to measure the X- and P-quadrature of the pilot tone. By making these measurements at a rate of exactly ω, he can determine any deviations from a fixed and temporarily constant reference phase. Any measured deviation from this reference phase is utilized to make the necessary adjustments to the measured phase of the quantum signal. Nevertheless, this pilot tone leads to heavy digital signal processing in the reconciliation step [Trigo Vidarte, 2019, Roumestan, 2022]. In the reconciliation process, error correction is usually carried out using low-density parity-check (LDPC) codes. Establishing such protocols will be part of a joint effort with the team of Eleni Diamanti in Laboratoire d'Informatique de Paris 6 (LIP6, Sorbonne Université).

d) Real-time data acquisition

From an operational point of view, our oscilloscope (a Teledyne LeCroy WaveRunner 8108HD) should be able to provide a sufficiently accurate measurement for the experimental demonstration. The bandwidth of 1 GHz is, in fact, 10 times larger than the repetition rate, thus the signal should not be distorted. Moreover the sampling rate[2] of 10 GS/s and the 12 bits vertical resolution are more than enough for an accurate measurement. Yet, real-time processing requires an advanced triggering system to be setup. Finally, efficient data storage should be considered for efficient data post-processing.

6.4 Extension to Multipartite key distribution

In Section. 6.2 we presented the total key rate achievable as a function of the channel loss as well as the key rate achievable per frequency channels, see Figure 6.2. It appears that the key rate is nearly proportionnal to the number of channels, thus we can exploit the source not only as a test-bed for frequency-multiplexed QKD (between two users only) but also as a resource to share a key with several users in a multipartite scenario. Practically such protocol does not necessitate more resource in the experimental setup. It mainly requires to attribute the detectors to the different users as in Figure 6.5. The key rate computation is then slightly more subtle to derive, depending on the trust given or not to the other users. Assuming first all users can be trusted, then the key rate for each users i is derived the following way

$$K = \beta I(A, B_i) - \chi(E|B_i) \tag{6.8}$$

In the condition where the other users can't be trusted we need to take into account the potential knowledge on the Key acquired by Eve through other users i.e.

$$K = \beta I(A, B_i) - \chi(E|B_i \text{ for all } i) \tag{6.9}$$

A comprehensive comparision between the two scenario is given in Figure 6.6. Demon-

[2] In Sample per second

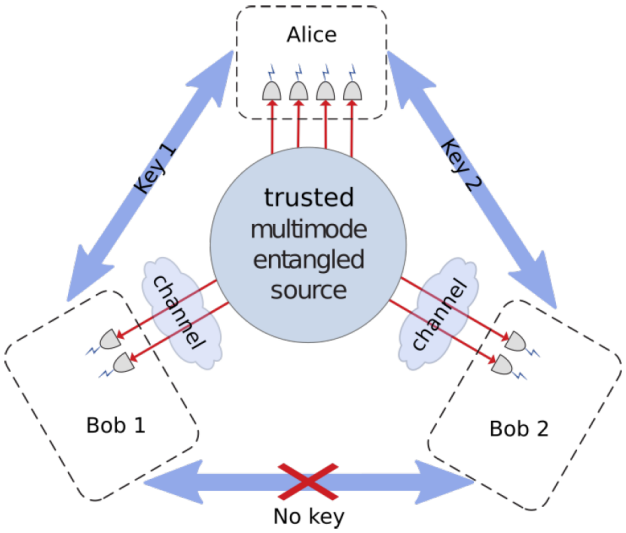

Fig. 6.5 ***Scheme in a 3-party scenario.***

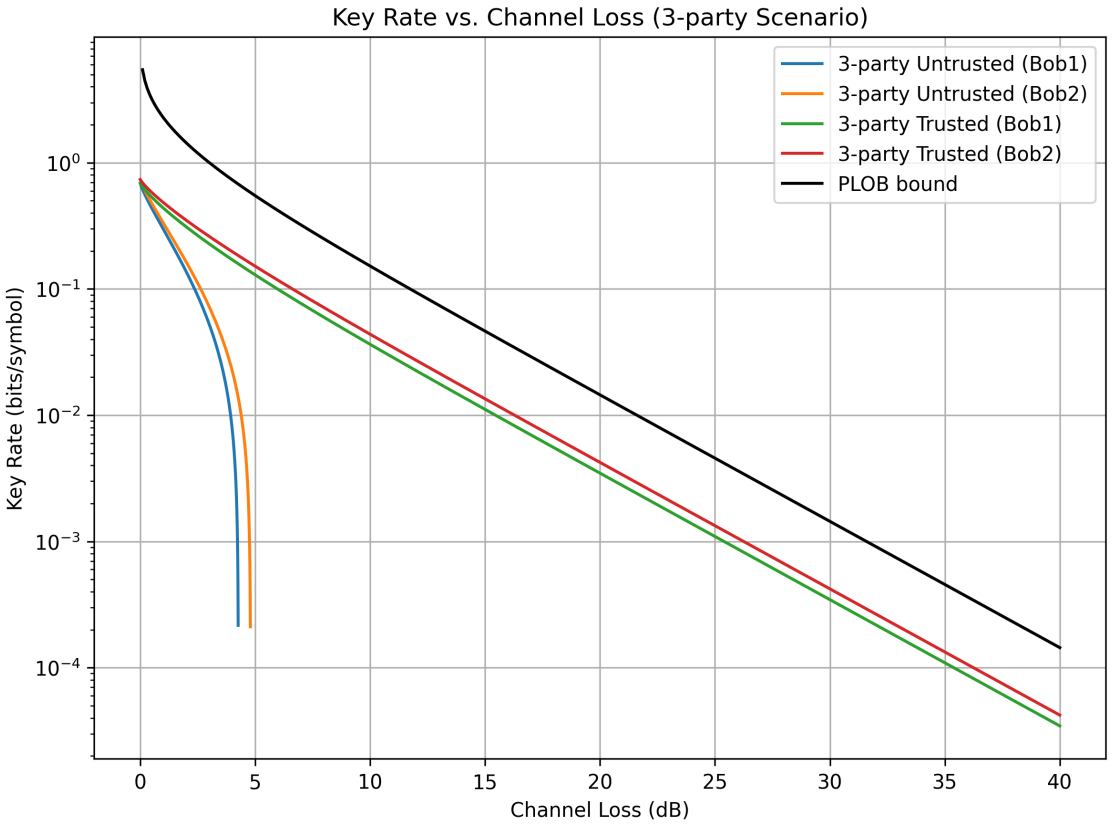

Fig. 6.6 ***Key rate in a 3-party scenario.*** *A comparision is given between two situations were the other parties can be considered as trusted or not.*

strations of multipartite cryptographic protocols are nowadays limited in the number of participants (4 in general), the source we designed can expect to perform some protocols with more than 30[3] simultaneous users at the metropolitan level.

[3]Due to the numerically simulated schmidt number to be K=34.

Chapter 7

Quantum Routing in Multipartite Complex Networks

Contents

The purpose of this chapter is now to extend our work to larger cluster states, approaching real world quantum networks. This almost started with a *Gedankenexperiment*. If a quantum internet [Kimble, 2008] should exist with continuous variable states, what should it look like? Should it mimic the classical internet in terms of architecture, or is

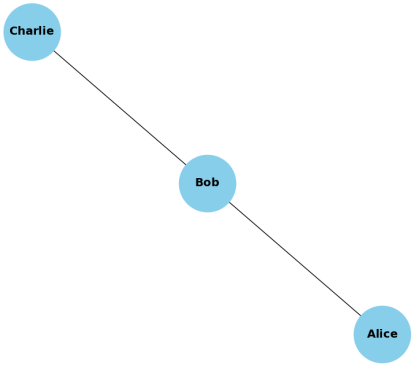

Fig. 7.1 ***A basic social network***. *Graphic representation of a social network, Alice and Charlie know Bob without knowing each other.*

there a better way to implement such a network? Let's approach this problem through the framework of quantum routing. Routing involves reshaping the network to coordinate information transfer. In the case of a quantum network, the easiest way to transfer information is via a teleportation protocol (described in Chapter 2). Our exploration of quantum routing will then begin by extracting an EPR pair between two selected nodes from a large network. This work builds upon the efforts in [Sansavini and Parigi, 2019]. I dedicated considerable time to improving the derandomized evolution algorithm, aiming to explore larger network topologies (>100 nodes). The goal was to study networks large enough to effectively outline their main properties, such as small-world characteristics and clustering. Along with the assistance of Ilya Karuscheik (PhD student in the group) and Antoine Debray (intern), we initiated an analytical approach to the problem on a small cluster state. Antoine and I also worked on running a large number of simulations with the algorithm. A recent development opens new perspectives on what appears to be a more general no-go theorem toward the extraction of a *perfect EPR pair*[1] from a cluster state.

7.1 Introduction to complex quantum networks

7.1.1 Quantum networks

A network represents a group, a system of interconnected agents who interact with one another. Complex networks describe a wide range of systems in nature and society, from the internet [Elmokashfi et al., 2010] and the world-wide web [Barabási and Albert, 1999] to brain connections [Sporns, 2011] and protein-protein interactions [Ispolatov et al., 2005]. It is usual to mathematically represent a network with a graph where the vertices are the agents of our system, and the edges represent the links between them (see Fig 7.1). In the case of continuous variable quantum networks, as introduced with cluster states, agents are modes of the electromagnetic field, and connections represent non-classical correlations (entanglement) between their quadratures. In Chapter 5, we demonstrated

[1] Maximally entangled state allowed by the level of squeezing used to build the cluster state

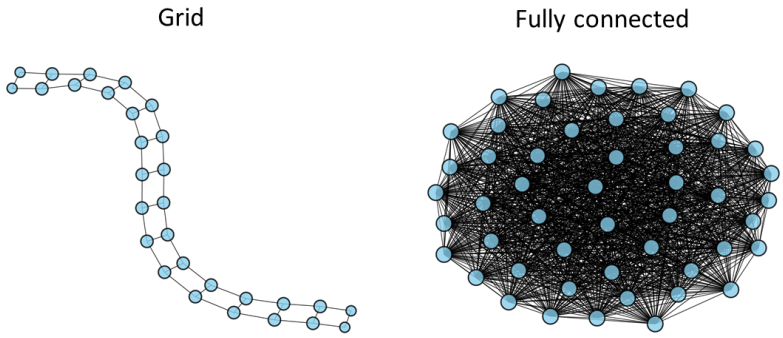

Fig. 7.2 ***Deterministic topologies used in this manuscript***. *On the left a grid network, Alice owns all the upper nodes. On the right, a fully connected network.*

how it was possible to experimentally produce and measure such a state with a limited number of modes. We now take more interest in the topologies that can be scaled up in terms of nodes. In particular, fully connected networks and rail cluster states are of interest for us as they have already been studied for quantum information protocols [Yokoyama et al., 2013a, Asavanant et al., 2019, Larsen et al., 2019, Arzani et al., 2019].

7.1.2 Toward real world complex networks

So far through this manuscript we took interest only in regular and deterministic networks i.e. networks with a completely determined adjacency matrix by a pattern repeting itself in space. In Chapter 5 for example, we studied some networks with linear, star or square shapes. In the context of quantum routing, we present some results based on deterministic topologies such as grid networks or fully connected networks, see Fig. 7.2. Moreover, we now model some probabilistics networks, beginning with fully random networks and gradually exploring the world of complex networks.

a) Random networks : the Erdos-Renyi model

Among all possibilities to generate networks, using probabilistic laws for building edges permits the generation of a wide range of networks, all linked by one randomness parameter. In the Erdos-Renyi model, we take interest in random networks $G_{N,n}$ where n is the number of vertices and N is the number of edges [Erdös and Rényi, 1959]. The N edges are chosen at random among the $\binom{n}{2}$ possible choices, leading to one network amid the $\binom{\binom{n}{2}}{N}$ possibilities. In modern approaches, random networks are built with a wiring probability $p \in [0, 1]$. For instance, a random network $G_{p=0.25,n=50}$ is represented in Fig. 7.3.

b) Small-world and the Watts-Strogatz model

The Watts-Strogatz networks, denoted as $G_{p,N,n}$, aim at exploring regions in-between regular and random networks, revealing new important properties such as clustering and

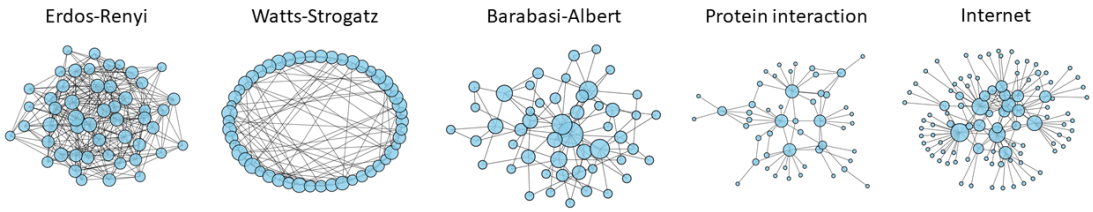

Fig. 7.3 ***Random and complex topologies used in this manuscript.*** *From left to right : An Erdos-Renyi network $G_{0.25,50}$. A Watts-Strogatz network $G_{0.4,6,50}$. A Barabasi-Albert network $G_{2,50}$. A Protein-protein interaction network $G_{2,50}$. A network resembling the Internet Autonomous System G_{100}.*

path length [Watts and Strogatz, 1998]. The model begins with a regular network having a ring shape, where each node has the same number of edges. Subsequently, each edge is rewired with a random probability p, leading to the first approach of small-world within networks. An example of such a network with 50 nodes, 6 links, and a rewiring probability of 0.4 is depicted in Fig. 7.3.

c) Scaling in random networks via Barabasi-Albert models

Some systems, such as the World Wide Web or social networks, cannot be accurately described by static models due to their dynamic properties, constantly adding new nodes to the network and growing bigger. Barabási and Albert addressed this challenge through the scaling construction of networks [Barabási and Albert, 1999]. In their model, new nodes are added one after the other, and their probability to get linked to another node depends on the current number of links that those nodes already have, forming what is commonly known as a power law distribution. In essence, the higher a node is connected, the higher is the probability for a new node created to connect to it. The parameter of interest, denoted as m_{BA}, represents the number of edges to attach from a new node to existing nodes. Barabasi-Albert networks played a pivotal role in the development of the field of complex networks. Over the years, these models have become increasingly accurate in describing a wide range of complex networks of interest, such as the brain, the Internet, or Protein-Protein interaction networks [Barabási and Pósfai, 2016,Newman, 2018].

7.2 Routing in quantum network

7.2.1 Context

There is not only one approach to quantum routing, when we want to extract an EPR pair from a network state a possible mechanism is based on measurement protocols [Centrone et al., 2023]. Indeed, [Gu et al., 2009] proposes two fundamental rules for quadrature measurements in a Gaussian network:

- **Vertex Removal**: A $\hat{X}$-measurement on a mode results in the removal of that

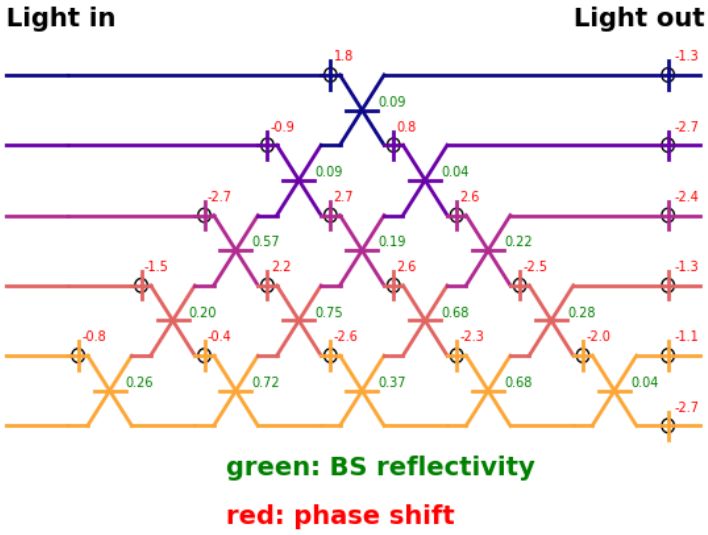

Fig. 7.4 ***Example of unitary decomposed in a multiport interferometer.***

mode from the network, along with all connecting edges.

- **Wire Shortening**: A $\hat{P}$-measurement on a mode is equivalent to a $\hat{X}$-measurement following a Fourier transform, corresponding to a phase rotation of $\pi/2$. While the node is removed, the phase shift induces correlations among neighboring edges. Therefore, momentum basis measurements effectively shorten linear graph states.

These rules can be understood utilizing the graphical calculus introduced by [Menicucci et al., 2011] as well. Another point of view rely on passive symplectic transformations on the mode quadratures [Sansavini and Parigi, 2019], this will be our approach. A less restrictive approach allowing all symplectic transformations (online squeezing included) was studied in [Zhang et al., 2009].

The main interest of our work is the capability to easily couple such theoretical result to a practical implementation. First, the passive symplectic (unitary transformation) found for Alice and Bob can be efficiently implemented via multiport interferometers [Clements et al., 2016]. In Fig 7.4 an example of such decomposition is given for $n = 6$. Such decomposition permits also to follow the covariance matrix evolution along the routing process, beam splitters after beam splitters as shown in Fig 7.4. After this step, the EPR pair is extracted with minimal loss and the teleportation can be implemented. Note that these two approaches, measurement based and via symplectic transformations, are complementary and nothing prevent to combine them in the future.

7.2.2 Global and Local transformation

Suppose we have access to all the nodes of a network state $|G_A\rangle$ and would like to rewire it completely to $|G_B\rangle$. Applying a global transformation on a cluster to switch from $|G_A\rangle$ to $|G_B\rangle$ is nearly trivial knowing how to build them via symplectic transformation,S_A and S_B, on vacuum squeezed states $(\hat{X}_s, \hat{P}_s)$.

$$\begin{pmatrix} \hat{X}_c^A \\ \hat{P}_c^A \end{pmatrix} = S_A \begin{pmatrix} \hat{X}_s \\ \hat{P}_s \end{pmatrix} \quad \begin{pmatrix} \hat{X}_c^B \\ \hat{P}_c^B \end{pmatrix} = S_B \begin{pmatrix} \hat{X}_s \\ \hat{P}_s \end{pmatrix} \tag{7.1}$$

The symplectic group structure allow then us to define $S = S_B S_A^{-1}$ and thus

$$\begin{pmatrix} \hat{X}_c^B \\ \hat{P}_c^B \end{pmatrix} = S \begin{pmatrix} \hat{X}_c^A \\ \hat{P}_c^A \end{pmatrix} \tag{7.2}$$

It is always possible, given a cluster, to implement a global transformation on it with the aim of creating an EPR channel out of two given nodes. Now let's try a more realistic communication scenario. We imagine to distribute the modes of the cluster to two spatially separated parties, Alice and Bob, such that each party is allowed to perform local linear optical transformations only on its set of nodes. This scenario is interesting because we want to check the versatility of a complex cluster as a resource to distribute, with the hope that it could be easily re-shaped according to the protocol the two parties would like to perform. Say n and p are the number of nodes of Alice and Bob respectively. Let's imagine we want to act with a local linear optical transformation S_{n_local} on the n modes of Alice and with a local linear optical transformation S_{p_local} on the p modes of Bob, namely

$$S_{n\_local} = \begin{pmatrix} X_1 & Y_1 \\ -Y_1 & X_1 \end{pmatrix} \quad S_{p\_local} = \begin{pmatrix} X_2 & Y_2 \\ -Y_2 & X_2 \end{pmatrix} \tag{7.3}$$

where X_1 and Y_1 are $n \times n$ matrices while X_2 and Y_2 are $p \times p$ matrices. The transformation acting on the whole set of modes then reads

$$S = \begin{pmatrix} X_1 & 0 & -Y_1 & 0 \\ 0 & X_2 & 0 & -Y_2 \\ Y_1 & 0 & X_1 & 0 \\ 0 & Y_2 & 0 & X_2 \end{pmatrix} \tag{7.4}$$

where the 0 on the first and third line represents a $n \times p$ null matrix while the 0 on the second and fourth line represents a $p \times n$ null matrix. We already saw in Chapter 1 that a linear transformation on the quadrature operators corresponds to a unitary operator $U = X + iY$ acting on the annihilation operators. We can thus rewrite the last matrix in terms of the unitary matrices as

$$S = \begin{pmatrix} Re(U_1) & 0 & -Im(U_1) & 0 \\ 0 & Re(U_2) & 0 & -Im(U_2) \\ Im(U_1) & 0 & Re(U_1) & 0 \\ 0 & Im(U_2) & 0 & Re(U_2) \end{pmatrix} \tag{7.5}$$

where U_1 and U_2 are two unitary matrices parametrized respectively by n^2 and p^2 parameters.

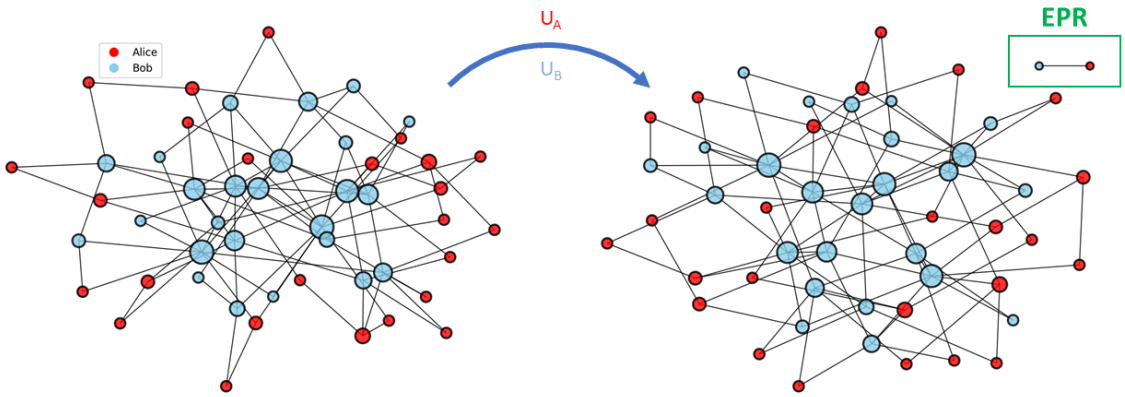

Fig. 7.5 ***Routing in a Barabasi-Albert network in a bipartite scenario.***

7.2.3 EPR vs two-mode cluster state with equal squeezing

Before going into the computation we should first define our general target state called earlier as an EPR pair by misuse of language. To be more precise we build a two-mode linear cluster state using linear optics as explained in Chapter 1. The adjacency matrix of the cluster state is trivial, reading

$$A_{\bullet\!-\!\bullet} = \begin{pmatrix} 0 & 1 \\ 1 & 0 \end{pmatrix} \tag{7.6}$$

and the transformation we need to implement on the momentum-squeezed modes to obtain such a cluster is

$$S_{\bullet\!-\!\bullet} = \begin{pmatrix} X_{\bullet\!-\!\bullet} & -Y_{\bullet\!-\!\bullet} \\ Y_{\bullet\!-\!\bullet} & X_{\bullet\!-\!\bullet} \end{pmatrix} = \frac{1}{\sqrt{2}} \begin{pmatrix} 1 & 0 & 0 & -1 \\ 0 & 1 & -1 & 0 \\ 0 & 1 & 1 & 0 \\ 1 & 0 & 0 & 1 \end{pmatrix} \tag{7.7}$$

where we recall that $X_{\bullet\!-\!\bullet}$ and $Y_{\bullet\!-\!\bullet}$ are linked to $A_{\bullet\!-\!\bullet}$ by the following relations

$$\begin{aligned} X_{\bullet\!-\!\bullet} &= \left(\mathbb{1} + A^2_{\bullet\!-\!\bullet}\right)^{-1/2} \\ Y_{\bullet\!-\!\bullet} &= A_{\bullet\!-\!\bullet} \left(\mathbb{1} + A^2_{\bullet\!-\!\bullet}\right)^{-1/2} \end{aligned} \tag{7.8}$$

The covariance matrix of the resulting finite-squeezed cluster state is given by $\Sigma_{\bullet\!-\!\bullet} = S_{\bullet\!-\!\bullet}\Sigma_{\text{sqz}}S^{\dagger}_{\bullet\!-\!\bullet}$ where Σ_{sqz} is the covariance matrix for the squeezed states, that reads

$$\Sigma_{\text{sqz}} = \sigma_0^2 \begin{pmatrix} e^{2r} & 0 & 0 & 0 \\ 0 & e^{2r} & 0 & 0 \\ 0 & 0 & e^{-2r} & 0 \\ 0 & 0 & 0 & e^{-2r} \end{pmatrix} \tag{7.9}$$

which permits us to get a covariance matrix

$$\Sigma_{\bullet-\bullet} = \sigma_0^2 \begin{pmatrix} \lambda & 0 & 0 & \mu \\ 0 & \lambda & \mu & 0 \\ 0 & \mu & \lambda & 0 \\ \mu & 0 & 0 & \lambda \end{pmatrix} \tag{7.10}$$

with $\lambda = \cosh(2r)$ and $\mu = \sinh(2r)$. $\Sigma_{\bullet-\bullet}$ exhibits similar correlation strenght as Σ_{EPR}, yet between XP and PX quadratures instead of XX and PP. From an information theory point of view these states can be considered as equivalent and $\Sigma_{\bullet-\bullet}$ can be used equivalently to perform a teleportation protocol simply by adjusting the feedforward classical post processing done between Alice and Bob [Pirandola and Mancini, 2006].

7.3 Local Routing via Derandomized Evolution Strategy

One way to address the problem of local routing is to find the appropriate unitaries (U_A, U_B) through a feedback loop, using a robust evolutionary algorithm capable of scanning a large parameter space. In particular, a cluster state of 50 nodes equally distributed between two parties, Alice and Bob, would have $D = 25^2 + 25^2 = 1250$ parameters to optimize. All these parameters together permit the generation of unitary matrices in a deterministic way. For example, if we choose to generate these unitaries using Hurwitz's parametrization [Zyczkowski and Kus, 1994], each parameter is an angle in the interval $[0, 2\pi[$. Among the different existing ways to design a robust evolutionary algorithm, we chose to follow a derandomized evolution strategy (DES) because it has already demonstrated efficient behavior when dealing with Covariance Matrix Adaptation [Hansen and Ostermeier, 2001, Shir et al., 2009]. DES is similar to genetic methods; that is, the way parameters are updated is not purely stochastic and depends on the quality of the existing offspring to realize the mutations, crossover, and selection.

Therefore to perform such an algorithm we need 3 important bricks :

- An evolutionary algorithm able to explore a large space of solutions;
- A fitness function to evaluate the quality of each offspring;
- An efficient way to generate our offsprings.

7.3.1 Covariance Matrix Adaptation Evolutionary Algorithm

A detailed description of the evolutionary algorithm is provided in Appendix B. The Covariance Matrix Adaptation Evolutionary Algorithm (CMA-ES) is an optimization method used to solve numerical optimization problems and belongs to the family of evolutionary algorithms.

The algorithm's operation relies on the adaptive update of a covariance matrix, capturing statistical relationships among variables in a group of candidate solutions. This covariance matrix models the multivariate distribution of the population and is iteratively adjusted to converge toward the optimal solution.

CMA-ES generates new solutions by combining the best current solutions with a stochastic perturbation based on the covariance matrix. This statistical covariance matrix

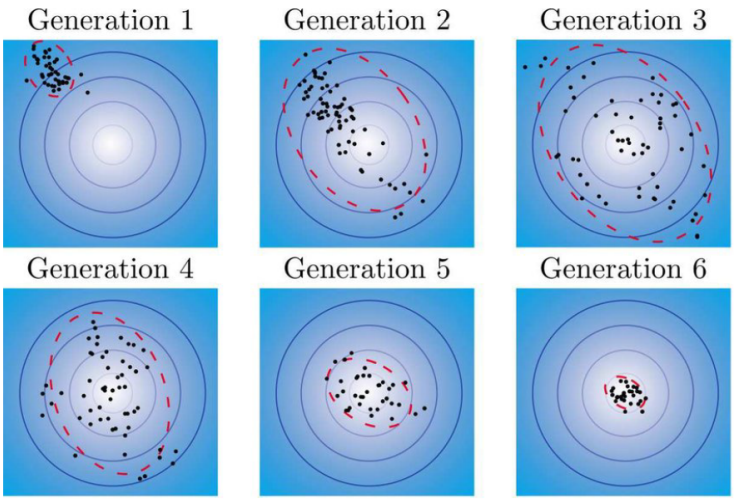

Fig. 7.6 ***Illustration of the operation of CMA-ES algorithms.***

is then coupled to a factor σ_g to model an expansion or contraction of the main path through the parameter space. The approach involves initially exploring a large diversity of offspring to limit the influence of local minima, progressively reducing diversity to pinpoint the precise solution of our problem. This process is illustrated in Figure 7.6. The most successful solutions guide the search towards promising areas of the search space.

7.3.2 Gell-mann parametrization of unitaries

As mentionned in 7.3.1, at each generation the algorithm needs to generate several elements of $U(n)$ to evaluate their score with the fitness function. For example, in the case of a cluster with 50 nodes ($D = 1250$), it requires 11 unitaries per generations. Considering that the algorithm needs approximately 10,000 generations to converge to an acceptable answer, it means that it computes a total of 110,000 elements of $U(n)$. To have the algorithm finding a solution within a minute, it would require an efficient subprogram that generates each unitary in 10^{-4} s. We achieve this using Gell-mann parametrization [Bertlmann and Krammer, 2008]. Other parametrizations such as [Zyczkowski and Kus, 1994] or [Golub and Loan, 1996] were used but lacked computational efficiency for dense explorations of a large space of parameters. The main idea behind the Gell-Mann parametrization is to use exponentiation of traceless hermitian matrices to generate elements of $U(n)$. Indeed any unitary U can be written

$$U = e^{iH} \tag{7.11}$$

where H is hermitian. Then here we make use of the generalized Gell-Mann matrices as generators for the unitary group. The Gell-Mann basis is composed of $n^2 - 1$ matrices which are constructed as follow and comprehends three different categories. Through all this part $E_{i,j}$ is a matrix composed of zeros only except for a one in position (i, j). It

composed of three sets of symmetric $\{\Lambda^s_{j,k}\}_{1\leq j<k\leq n}$, antisymmetric $\{\Lambda^a_{j,k}\}_{1\leq j<k\leq n}$ and diagonal matrices $\{\Lambda_l\}_{1\leq l\leq n-1}$ as follow

$$\begin{aligned}\Lambda^s_{j,k} &= E_{j,k} + E_{k,j}\\ \Lambda^a_{j,k} &= -i(E_{j,k} - E_{k,j})\\ \Lambda_l &= \sqrt{\frac{2}{l(l+1)}}\left(\sum_{j=1}^{l} E_{j,j} - lE_{l+1,l+1}\right)\end{aligned} \tag{7.12}$$

Renaming all the matrices as $\Lambda_1, ...\Lambda_{n^2-1}$ we can now construct any $n\times n$ hermitian matrix through this basis with our parameters $\{\epsilon_i\}_{i\in\{1,...n^2-1\}}$ and then obtain the corresponding unitary through exponentiation

$$H = \sum_{i=1}^{n^2-1} \epsilon_i \Lambda_i \tag{7.13}$$

and the coordinates $\{\epsilon_i\}_{i=1,..,n^2-1}$ of H in the Gell-Mann basis are the parameters we optimize with the evolutionary algorithm.

7.3.3 Fitness function

To evaluate our different offsprings we make use of the Froebenius norm ($\|\cdot\|_2$) between their associated covariance matrix and the ideal covariance matrix we target. Yet, not all correlations between the quadratures are fixed in our problem, only those of the two nodes selected that should exhibit the noise correlation of an EPR pair and no further correlations with other modes. In practice we look at a reduced covariance matrix. We define the ideal covariance matrix $\Sigma_{\text{ideal}}(n_1, n_2)$ as a generalization of the two-mode cluster state between nodes n_1 and n_2 as the following element of $\mathcal{M}_{4\times 2(n+p)}(\mathbf{R})$.

$$\begin{aligned}&\Sigma_{\text{ideal}}(n_1,n_2)_{1,n_1} = \Sigma_{\text{ideal}}(n_1,n_2)_{2,n_2} = \Sigma_{\text{ideal}}(n_1,n_2)_{3,n_1+n+p} = \Sigma_{\text{ideal}}(n_1,n_2)_{4,n_2+n+p} = \lambda\\ &\Sigma_{\text{ideal}}(n_1,n_2)_{1,n_2+n+p} = \Sigma_{\text{ideal}}(n_1,n_2)_{2,n_1+n+p} = \Sigma_{\text{ideal}}(n_1,n_2)_{3,n_2} = \Sigma_{\text{ideal}}(n_1,n_2)_{4,n_1} = \mu\\ &\Sigma_{\text{ideal}}(n_1,n_2)_{i,j} = 0 \quad \forall (i,j) \notin \{n_1,n_2\}\end{aligned} \tag{7.14}$$

where λ and μ are defined as in section 7.2. We then compare the reduced covariance matrix $\Sigma_{\text{reduced}}(n_1, n_2)$ generated via the lines of interest of the covariance matrix of our offspring Σ:

$$\Sigma_{\text{reduced}}(n_1,n_2) = \begin{pmatrix}\Sigma_{n_1}\\ \Sigma_{n_2}\\ \Sigma_{n_1+n+p}\\ \Sigma_{n_2+n+p}\end{pmatrix}. \tag{7.15}$$

Another important covariance matrix to consider is the 4×4 matrix of the two nodes of interest (n_1, n_2) obtained when tracing out all the other modes. We call this matrix Σ_{routed}. In the case of a successful routing Σ_{routed} should be identical to $\Sigma_{\bullet\!-\!\bullet}$. Finally, we define

$$f_{opt} = \|\Sigma_{\text{ideal}}(n_1,n_2) - \Sigma_{\text{reduced}}(n_1,n_2)\|_2 + \frac{1}{2}\left[1 - \gamma(\Sigma_{\text{routed}}(n_1,n_2))\right] \tag{7.16}$$

where we recall that γ is the Purity of the gaussian state as defined in Chapter 1. We were initially performing the algorithm with the Frobenius norm only, but then the algorithm was less tolerant to local minima, especially in situations where an exact solution appears not to exist.

7.4 Simulation results

We now present the most recent results obtained based on our evolutionary algorithm. We explored several different topologies, ranging from deterministic to complex networks. Finally, we provide some insight into the performance of the algorithm in terms of execution time and convergence.

7.4.1 Fully connected networks

One behaviour observed in [Sansavini and Parigi, 2019] was the impossibility to achieve a perfect TMSV cluster state with networks that are defined by a set of n nodes, all interconnected. When performing the derandomized algorithm on such networks, we observe two distinct behaviours

1. The algorithm is never able to fully converge toward a perfect EPR pair for any selection of two nodes shared between Alice and Bob. Moreover the algorithm stops to improve atfter a few hundreds of generations;

2. The algorithm always converge toward an accurate EPR pair when the two nodes belong to one party, Alice for example. Indeed, it appears that the algorithm converges perfectly with a final optimization function value of $f_{opt} = \mathcal{O}(10^{-15})$.

In Figure 7.7, we plot the value of the optimization function f_{opt} after each generation to illustrate this phenomenon. Figure 7.7a represents a situation where the algorithm converges perfectly. It was done with a fully connected network with 50 nodes and internal routing. This figure illustrates that the algorithm continues to learn over generations, reaching the lowest possible value achievable in computer memory. On the other hand, Figure 7.7b shows the convergence on the same network, but this time the two nodes of interest belong to Alice and Bob. Here, the evolutionary algorithm quickly stops learning and fails to converge. In the second scenario, considering two nodes on Alice's side without loss of generality, the final covariance matrix $\Sigma_{\text{routed, full, AA}}$ is identical to

$$\Sigma_{\text{routed, full, AA}} = \begin{pmatrix} 5.05 & \mathcal{O}(10^{-15}) & \mathcal{O}(10^{-15}) & -4.95 \\ \mathcal{O}(10^{-15}) & 5.05 & -4.95 & \mathcal{O}(10^{-15}) \\ \mathcal{O}(10^{-15}) & -4.95 & 5.05 & \mathcal{O}(10^{-15}) \\ -4.95 & \mathcal{O}(10^{-15}) & \mathcal{O}(10^{-15}) & 5.05 \end{pmatrix} \tag{7.17}$$

In the first scenario, the purity of the state is also close to 100% yet this time some unwanted correlations between the quadratures remain.

$$\Sigma_{\text{routed, full, AB}} = \begin{pmatrix} 3.63 & \mathcal{O}(10^{-9}) & 2.35 & -4.11 \\ \mathcal{O}(10^{-9}) & 3.63 & -4.11 & -2.35 \\ 2.35 & -4.11 & 6.47 & \mathcal{O}(10^{-9}) \\ -4.11 & -2.35 & \mathcal{O}(10^{-9}) & 6.47 \end{pmatrix} \tag{7.18}$$

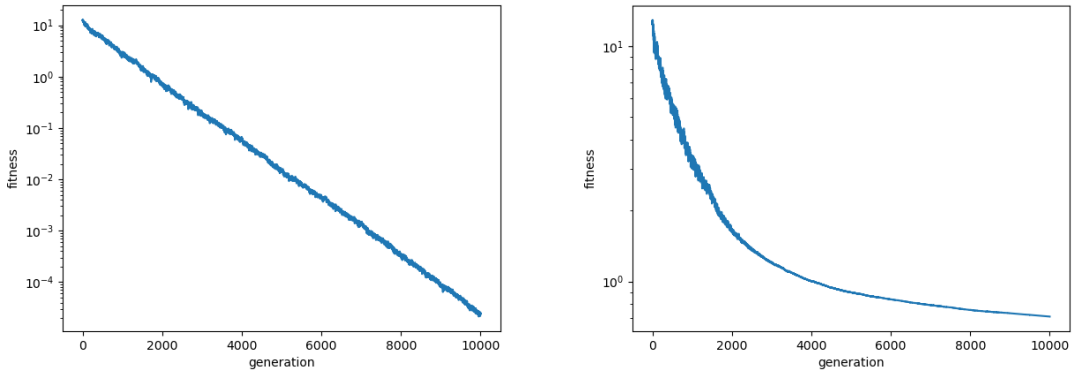

(a) (b)

Fig. 7.7 ***Illustration of the two different convergence scenario***. *The evolution of the optimization function with the number of generations is presented.*

7.4.2 Grid

In this section, we present the routed covariance matrices obtained from grid-type networks. These networks exhibit two distinct behaviors as well, depending on the parity of the number of nodes each party possesses. A result that was already observed in [Sansavini and Parigi, 2019] is the difference in the convergence of the objective function depending on the parity of the number of nodes distributed between Alice and Bob in a grid network. The conclusion at the time was:

- if Alice and Bob possess an odd number of modes, then up to a sufficient number of generation the objective function can drop to nearly 0 ($\mathcal{O}(10^{-14})$).
- if Alice and Bob possess an even number of modes, then the algorithm stops to learn after few generations (≈ 1000 for $n < 14$) and the final objective function value is typically in $\mathcal{O}(10^{-1})$.

We have confirmed this behaviour for all possible grids of sizes 4 to 100 nodes, see Table 7.1. Moreover, in an odd scenario we get a perfect covariance matrix of an TMSV cluster state as a result, typically for a grid of size $n = 6$, tracing out all the modes to keep only the covariance matrix between the two modes of interest we get

$$\Sigma_{\text{routed, odd}} = \begin{pmatrix} 5.05 & \mathcal{O}(10^{-15}) & \mathcal{O}(10^{-15}) & -4.95 \\ \mathcal{O}(10^{-15}) & 5.05 & -4.95 & \mathcal{O}(10^{-15}) \\ \mathcal{O}(10^{-15}) & -4.95 & 5.05 & \mathcal{O}(10^{-15}) \\ -4.95 & \mathcal{O}(10^{-15}) & \mathcal{O}(10^{-15}) & 5.05 \end{pmatrix} \tag{7.19}$$

here 5.05 and -4.95 are the numerical values of λ and μ respectively for s = 10. On the contrary for an even scenario due to the objective function not converging toward 0 the final result is more of this form (example with $n = 8$)

$$\Sigma_{\text{routed, even}} = \begin{pmatrix} 4.88 & \mathcal{O}(10^{-3}) & 0.86 & -4.86 \\ \mathcal{O}(10^{-3}) & 4.88 & -4.86 & -0.86 \\ 0.86 & -4.86 & 5.22 & \mathcal{O}(10^{-3}) \\ -4.86 & -0.86 & \mathcal{O}(10^{-3}) & 5.22 \end{pmatrix}. \tag{7.20}$$

n	$\|\cdot\|_2$	γ	f_{opt}
4	4.55	100	4.55
6	$\mathcal{O}(10^{-14})$	100	$\mathcal{O}(10^{-14})$
8	1.86	99.99	1.86
10	$7.32.10^{-5}$	99.99	$7.32.10^{-5}$
12	0.98	96.73	0.99
14	0.40	96.20	0.42
16	0.59	98.96	0.60
18	0.19	99.08	0.19
20	0.40	99.09	0.40
22	0.40	96.09	0.42
24	0.29	99.90	0.29
26	0.19	99.04	0.19
28	0.49	95.21	0.52
30	0.56	95.13	0.58
32	0.19	99.67	0.19
34	0.29	95.13	0.30
36	0.28	98.69	0.28
38	0.15	99.47	0.15
40	0.34	97.99	0.35
42	0.23	98.99	0.23
44	0.31	98.06	0.32
46	0.38	98.54	0.39
48	0.37	97.21	0.38
50	0.27	98.43	0.28

Table 7.1: **Algorithm Performance Summary on Grid Networks**. The result of the evaluation by the optimization function is given in the last column. The others corresponds in order to the size of the graph considered n, the Froebenius evaluation $\|\Sigma_{\text{ideal}}(n_1, n_2) - \Sigma_{\text{reduced}}(n_1, n_2)\|_2$ and the purity $\gamma(\Sigma_{\text{routed}}(n_1, n_2))$ of the best offspring. While for larger number of nodes, the difference between the two described scenario is not clear in this table, there is a clearer difference when we look at the convergence of the optimization function. Indeed they exhibit similar patters as the one presented in Figure 7.7.

Yet, as shown in Table 7.1, the purity of the state is still nearly 1; thus, the state is decorrelated from the rest of the network but does not exhibit the exact correlations of a TMSV cluster state. Diagonalizing such a matrix gives eigenvalues of 10, 10, 0.1, 0.1, meaning that the traced state is indeed associated with two squeezed modes with a squeezing parameter of $s = 10$. The difference between behaviors decreases with the size of the network for a constant number of generations, but simply observing the difference in convergence speed is enough to convince oneself that it persists, cf. Figure 7.7. Moreover, this difference in behavior has the primary consequence of the remaining correlations at the end of the execution, see (7.20).

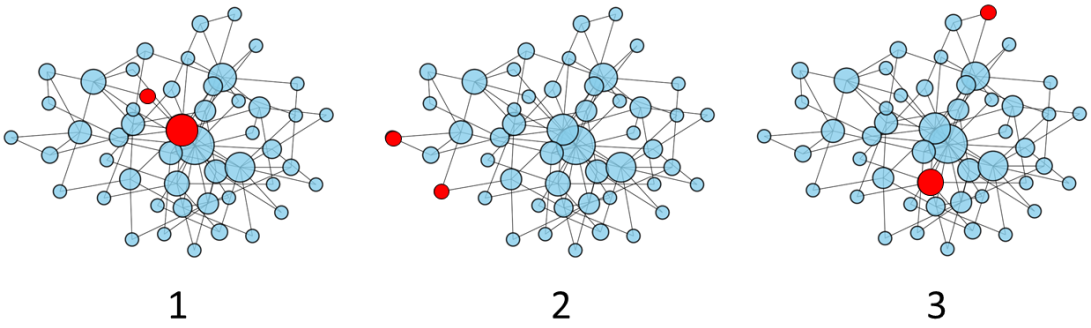

Fig. 7.8 ***Illustration of the different scenario explored.*** *The different scenario labels are related to the description given in the main text.*

7.4.3 Complex networks

The implementation of complex clusters in our problem allows us to study models that closely resemble real networks. We examine the protocol for extracting TMSV cluster state on a complex topology: the Barabási-Albert model.We present results for this topology, as it is the only one for which we have conducted enough simulations to provide relevant statistics. Nevertheless, a few simulations were performed with Internet Autonomous System and Protein-Protein Interaction networks and yielded similar results. Using this model, we will employ the EPR pair extraction protocol in three different scenarios, posing the following questions: Is it possible to extract an EPR pair between

1. A hub and a node with low degree?
2. Two nodes with low degrees?
3. Two distant nodes?

A graphic visualization of the scenario are given in Figure 7.8. To answer these questions, we apply the extraction algorithm over 10,000 generations, one hundred times to BA networks with $n = 100$ nodes and a parameter of $m_{BA} = 2$. The results are presented in Table. 7.2 based on the scenario under investigation. The algorithm appears to converge

Scenario	1	2	3
$\bar{\gamma}$ (%)	91.04	90.48	90.85
std(γ) (%)	3.57	3.49	3.02
$\bar{f}_{opt}$	0.77	0.80	0.77
std(f_{opt})	0.18	0.15	0.14

Table 7.2: **Performance Summary on Complex Networks by the Algorithm**. $\bar{\gamma}$ is the average purity obtained over the 100 simulations and std(γ) the standard deviation. Similar conventions are adopted for the objective function $\bar{f}_{opt}$ and std(f_{opt})

correctly; however, the optimization function is not yet on the order of magnitude of $\mathcal{O}(10^{-14})$ as for smaller graphs. To draw a conclusive analysis, we need to study the

influence of the number of generations. Therefore, we increased the number of generations from 10,000 to 30,000. Due to temporal complexity concerns with our algorithm, we are reducing the number of algorithm executions by a factor of 10. As a result, the statistics presented in Table 7.3 are based on a smaller population. We observe that the algorithm's

Scenario	1	2	3
$\bar{\gamma}$ (%)	98.07	98.21	98.14
std(γ) (%)	1.98	1.09	1.41
$\bar{f}_{opt}$	0.36	0.40	0.41
std(f_{opt})	0.14	0.13	0.18

Table 7.3: **Performance Summary on Complex Networks by the Algorithm with more generations**. $\bar{\gamma}$ is the average purity obtained over the 100 simulations and std(γ) the standard deviation. Similar conventions are adopted for the objective function $\bar{f}_{opt}$ and std(f_{opt})

ability to converge in the case of the BA model appears to be directly proportional to the number of generations. The purity as of the final state has increased and the optimisation function decreased by nearly a factor 2. Thus, in all three cases studied (excluding the hub-hub case), it seems possible to extract an EPR pair from a Barabasi–Albert network using linear optical operations. None of the three cases appears to be preferential; all the results are comparable in terms of magnitude. The degree of the nodes chosen to form the EPR pair seems to have no impact on the extraction capacity (the same holds for the distance between the nodes). Some simulations with an even larger number of generations would be necessary. The question we should answer is then how much?

7.4.4 Execution time scaling with problem size

We conclude this preliminary study by providing a rough estimate of how fast our algorithm converges depending on the size of the network. We performed numerical optimization on networks for which we knew convergence would occur and counted the number of generations necessary to achieve such performance. When plotting this number of generations as a function of the number of parameters to optimize in our algorithm (see Fig. 7.9), we find there is nearly a linear relationship between the two quantities. The criterion chosen for stopping the algorithm, $f_{\text{opt}} < 10^{-4}$, is selected arbitrarily but within a relevant range when compared to the number of significant digits in our problem. A linear regression allows us to estimate the approximate number of generations necessary to optimize for a given parameter, which appears to be about 7. This analysis is consistent with results on complex networks presented in the last section where we optimized 5000 parameters and achieved satisfying results after 30,000 generations.

7.5 Analytical approach

7.5.1 Square network

The essence of this section is to acquire a little bit of intuition on the general problem that was tackled so far using a derandomized evolution algorithm. When working with a very

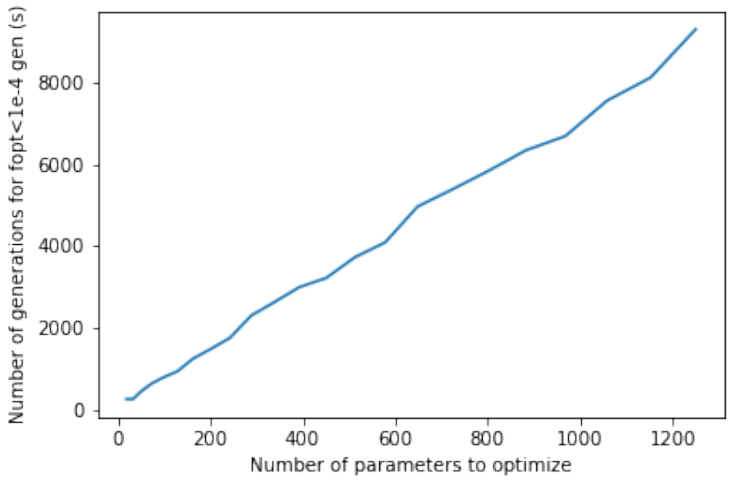

Fig. 7.9 ***Optimization Journey**: Required Generations for Objective Function* $< 10^{-4}$ *vs. Parameter Count.*

small cluster (only 4 modes here shared between Alice and Bob) the passive transformation on each side is essentially a beam splitter combined with phase rotation meaning that the number of parameters permits to look for a manual optimization. We then proceed with an analytical demonstration in a simple case. Here, we will analytically study the 4-node network represented in Figure 7.10, which is one of the first non-trivial case of our problem. We recall that a grid with an even number of modes for Alice and Bob appears to not have an optimal solution from our algorithm point of view. The idea is as follows: once again, we aim to extract an EPR pair from the system. In a preliminary approach, we will, in a naive manner, analytically apply two beam-splitters, one between the two nodes of Alice and the other between the two nodes of Bob. Following this operation, we expect to obtain two decoupled EPR pairs between nodes 1-3 and 2-4. Let's start by constructing the initial covariance matrix of the 4-node network. Such network has an adjacency matrix given by

$$A_{\blacksquare} = \begin{pmatrix} 0 & 1 & 1 & 0 \\ 1 & 0 & 0 & 1 \\ 1 & 0 & 0 & 1 \\ 0 & 1 & 1 & 0 \end{pmatrix}. \tag{7.21}$$

We construct the two basic blocks, $X_{\blacksquare}$ and $Y_{\blacksquare}$, of the symplectic matrix $S_{\blacksquare}$ once using equations (1.97) (assuming once again that $O = \mathbb{1}$). Thus, the initial covariance matrix of the state is

$$\Sigma_{\blacksquare} = S_{\blacksquare} L S_{\blacksquare}^{T} \tag{7.22}$$

where $L = \sigma_0^2 \mathrm{diag}(s, s, s, s, 1/s, 1/s, 1/s, 1/s)$ is the covariance matrix in the supermode basis with squeezing parameter $s = e^{2r}$. The analytical form of the initial covariance

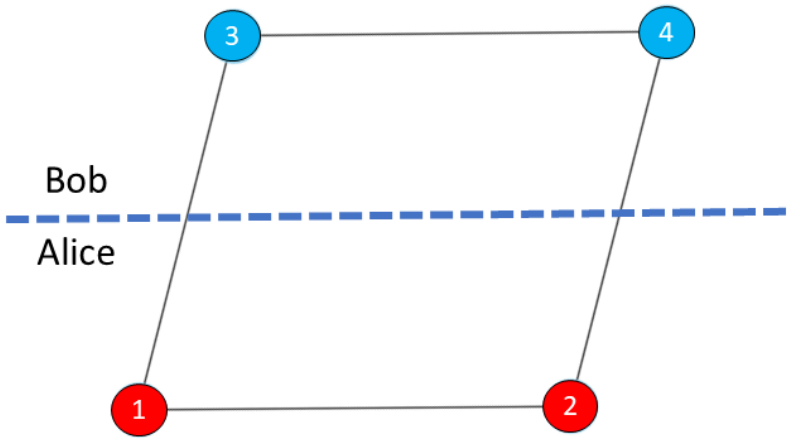

Fig. 7.10 ***Graphic representation of a square network.*** *The network is shared between Alice and Bob. They own respectively the nodes labeled 1,2 and 3,4.*

matrix, **in the convention** $(X_1, X_2, P_1, P_2, X_3, X_4, P_3, P_4)$[2], is as follows

$$\Sigma_{\blacksquare} = \begin{pmatrix} \frac{3s}{5}+\frac{2}{5s} & 0 & 0 & \frac{s^2-1}{5s} & 0 & -\frac{2(s^2-1)}{5s} & \frac{s^2-1}{5s} & 0 \\ 0 & \frac{3s}{5}+\frac{2}{5s} & \frac{s^2-1}{5s} & 0 & -\frac{2(s^2-1)}{5s} & 0 & 0 & \frac{s^2-1}{5s} \\ 0 & \frac{s^2-1}{5s} & \frac{2s}{5}+\frac{3}{5s} & 0 & \frac{s^2-1}{5s} & 0 & 0 & \frac{2(s^2-1)}{5s} \\ \frac{s^2-1}{5s} & 0 & 0 & \frac{2s}{5}+\frac{3}{5s} & 0 & \frac{s^2-1}{5s} & \frac{2(s^2-1)}{5s} & 0 \\ 0 & -\frac{2(s^2-1)}{5s} & \frac{s^2-1}{5s} & 0 & \frac{3s}{5}+\frac{2}{5s} & 0 & 0 & \frac{s^2-1}{5s} \\ -\frac{2(s^2-1)}{5s} & 0 & 0 & \frac{s^2-1}{5s} & 0 & \frac{3s}{5}+\frac{2}{5s} & \frac{s^2-1}{5s} & 0 \\ \frac{s^2-1}{5s} & 0 & 0 & \frac{2(s^2-1)}{5s} & 0 & \frac{s^2-1}{5s} & \frac{2s}{5}+\frac{3}{5s} & 0 \\ 0 & \frac{s^2-1}{5s} & \frac{2(s^2-1)}{5s} & 0 & \frac{s^2-1}{5s} & 0 & 0 & \frac{2s}{5}+\frac{3}{5s} \end{pmatrix} \tag{7.23}$$

Thus the target state is built from the covariance matrix associated to two TMSV cluster states, read

$$\Sigma_{\text{target}} = \begin{pmatrix} \lambda & 0 & 0 & 0 & 0 & 0 & \mu & 0 \\ 0 & \lambda & 0 & 0 & 0 & 0 & 0 & \mu \\ 0 & 0 & \lambda & 0 & \mu & 0 & 0 & 0 \\ 0 & 0 & 0 & \lambda & 0 & \mu & 0 & 0 \\ 0 & 0 & \mu & 0 & \lambda & 0 & 0 & 0 \\ 0 & 0 & 0 & \mu & 0 & \lambda & 0 & 0 \\ \mu & 0 & 0 & 0 & 0 & 0 & \lambda & 0 \\ 0 & \mu & 0 & 0 & 0 & 0 & 0 & \lambda \end{pmatrix}. \tag{7.24}$$

Now, let's construct the transformations performed by Alice and Bob on their respective subsystems. These transformations are governed by four parameters: $\phi_{1A}, \phi_{2A}, \phi_{3A}, \theta_A$

[2]With this definition, assuming Alice has the modes 1 and 2, and Bob the modes 3 and 4, the upper left part of $\Sigma_{\blacksquare}$ is the local state of Alice and analogously the lower right part belongs to Bob.

(and likewise for Bob $\phi_{1B}, \phi_{2B}, \phi_{3B}, \theta_B$). We denote this set of parameters as $\mathfrak{X}$ for the sake of brevity. The unitary matrices associated with these transformations are the product of a rotation matrix and a phase-shift matrix, which allows us to study the situation in the most general way

$$U_{A/B} = \begin{pmatrix} e^{i\phi_{2A/B}} \cos(\theta_{A/B}) & -e^{i(\phi_{1A/B}+\phi_{2A/B})} \sin(\theta_{A/B}) \\ e^{i\phi_{3A/B}} \sin(\theta_{A/B}) & e^{i(\phi_{1A/B}+\phi_{3A/B})} \cos(\theta_{A/B}) \end{pmatrix}. \tag{7.25}$$

From U_A and U_B we build the overall simplectic transformation on the state

$$S_1 = \begin{pmatrix} S_A & 0 \\ 0 & S_B \end{pmatrix} \tag{7.26}$$

where

$$S_{A/B} = \begin{pmatrix} \cos(\theta_{A/B})\cos(\phi_{2A/B}) & -\sin(\theta_{A/B})\cos(\phi_{1A/B}+\phi_{2A/B}) & \cos(\theta_{A/B})\sin(\phi_{2A/B}) & -\sin(\theta_{A/B})\sin(\phi_{1A/B}+\phi_{2A/B}) \\ \sin(\theta_{A/B})\cos(\phi_{3A/B}) & \cos(\theta_{A/B})\cos(\phi_{1A/B}+\phi_{3A/B}) & \sin(\theta_{A/B})\sin(\phi_{3A/B}) & \cos(\theta_{A/B})\sin(\phi_{1A/B}+\phi_{3A/B}) \\ -\cos(\theta_{A/B})\sin(\phi_{2A/B}) & \sin(\theta_{A/B})\sin(\phi_{1A/B}+\phi_{2A/B}) & \cos(\theta_{A/B})\cos(\phi_{2A/B}) & -\sin(\theta_{A/B})\cos(\phi_{1A/B}+\phi_{2A/B}) \\ -\sin(\theta_{A/B})\sin(\phi_{3A/B}) & -\cos(\theta_{A/B})\sin(\phi_{1A/B}+\phi_{3A/B}) & \sin(\theta_{A/B})\cos(\phi_{3A/B}) & \cos(\theta_{A/B})\cos(\phi_{1A/B}+\phi_{3A/B}) \end{pmatrix} \tag{7.27}$$

which leads us to the final cluster state covariance matrix in its most general form

$$\Sigma_{gen} = S_1 \Sigma_{\blacksquare} S_1^T \tag{7.28}$$

The problem thus reduces to finding a solution to the equation $\Sigma_{gen} = \Sigma_{\text{target}}$ for the set of parameters. The first method tested to attempt to solve the problem is to analytically search for values of $\mathfrak{X}$ for which Σ_{gen} is zero in positions where Σ_{target} is zero. In other words, we are looking for values of $\mathfrak{X}$ such that

$$(\Sigma_{gen})_{i,j}(\mathfrak{X}) = 0 \;\text{ iff }\; (\Sigma_{\text{target}})_{i,j} = 0 \tag{7.29}$$

One known method for correlating or decorrelating two nodes in the systems we are studying here is to use symmetric beam-splitters, so we set $\theta_A = \theta_B = \pi/4$ in the preliminary approach. Then, it is possible to find 'by hand' a set of values that satisfy the problem for all (i, j) satisfying (7.29). Using this approach we are not able to fully recover the covariance matrix of an EPR pair, yet we find

$$\Sigma_{gen} = \begin{pmatrix} \lambda' & 0 & 0 & \mu \\ 0 & \lambda' & \mu & 0 \\ 0 & \mu & \lambda" & 0 \\ \mu & 0 & 0 & \lambda" \end{pmatrix} \tag{7.30}$$

with

$$\left\{ \mu = \frac{s^2-1}{\sqrt{5}s}, \lambda' = \frac{(\sqrt{(}5)+5)s^2 - \sqrt{(}5)+5}{10s}, \lambda" = \frac{-(\sqrt{(}5)+5)s^2 + \sqrt{(}5)+5}{10s} \right\} \tag{7.31}$$

It appears that the problem has no solution in the case of symmetric beam-splitters (with lambda fixed). This impossibility was also extended to a scenario where no assumption is made on $\theta_{A/B}$. Looking at the analytical expression of Σ_{gen} we find

$$\begin{aligned} Cov(\hat{X}_1, \hat{X}_2) &\propto [\sin(\theta_A)\cos(\theta_A)\sin(\phi_{1A}) + \cos(2\theta_A)]\sin(\phi_{1A}+\phi_{2A}+\phi_{3A}) \\ &\propto [\sin(\theta_A)\cos(\theta_A)\sin(\phi_{1A}) + \cos(2\theta_A)]\cos(\phi_{1A}+\phi_{2A}+\phi_{3A}) \end{aligned} \tag{7.32}$$

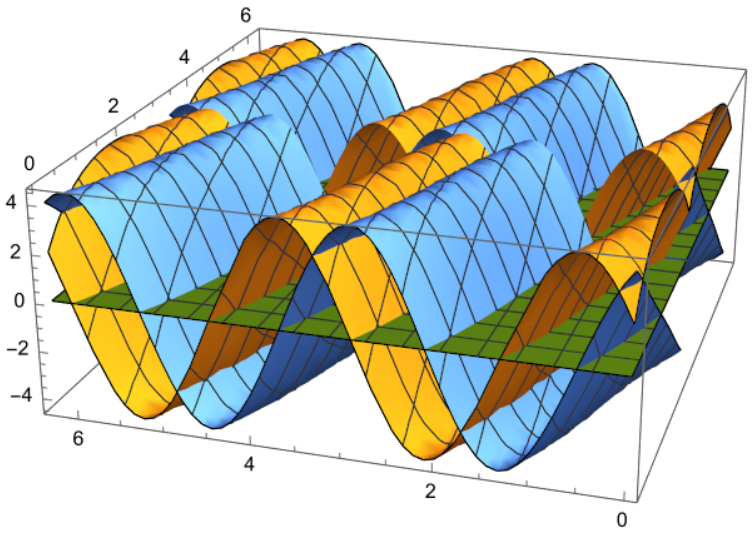

Fig. 7.11 $\Delta^2\hat{X}_1 - \lambda$ *et* $Cov(\hat{X}_1, \hat{P}_1)$ *pour* $\phi_{1A} \in [0, 2\pi]$ *et* $\phi_{2A} \in [0, 2\pi]$. *It appears that the two functions are never 0 at the same point of the space, thus showing the impossibility of a perfect routing in square networks.*

which leads to the condition

$$\sin(\theta_A)\cos(\theta_A)\sin(\phi_{1A}) + \cos(2\theta_A) = 0 \tag{7.33}$$

and thus

$$\theta_A = \frac{1}{2}\cot^{-1}\left(-\frac{\sin(\phi_{1A})}{2}\right) \tag{7.34}$$

We can now analytically assess $\Delta^2\hat{X}_1 - \lambda$ and $Cov(\hat{X}_1, \hat{P}_1)$, are two functions of ϕ_{1A} and ϕ_{2A} for the determined θ_A. We plot these two functions in Fig. 7.11. There are no values of (ϕ_{1A}, ϕ_{2A}) for which both covariances vanish at the same point, indicating that the problem has no solution even in the case of an unbalanced beam-splitter. Overall, it appears that in the case of a square cluster, if our evolutionnary strategy does not converge perfectly it is indeed due to an impossibility to find a solution. However, this result cannot be generalized yet to all cluster topologies with $n > 4$.

7.5.2 General approach and Williamson decomposition

A recent development in the subject involves not looking anymore at the state that Alice and Bob share together but rather at the final state that Alice and Bob should hold individually. If, after their transformation, they own an EPR pair, then locally Alice and Bob see a thermal state with a temperature associated with photon number $\lambda = \cosh(2r)$. This state is completely separated from the rest of all other local nodes. Then, if Alice and Bob apply local symplectic transformations S_{wA} and S_{wB} that correspond to the Williamson decomposition of their local state, the state they should see is locally a set of thermal states.

In essence, we can provide a no-go theorem on extracting an EPR pair from the cluster state by looking at the symplectic eigenvalues of the state. If one of them is exactly λ, then perfect routing is doable, and the symplectic transformation of the Williamson decomposition is the solution to our problem. Moreover, it appears that in a scenario where local routing appears doable (as in 7.4.1), the set of symplectic eigenvalues always presents the value 1 with multiplicity 2. The value 1 indicates that some modes of the subsystem are pure and thus decorrelated from Bob completely. This value (1) is very often present in complex topologies scenarios.

This result is not enough to identify a topology, among the ones explored so far, as a universal candidate for quantum routing. Further work is necessary to determine the potential impact that the orthogonal matrix O presented in equation (1.97) and taken to the identity matrix in our case because the clusters are built with identical squeezing. Choosing appropriately the value of O permits to optimize the squeezing distribution in the network [Sansavini and Parigi, 2019]. Thus, in a more realistic scenario, this orthogonal matrix could be an extra crucial parameter.

Finally, more work should be done to explore how the imperfect EPR pair affects the teleportation protocol presented in Chapter 2.4.

Conclusion & Outlook

In this thesis, we have examined the single-pass generation of multimode squeezed states of light at telecom wavelengths in ppKTP waveguide. This is, to my knowledge, the first time such multimode quantum states are produced at these wavelengths. We gave through this manuscript a dedicated focus on the detection setup as I was especially in charge of its design, as well as a focus on how to properly acquire the different data for the caracterization of the source (squeezing curves, covariance matrix and nullifiers of cluster states). Moreover, we provided a comprehensive framework for selecting the appropriate waveguide to work as a source in our experiment. This framework might not be complete but it is what I know at the time of writing my thesis. Indeed the experiment was not only designed during my Ph.D, but also built, rebuilt from scratch, and characterized extensively each time. Our results have demonstrated that such technique for producing non classical states of light is promising for a wide range of applications in quantum information. Indeed the squeezing level per mode [over 2 dB in the first 4 modes] appears as a very promising result. Generation at such wavelengths is especially important, as it can enable quantum information, communication, and sensing beyond the laboratory scale with fibered components.

We have also addressed the question of an application of the source toward frequency-multiplexing quantum key distribution and provided a proposal for an experimental implementation. Finally, we have explored Quantum Routing in large complex multipartite networks and derived some important criteria for the construction of quantum network.

The completion of this thesis opens the door to new research possibilities. Here are some avenues for future research that stem from our findings and limitations:

1. **Measuring the exact supermodes**: A deeper exploration of the quantum state produced may reveal unexplored nuances. This would certainly lead to higher squeezing level per mode as well as the production of accurate cluster states. Further studies could investigate the role of spectrum modulation inside the waveguide for a more comprehensive understanding. Moreover the issue of spatial mode-matching should be adressed as well to reduce optical losses in the system. This is a necessary step in order to move from source caracterization to several case of study such as quantum cryptography, quantum computing or quantum metrology.

2. **Multimode photon addition and/or subtraction**: Future research can be dedicated on producing non-gaussian quantum states from photon addition or photon subtraction on the generated multimode squeezed state. Applying these findings to certification of non-gaussian states could open new research perspectives. Recently

the group acquired superconducting nanowire single-photon detector (SNSPDs) for this purpose.

3. **Waveguide engineering**: Technology and methodologies are constantly evolving. Advances in waveguide engineering, via aperiodic poling for example, could enable more sophisticated quantum source toward the direct production of cluster states in the frequency domain.

4. **Toward Quantum Information protocols**: Integrating Quantum Cryptography and/or Computing [Yokoyama et al., 2013a, Asavanant et al., 2019, Larsen et al., 2019] with the conclusions of this thesis might provide a more comprehensive interdisciplinary understanding of the potential of the source for real world applications.

In conclusion, there is still much to explore in this field, and the outlook for future research offers exciting opportunities to expand our knowledge and deepen our understanding. I hope this thesis will serve as a strong foundation for future research in this area.

Appendix A

Source caracterization data

Contents

A.1 Squeezing measurement

A.1.1 Hermite-Gauss Basis

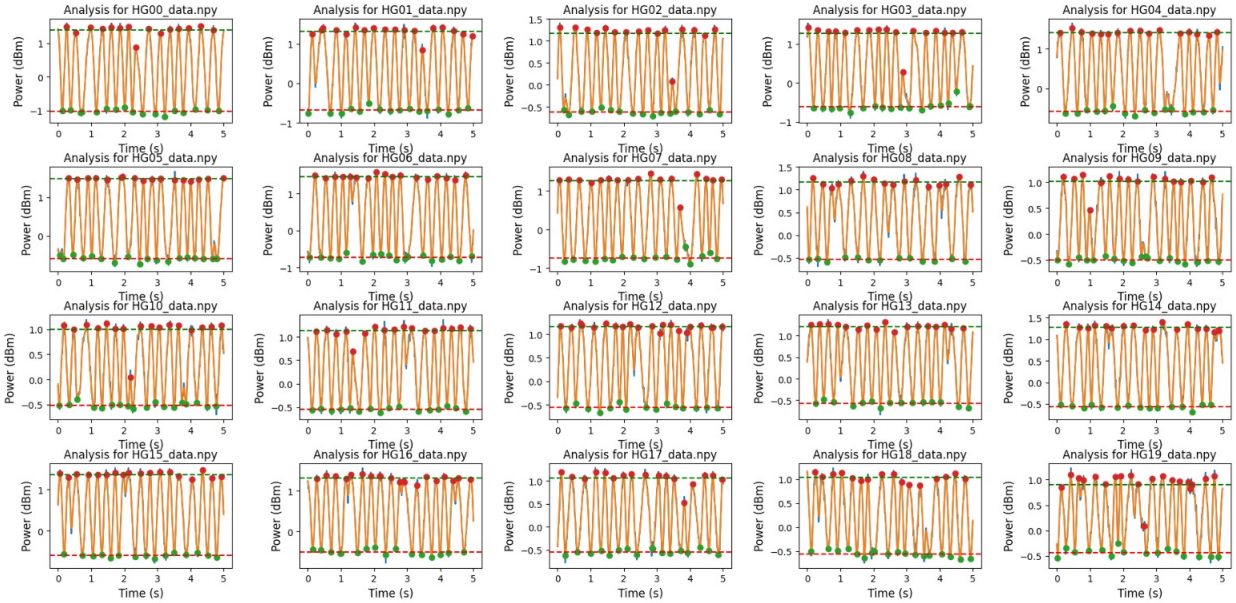

Fig. A.1 ***20 mode curve acquisition***. *The masks applied for the acquisition on the Local Oscillator were HG functions with respective FWHM (nm) in amplitude : 45, 31, 28.5, 27, 26, 25.5, 25.2, 24.9, 24.7, 24.6, 24.5, 24.4, 24.2, 24, 24, 24, 24, 24, 24, 24, 24*

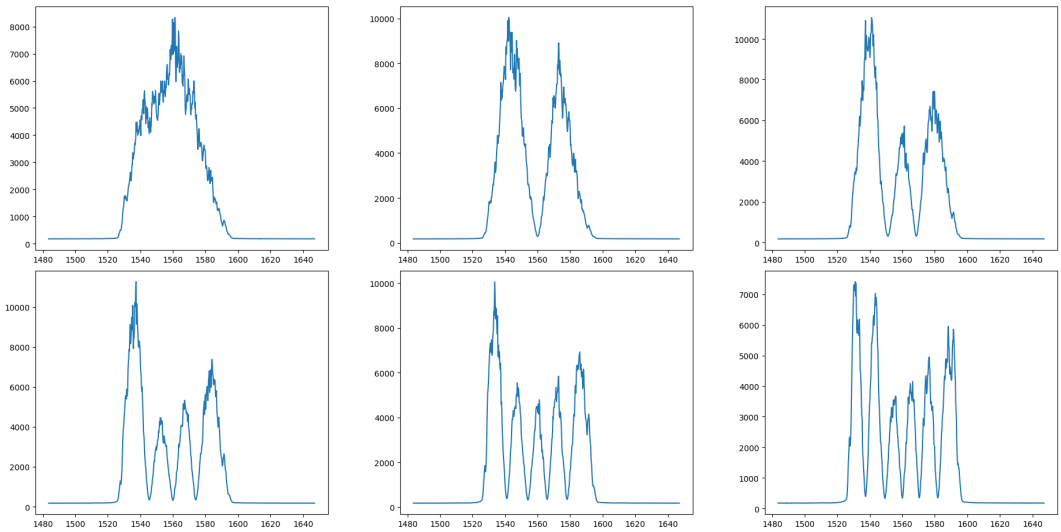

Fig. A.2 ***First 6 HG masks acquisition at the output of the pulse shaper***.

A.1.2 Flat-mode basis

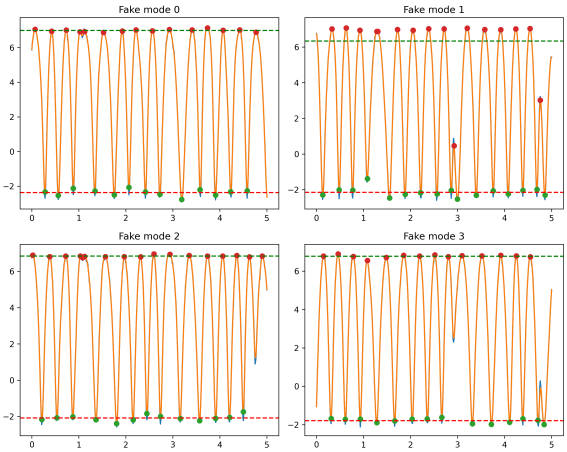

Fig. A.3 ***Flat mode curve acquisition***. *The masks applied for the acquisition on the Local Oscillator were flat modes presented in Chapter 5.*

A.2 Covariance matrix reconstruction

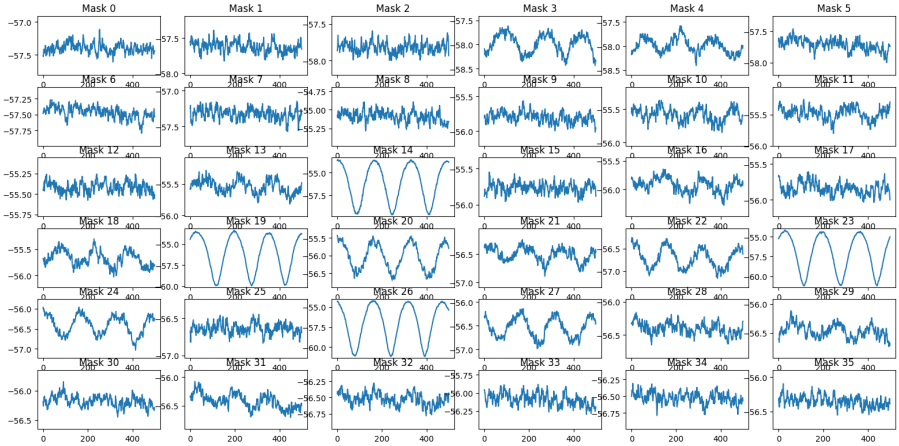

Fig. A.4 ***Covariance matrix acquisition curve***. *The 8 first masks corresponds to the 8 individual frexels, and the rest are acquired with masks as combinations of 2 different frexels*

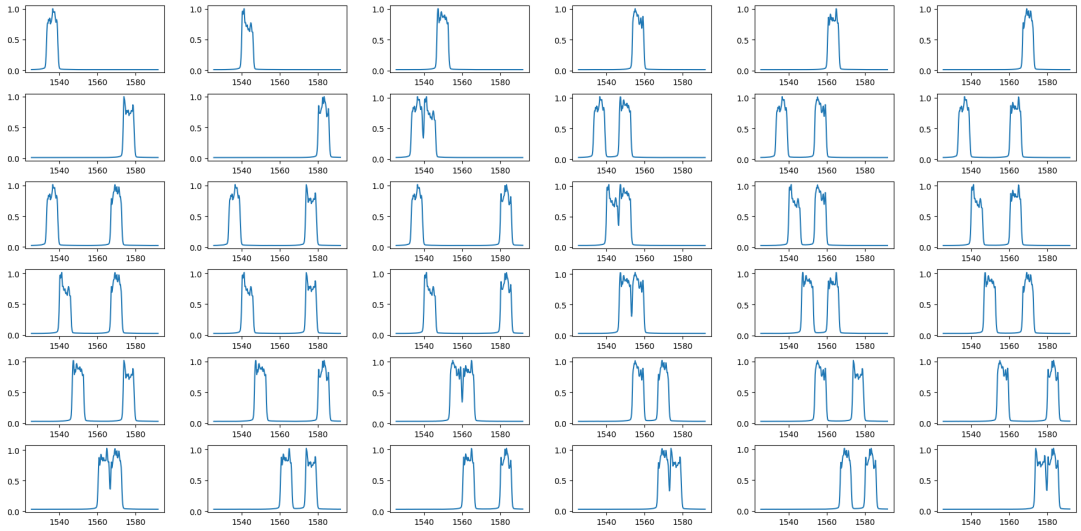

Fig. A.5 ***Covariance matrix mask order***. *All the mask use for the reconstruction in the same order as the acquisition curve.*

A.3 Cluster state measurement

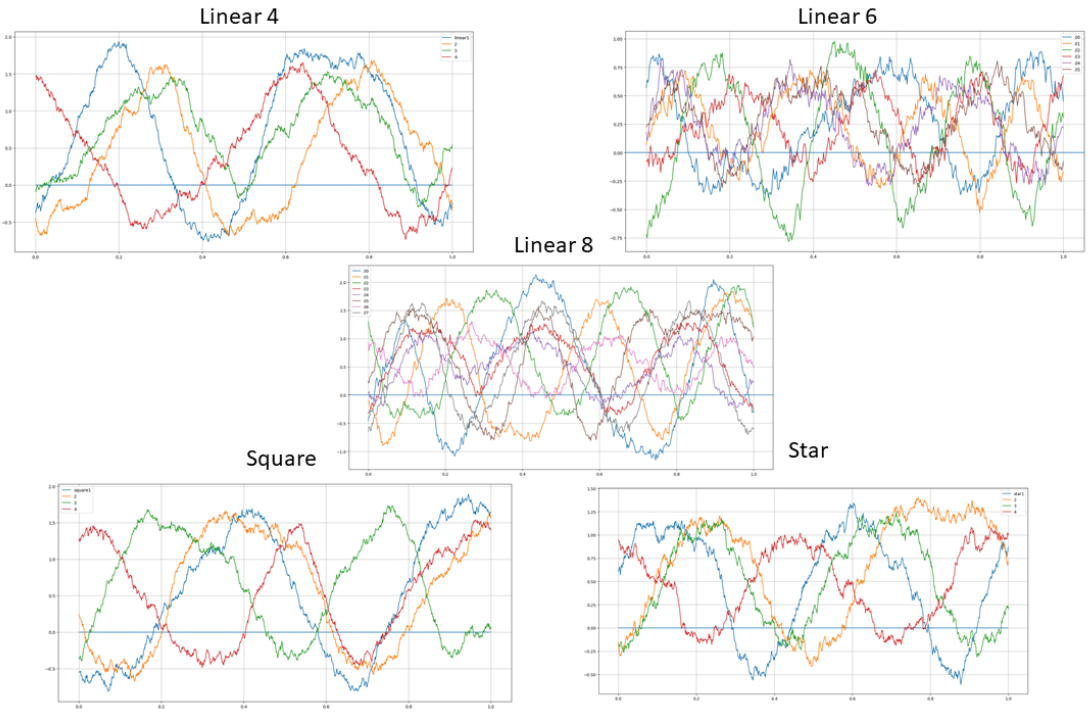

Fig. A.6 ***Cluster nullifiers curve acquisition***. *The masks applied for the acquisition on the Local Oscillator are shown after.*

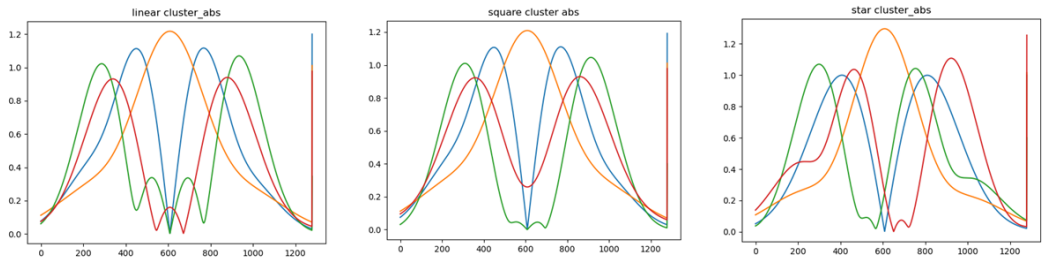

Fig. A.7 ***Cluster nullifiers masks***.

A.4 Other parameters

A.4.1 Coherence

A.4.2 Spectral amplification and deamplification

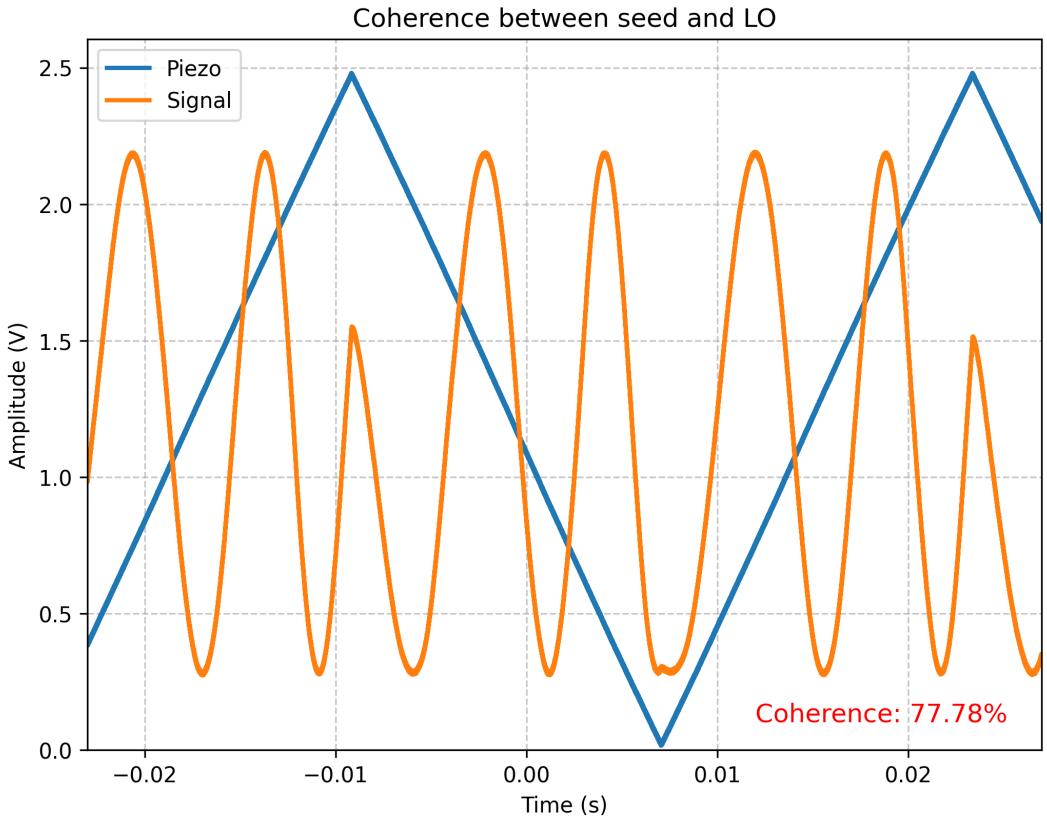

Fig. A.8 ***Coherence acquisition curve***. *Coherence between the local oscillator and the seed.*

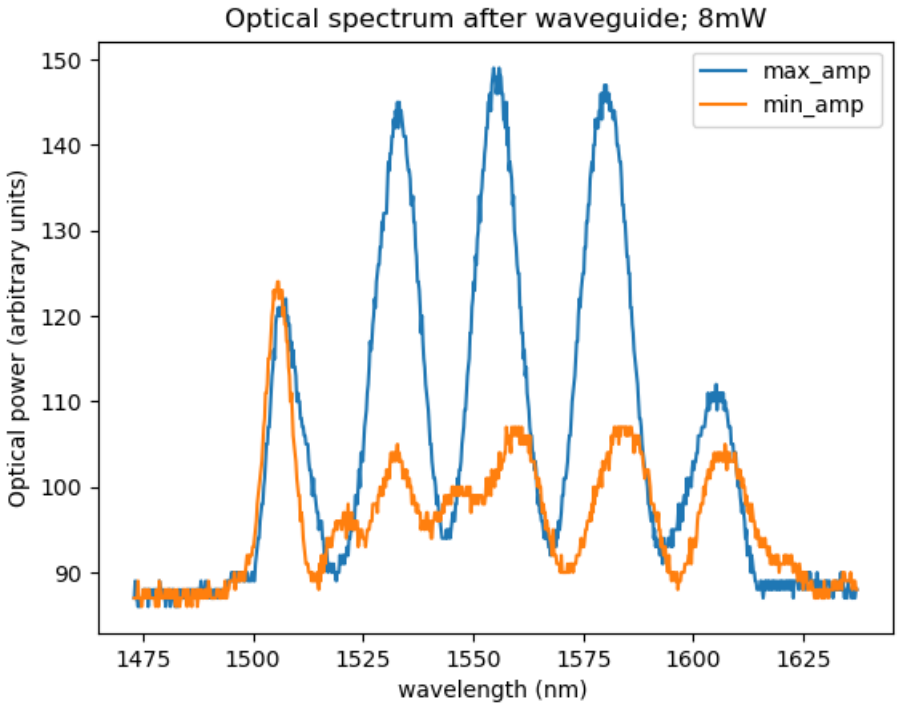

Fig. A.9 ***Phase sensitive amplification in the seed spectrum***. *By looking at the portion of the spectrum that is amplified or deamplified, we can evaluate the order of magnitude of the total bandwith of the signal field. It appears to be about 80 nm in this figure.*

Appendix B

Covariance Matrix Adaptation Evolutionary Algorithm

We give a detailed description of the so-called (μ, λ) Covariance Matrix Adaptation evolutionary algorithm[1] where λ is the number of generated mutants per generation, and μ are the individuals selected to become subsequent parents [Shir et al., 2009]. λ is designed to scale with the dimensionality D of our problem such that :

$$\begin{aligned} \lambda &= 4 + \ln(D) \\ \mu &= \lfloor \frac{\lambda}{2} \rfloor \end{aligned} \tag{B.1}$$

To produce a new generation the algorithm first generates λ perturbations $\vec{z_k} \sim \mathcal{N}(0, 1)$ from the former control point $\langle \vec{x} \rangle^{(i)}$ combined with a multivariate normal distribution parametrized by the statistically learned covariance matrix $\mathbf{\Sigma}$ such as :

$$\Phi_{\mathcal{N}}(\vec{z}) = \frac{1}{\sqrt{(2\pi)^D \det \mathbf{\Sigma}}} \exp\left(-\frac{1}{2} \vec{z}^{\,T} \mathbf{\Sigma}^{-1} \vec{z}\right). \tag{B.2}$$

Σ is a weighted history of the successful evolution path $\vec{p_c}$ in an effort to minimize the effects of noise. The evolution path is calculated this way :

$$\vec{p_c}^{(i+1)} = (1 - c_c)\vec{p_c}^{(i)} + \sqrt{c_c(2 - c_c)\mu_{eff}}\mathbf{R}^{(i)}\Lambda^{(i)1/2}\langle \vec{z} \rangle^{(i+1)}, \tag{B.3}$$

where $c_c = \frac{4}{D+4}$, $\mu_{eff} = \frac{1}{\sum_{k=1}^{\mu} \omega_k^2}$, $\mathbf{R}$ and Λ come from the eigendecomposition of $\mathbf{\Sigma} = \mathbf{R}\Lambda\mathbf{R}^t$. The weights ω_k are defined in (B.11). $\mathbf{\Sigma}$ is then updated according to:

$$\begin{aligned} \mathbf{\Sigma}^{(i+1)} =& (1 - c_{cov})\mathbf{\Sigma}^{(i)} + \frac{c_{cov}}{\mu_{eff}} \vec{p_c}^{(i+1)} \vec{p_c}^{(i+1)T} \\ &+ c_{cov}\left(1 - \frac{1}{\mu_{eff}}\right) \mathbf{R}^{(i)}\Lambda^{(i)1/2} \left(\sum_{k=1}^{\mu} \omega_k \vec{z_k}^{(i+1)} \vec{z_k}^{(i+1)T}\right) \left(\mathbf{R}^{(i)}\Lambda^{(i)1/2}\right)^T \end{aligned} \tag{B.4}$$

[1] In this part λ and μ are standard notation linked to the algorithm, they are different than the correlation strength of the EPR pair described in the main text.

Where $c_{cov} = \frac{2}{(D+\sqrt{2})^2}$ and $\mathbf{\Sigma}^{(0)} = \mathbb{1}$. This statistical covariance matrix is then coupled to a factor σ_g to model an expansion or contraction of the main path. The idea is to begin by exploring a large diversity of offspring, to limit the influence of local minima and then progressively reducing the diversity to look for the precise solution of our problem, as illustrated in Figure 7.6. It is updated as follow

$$\sigma_g^{(i+1)} = \sigma_g^{(i)} \exp\left[\frac{c_\sigma}{d_\sigma}\left(\frac{\left\|\vec{p}_\sigma^{(i+1)}\right\|}{\langle\|\mathcal{N}(0,\mathbf{1})\|\rangle} - 1\right)\right] \tag{B.5}$$

with

$$\begin{aligned} c_\sigma &= \frac{(\mu_{eff}+2)}{(D+\mu_{eff}+3)} \\ d_\sigma &= 1 + c_\sigma \end{aligned} \tag{B.6}$$

and

$$p_\sigma^{(i+1)} = (1-c_\sigma)\vec{p}_\sigma^{(i)} + \sqrt{c_\sigma(2-c_\sigma\mu_{eff})}\mathbf{R}^{(i)}\langle\vec{z}\rangle^{(i+1)}. \tag{B.7}$$

Finaly the λ trial solutions are

$$\vec{x}_k^{(i+1)} = \langle\vec{x}\rangle^{(i)} + \sigma_g^{(i)}\mathbf{R}^{(i)}\Lambda^{(i)1/2}\vec{z}_k^{(i+1)} \tag{B.8}$$

thus we have our new generation of offsprings. We now only need to compute our future control point $\langle\vec{x}\rangle^{(i+1)}$. First we need to evaluate each offspring of the new generation to determine the μ best candidates via the objective function f. We reorder our offspring $(\vec{x}_1, ...\vec{x}_\lambda)$ such that :

$$f(\vec{x}_1) < f(\vec{x}_2) < ... < f(\vec{x}_\lambda) \tag{B.9}$$

then keeping only the μ best candidates we build

$$\langle\vec{x}\rangle^{(i+1)} = \sum_{k=1}^{\mu}\omega_k\vec{x}_k^{(i+1)} \tag{B.10}$$

where the weights are set to give a higher importance to offsprings with better fitness function

$$\omega_k = \frac{\ln\left[(\mu+1)/k\right]}{\sum_{j=1}^{\mu}\ln\left[(\mu+1)/j\right]} \tag{B.11}$$

Bibliography

[Agostini and DiMauro, 2004] Agostini, P. and DiMauro, L. F. (2004). The physics of attosecond light pulses. *Reports on Progress in Physics*, 67(6):813. 50

[Akturk et al., 2006] Akturk, S., Gu, X., Kimmel, M., and Trebino, R. (2006). Extremely simple single-prism ultrashort-pulse compressor. *Opt. Express*, 14(21):10101–10108. 56

[Albash and Lidar, 2018] Albash, T. and Lidar, D. A. (2018). Adiabatic quantum computation. *Reviews of Modern Physics*, 90(1). xii

[Albero et al., 2012] Albero, J., Moreno, I., Davis, J. A., Cottrell, D. M., and Sand, D. (2012). Generalized phase diffraction gratings with tailored intensity. *Optics Letters*, 37(20):4227–4229. Publisher: Optical Society of America. 60

[Andersen et al., 2015] Andersen, U. L., Neergaard-Nielsen, J. S., van Loock, P., and Furusawa, A. (2015). Hybrid discrete and continuous-variable quantum information. *Nature Physics*, 11(9):713–719. xii

[Antoine et al., 1996] Antoine, P., L'Huillier, A., and Lewenstein, M. (1996). Attosecond pulse trains using high–order harmonics. *Phys. Rev. Lett.*, 77:1234–1237. 50

[Appas et al., 2021] Appas, F., Baboux, F., Amanti, M. I., Lemaítre, A., Boitier, F., Diamanti, E., and Ducci, S. (2021). Flexible entanglement-distribution network with an AlGaAs chip for secure communications. *npj Quantum Information*, 7(1). 105

[Appel et al., 2007] Appel, J., Hoffman, D., Figueroa, E., and Lvovsky, A. I. (2007). Electronic noise in optical homodyne tomography. *Physical Review A*, 75(3). 93

[Arvind et al., 1995] Arvind, Dutta, B., Mukunda, N., and Simon, R. (1995). The real symplectic groups in quantum mechanics and optics. *Pramana*, 45(6):471–497. 20

[Arzani et al., 2018] Arzani, F., Fabre, C., and Treps, N. (2018). Versatile engineering of multimode squeezed states by optimizing the pump spectral profile in spontaneous parametric down-conversion. *Phys. Rev. A*, 97:033808. xii, 74

[Arzani et al., 2019] Arzani, F., Ferrini, G., Grosshans, F., and Markham, D. (2019). Random coding for sharing bosonic quantum secrets. *Phys. Rev. A*, 100:022303. 119

[Asavanant et al., 2019] Asavanant, W., Shiozawa, Y., Yokoyama, S., Charoensombutamon, B., Emura, H., Alexander, R. N., Takeda, S., ichi Yoshikawa, J., Menicucci, N. C., Yonezawa, H., and Furusawa, A. (2019). Generation of time-domain-multiplexed two-dimensional cluster state. *Science*, 366(6463):373–376. 119, 138

[Aspect, 2015] Aspect, A. (2015). Closing the Door on Einstein and Bohr's Quantum Debate. *Physics*, 8. Publisher: American Physical Society. xi

[Aspect et al., 1982a] Aspect, A., Dalibard, J., and Roger, G. (1982a). Experimental test of bell's inequalities using time-varying analyzers. *Phys. Rev. Lett.*, 49:1804–1807. xi

[Aspect et al., 1981] Aspect, A., Grangier, P., and Roger, G. (1981). Experimental tests of realistic local theories via bell's theorem. *Phys. Rev. Lett.*, 47:460–463. xi

[Aspect et al., 1982b] Aspect, A., Grangier, P., and Roger, G. (1982b). Experimental realization of einstein-podolsky-rosen-bohm gedankenexperiment: A new violation of bell's inequalities. *Phys. Rev. Lett.*, 49:91–94. xi

[Averchenko et al., 2016] Averchenko, V., Jacquard, C., Thiel, V., Fabre, C., and Treps, N. (2016). Multimode theory of single-photon subtraction. *New Journal of Physics*, 18(8):083042. xii

[Aymeric, 2022] Aymeric, R. (2022). *Convergence of quantum and classical communications*. PhD thesis. Thèse de doctorat dirigée par Jaouën, Yves et Alléaume, Romain Réseaux, Information et Communications Institut polytechnique de Paris 2022. 36

[Barabási and Albert, 1999] Barabási, A.-L. and Albert, R. (1999). Emergence of scaling in random networks. *Science*, 286(5439):509–512. 118, 120

[Barabási and Pósfai, 2016] Barabási, A.-L. and Pósfai, M. (2016). *Network science*. Cambridge University Press, Cambridge. 120

[Barnett, 2009] Barnett, S. (2009). *Quantum information*, volume 16. Oxford University Press. 31

[Bednorz and Müller, 1988] Bednorz, J. G. and Müller, K. A. (1988). Perovskite-type oxides—the new approach to high-T_c superconductivity. *Rev. Mod. Phys.*, 60:585–600. x

[Bell, 1964] Bell, J. S. (1964). On the einstein podolsky rosen paradox. *Physics Physique Fizika*, 1:195–200. xi

[Bennett and Brassard, 1884] Bennett, C. H. and Brassard, G. (1884). Quantum cryptography: Public key distribution and coin tossing. *Theoretical Computer Science*, 560:7–11. xi, 33

[Bertlmann and Krammer, 2008] Bertlmann, R. A. and Krammer, P. (2008). Bloch vectors for qudits. *Journal of Physics A: Mathematical and Theoretical*, 41(23):235303. 125

[Bloch and Messiah, 1962] Bloch, C. and Messiah, A. (1962). The canonical form of an antisymmetric tensor and its application to the theory of superconductivity. *Nuclear Physics*, 39:95–106. 21

[Bohr et al., 1924] Bohr, N., Kramers, H., and Slater, J. (1924). Lxxvi. the quantum theory of radiation. *The London, Edinburgh, and Dublin Philosophical Magazine and Journal of Science*, 47(281):785–802. 4

[Bouwmeester et al., 1997] Bouwmeester, D., Pan, J.-W., Mattle, K., Eibl, M., Weinfurter, H., and Zeilinger, A. (1997). Experimental quantum teleportation. *Nature*, 390(6660):575–579. xi

[Boyd, 2011] Boyd, R. W. (2011). *Non linear optics*. Acad. Press., Amsterdam, Elsevier. 62

[Brausntein and van Loock, 2005] Brausntein, S. and van Loock, P. (2005). Quantum information with continuous variables. *Rev. Mod. Phys.*, 77. 5, 40, 97

[Brecht, 2014] Brecht, B. (2014). *Engineering ultrafast quantum frequency conversion*. PhD thesis. 12, 73, 95

[Browaeys and Lahaye, 2020] Browaeys, A. and Lahaye, T. (2020). Many-body physics with individually controlled rydberg atoms. *Nature Physics*, 16(2):132–142. xi

[Burnham and Weinberg, 1970] Burnham, D. C. and Weinberg, D. L. (1970). Observation of simultaneity in parametric production of optical photon pairs. *Phys. Rev. Lett.*, 25:84–87. 67

[Cai et al., 2017] Cai, Y., Roslund, J., Ferrini, G., Arzani, F., Xu, X., Fabre, C., and Treps, N. (2017). Multimode entanglement in reconfigurable graph states using optical frequency combs. *Nature Communications*, 8:15645. xii, 111

[Cai et al., 2021] Cai, Y., Roslund, J., Thiel, V., Fabre, C., and Treps, N. (2021). Quantum enhanced measurement of an optical frequency comb. *npj Quantum Information*, 7. 96

[Carter and Wegman, 1979] Carter, J. and Wegman, M. N. (1979). Universal classes of hash functions. *Journal of Computer and System Sciences*, 18(2):143–154. 35

[Centrone et al., 2023] Centrone, F., Grosshans, F., and Parigi, V. (2023). Cost and routing of continuous variable quantum networks. 120

[Chabaud et al., 2021] Chabaud, U., Roeland, G., Walschaers, M., Grosshans, F., Parigi, V., Markham, D., and Treps, N. (2021). Certification of non-gaussian states with operational measurements. *PRX Quantum*, 2:020333. xii

[Chalopin et al., 2009] Chalopin, B., Patera, G., de Valcárcel, G. J., Treps, N., and Fabre, C. (2009). Multimode opos as sources for multipartite entanglement. In *Conference on Lasers and Electro-Optics/International Quantum Electronics Conference*, page IThK2. Optica Publishing Group. xii

[Cladé et al., 2019] Cladé, P., Nez, F., Biraben, F., and Guellati-Khelifa, S. (2019). State of the art in the determination of the fine-structure constant and the ratio h/mu. *Comptes Rendus Physique*, 20(1-2):77–91. 49

[Clauser et al., 1969] Clauser, J. F., Horne, M. A., Shimony, A., and Holt, R. A. (1969). Proposed experiment to test local hidden-variable theories. *Phys. Rev. Lett.*, 23:880–884. xi

[Clements et al., 2016] Clements, W. R., Humphreys, P. C., Metcalf, B. J., Kolthammer, W. S., and Walmsley, I. A. (2016). Optimal design for universal multiport interferometers. *Optica*, 3(12):1460–1465. 121

[Crystals, 2016] Crystals, U. (2016). Properties of ktp/kta single crystal. 72

[Dabbousi et al., 1997] Dabbousi, B. O., Rodríguez-Viejo, J., Mikulec, F. V., Heine, J., Mattoussi, H., Ober, R., Jensen, K. F., and Bawendi, M. G. (1997). (cdse)zns core-shell quantum dots: synthesis and characterization of a size series of highly luminescent nanocrystallites. *The Journal of Physical Chemistry B*, 101:9463–9475. xi

[Daor et al., 1999] Daor, J., Daemen, J., and Rijmen, V. (1999). Aes proposal: rijndael. 33

[Darrigol, 2012] Darrigol, O. (2012). *A History of Optics From Greek Antiquity to the Nineteenth Century*. Oxford University Press. ix

[de Valcárcel et al., 2006] de Valcárcel, G. J., Patera, G., Treps, N., and Fabre, C. (2006). Multimode squeezing of frequency combs. *Phys. Rev. A*, 74:061801. xii

[Delsart, 2008] Delsart, C. (2008). *Lasers et optique non linéaire: cours, exercices et problèmes corrigés*. Physique-LMD, universités-écoles d'ingénieurs. Ellipses. 48

[Demarie, 2012] Demarie, T. F. (2012). Pedagogical introduction to the entropy of entanglement for gaussian states. 32

[den Nest et al., 2006] den Nest, M. V., Miyake, A., Dür, W., and Briegel, H. J. (2006). Universal resources for measurement-based quantum computation. *Physical Review Letters*, 97(15). 22

[Denys et al., 2021] Denys, A., Brown, P., and Leverrier, A. (2021). Explicit asymptotic secret key rate of continuous-variable quantum key distribution with an arbitrary modulation. *Quantum*, 5:540. 35

[Deutsch and Jozsa, 1992] Deutsch, D. and Jozsa, R. (1992). Rapid solution of problems by quantum computation. *Proceedings of the Royal Society of London. Series A: Mathematical and Physical Sciences*, 439(1907):553–558. xi

[Devetak and Winter, 2005] Devetak, I. and Winter, A. (2005). Distillation of secret key and entanglement from quantum states. *Proceedings of the Royal Society A: Mathematical, Physical and Engineering Sciences*, 461(2053):207–235. 39

[Diffie and Hellman, 1976] Diffie, W. and Hellman, M. E. (1976). New directions in cryptography. *IEEE Trans. Inf. Theory*, 22(6):644–654. 33

[Doherty et al., 2013] Doherty, M. W., Manson, N. B., Delaney, P., Jelezko, F., Wrachtrup, J., and Hollenberg, L. C. (2013). The nitrogen-vacancy colour centre in diamond. *Physics Reports*, 528(1):1–45. xi

[Domeneguetti et al., 2023] Domeneguetti, R., Stefszky, M., Herrmann, H., Silberhorn, C., Andersen, U. L., Neergaard-Nielsen, J. S., and Gehring, T. (2023). Fully guided and phase locked ti:ppln waveguide squeezing for applications in quantum sensing. *Opt. Lett.*, 48(11):2999–3002. 69

[Ducci et al., 2001] Ducci, S., Treps, N., Maître, A., and Fabre, C. (2001). Pattern formation in optical parametric oscillators. *Phys. Rev. A*, 64:023803. xii

[Dufour, 2018] Dufour, A. (2018). *Ingénierie d'états quantiques multimodes avec des impulsions femtosecondes*. Theses, Sorbonne Université. xii, 101

[Dür et al., 2003] Dür, W., Aschauer, H., and Briegel, H.-J. (2003). Multiparticle entanglement purification for graph states. *Phys. Rev. Lett.*, 91:107903. 22

[Dushman, 1935] Dushman, S. (1935). *The Elements of Quantum Theory, chapter 4 : the linear harmonic oscillator*. The Elements of Quantum Mechanics. 4

[Dutton, 1998] Dutton, H. (1998). *Understanding Optical Communications*. Prentice Hall. 68

[Ehrenfest, 1911] Ehrenfest, P. (1911). Welche Züge der Lichtquantenhypothese spielen in der Theorie der Wärmestrahlung eine wesentliche Rolle? ix

[Einstein et al., 1935] Einstein, A., Podolsky, B., and Rosen, N. (1935). Can quantum-mechanical description of physical reality be considered complete? *Phys. Rev.*, 47:777–780. x, 18

[Ekert, 1991] Ekert, A. K. (1991). Quantum cryptography based on bell's theorem. *Phys. Rev. Lett.*, 67:661–663. xi, 33

[Elmokashfi et al., 2010] Elmokashfi, A., Kvalbein, A., and Dovrolis, C. (2010). On the scalability of bgp: The role of topology growth. *IEEE Journal on Selected Areas in Communications*, 28(8):1250–1261. 118

[Erdös and Rényi, 1959] Erdös, P. and Rényi, A. (1959). On random graphs i. *Publicationes Mathematicae Debrecen*, 6:290. 119

[Fabre, 1997] Fabre, C. (1997). Quantum fluctuations in light beams. 82

[Fabre et al., 1989] Fabre, C., Giacobino, E., Heidmann, A., and Reynaud, S. (1989). Noise characteristics of a non-degenerate optical parametric oscillator - application to quantum noise reduction. *Journal De Physique*, 50:1209–1225. xii

[Fabre et al., 1994] Fabre, C., Pinard, M., Bourzeix, S., Heidmann, A., Giacobino, E., and Reynaud, S. (1994). Quantum-noise reduction using a cavity with a movable mirror. *Phys. Rev. A*, 49:1337–1343. xii

[Fabre and Treps, 2020] Fabre, C. and Treps, N. (2020). Modes and states in quantum optics. *Reviews of Modern Physics*, 92(3):035005. Publisher: American Physical Society. 7, 57

[Fano, 1961] Fano, U. (1961). Quantum Theory of Interference Effects in the Mixing of Light from Phase-Independent Sources. *American Journal of Physics*, 29(8):539–545. 67

[Ferraro et al., 2005] Ferraro, A., Olivares, S., and Paris, M. G. A. (2005). Gaussian states in continuous variable quantum information. 13

[Ferrini et al., 2015] Ferrini, G., Roslund, J., Arzani, F., Cai, Y., Fabre, C., and Treps, N. (2015). Optimization of networks for measurement-based quantum computation. *Physical Review A*, 91(3). 24

[Feynman, 1982] Feynman, R. P. (1982). Simulating physics with computers. *International journal of theoretical physics*, 21(6/7):467–488. xi

[Fortier and Baumann, 2019] Fortier, T. and Baumann, E. (2019). 20 years of developments in optical frequency comb technology and applications. *Communications Physics*, 2(1). 49

[Freedman and Clauser, 1972] Freedman, S. J. and Clauser, J. F. (1972). Experimental test of local hidden-variable theories. *Phys. Rev. Lett.*, 28:938–941. xi

[Froehly et al., 1983] Froehly, C., Colombeau, B., and Vampouille, M. (1983). Ii shaping and analysis of picosecond light pulses. volume 20 of *Progress in Optics*, pages 63–153. Elsevier. 57

[Furusawa et al., 1998] Furusawa, A., Sørensen, J. L., Braunstein, S. L., Fuchs, C. A., Kimble, H. J., and Polzik, E. S. (1998). Unconditional quantum teleportation. *Science*, 282(5389):706–709. xii

[Georgescu et al., 2014] Georgescu, I., Ashhab, S., and Nori, F. (2014). Quantum simulation. *Reviews of Modern Physics*, 86(1):153–185. xii

[Ghosh and Mandel, 1987] Ghosh, R. and Mandel, L. (1987). Observation of nonclassical effects in the interference of two photons. *Phys. Rev. Lett.*, 59:1903–1905. xi

[Gigan, 2004] Gigan, S. (2004). *Amplification paramétrique d'images en cavité : effets classiques et quantiques*. PhD thesis. Thèse de doctorat dirigée par Fabre, Claude Laser et matière Paris 6 2004. 86

[Gisin et al., 2002] Gisin, N., Ribordy, G., Tittel, W., and Zbinden, H. (2002). Quantum cryptography. *Rev. Mod. Phys.*, 74:145–195. 68

[Giustina et al., 2015] Giustina, M., Versteegh, M. A. M., Wengerowsky, S., Handsteiner, J., Hochrainer, A., Phelan, K., Steinlechner, F., Kofler, J., Larsson, J.-A., Abellán, C., Amaya, W., Pruneri, V., Mitchell, M. W., Beyer, J., Gerrits, T., Lita, A. E., Shalm, L. K., Nam, S. W., Scheidl, T., Ursin, R., Wittmann, B., and Zeilinger, A. (2015). Significant-loophole-free test of bell's theorem with entangled photons. *Phys. Rev. Lett.*, 115:250401. xi

[Glauber, 1963] Glauber, R. J. (1963). Coherent and incoherent states of the radiation field. *Phys. Rev.*, 131:2766–2788. 11, 67

[Golub and Loan, 1996] Golub, G. H. and Loan, C. F. V. (1996). *Matrix computations*. Johns Hopkins Universtiy Press. 125

[Grosshans, 2005] Grosshans, F. (2005). Collectiveattacks and unconditional security in continuous variable quantum keydistribution. *Phys. Rev. Lett.*, 94:020504. 112

[Grosshans et al., 2003] Grosshans, F., Cerf, N. J., Wenger, J., Tualle-Brouri, R., and Grangier, P. (2003). Virtual entanglement and reconciliation protocols for quantum cryptography with continuous variables. 35

[Grosshans and Grangier, 2002] Grosshans, F. and Grangier, P. (2002). Continuous variable quantum cryptography using coherent states. *Phys. Rev. Lett.*, 88:057902. xii, 34

[Grover, 1996] Grover, L. K. (1996). A fast quantum mechanical algorithm for database search. xi

[Grynberg et al., 2010] Grynberg, G., Aspect, A., and Fabre, C. (2010). *Introduction to Quantum Optics: From the Semi-classical Approach to Quantized Light*. Cambridge University Press. 8, 46, 80

[Gu et al., 2009] Gu, M., Weedbrook, C., Menicucci, N. C., Ralph, T. C., and van Loock, P. (2009). Quantum computing with continuous-variable clusters. *Phys. Rev. A*, 79:062318. 120

[Gupta et al., 2020] Gupta, P., Speirs, R. W., Jones, K. M., and Lett, P. D. (2020). Effect of imperfect homodyne visibility on multi-spatial-mode two-mode squeezing measurements. *Optics Express*, 28(1):652. 95

[Hache, 2016] Hache, F. (2016). *Optique non linéaire*. EDP Sciences. 46, 47, 55, 64, 66, 70

[Hall, 2006] Hall, J. L. (2006). Nobel lecture: Defining and measuring optical frequencies. *Rev. Mod. Phys.*, 78:1279–1295. xii

[Hänsch, 1972] Hänsch, T. W. (1972). Repetitively pulsed tunable dye laser for high resolution spectroscopy. *Appl. Opt.*, 11(4):895–898. xii

[Hansen and Ostermeier, 2001] Hansen, N. and Ostermeier, A. (2001). Completely derandomized self-adaptation in evolution strategies. *Evolutionary Computation*, 9(2):159–195. 124

[Harris et al., 1967] Harris, S. E., Oshman, M. K., and Byer, R. L. (1967). Observation of tunable optical parametric fluorescence. *Phys. Rev. Lett.*, 18:732–734. 67

[Heidmann et al., 1987] Heidmann, A., Horowicz, R. J., Reynaud, S., Giacobino, E., Fabre, C., and Camy, G. (1987). Observation of quantum noise reduction on twin laser beams. *Phys. Rev. Lett.*, 59:2555–2557. xii

[Hein et al., 2006] Hein, M., Dür, W., Eisert, J., Raussendorf, R., den Nest, M. V., and Briegel, H. J. (2006). Entanglement in graph states and its applications. 22

[Heisenberg, 1927] Heisenberg, W. (1927). Über den anschaulichen inhalt der quantentheoretischen kinematik und mechanik. *Zeitschrift für Physik*. 5

[Hensen et al., 2015] Hensen, B., Bernien, H., Dréau, A. E., Reiserer, A., Kalb, N., Blok, M. S., Ruitenberg, J., Vermeulen, R. F. L., Schouten, R. N., Abellán, C., Amaya, W., Pruneri, V., Mitchell, M. W., Markham, M., Twitchen, D. J., Elkouss, D., Wehner, S., Taminiau, T. H., and Hanson, R. (2015). Loophole-free Bell inequality violation using electron spins separated by 1.3 kilometres. *Nature*, 526(7575):682–686. Number: 7575 Publisher: Nature Publishing Group. xi

[Holevo, 1973] Holevo, A. S. (1973). Bounds for the quantity of information transmitted by a quantum communication channel. 33

[Horodecki et al., 2009] Horodecki, R., Horodecki, P., Horodecki, M., and Horodecki, K. (2009). Quantum entanglement. *Reviews of Modern Physics*, 81(2):865–942. 75

[Horoshko et al., 2019] Horoshko, D. B., Volpe, L. L., Arzani, F., Treps, N., Fabre, C., and Kolobov, M. I. (2019). Bloch-messiah reduction for twin beams of light. *Physical Review A*, 100(1). 21

[Huo et al., 2020] Huo, N., Liu, Y., Li, J., Cui, L., Chen, X., Palivela, R., Xie, T., Li, X., and Ou, Z. (2020). Direct temporal mode measurement for the characterization of temporally multiplexed high dimensional quantum entanglement in continuous variables. *Physical Review Letters*, 124(21). 87

[Husimi, 1940] Husimi, K. (1940). Some formal properties of the density matrix. 11

[Hänsel et al., 2017] Hänsel, W., Hoogland, H., Giunta, M., Schmid, S., Steinmetz, T., Doubek, R., Mayer, P., Dobner, S., Cleff, C., Fischer, M., and Holzwarth, R. (2017). All polarization-maintaining fiber laser architecture for robust femtosecond pulse generation. *Applied Physics B*, 123. 50, 53

[Ispolatov et al., 2005] Ispolatov, I., Krapivsky, P. L., and Yuryev, A. (2005). Duplication-divergence model of protein interaction network. *Phys. Rev. E*, 71:061911. 118

[Jaksch et al., 2000] Jaksch, D., Cirac, J. I., Zoller, P., Rolston, S. L., Côté, R., and Lukin, M. D. (2000). Fast quantum gates for neutral atoms. *Physical Review Letters*, 85(10):2208–2211. xi

[Jouguet et al., 2011] Jouguet, P., Kunz-Jacques, S., and Leverrier, A. (2011). Long-distance continuous-variable quantum key distribution with a gaussian modulation. *Physical Review A*, 84(6). 35

[Kadowaki and Nishimori, 1998] Kadowaki, T. and Nishimori, H. (1998). Quantum annealing in the transverse ising model. *Phys. Rev. E*, 58:5355–5363. xii

[Kapitza, 1967] Kapitza (1967). *Collected Papers of P.L. Kapitza. Volume 3*. Elsevier. x

[Kimble, 2008] Kimble, H. J. (2008). The quantum internet. *Nature*, 453(7198):1023–1030. 117

[Kleis et al., 2017] Kleis, S., Rueckmann, M., and Schaeffer, C. G. (2017). Continuous variable quantum key distribution with a real local oscillator using simultaneous pilot signals. *Opt. Lett.*, 42(8):1588–1591. 113

[Koblitz, 1987] Koblitz, N. (1987). Elliptic curve cryptosystems. *Mathematics of Computation*, 48:203–209. 33

[Kolobov and Fabre, 2000] Kolobov, M. I. and Fabre, C. (2000). Quantum limits on optical resolution. *Phys. Rev. Lett.*, 85:3789–3792. xii

[Kouadou, 2021] Kouadou, T. (2021). *Single-Pass Generation and Detection of Ultrafast Multimode Squeezed Light*. Theses, Sorbonne Université. 60, 111

[Kouadou et al., 2023] Kouadou, T., Sansavini, F., Ansquer, M., Henaff, J., Treps, N., and Parigi, V. (2023). Spectrally shaped and pulse-by-pulse multiplexed multimode squeezed states of light. *APL Photonics*, 8(8). xiii, 73, 77, 111

[Kouadou et al., 2019] Kouadou, T., Volpe, L. L., De, S., Fabre, C., Parigi, V., and Treps, N. (2019). Single-pass generation of spatial and spectral multimode squeezed states of light. In *Frontiers in Optics + Laser Science APS/DLS*, page FTh3B.7. Optica Publishing Group. xii

[Kovalenko et al., 2021] Kovalenko, O., Ra, Y.-S., Cai, Y., Usenko, V. C., Fabre, C., Treps, N., and Filip, R. (2021). Frequency-multiplexed entanglement for continuous-variable quantum key distribution. *Photon. Res.*, 9(12):2351–2359. 106, 108, 111

[Krausz, 2016] Krausz, F. (2016). The birth of attosecond physics and its coming of age. *Physica Scripta*, 91(6):063011. 50

[Kulkarni et al., 2022] Kulkarni, G., Rioux, J., Braverman, B., Chekhova, M. V., and Boyd, R. W. (2022). Classical model of spontaneous parametric down-conversion. *Physical Review Research*, 4(3). 67

[Kumar et al., 2012] Kumar, R., Barrios, E., MacRae, A. J., Cairns, E. C., Huntington, E. H., and Lvovsky, A. I. (2012). Versatile wideband balanced detector for quantum optical homodyne tomography. *Optics Communications*, 285:5259–5267. 93

[La Porta and Slusher, 1991] La Porta, A. and Slusher, R. E. (1991). Squeezing limits at high parametric gains. *Phys. Rev. A*, 44:2013–2022. 86

[La Volpe, 2019] La Volpe, L. (2019). *Géneration d'états comprimés en simple passage et modes spatio-temporels*. PhD thesis. Thèse de doctorat dirigée par Treps, Nicolas et Fabre, Claude Physique Sorbonne université 2019. 7

[La Volpe et al., 2018] La Volpe, L., De, S., Kouadou, T., Parigi, V., Fabre, C., and Treps, N. (2018). A single-pass quantum source of multimode squeezed states of light. In *2018 European Conference on Optical Communication (ECOC)*, pages 1–3. xii

[Larsen et al., 2019] Larsen, M. V., Guo, X., Breum, C. R., Neergaard-Nielsen, J. S., and Andersen, U. L. (2019). Deterministic generation of a two-dimensional cluster state. *Science*, 366(6463):369–372. 119, 138

[Laudenbach et al., 2018] Laudenbach, F., Pacher, C., Fung, C.-H. F., Poppe, A., Peev, M., Schrenk, B., Hentschel, M., Walther, P., and Hübel, H. (2018). Continuous-variable quantum key distribution with gaussian modulation—the theory of practical implementations. *Advanced Quantum Technologies*, 1(1). 30, 34, 110

[Laurat et al., 2003] Laurat, J., Coudreau, T., Treps, N., Maître, A., and Fabre, C. (2003). Conditional preparation of a quantum state in the continuous variable regime: Generation of a sub-poissonian state from twin beams. *Phys. Rev. Lett.*, 91:213601. xii

[Leibfried et al., 2003] Leibfried, D., Blatt, R., Monroe, C., and Wineland, D. (2003). Quantum dynamics of single trapped ions. *Rev. Mod. Phys.*, 75:281–324. xi

[Leonhardt and Beck, 1998] Leonhardt, U. and Beck, M. (1998). Measuring the Quantum State of Light. *American Journal of Physics*, 66(6):550–551. 29

[Leverrier, 2015] Leverrier, A. (2015). Composable security proof for continuous-variable quantum key distribution with coherent states. *Phys. Rev. Lett.*, 114:070501. 34, 112

[Leverrier et al., 2008] Leverrier, A., Allé aume, R., Boutros, J., Zémor, G., and Grangier, P. (2008). Multidimensional reconciliation for a continuous-variable quantum key distribution. *Physical Review A*, 77(4). 35

[Leverrier et al., 2013] Leverrier, A., García-Patrón, R., Renner, R., and Cerf, N. J. (2013). Security of continuous-variable quantum key distribution against general attacks. *Phys. Rev. Lett.*, 110:030502. 108

[Leverrier and Grangier, 2009] Leverrier, A. and Grangier, P. (2009). Unconditional security proof of long-distance continuous-variable quantum key distribution with discrete modulation. *Phys. Rev. Lett.*, 102:180504. 34

[Leverrier and Grangier, 2010] Leverrier, A. and Grangier, P. (2010). Simple proof that gaussian attacks are optimal among collective attacks against continuous-variable quantum key distribution with a gaussian modulation. *Phys. Rev. A*, 81:062314. 37

[Leverrier et al., 2010] Leverrier, A., Grosshans, F., and Grangier, P. (2010). Finite-size analysis of a continuous-variable quantum key distribution. *Physical Review A*, 81(6). 37

[Liu et al., 2016] Liu, N., Liu, Y., Li, J., Yang, L., and Li, X. (2016). Generation of multi-mode squeezed vacuum using pulse pumped fiber optical parametric amplifiers. *Opt. Express*, 24(3):2125–2133. 106

[Loudon, 1983] Loudon, R. (1983). *The Quantum Theory of Light*. Oxford science publications. Clarendon Press. 16, 81

[Lugiato et al., 1988] Lugiato, L. A., Oldano, C., Fabre, C., Giacobino, E., and Horowicz, R. J. (1988). Bistability, self-pulsing and chaos in optical parametric oscillators. *Il Nuovo Cimento D*, 10:959–977. xii

[Lvovsky and Raymer, 2009] Lvovsky, A. I. and Raymer, M. G. (2009). Continuous-variable optical quantum-state tomography. *Rev. Mod. Phys.*, 81:299–332. 105

[Ma et al., 2007] Ma, X., Fung, C.-H. F., and Lo, H.-K. (2007). Quantum key distribution with entangled photon sources. *Physical Review A*, 76(1). 105

[Madsen et al., 2012] Madsen, L. S., Usenko, V. C., Lassen, M., Filip, R., and Andersen, U. L. (2012). Continuous variable quantum key distribution with modulated entangled states. *Nature Communications*. 105

[Magde and Mahr, 1967] Magde, D. and Mahr, H. (1967). Study in ammonium dihydrogen phosphate of spontaneous parametric interaction tunable from 4400 to 16 000 å. *Phys. Rev. Lett.*, 18:905–907. 67

[Maiman, 1960] Maiman, T. H. (1960). Ruby laser systems. US Patent. x

[Mari and Eisert, 2012] Mari, A. and Eisert, J. (2012). Positive wigner functions render classical simulation of quantum computation efficient. *Phys. Rev. Lett.*, 109:230503. xii

[Maxwell, 1865] Maxwell, J. C. (1865). Viii. a dynamical theory of the electromagnetic field. *Philosophical Transactions of the Royal Society of London*, 155:459–512. ix

[Medeiros de Araújo et al., 2014] Medeiros de Araújo, R., Roslund, J., Cai, Y., Ferrini, G., Fabre, C., and Treps, N. (2014). Full characterization of a highly multimode entangled state embedded in an optical frequency comb using pulse shaping. *Phys. Rev. A*, 89:053828. 77

[Menicucci, 2014] Menicucci, N. C. (2014). Fault-tolerant measurement-based quantum computing with continuous-variable cluster states. *Phys. Rev. Lett.*, 112:120504. 22

[Menicucci et al., 2011] Menicucci, N. C., Flammia, S. T., and van Loock, P. (2011). Graphical calculus for gaussian pure states. *Phys. Rev. A*, 83:042335. 22, 121

[Menicucci et al., 2006] Menicucci, N. C., van Loock, P., Gu, M., Weedbrook, C., Ralph, T. C., and Nielsen, M. A. (2006). Universal quantum computation with continuous-variable cluster states. *Phys. Rev. Lett.*, 97:110501. xii, 22

[Mertz et al., 1991] Mertz, J., Debuisschert, T., Heidmann, A., Fabre, C., and Giacobino, E. (1991). Improvements in the observed intensity correlation of optical parametric oscillator twin beams. *Opt. Lett.*, 16(16):1234–1236. xii

[Michel, 2021] Michel, T. (2021). *Optimization of the pump spectral shape in a parametric down conversion process to generate multimode entangled states.* PhD thesis, Research School of Physics, ANU College of Science, The Australian National University. 59, 61

[Miller, 1986] Miller, V. S. (1986). Use of elliptic curves in cryptography. In Williams, H. C., editor, *Advances in Cryptology — CRYPTO '85 Proceedings*, pages 417–426, Berlin, Heidelberg. Springer Berlin Heidelberg. 33

[Monmayrant, 2019] Monmayrant, A. (2019). *Lumière façonnée et matière structurée (et vice versa).* Habilitation à diriger des recherches, Institut national polytechnique de Toulouse (INPT). 59

[Monmayrant et al., 2010] Monmayrant, A., Weber, S., and Chatel, B. (2010). A newcomer's guide to ultrashort pulse shaping and characterization. *Journal of Physics B: Atomic, Molecular and Optical Physics*, 43(10):103001. 57

[Neumann, 1932] Neumann, J. v. (1932). *Mathematical Foundations of Quantum Mechan.* 10, 32

[Newman, 2018] Newman, M. (2018). *Networks*. OUP Oxford. 120

[Nielsen and Chuang, 2010] Nielsen, M. A. and Chuang, I. L. (2010). *Quantum Computation and Quantum Information: 10th Anniversary Edition*. Cambridge University Press. 5, 11, 29

[Nokkala et al., 2018] Nokkala, J., Arzani, F., Galve, F., Zambrini, R., Maniscalco, S., Piilo, J., Treps, N., and Parigi, V. (2018). Reconfigurable optical implementation of quantum complex networks. *New Journal of Physics*, 20(5):053024. xii, 22

[Nokkala et al., 2020] Nokkala, J., Martínez-Peña, R., Giorgi, G. L., Parigi, V., Soriano, M. C., and Zambrini, R. (2020). Gaussian states provide universal and versatil quantum reservoir computing. xiii

[O'Brien, 2007] O'Brien, J. L. (2007). Optical quantum computing. *Science*, 318(5856):1567–1570. 68

[Onnes, 1991] Onnes, H. K. (1991). *Further experiments with Liquid Helium. G. On the Electrical Resistance of Pure Metals, etc. VI. On the Sudden Change in the Rate at which the Resistance of Mercury Disappears.*, pages 267–272. Springer Netherlands, Dordrecht. x

[Pacher et al., 2015] Pacher, C., Abidin, A., Lorünser, T., Peev, M., Ursin, R., Zeilinger, A., and Larsson, J.-Å. (2015). Attacks on quantum key distribution protocols that employ non-ITS authentication. *Quantum Information Processing*, 15(1):327–362. 36

[Patera et al., 2009] Patera, G., Treps, N., Fabre, C., and de Valcárcel, G. J. (2009). Quantum theory of synchronously pumped type i optical parametric oscillators: characterization of the squeezed supermodes. *The European Physical Journal D*, 56(1):123–140. xii, 73

[Paulsen, 2003] Paulsen, V. (2003). *Completely Bounded Maps and Operator Algebras.* 28

[Pinel et al., 2012] Pinel, O., Jian, P., de Araújo, R. M., Feng, J., Chalopin, B., Fabre, C., and Treps, N. (2012). Generation and characterization of multimode quantum frequency combs. *Phys. Rev. Lett.*, 108:083601. xii, 68

[Pirandola et al., 2020] Pirandola, S., Andersen, U. L., Banchi, L., Berta, M., Bunandar, D., Colbeck, R., Englund, D., Gehring, T., Lupo, C., Ottaviani, C., Pereira, J. L., Razavi, M., Shaari, J. S., Tomamichel, M., Usenko, V. C., Vallone, G., Villoresi, P., and Wallden, P. (2020). Advances in quantum cryptography. *Adv. Opt. Photon.*, 12(4):1012–1236. xi, 34

[Pirandola et al., 2015] Pirandola, S., Laurenza, R., Ottaviani, C., and Banchi, L. (2015). Fundamental limits of repeaterless quantum communications. *Nature Communications*, 8. 40

[Pirandola and Mancini, 2006] Pirandola, S. and Mancini, S. (2006). Quantum teleportation with continuous variables: A survey. *Laser Physics*, 16(10):1418–1438. 124

[Planck, 1900] Planck, M. (1900). 1 - on an improvement of wien's equation for the spectrum. ix

[Qi et al., 2015] Qi, B., Lougovski, P., Pooser, R., Grice, W., and Bobrek, M. (2015). Generating the local oscillator "locally" in continuous-variable quantum key distribution based on coherent detection. *Phys. Rev. X*, 5:041009. 113

[Qu and Djordjevic, 2017] Qu, Z. and Djordjevic, I. B. (2017). High-speed free-space optical continuous-variable quantum key distribution enabled by three-dimensional multiplexing. *Opt. Express*, 25(7):7919–7928. 105

[Ra et al., 2019] Ra, Y.-S., Dufour, A., Walschaers, M., Jacquard, C., Michel, T., Fabre, C., and Treps, N. (2019). Non-gaussian quantum states of a multimode light field. *Nature Physics*, 16(2):144–147. xii

[Raabe et al., 2017] Raabe, N., Feng, T., Mero, M., Tian, H., Song, Y., Hänsel, W., Holzwarth, R., Sell, A., Zach, A., and Steinmeyer, G. (2017). Excess carrier-envelope phase noise generation in saturable absorbers. *Opt. Lett.*, 42(6):1068–1071. 53

[Rasputnyi et al., 2022] Rasputnyi, A. V., Kopylov, D. A., Murzina, T. V., and Chekhova, M. V. (2022). Cascaded frequency up-conversion of bright squeezed vacuum: spectral and correlation properties. *Opt. Lett.*, 47(4):766–769. 66

[Raussendorf and Briegel, 2001] Raussendorf, R. and Briegel, H. J. (2001). A one-way quantum computer. *Phys. Rev. Lett.*, 86:5188–5191. 22

[Raussendorf et al., 2003] Raussendorf, R., Browne, D. E., and Briegel, H. J. (2003). Measurement-based quantum computation on cluster states. *Phys. Rev. A*, 68:022312. 22

[Renault, 2022] Renault, P. (2022). *Non Markovian behavior and spectral density measurement in optical quantum networks*. Theses, Sorbonne Université. 60, 61

[Renault et al., 2023] Renault, P., Nokkala, J., Roeland, G., Joly, N., Zambrini, R., Maniscalco, S., Piilo, J., Treps, N., and Parigi, V. (2023). Experimental optical simulator of reconfigurable and complex quantum environment. xiii, 22

[Renner and Cirac, 2009] Renner, R. and Cirac, J. I. (2009). de finetti representation theorem for infinite-dimensional quantum systems and applications to quantum cryptography. *Phys. Rev. Lett.*, 102:110504. 108

[Richardson and Urbanke, 2008] Richardson, T. and Urbanke, R. (2008). *Modern Coding Theory*. 35

[Rivest et al., 1978] Rivest, R. L., Shamir, A., and Adleman, L. (1978). A method for obtaining digital signatures and public-key cryptosystems. *Commun. ACM*, 21(2):120–126. 33

[Robertson, 1929] Robertson, H. P. (1929). The uncertainty principle. *Phys. Rev.*, 34:163–164. 5

[Román Rodríguez, 2022] Román Rodríguez, V. (2022). *Quantum Optics Systems for Long-Distance Cryptography and Quantum Networks*. Theses, Sorbonne Université. xiii, 69, 80, 84

[Roman-Rodriguez et al., 2021] Roman-Rodriguez, V., Brecht, B., K, S., Silberhorn, C., Treps, N., Diamanti, E., and Parigi, V. (2021). Continuous variable multimode quantum states via symmetric group velocity matching. *New Journal of Physics*, 23(4):043012. xiii, 53, 64, 68, 74, 83

[Roman-Rodriguez et al., 2023] Roman-Rodriguez, V., Fainsin, D., Zanin, G. L., Treps, N., Diamanti, E., and Parigi, V. (2023). Spectrally multimode squeezed states generation at telecom wavelengths. xiii, 73, 80

[Roslund et al., 2013] Roslund, J., de Araújo, R. M., Jiang, S., Fabre, C., and Treps, N. (2013). Wavelength-multiplexed quantum networks with ultrafast frequency combs. *Nature Photonics*, 8(2):109–112. xii

[Roumestan, 2022] Roumestan, F. (2022). *Advanced signal processing techniques for continuous variable quantum key distribution over optical fiber*. Theses, Sorbonne Université. 113

[Sansavini and Parigi, 2019] Sansavini, F. and Parigi, V. (2019). Continuous variables graph states shaped as complex networks: Optimization and manipulation. *Entropy*, 22(1):26. xiii, 118, 121, 127, 128, 136

[Scarani et al., 2009] Scarani, V., Bechmann-Pasquinucci, H., Cerf, N. J., Dušek, M., Lütkenhaus, N., and Peev, M. (2009). The security of practical quantum key distribution. *Rev. Mod. Phys.*, 81:1301–1350. 34, 36

[Schlingemann and Werner, 2001] Schlingemann, D. and Werner, R. F. (2001). Quantum error-correcting codes associated with graphs. *Phys. Rev. A*, 65:012308. 22

[Schmidt, 1907] Schmidt, E. I. G. (1907). Zur theorie der linearen und nichtlinearen integralgleichungen. *Mathematische Annalen*, 63:433–476. 11

[SCHOTT, 2017] SCHOTT (2017). Refractive index of sf10. 57

[Schwob et al., 1998] Schwob, C., Cohadon, P., Fabre, C., Marte, M., Ritsch, H., Gatti, A., and Lugiato, L. (1998). Transverse effects and mode couplings in opos. *Applied Physics B: Lasers and Optics*, 66:685–699. xii

[Serafini, 2017] Serafini, A. (2017). *Quantum Continuous Variables: A Primer of Theoretical Methods*. CRC Press. 17, 19

[Serkland et al., 1995] Serkland, D. K., Fejer, M., Byer, R. L., and Y.Yamamoto (1995). Squeezing in a quasi-phase-matched linbo3 waveguide. *Opt. Lett.*, 20(15):1068–1071. 86

[Shannon, 1948] Shannon, C. E. (1948). A mathematical theory of communication. *Bell System Technical Journal*, 27(3):379–423. 31

[Shannon, 1949] Shannon, C. E. (1949). Communication theory of secrecy systems. *The Bell System Technical Journal*, 28(4):656–715. 33

[Shir et al., 2009] Shir, O. M., Roslund, J., and Rabitz, H. (2009). Evolutionary multi-objective quantum control experiments with the covariance matrix adaptation. In Rothlauf, F., editor, *Genetic and Evolutionary Computation Conference, GECCO 2009, Proceedings, Montreal, Québec, Canada, July 8-12, 2009*, pages 659–666. ACM. 124, 147

[Shor, 1994] Shor, P. W. (1994). Algorithms for quantum computation: discrete logarithms and factoring. *Proceedings 35th Annual Symposium on Foundations of Computer Science*, pages 124–134. xi, 33

[Simon, 2000] Simon, R. (2000). Peres-horodecki separability criterion for continuous variable systems. *Physical Review Letters*, 84(12):2726–2729. 75

[Sinha et al., 2010] Sinha, U., Couteau, C., Jennewein, T., Laflamme, R., and Weihs, G. (2010). Ruling out multi-order interference in quantum mechanics. *Science*, 329(5990):418–421. 68

[Soh et al., 2015] Soh, D. B. S., Brif, C., Coles, P. J., Lütkenhaus, N., Camacho, R. M., Urayama, J., and Sarovar, M. (2015). Self-referenced continuous-variable quantum key distribution protocol. *Phys. Rev. X*, 5:041010. 113

[Somaschi et al., 2016] Somaschi, N., Giesz, V., Santis, L. D., Loredo, J. C., Almeida, M. P., Hornecker, G., Portalupi, S. L., Grange, T., Antón, C., Demory, J., Gómez, C., Sagnes, I., Lanzillotti-Kimura, N. D., Lemaítre, A., Auffeves, A., White, A. G., Lanco, L., and Senellart, P. (2016). Near-optimal single-photon sources in the solid state. *Nature Photonics*, 10(5):340–345. xi

[Sporns, 2011] Sporns, O. (2011). *Networks of the brain.* MIT Press. 118

[Staudinger, 1920] Staudinger, H. (1920). Über polymerisation. *Berichte der deutschen chemischen Gesellschaft (A and B Series)*, 53(6):1073–1085. x

[Sudarshan, 1963] Sudarshan, E. C. G. (1963). Equivalence of semiclassical and quantum mechanical descriptions of statistical light beams. *Phys. Rev. Lett.*, 10:277–279. 11

[Suleiman et al., 2022] Suleiman, I., Nielsen, J. A. H., Guo, X., Jain, N., Neergaard-Nielsen, J., Gehring, T., and Andersen, U. L. (2022). 40 km fiber transmission of squeezed light measured with a real local oscillator. *Quantum Science and Technology*, 7(4):045003. 113

[Thiel, 2015] Thiel, V. (2015). *Modal analysis of an ultrafast frequency comb : from classical to quantum spectral correlations*. Theses, Université Pierre et Marie Curie - Paris VI. 111

[Treps et al., 2002] Treps, N., Andersen, U., Buchler, B., Lam, P. K., Maître, A., Bachor, H.-A., and Fabre, C. (2002). Surpassing the standard quantum limit for optical imaging using nonclassical multimode light. *Phys. Rev. Lett.*, 88:203601. xii

[Treps et al., 2003] Treps, N., Grosse, N., Bowen, W. P., Fabre, C., Bachor, H.-A., and Lam, P. K. (2003). A quantum laser pointer. *Science*, 301(5635):940–943. xii

[Trigo Vidarte, 2019] Trigo Vidarte, L. (2019). *Design and implementation of high-performance devices for continuous-variable quantum key distribution*. Theses, Université Paris Saclay (COmUE). 113

[Udem et al., 2002] Udem, T., Holzwarth, R., and Hänsch, T. (2002). Optical frequency metrology. *Nature*, 416(6877):233—237. 49

[Umeki et al., 2011] Umeki, T., Tadanaga, O., Takada, A., and Asobe, M. (2011). Phase sensitive degenerate parametric amplification using directly-bonded ppln ridge waveguides. *Opt. Express*, 19(7):6326–6332. 86

[Usenko et al., 2012] Usenko, V. C., Heim, B., Peuntinger, C., Wittmann, C., Marquardt, C., Leuchs, G., and Filip, R. (2012). Entanglement of gaussian states and the applicability to quantum key distribution over fading channels. *New Journal of Physics*, 14(9):093048. 108

[Usenko et al., 2014] Usenko, V. C., Ruppert, L., and Filip, R. (2014). Entanglement-based continuous-variable quantum key distribution with multimode states and detectors. *Phys. Rev. A*, 90:062326. 106

[Van Assche et al., 2004] Van Assche, G., Cardinal, J., and Cerf, N. (2004). Reconciliation of a quantum-distributed gaussian key. *IEEE Transactions on Information Theory*, 50(2):394–400. 35

[van Loock and Furusawa, 2003] van Loock, P. and Furusawa, A. (2003). Detecting genuine multipartite continuous-variable entanglement. *Physical Review A*, 67(5). 25

[Van Loock et al., 2007] Van Loock, P., Weedbrook, C., , and Gu, M. (2007). Building gaussian cluster states by linear optics. *Phys. Rev. A*, 76:032321. 102

[Volpe et al., 2020] Volpe, L. L., De, S., Kouadou, T., Horoshko, D., Kolobov, M. I., Fabre, C., Parigi, V., and Treps, N. (2020). Multimode single-pass spatio-temporal squeezing. *Optics Express*, 28(8):12385. 69

[Volpe et al., 2019] Volpe, L. L., De, S., Kouadou, T., Michel, T., Ra, Y.-S., Walschaers, M., Fabre, C., Treps, N., and Parigi, V. (2019). Quantum frequency comb for quantum complex networks. In *Quantum Information and Measurement (QIM) V: Quantum Technologies*, page S2B.2. Optica Publishing Group. xii

[Wallraff et al., 2004] Wallraff, A., Schuster, D., Blais, A., Frunzio, L., Huang, R., Majer, J., Kumar, S., Girvin, S., and Schoelkopf, R. (2004). Strong coupling of a single photon to a superconducting qubit using circuit quantum electrodynamics. *Nature*, 431:162–7. xi

[Walschaers, 2021] Walschaers, M. (2021). Non-gaussian quantum states and where to find them. *PRX Quantum*, 2:030204. 12, 29

[Walschaers et al., 2017a] Walschaers, M., Fabre, C., Parigi, V., and Treps, N. (2017a). Entanglement and wigner function negativity of multimode non-gaussian states. *Phys. Rev. Lett.*, 119:183601. xii

[Walschaers et al., 2017b] Walschaers, M., Fabre, C., Parigi, V., and Treps, N. (2017b). Statistical signatures of multimode single-photon-added and -subtracted states of light. *Phys. Rev. A*, 96:053835. xii

[Wang et al., 2019] Wang, Y., Mao, Y., Huang, W., Huang, D., and Guo, Y. (2019). Optical frequency comb-based multichannel parallel continuous-variable quantum key distribution. *Opt. Express*, 27(18):25314–25329. 105

[Watts and Strogatz, 1998] Watts, D. J. and Strogatz, S. H. (1998). Collective dynamics of 'small-world' networks. *Nature*, 393:440–442. 120

[Weedbrook et al., 2012] Weedbrook, C., Pirandola, S., García-Patrón, R., Cerf, N. J., Ralph, T. C., Shapiro, J. H., and Lloyd, S. (2012). Gaussian quantum information. *Reviews of Modern Physics*, 84(2):621–669. 13, 32, 36

[Weiner, 2011] Weiner, A. (2011). Ultrafast optical pulse shaping: A tutorial review. *Optics Communications*, 284(15):3669–3692. 62

[Wigner, 1932] Wigner, E. (1932). On the quantum correction for thermodynamic equilibrium. *Phys. Rev.*, 40:749–759. 11

[Williamson, 1936] Williamson, J. (1936). On the algebraic problem concerning the normal forms of linear dynamical systems. *American Journal of Mathematics*, 58(1):141–163. 21

[Yokoyama et al., 2013] Yokoyama, S., Ukai, R., Armstrong, S. C., Sornphiphatphong, C., Kaji, T., Suzuki, S., ichi Yoshikawa, J., Yonezawa, H., Menicucci, N. C., and Furusawa, A. (2013). Ultra-large-scale continuous-variable cluster states multiplexed in the time domain. *Nature Photonics*, 7(12):982–986. 119, 138

[Young, 1804] Young, T. (1804). I. the bakerian lecture. experiments and calculations relative to physical optics. *Philosophical Transactions of the Royal Society of London*, 94:1–16. ix

[Zhang et al., 2009] Zhang, J., Adesso, G., Xie, C., and Peng, K. (2009). Quantum teamwork for unconditional multiparty communication with gaussian states. *Phys. Rev. Lett.*, 103:070501. 121

[Zyczkowski and Kus, 1994] Zyczkowski, K. and Kus, M. (1994). Random unitary matrices. *Journal of Physics A: Mathematical and General*, 27(12):4235. 124, 125

David FAINSIN **19 Décembre 2023**

Sujet : Continuous Variable Multimode Quantum States at Telecommunication Wavelengths for Quantum Networks

Résumé : Le but de cette thèse est le montage d'une source d'états comprimés du vide multimode aux longueurs d'ondes utilisées pour les télécommunications. Pour ce faire, nous utilisons la conversion paramétrique descendante en simple passage d'un peigne de fréquence dans le proche infrarouge à l'aide d'un guide d'onde ppKTP de type-0. Cette méthode possède beaucoup d'avantages, tout d'abord la production est totalement déterministe ce qui lui offre beaucoup de fiabilité. D'autre part, elle ne nécessite aucun système de cryogénie pour fonctionner. Enfin, elle a été construite à l'aide d'éléments d'optique intégrée (guide d'onde) ce qui laisse à imaginer une intégration sur une puce photonique. Le choix de la longueur d'onde pour les télécommunications n'est pas un hasard non plus, étant donné notre volontée future de transmettre cette source avec le moins de pertes possibles. Nous présentons les résultats du montage et de la caractérisation mode-à-mode de la source allant jusqu'à la production de canevas quantiques. Plus précisément, nous montrons la présence de plus de 20 modes et un degré de compression du vide dans le premier mode supérieur à 2.5dB. En parallèle, nous présentons une proposition expérimentale pour aller vers une application directe de cette source pour des protocoles de cryptographie quantique à variables continues. Enfin, une étude plus théorique est réalisée sur le routage dans les canevas quantiques à structures complexes.

Mots clés : Quantique, Optique, Information

Subject : Continuous Variable Multimode Quantum States at Telecommunication Wavelengths for Quantum Networks

Abstract: The goal of this thesis is to build a source of multimode vacuum squeezed states of light at telecommunication wavelength. We achieve this via in a single-pass spontaneous parametric down-conversion of a frequency comb in the near-infrared using a type-0 ppKTP waveguide. This method offers numerous advantages. Firstly, the production is entirely deterministic, providing a high level of reliability. Additionally, it doesn't require any cryogenic systems to operate. Furthermore, it was constructed using integrated optics elements (waveguides), which suggests the potential for integration on a photonic chip. The choice of wavelength for telecommunications is also deliberate, given our future intention to transmit this source with minimal losses. We present the results of the assembly and mode-to-mode characterization of the source, extending to the production of clusters. More specifically, we demonstrate the presence of over 20 squeezed modes and a degree of squeezing in the first mode exceeding 2.5 dB. In parallel, we present an experimental proposal to move towards a direct application of this source for continuous-variable quantum cryptography protocols. Finally, a more theoretical study is conducted on routing in complex cluster states.

Keywords : Quantum, Optics, Information